Technische Universität München
Institut für Energietechnik

Lehrstuhl für Thermodynamik

# Multi-Effect Vacuum Membrane Distillation for High-Recovery Desalination

## Florian Kiefer

## Acknowledgements

## Abstract

This study investigated the application of Multi-Effect Vacuum Membrane Distillation for treatment of brines with elevated salt content. The underlying objective was to extend the applicability of this hybrid thermal-membrane technology to water extraction from desalination brines and liquid desiccants. A set of tools and experimental methods was developed to support the design process of Vacuum Membrane Distillation systems. An experimentally validated system simulation model helped to predict the performance of multistage systems for a wide range of applications. It was combined with an in-depth analysis of heat and mass transfer phenomena in spacer-filled channels and an approach to predict inorganic membrane fouling. Experimental investigations of scale formation on the membranes helped to quantify the kinetics of crystal growth and the impact on the process. This included flux decline through membrane coverage with salt crystals and membrane wetting induced by crystals.

## Kurzfassung

In dieser Arbeit wurde die Anwendung der mehrstufigen Vakuum-Membrandestillation zur Behandlung von stark salzhaltigen Lösungen untersucht. Das zugrundeliegende Ziel war die Erweiterung des Anwendungsspektrums dieses thermischen Membranverfahrens auf die Wassergewinnung aus Solen von Entsalzungsanlagen und aus flüssigen Trocknungsmitteln. Zur Unterstützung des Auslegungsprozesses von Vakuum-Membrandestillationssystemen wurden Simulationswerkzeuge und experimentelle Methoden entwickelt. Ein experimentell validiertes Simulationsprogramm ermöglichte die Charakterisierung des Betriebsverhaltens von mehrstufigen Anlagen für ein breites Anwendungsspektrum. Dies wurde mit einer eingehenden Analyse von Wärme- und Stofftransportphänomenen in Membrankanälen und einem Programm zur Vorhersage von anorganischen Ablagerungen auf Membranen kombiniert. Darüber hinaus konnten die Kinetik des Kristallwachstums auf Membranen und die daraus resultierenden Auswirkungen auf den Prozess experimentell bestimmt werden.

# Contents

CONTENTS

# List of Figures

# LIST OF FIGURES

# List of Tables

# Nomenclature

**Abbreviations**

| | |
|---|---|
| BHR | Brine Heat Recovery |
| CO | Condenser |
| D-DCMD | Deaerated DCMD |
| DOF | Depth of Focus |
| EDS | Energy-Dispersive X-ray Spectroscopy |
| FOV | Field of View |
| GDPD | Gross Driving Pressure Difference |
| IMD | Isothermal Membrane Distillation |
| LEP | Liquid Entry Pressure |
| MEVMD | Multi-Effect Vacuum Membrane Distillation |
| MF | Microfiltration |
| NCG | Non-Condensable Gases |
| NDPD | Net Driving Pressure Difference |
| OMD | Osmotic Membrane Distillation |
| PP | Polypropylene |
| AGMD | Air Gap Membrane Distillation |
| DCMD | Direct Contact Membrane Distillation |
| ED | Electrodialysis |
| LDAC | Liquid Desiccant Air Conditioning |
| MD | Membrane Distillation |
| MED | Multi-Effect Distillation |
| MSF | Multi-Stage Flash |

| NF | Nanofiltration |
| PGMD | Permeate Gap Membrane Distillation |
| RO | Reverse Osmosis |
| SGMD | Sweep Gas Membrane Distillation |
| VMD | Vacuum Membrane Distillation |
| ZLD | Zero Liquid Discharge |
| PTFE | Polytetrafluoroethylene |
| PVDF | Polyvinylidene fluoride |
| SEM | Scanning Electron Microscope |
| SR | Steam Raiser (in MEVMD plant) |
| TDS | Total amount of Dissolved Solids |
| UF | Ultrafiltration |

## Constants

| $k_B$ | Boltzmann constant | $\left[\mathrm{J\,K^{-1}}\right]$ |
| $R$ | Gas constant | $\left[\mathrm{J\,K^{-1}\,mol^{-1}}\right]$ |

## Dimensionless Numbers

| Kn | Knudsen number |
| Nu | Nusselt number |
| Pr | Prandtl number |
| Re | Reynolds number |
| Sc | Schmidt number |
| Sh | Sherwood number |

## Exponents

| actual | Actual property of real solution |
| E | Excess quantity |
| ideal | Ideal (solution) property |
| ig | Ideal gas |

| in | Value at inlet | |
|---|---|---|
| $j$ | Index of volume element | |
| $\phi$ | Apparent property | |
| sat | Saturated state (equilibrium solubility) | |
| ⊖ | Standard state | |
| * | Pure substance | |

## Greek Symbols

| $\alpha$ | Heat transfer (film) coefficient | $[\text{W}\,\text{m}^2\,\text{K}^{-1}]$ |
|---|---|---|
| $\beta$ | Mass transfer (film) coefficient | $[\text{m}\,\text{s}^{-1}]$ |
| $\chi$ | Tortuosity | $[-]$ |
| $\delta$ | Layer thickness | $[\text{m}]$ |
| $\gamma_{\pm}$ | Mean molal activity coefficient | $[-]$ |
| $\gamma_i$ | Molal activity coefficient of component $i$ | $[-]$ |
| $\mu$ | Chemical potential | $[\text{J}\,\text{mol}^{-1}]$ |
| $\nu$ | Kinematic viscosity | $[\text{m}^2\,\text{s}^{-1}]$ |
| $\Phi$ | Scalar field | |
| $\phi$ | Osmotic coefficient | $[-]$ |
| $\rho$ | Density | $[\text{kg}\,\text{m}^{-3}]$ |
| $\sigma$ | Surface energy | $[\text{J}\,\text{m}^{-2}]$ |
| $\sigma_{\text{coll}}$ | Collision diameter | $[\text{m}]$ |
| $\theta$ | Contact angle | $[°]$ |
| $\varepsilon$ | Porosity, void fraction | $[-]$ |
| $\varphi$ | Ratio free energy of heterog. to homog. nucleation | $[-]$ |
| $\zeta$ | Friction coefficient | $[-]$ |

## Indices

| $\delta$ | Property averaged across the film layer |
|---|---|
| $i$ | Running index, component index |
| $j$ | Current component index |
| 11, 12 | Steam raiser inlet and outlet (Memsys nomenclature) |
| $2i$ | Salt solution (Memsys nomenclature), e.g. index 21 for feed to first |

|          | stage |
|----------|-------|
| 31       | Brine at outlet of last stage (Memsys nomenclature) |
| 41       | Distillate outlet (Memsys nomenclature) |
| 61, 62   | Condenser inlet and outlet (Memsys nomenclature) |
| $7i$     | Steam heating stage $i$ (Memsys nomenclature) |
| A        | Solvent |
| B        | Bulk |
| B        | Solute |
| C        | Crystal phase |
| Chem     | Chemicals |
| CO       | Condensate; condenser |
| crit     | At critical volume during nucleation |
| D        | Distillate |
| dil      | Dilution (state change) |
| entry    | Pore entry (cf. LEP) |
| eq       | Equilibrium state |
| F        | Feed solution |
| het      | Heterogeneous |
| hom      | Homogeneous |
| hydr     | Hydrostatic |
| ig       | Ideal gas |
| in       | Value at inlet |
| ind      | Induction period |
| interface | Interface or phase boundary |
| Kn       | Knudsen flow |
| last     | Last heat of solution |
| M        | Membrane; at the membrane surface |
| m        | Molar value |
| max      | Maximum |
| meas     | Measured value |
| min      | Minimum |
| mix      | Mixing (state change) |
| out      | Value at outlet |
| P        | Permeate |

| | | |
|---|---|---|
| pore | Membrane pore | |
| prim | Primary | |
| red | Reduced | |
| ref | Reference state | |
| s | Solute or salt | |
| sat | Saturation | |
| sec | Secondary | |
| sep | Separation | |
| set | Boundary value set by user | |
| tot | Total amount; all components in a multi-component system | |
| V | Volume | |
| v | Vapor | |
| V,SP | Volume specific | |
| vac | Vacuum | |
| VC | Vapor channel | |
| Vis | Viscous flow | |
| w | Water | |

## Variables

| | | |
|---|---|---|
| $A$ | Area | $\left[\text{m}^2\right]$ |
| $a$ | Activity | $[-]$ |
| $a$ | Thermal diffusivity | $\left[\text{m}^2\,\text{s}^{-1}\right]$ |
| $A_{\text{BCF}}$ | Rate constant in BCF crystal growth model | $\left[\text{m}^{-1}\,\text{s}\right]$ |
| $A_{\text{DHLS}}$ | Debye-Hückel limiting slope | $[-]$ |
| $A_{\text{N}}$ | Rate constant in nucleation rate equation | $\left[\text{s}^{-1}\right]$ |
| $A_{\text{V,SP}}$ | Volume specific surface of spacer | $\left[\text{m}^2\right]$ |
| $a_1$ | Empirical constant in Sherwood correlation | $[-]$ |
| $a_2$ | Empirical constant in Nusselt correlation | $[-]$ |
| $B$ | Correction factor for pore geometry (LEP definition) | $[-]$ |
| $b$ | Molality $n_i / m_{\text{solvent}}$ | $\left[\text{mol\,kg}^{-1}\right]$ |
| $B_{\text{BCF}}$ | Constant in BCF crystal growth model | $\left[\text{m}^{-1}\,\text{s}\right]$ |
| $B_{\text{N}}$ | Exponential factor in nucleation rate equation | $[-]$ |
| $b_1$ | Empirical constant in Sherwood correlation | $[-]$ |

| | | |
|---|---|---|
| $b_2$ | Empirical constant in Nusselt correlation | $[-]$ |
| $c$ | Molar concentration $n_i/V$ | $\left[\mathrm{mol\,m^{-3}}\right]$ |
| $c_1$ | Empirical constant in Sherwood correlation | $[-]$ |
| $c_2$ | Empirical constant in Nusselt correlation | $[-]$ |
| $c_p$ | Specific heat capacity | $\left[\mathrm{J\,kg^{-1}\,K^{-1}}\right]$ |
| $C_{p,\mathrm{rel}}$ | Total relative heat capacity of a system | $\left[\mathrm{J\,K^{-1}}\right]$ |
| $D$ | Diffusion coefficient | $\left[\mathrm{m^2\,s^{-1}}\right]$ |
| $d$ | Diameter | $[\mathrm{m}]$ |
| $d_{\mathrm{hydr}}$ | Hydraulic diameter | $[\mathrm{m}]$ |
| $G$ | Gibbs energy | $[\mathrm{J}]$ |
| $g$ | Growth order | $[-]$ |
| $G_{\mathrm{V}}$ | Gibbs volume energy | $\left[\mathrm{J\,m^{-3}}\right]$ |
| $H$ | Channel height | $[\mathrm{m}]$ |
| $H$ | Enthalpy | $[\mathrm{J}]$ |
| $h$ | Specific enthalpy | $\left[\mathrm{J\,kg^{-1}}\right]$ |
| $H_{\mathrm{rel}}$ | Total relative enthalpy of a system | $[\mathrm{J}]$ |
| $I$ | Ionic strength | $[-]$ |
| IAP | Ion activity product | $[-]$ |
| $j$ | Mass flux | $\left[\mathrm{kg\,m^{-2}\,s^{-1}}\right]$ |
| $K_{\mathrm{G}}$ | Overall growth coefficient | $\left[\mathrm{m\,kg\,mol^{-1}\,s^{-1}}\right]$ |
| $K_{\mathrm{M}}$ | Membrane permeability | $\left[\mathrm{kg\,m^{-2}\,s^{-1}\,Pa^{-1}}\right]$ |
| $k_{\mathrm{N}}$ | Empirical rate constant for nucleation rate | $\left[\mathrm{m^3 mol^{-1} s^{-1}}\right]$ |
| $K_{\mathrm{sp}}$ | Solubility product | $[-]$ |
| $K_i$ | Solubility product of component $i$ | $[-]$ |
| $L$ | Length | $[\mathrm{m}]$ |
| $\ell$ | Mean free path length | $[\mathrm{m}]$ |
| LEP | Liquid Entry Pressure | $[\mathrm{Pa}]$ |
| $M$ | Molar mass | $\left[\mathrm{kg\,mol^{-1}}\right]$ |
| $m$ | Mass | $[\mathrm{kg}]$ |
| $\dot{m}$ | Mass flow rate | $\left[\mathrm{kg\,s^{-1}}\right]$ |
| $N$ | Number | $[-]$ |
| $n$ | Mole number | $[\mathrm{mol}]$ |
| $\dot{N}$ | Mole flow rate | $\left[\mathrm{mol\,s^{-1}}\right]$ |
| $\dot{N}$ | Nucleation rate | $\left[\mathrm{s^{-1}}\right]$ |

| | | |
|---|---|---|
| $\dot{n}$ | Molar flux | $\left[\mathrm{mol\,m^{-2}\,s^{-1}}\right]$ |
| $\mathbf{n}_\mathrm{M}$ | Membrane normal vector | $[-]$ |
| $p$ | Pressure | $[\mathrm{Pa}]$ |
| $\dot{Q}$ | Heat flow rate | $[\mathrm{W}]$ |
| $r$ | Radius | $[\mathrm{m}]$ |
| $R_\mathrm{G}$ | Growth rate | $\left[\mathrm{m\,s^{-1}}\right]$ |
| $R_A$ | Areal growth rate | $\left[\mathrm{m^2\,s^{-1}}\right]$ |
| RR | Recovery rate | $[-]$ |
| $\mathrm{RR_m}$ | Molar water recovery rate | $[-]$ |
| $S$ | Entropy | $\left[\mathrm{J\,K^{-1}}\right]$ |
| $S$ | Supersaturation | $[-]$ |
| $S_\mathrm{rel}$ | Relative supersaturation | $[-]$ |
| SI | Saturation index | $[-]$ |
| $T$ | Temperature | $[\mathrm{K}]$ |
| $u$ | Velocitiy | $\left[\mathrm{m\,s^{-1}}\right]$ |
| $V$ | Volume | $\left[\mathrm{m^3}\right]$ |
| $V_\mathrm{A}$ | Partial molar volume of the solvent | $\left[\mathrm{m^3 mol^{-1}}\right]$ |
| $w$ | Mass fraction $m_\mathrm{solute}/m_\mathrm{solution}$ | $\left[\mathrm{kg\,kg^{-1}}\right]$ |
| $\dot{W}$ | Mechanical work | $[\mathrm{W}]$ |
| $x$ | Mole fraction $n_i/n$ | $\left[\mathrm{mol\,mol^{-1}}\right]$ |
| $z_+, z_-$ | Charge number | $[-]$ |

# 1 Introduction

Water scarcity and limited access to clean water are issues in many regions around the world. Stress on existing clean water resources is increasing as a result of growing demand, depletion of resources, pollution, and desertification. Drought associated with climate change will further intensify the problem [1]. Methods which address these problems are water treatment and reuse, as well as desalination of sea or brackish water. The energy required for desalination is a drawback of accessing this generally unlimited source of clean water [2]. In addition, desalination plants reject a brine stream with an increased salt content and additional chemicals, which further impacts the environment [3].

## 1.1 Background and Motivation

Today[1], the amount of water produced by desalination worldwide is 95.37 million $m^3$ per day, which has an energy requirement of 430 MWh per day [2] leading to an average $CO_2$ footprint of 0.4-26.9 kg m$^{-3}$ [5] depending on the water source, the technology used, and the energy mix[2]. From this total desalination capacity, 25% relies on thermal energy, mainly coupled with thermal power plants[1]. Almost all of the rest is provided by Reverse Osmosis (RO), a membrane desalination technology that has been subject to exponential growth since the beginning of the 21st century. It has reached a share of 69% of the worldwide desalination capacity and 53% for sea and brackish water[1]. RO is one of the most energy efficient desalination technologies, but relies on electricity for driving the water through the membranes. The remaining 5% of desalination capacity is also covered mainly by membrane technologies[3].

---

[1] Current state according to Jones et al. (2019) [4].

[2] Total equivalent electrical energy requirement for different desalination technologies. Thermal: Multi-Effect Distillation (MED) 6.0-10 kWh/m$^3$, Multi-Stage Flash (MSF) 13.5-23.5 kWh/m$^3$; Membrane: Reverse Osmosis (RO) 4.0-4.5 kWh/m$^3$ [5].

[3] Nanofiltration (NF) with 3% and Electrodialysis (ED) with 2%, other technologies with less than 1% [4].

What these desalination plants have in common is that they produce a product with reduced salt concentration and a concentrated waste stream called brine. The latter contains an increased amount of salt as well as chemicals which have been added during the process. Since desalination plants are optimized for energy efficiency and low product cost, the average amount of potable water recovered from seawater lies in the range of 22 to 25% for thermal plants and 42% for RO [4]. This leads to a total brine production of $141.5{\cdot}10^6\,\mathrm{m}^3$ per day [4] which has finally caught public attention. In the desalination community, the topic has been an object of research for several years [6]. The research focus has been on an increase of water recovery, which includes investigation into complete separation of solids and liquids. These technological approaches are summarized under the term Zero Liquid Discharge (ZLD).

There are mainly three drivers to apply high-recovery desalination. First, the brine disposal is linked to severe environmental impact. The high solute concentration and other waste chemicals impact the flora and fauna near the discharge site. Proper disposal and distribution of brine is associated with significant investment cost. Especially for inland desalination, the disposal creates 5-35% of the total water cost. Secondly, the pretreatment cost decreases with increasing water recovery. Thirdly, in arid regions or due to expensive wells and associated pumping, the limited and expensive raw water makes desalination plants more profitable if they operate at higher recovery ratios. Further drivers for greater water recovery could be the recovery of minerals as by-product or energy recovery from brine. Both could bring an additional financial asset. [7]

Besides the aim to reduce liquid discharge from desalination plants, there are further application areas for technologies which extract water from solutions with high osmotic pressure or low vapor pressure. Salt solutions at elevated concentration are used for technologies where an osmotic driving potential is needed. This is the case for Forward Osmosis and Pressure Retarded Osmosis. For air dehumidification purposes, a reduced equilibrium vapor pressure is required in Liquid Desiccant Air Conditioning (LDAC).

Figure 1.1 provides an overview of desalination techniques and their range

of application with respect to feed and brine concentration. It is evident, that two main limiting factors exist. One is the osmotic pressure of 70 bar at around 80 g kg$^{-1}$, which limits the operation of RO. Further, the saturation limit of sparingly soluble salts impacts the operation of a wide range of technologies. Finally, the solubility limit of NaCl is reached near 260 g kg$^{-1}$. A large gap exists between technologies designed for desalination and brine crystallization.

In this context, the technology of Membrane Distillation (MD) is investigated in the work at hand. It is a hybrid thermal-membrane desalination technology with the theoretical capability to bridge the above mentioned gap. The general objectives are an operation range extended beyond the applicability of RO for the purpose of high-recovery desalination, brine concentration, and regeneration of solutions with reduced vapor pressure or elevated osmotic pressure. Current research is concerned with methods for reducing energy requirement (1, Fig. 1.1) and expanding the operation range (2).

| Abbrev. | Name |
|---|---|
| BC | Brine concentrator |
| Brine Cryst. | Brine crystallizer (mainly MVC) |
| BW-RO | Brackish water RO |
| ED | Electrodialysis |
| EDR | ED Reversal |
| MD | Membrane Distillation |
| MED | Multi-Effect Distillation |
| MSF | Multi-Stage Flash |
| MVC | Mechanical Vapor Compression |
| RO | Reverse Osmosis |
| SW-RO | Sea water RO |
| (th.) | only thermal |
| (tot. eq.) | total equivalent electrical energy requirement |
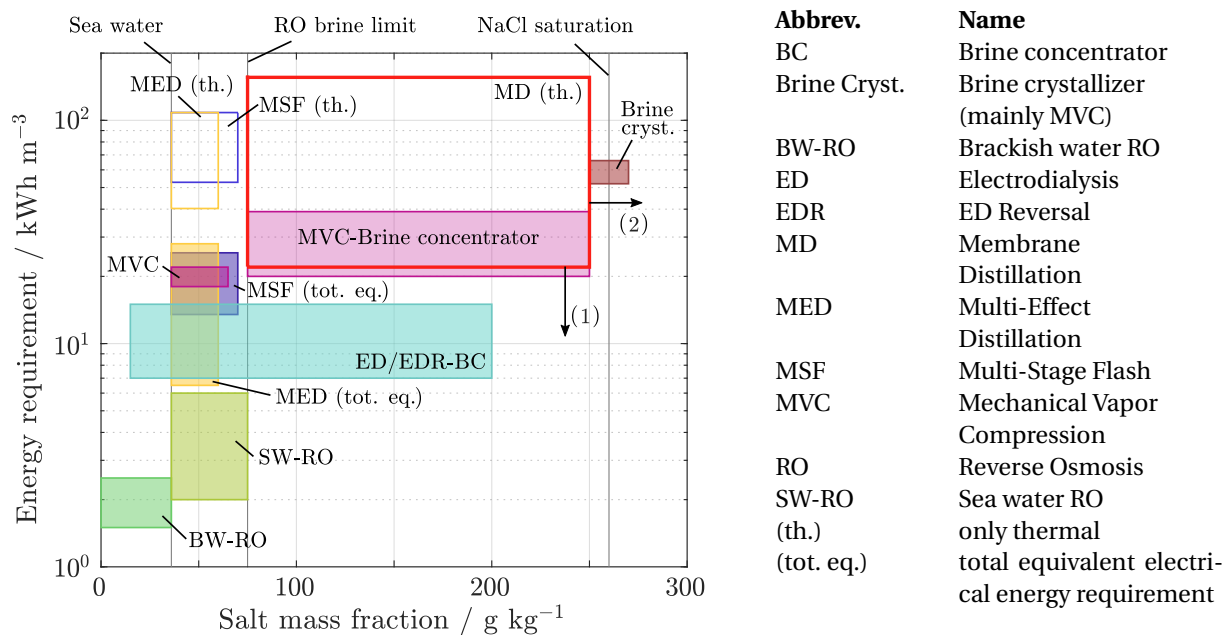
**Figure 1.1:** Desalination technologies classified according to their operation range concerning salt concentration and specific energy requirement (electrical, if not marked as total equivalent electrical or thermal) according to Refs. [6, 8, 9], MD: Refs. [6, 10, 11].

## 1.2   State of Technology in Membrane Distillation

In the context of water scarcity, brine disposal, and $CO_2$ emissions, MD is one of the most frequently and most controversially discussed technologies. Dating back to its first description in the 1960s by Findley [12], the technology has not yet had any substantial market impact. In the last years, it has been commonly accepted that MD will not be economically competitive with RO or ED for desalination of sea and brackish water. However, it has advantages in fields of application where higher salt concentrations and therefore large osmotic pressures prevail. With this background, the general working principles and the key features of MD are introduced in the following. Based on the challenges arising from the application area, the following sections present the objectives and introduce to the approach to solutions.

The key characteristic of Membrane Distillation is the evaporation of volatile feed components through a hydrophobic, microporous membrane [13]. Arising from this, the driving force for the separation process is a partial pressure difference of the volatile substances across the membrane. The present work focuses on the treatment of aqueous solutions such as sea water. Therefore, the following description is reduced to water being the major volatile component.

Different types of MD processes have been developed over the years. Findley [12] started with Direct Contact Membrane Distillation (DCMD). He called it "infinite stage distillation" [12], since the membrane is in contact with two liquid streams and the vapor phase only exists inside the membrane pores (c.f. Fig. 1.2). The vapor pessure difference across the membrane results from the temperature difference between the feed stream and the distillate stream. Therefore, DCMD systems are compact but are subject to significant heat loss across the membrane, from hot feed to cold distillate. Therefore, only small temperature differences are applied in a counterflow configuration of feed and distillate stream [14]. However, this leads to small distillate fluxes specific to the membrane area. To further reduce heat losses, different configurations of the permeate side have been investigated. Air Gap Membrane Distillation (AGMD) moves the condensation away from the membrane. A thin
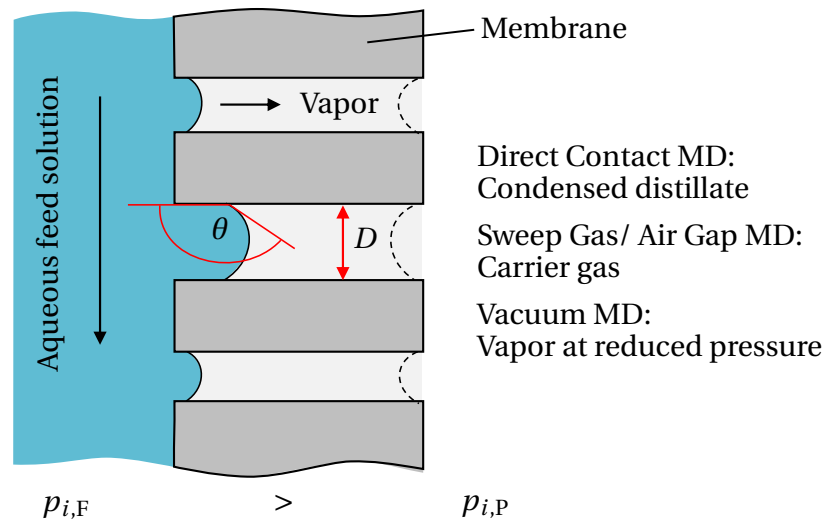
**Figure 1.2:** Membrane Distillation process concept for different permeate channel types: the partial vapor pressure difference across the membrane $p_{i,F} - p_{i,P}$ depends on the feed (index F) and permeate (index P) side temperature and composition.

air layer lies between the membrane and a cooled condenser surface. This reduces heat transfer across the membrane, but leads to an increased transport resistance for vapor to reach the condenser surface. A combination of the two techniques, called Permeate Gap Membrane Distillation (PGMD) has been commercialized by SolarSpring GmbH, Germany. The spiral wound modules developed by Koschikowski [10] provide distillate fluxes of 0.5-3.1 kg m$^{-2}$ h$^{-1}$ at a thermal energy requirement of 120-260 kWh m$^{-3}$ and feed inlet and condenser inlet temperatures of 60-85 °C and 23 °C respectively. He observed a reduction in permeate flux for sea water desalination. At 50% water recovery he discovered a reduction in permeate flux of up to 40% compared to operation with pure water.

Vacuum Membrane Distillation (VMD) has been suggested as a way to overcome the drawback of low distillate production and heat losses across the membrane [15]. The key feature is that the permeate channel operates at a pressure below the equilibrium vapor pressure of the feed solution. The vapor is extracted from this channel and led to a separate condenser. This way, noncondensable gases are removed from the membrane pores and the condenser surface. This significantly reduces the transport resistance in the pores and

improves condensation. The results are higher distillate fluxes specific to the membrane area. Mericq et al. [16] report fluxes of 7.5-10 kg m$^{-2}$ h$^{-1}$ for feed temperatures of 50 °C and vacuum pressures of 45-70 mbar. They calculated distillate specific energy requirements in the range of 95-180 kWh m$^{-3}$.

The vapor has to be condensed upstream of the vacuum pump. Finally, the condenser temperature determines the vapor channel pressure. The heat of condensation has to be rejected or better integrated into the process. To increase energy efficiency, multi-effect arrangements, as known from Multi-Effect Distillation (MED) and Multi-Stage Flash (MSF) desalination plants, were proposed by Zhao et al. [11] and Summers et al. [17] respectively. The MED-like approach was commercialized by Memsys Tec AG and is investigated in parts of this work. Section 2.1.3 describes the functional principle in detail. In the following, this configuration is referred to as Multi-Effect Vacuum Membrane Distillation (MEVMD). The resulting distillate fluxes and the energy requirement of MEVMD systems depend on the number of stages, which determine the internal reuse of heat. Moreover, the heating temperature at the highest level and the heat rejection temperature found at the final condenser determine the overall driving potential applied to the system. Zhao et al. [11] measured distillate fluxes of 3.8 and 3.0 kg m$^{-2}$ h$^{-1}$ leading to a thermal energy requirement of 356 and 235 kWh m$^{-3}$ for a system with two or four effects respectively. The feed was pure water, the heating temperature at 60 °C, and the condenser temperature at 25 °C. Wenzel et al. [18] investigated the same system with up to 24% brine salt mass content and demonstrated that the plant is able to provide very low product salinity for long-term operation. Nevertheless, a significant influence of the salt content on the distillate amount was observed.

The feed's salt concentration influences its equilibrium vapor pressure and leads to a reduced driving potential across the membrane. Therefore, all types of MD systems suffer from increased salt concentration in terms of reduced distillate flux. To overcome this, the feed temperature level can be increased. This leads to reduced exergy efficiency and is finally limited by the materials in use. For the system investigated, this maximum temperature lies at around 90 °C for the membrane backing and frame material Polypropylene (PP). Fi-

nally, the whole multi-stage system shows a complex response to the vapor pressure reduction caused by increased salt concentration in the feed. It is not possible to predict this behavior on the basis of integral heat and mass balancing or a lumped parameter model [19]. Therefore, a more advanced simulation approach was implemented which is documented in Sec. 3.3.

## 1.3 Challenges Faced in High-Recovery Desalination using Membrane Distillation

Water recovery from a salty water source leads to an increase in the salt concentration of the remaining feed solution. The increase in salt concentration causes an increase in osmotic pressure and a decrease in equilibrium vapor pressure. After a certain concentration is reached, one or more solutes will reach their solubility limit and create a second phase. This describes the two major challenges of high-recovery desalination. First, a greater effort is needed to extract water from the solution. Secondly, dissolved solids, which crystallize inside the desalination equipment, settle on membranes, pipes, or other process equipment and cause an increase in resistance to heat and mass transfer. This crystallization is referred to as scaling.

### 1.3.1 Fouling in Membrane Distillation

Fouling is the comprehensive term for scaling, as well as inorganic and organic deposits and micro-organisms which grow into a biofilm. It is a severe issue for all types of heat and mass exchangers. In the case of membrane distillation, the following characteristics have been described:

- The risk of particulate fouling in MD is similar to that of all other membrane desalination techniques [20, 21]. Especially the spacers in the feed channel cause particulate deposition in regions with low flow velocity at the spacer filaments [22]. In contrast to RO, and especially to filtration techniques such as Ultrafiltration (UF) and Microfiltration (MF), the lower fluxes across the membrane cause a lower drag force towards the

membrane and therefore reduced deposition.

- Although particulate fouling of organic matter can take place in an MD system, the risk of biofouling is reduced if the plants are operated at feed temperatures above 60 °C [20]. The transport of organic matter into the system does not lead to a biofilm growth if the plant runs continuously at elevated temperatures.
- Scaling is a major issue in MD [20, 23, 24]. There are two reasons. First, the application in brine treatment results in a generally higher salt concentration compared to sea or brackish water. Secondly, the elevated operating temperature level increases the scaling propensity of salts having an inverse solubility (e.g., species of calcium carbonate and calcium sulphate).

In comparison to other MD technologies, VMD shows high distillate fluxes. Therefore, a more pronounced susceptibility towards scaling can be expected. Since the permeate channel pressure will be approximately constant over the whole membrane channel, the cross flow arrangement of the feed and vacuum side lead to greater differences in the driving force over the length of a channel than for counterflow DCMD. This shows why it is necessary to distinguish between different MD technologies in order to interpret experimental findings.

### 1.3.2 Membrane Wetting

One major threat to MD is the wetting of the membrane. It takes place when the pressure difference between feed and permeate exceeds the capillary pressure of membrane pores. This can be caused by an increased feed pressure or by a change in membrane hydrophobicity through material degradation, fouling, or adsorption of surfactants (cf. Fig. 1.2 and Sec. 2.1.1). Gryta [23] linked membrane wetting to scaling. He predicted salt crystallization inside the pores as shown in Fig. 1.3. The meniscus moves into the pore due to continuous scale growth. When it reaches the permeate side, permanent leakage is established. This has to be prevented, since the pressure difference $p_{\text{hydr,F}} - p_{\text{vac}}$ applied across the membrane pumps liquid feed to the permeate side. Only particles are filtered out according to the pore size of the membrane in use.
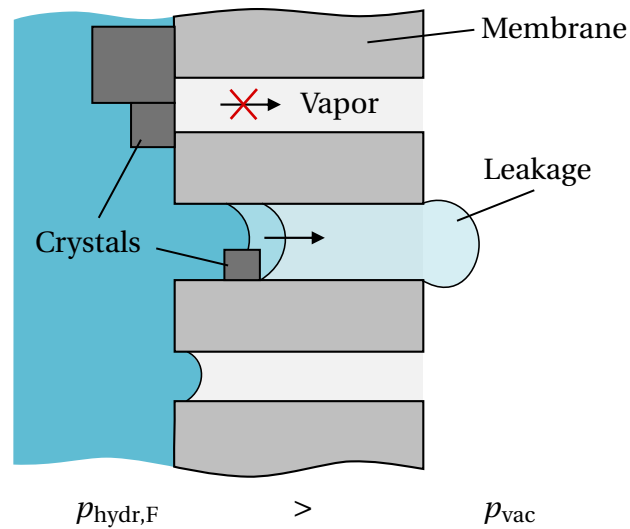
**Figure 1.3:** Pore model for scaling-induced membrane wetting based on Gryta [23] and extended to VMD.

Consequently, the leakage pollutes the permeate. For VMD, leakage results in depleted vacuum pressure and problems in plant operation. The evaporation of leaking feed solution results in crystallization of salts in the permeate channel. By measuring the cross-membrane impedance in a DCMD system, Chen et al. [25] were able to show that membrane wetting can be a continuously advancing process in which the salt solution enters the membrane and propagates through it until a breakthrough occurs. Their experiments show that the process is dominated by diffusion and adsorption of the wetting agent used.

### 1.3.3 Integration of Membrane Distillation in Zero Liquid Discharge Systems

One way to overcome the problem of the disposal of brines from desalination or industry is to implement a complete separation of solids and liquids in a so called Zero Liquid Discharge (ZLD) system. The first stage of this system would be an energy efficient desalination approach such as RO. It rejects brine at a concentration of around 70 000 ppm and requires further stages to increase the salt concentration of the brine. Pursuing the use of Membrane

Distillation in this brine treatment system, two different possible points for its integration can be identified (c.f. Fig. 1.4) [6]. Those are the further recovery of water until the brine is nearly saturated for one or more solutes, and to generate supersaturated brine to feed a crystallizer. The conceptualization of such a system is mainly influenced by the composition of the brine rejected at the RO stage. For brackish water desalination, RO generally operates a recovery rate up to the saturation of sparingly soluble salts. These would have to be removed before further water recovery in an MD subsystem. This can be done by chemical softening, Ion Exchange (IX), or pH adjustment during pretreatment (PT) or intermediate treatment (IT) [26, 27]. If the RO is fed with seawater, it is not unusual that the brine does not reach saturation limit of any solute and a further increase in recovery using MD is possible. For the first MD stage, pursuing the increase of water recovery, the requirements for the system are energy efficiency and robustness to withstand fluctuations in feed water composition. Chapter 6 contains necessary design considerations. A general advantage of MD in this respect is that it mainly relies on low temperature heat and might be operated with waste heat or solar thermal heat. The second point for the integration of MD into the ZLD process, shown in Fig. 1.4, is generating a supersaturated solution to feed the crystallizer. A low cost alternative to this MD-crystallizer combination would be an evaporation pond.

Various authors, e.g. Refs. [23, 28–35], described the combination of MD with crystallizers. The MD module is used to generate a saturated or supersatu-
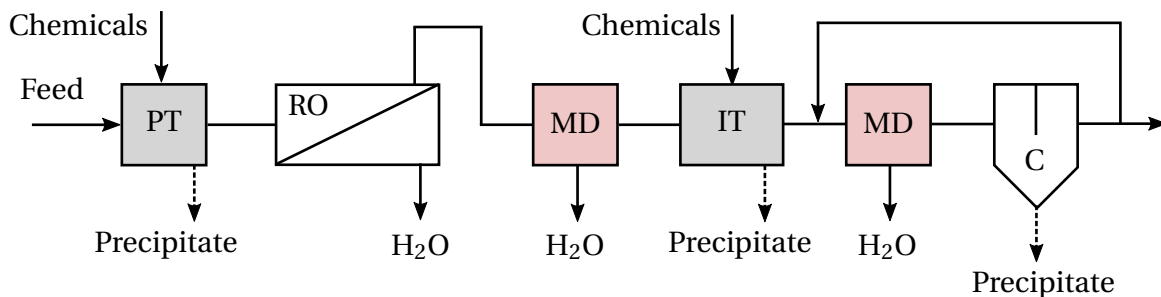


**Figure 1.4:** Integrated Zero Liquid Discharge (ZLD) process using Reverse Osmosis (RO), Membrane Distillation (MD), crystallization (C), as well as pre- (PT) and intermediate treatment (IT).

rated state. The downstream crystallizer is then used to reduce the supersaturation. The brine is filtrated, recycled, and diluted with makeup, whereas the crystals are separated. Pantoja et al. [28] distinguish between processes using isothermal crystallizers and cooled crystallizers. For solutes with low temperature dependency of the solubility curve, for example NaCl, it is necessary to reach supersaturation already in the MD module without risking scale formation. However, there exists a gap of knowledge with regard to the prediction of scaling kinetics and the interaction of scales with the membrane. This gap is to be closed to predict the scaling in MEVMD systems and to design the systems for use in ZLD.

## 1.4   Objectives and Structure of this Work

The objectives of this thesis were derived from the technical challenges arising when an MEVMD plant is integrated into a high-recovery or ZLD desalination system. Therefore, the first objective was to develop a tool that helps to predict the behavior of MEVMD systems operated at elevated feed concentrations. The resulting simulation program is able to describe the system on a mechanistic basis and allows performance prediction and application specific plant design.

From this system level, critical operation conditions and spots endangered by scaling were identified. These spots were then investigated on a more detailed level to describe the interplay of fluid flow, heat and mass transfer across the membrane, and scale formation on the membrane. The underlying objective was to develop an approach to predict the scaling propensity based on the spatially averaged state in the membrane channel calculated with the system simulation tool.

Finally, at an even higher spatial resolution of the phenomena which occur at the membrane, the interplay of scaling and membrane wetting was investigated. The objective was to identify scalants and operating conditions which trigger membrane wetting. Together, these three steps from a system level analysis down to the membrane-scalant interaction support the design of MEVMD in ZLD applications.

Accordingly, the work at hand is structured as follows: Chapter 2 provides the basic principles of MEVMD with a focus on transport processes for later mechanistic modeling. Further, it summarizes necessary fundamentals on the thermophysical behavior of salt solutions. Chapter 3 describes the experimental investigation of the MEVMD system and the model derivation and verification. Subsequently, in Ch. 4 Computational Fluid Dynamics (CFD) methods are utilized to predict the thermophysical state at the membrane. This closes the gap from the system simulation tool to the investigation of scaling and membrane wetting described in Ch. 5. The findings and methods are applied in Ch. 6 to derive application specific plant optimization strategies and describe application limits of the MEVMD technology.

# 2  Fundamentals and Definitions

This chapter reviews the fundamentals of the Membrane Distillation process and associated transport phenomena. Further, the thermodynamic fundamentals of electrolyte solutions and the basic principles of membrane scaling are introduced.

## 2.1  Membrane Distillation Process

### 2.1.1  Characterization of the Process

General prerequisites for the MD process are a hydrophobic or partially hydrophobic, porous membrane which is not wetted. This means there is no condensed vapor inside the pores and, therefore, the driving force for mass transfer across the membrane is established by a partial pressure difference of volatile components. The flux across the membrane is then determined by

$$j_{\mathrm{P}} = K_{\mathrm{M}} \, (p_{i,\mathrm{M,F}} - p_{i,\mathrm{M,P}}), \tag{2.1}$$

with a membrane permeability $K_{\mathrm{M}}$. The difference in partial pressures of a volatile component $i$ at the feed side $p_{i,\mathrm{M,F}}$ and the permeate side $p_{i,\mathrm{M,P}}$ of the membrane establishes the driving force for mass transfer of component $i$ across the membrane. The task of the membrane is to stabilize the liquid-vapor interface. Thus, thin feed channels with large specific surface areas and well defined feed flow can be constructed.

Hydrophobic polymers that can withstand the desired temperature range are chosen as membrane material. Generally, active membrane surfaces are manufactured from PTFE, PVDF, or PP. The backing material does not have to be hydrophobic. It provides mechanical stabilization and is often manufac-

tured from PP. Figure 2.1 shows a Scanning Electron Microscope (SEM) micrograph of the active membrane layer (left) and the backing structure (right). The membrane is a GE Aspire Microfiltration membrane [36] as used in the experiments conducted for this work. The active layer is made from expanded PTFE, the backing structure is made of PP.

To establish a large liquid-vapor interface area and reduce transport resistance across the membrane, a high level of porosity is necessary. Membrane reference pore radii are generally in a range of 0.1 to 5 µm [13]; a narrow band width is desirable. The pressure difference between the feed and permeate side must not exceed the Liquid Entry Pressure (LEP) of the membrane in order to hinder liquid feed solution from leaking through the pores. This value is defined based on the capillary pressure difference according to Young-Laplace applied to arbitrary shaped pores [37], as

$$p_{\mathrm{hydr,F}} - p_{\mathrm{vac}} \approx \Delta p_{\mathrm{interface}} < \Delta p_{\mathrm{entry}} = \mathrm{LEP} = \left| \frac{4B\sigma}{d_{\mathrm{pore,max}}} \cos\theta \right|. \qquad (2.2)$$

This takes into account the surface tension $\sigma$ of the liquid-vapor interface inside the pore, the diameter $d_{\mathrm{pore,max}}$ of the largest pore, the contact angle $\theta$ between the fluid and the membrane material, and the pore geometry. The pore geometry is correlated with experiments in terms of a correction factor $B$ that includes the deviation from a circular shape. Qtaishat and Matsuura [38]



Mag = 5000 X
WD = 13 mm
EHT = 10.00 kV

10 µm

100 µm

Mag = 500 X
WD = 13 mm
EHT = 10.00 kV
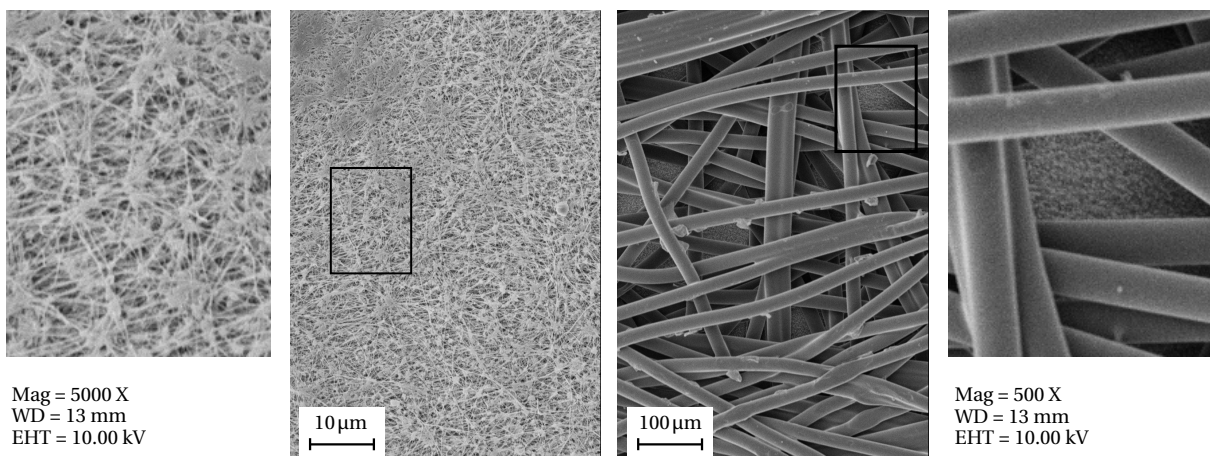
**Figure 2.1:** SEM images of the membrane active layer (left) and the backing structure (right) of a GE Aspire Microfiltration membrane [36].

extended this model and showed that contact angles below 90° can be tolerated when a partial intrusion into the pore is accepted.

In general, LEP models do not include a realistic description of the membrane pore. Pore geometry parameters are determined by experiments. The LEP and the pore intrusion are significantly influenced by surface properties and especially by material deposits.

### 2.1.2   Classification of Process Variants

Different process configurations are summarized under the term Membrane Distillation. These configurations share the membrane type and the basic separation principle, but show fundamental differences in underlying transport processes. Figure 2.2 summarizes and classifies the different MD types. Systems containing a significant amount of non-condensable gases (NCG) can be distinguished from deaerated or vacuum systems. The NCG content influences the transport regime in the membrane pores and the efficiency of vapor condensation [39].

Further, the process configurations differ in how the permeate channel is used. In Direct Contact MD (DCMD) cold distillate circulates on the permeate side of the membrane. The vapor passing the pores from feed to permeate directly condenses at the vapor-liquid interface on the permeate side [40]. If the system is deaerated, it is called D-DCMD [39]. In Air Gap MD (AGMD) the permeate channel is filled with air to reduce heat losses from the feed channel. The vapor diffuses through the membrane and the air channel to condense on a surface which separates the cooling and air channels [41]. If this air channel is allowed to fill with condensate, the plant configuration is called Permeate Gap MD (PGMD) [10]. Similar to AGMD, in Sweep Gas MD (SGMD) the permeate channel is filled with a non-condensable gas. The dry carrier gas is circulated through the channel where it is humidified. The vapor is condensed in an external condenser [41]. An external condenser is used in Vacuum MD (VMD) systems, too. These systems operate under reduced pressure so that the permeate channel is only used to collect the vapor and lead it to the condenser [15]. Osmotic MD (OMD), also referred to as Isothermal MD (IMD) is

similar to DCMD only that the reduced equilibrium vapor pressure of the fluid on the permeate side is attained chemically and not through temperature reduction [42].

Finally, the systems can be classified by the way the driving partial pressure difference is established, so there are two groups: OMD, SGMD, and VMD systems can be operated without a significant temperature gradient across the membrane, whereas in all other systems the driving force is established by a temperature difference across the membrane or from one stage to the next stage (for AGMD and Multi-Effect VMD).

In this work, VMD and Multi-Effect VMD (MEVMD) are investigated. Nevertheless, their differences and common features in relation to other MD types are worth knowing so that the findings can be applied to other systems. In addition to mass transport resistance across the membrane, all process types show rate limiting convective or diffusive transport resistances at the membrane and all heat transfer surfaces. Due to the exponential increase in vapor pressure with increasing temperature and the high latent heat of evaporation
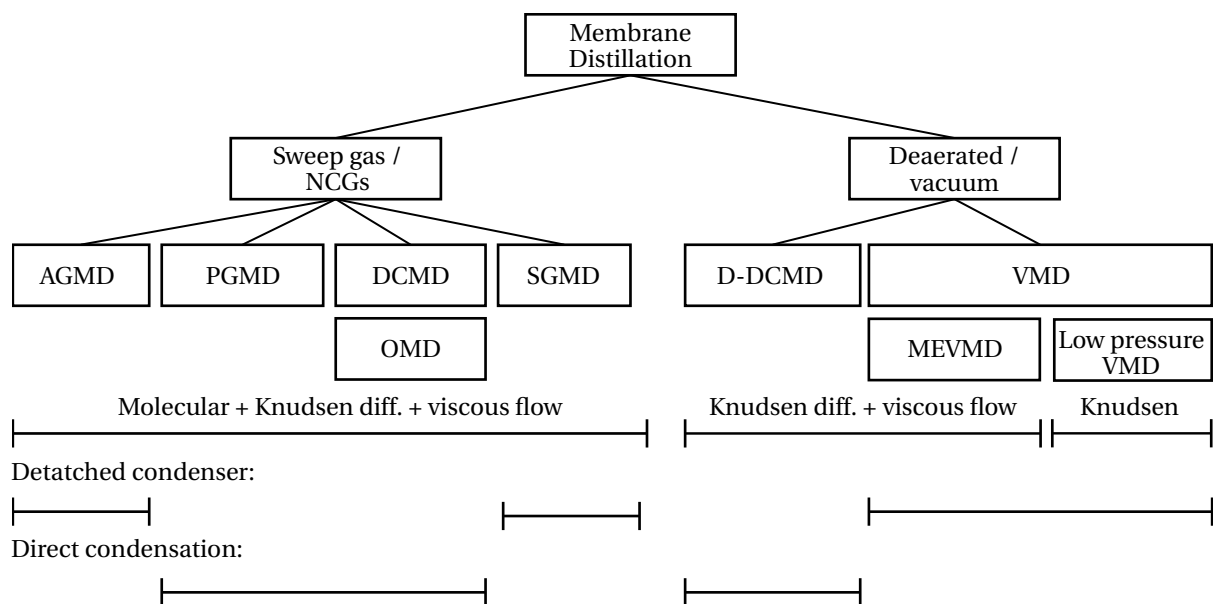
**Figure 2.2:** Classification of process variants in Membrane Distillation, relevant transport mechanisms in the membranes, and location of condensation.

of water, temperature polarization effects have a major influence on all MD configurations, except for OMD of volatile components other than water.

### 2.1.3 Multi-Effect Vacuum Membrane Distillation

The motivation behind constructing a multi-stage configuration of VMD is the same as that for utilizing multiple stages in conventional Multi-Effect Distillation (MED) or Multi-Stage Flash (MSF). The processes recover the heat of condensation while heating the feed of a following stage, or preheating the feed before it enters the first stage. The Multi-Effect Vacuum Membrane Distillation (MEVMD) process investigated in this work implements the first approach of heat recovery. As shown in Fig. 2.3, vapor at a pressure $p_{i-1}$ heats the feed solution in stage $i$. At the same time, the feed partially vaporizes at the membrane and produces vapor at a lower pressure $p_i$. This vapor is led to the following stage. Another multi-stage VMD configuration is described by Chung et al. [43]. It implements heat recovery through preheating of feed before it enters the first stage. For both multi-stage VMD types, and in contrast to MED and MSF, the absolute pressure of the feed solution can be higher than the pressure of the vapor produced. However, the pressure difference across the membrane must not exceed the LEP.

This work focuses on the MEVMD process that is based on the concept commercialized by Memsys tec AG [44]. It implements the multi-stage principle in a plate and frame setup and uses a thin foil to separate condenser and feed channels. Fig. 2.3 (left) shows one channel assembly consisting of a condenser channel (CO), a foil (HF), a feed channel (F), a membrane (M), and a vapor channel (VC). These channel assemblies are arranged in parallel to modules called stages (S1, ..., SN). Fig. 2.3 (right) shows the first and the last stage of an MEVMD system with two channel assemblies per stage. The membrane area is scaled up by increasing the number of channel assemblies connected in parallel.

The stages are connected with each other via channels in the end plates (grey walls). The feed solution is routed from stage to stage in a serpentine arrangement. In each stage it is distributed to the feed channels connected in paral-
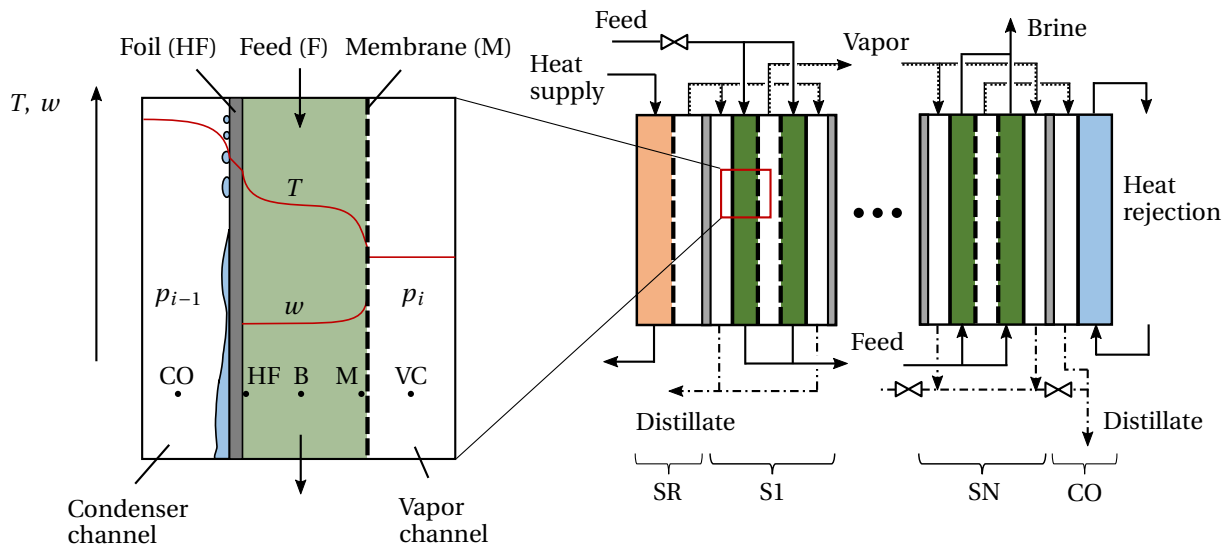
**Figure 2.3:** Functional principle of an MEVMD system and detail of one channel assembly. SR: Steam raiser, S1: Stage 1, SN: Stage N, CO: Condenser.

lel and collected again at the outlet. The steam from one stage feeds to the condenser channels of the next stage, where it condenses and discharges via distillate channels.

In addition to the stages, a steam raiser (SR) produces vapor for heating the first stage. It is built as a membrane block similar to the stages, but equipped only with membranes. The connected heating circuit operates using distilled water. The vapor condensed in the first stage is recirculated to the heater. There are two main reasons for heating the first stage with steam from a SR instead of sensible heating: the first stage equals all following stages and the heat transfer rate through condensation is significantly higher than through sensible heating.

The steam from the last stage (SN) finally condenses in a condenser block (CO). This condenser block is similar to the steam raiser but equipped with foils instead of membranes.

A driving potential difference can be defined in terms of a gradient in saturation temperature or saturation vapor pressure from the vapor channel of one stage $(i-1)$ to that of the next stage $(i)$. This driving potential is reduced

mainly by three factors, displayed in Fig. 2.4. The figure shows the temperature dependent vapor pressure $p_\mathrm{v}^*(T)$ of the pure solvent and the reduced vapor pressure $p_\mathrm{v}(T, w)$ above a solution with salt mass fraction $w$. The vapor from the previous stage with pressure $p_{i-1}$ condenses at the saturation temperature $T_{\mathrm{v},i-1}$. First, heat transfer resistances across the condensate film, foil, and boundary layers reduce the temperature at the membrane surface. Secondly, a vapor pressure reduction $\Delta p_{\mathrm{v,red}}$, caused by the feed salt content, leads to an additional loss in vapor pressure. Thirdly, the concentration polarization increases the solute concentration at the membrane. Both concentration and temperature polarization lead to a decrease in saturation vapor pressure $p_{\mathrm{v,M}}$ on the feed side of the membrane.

Altogether, the gross driving pressure difference GDPD, from one stage to another

$$\mathrm{GDPD}_i = p_{i-1} - p_i = \Delta p_{\mathrm{v,CO \to B}} + \Delta p_{\mathrm{v,red}} + \Delta p_{\mathrm{v,M}}, \qquad (2.3)$$

is reduced to a net driving pressure difference (NDPD) from the feed bulk saturation vapor pressure $p_{\mathrm{v,B},i}$ across the membrane to the vacuum channel pres-
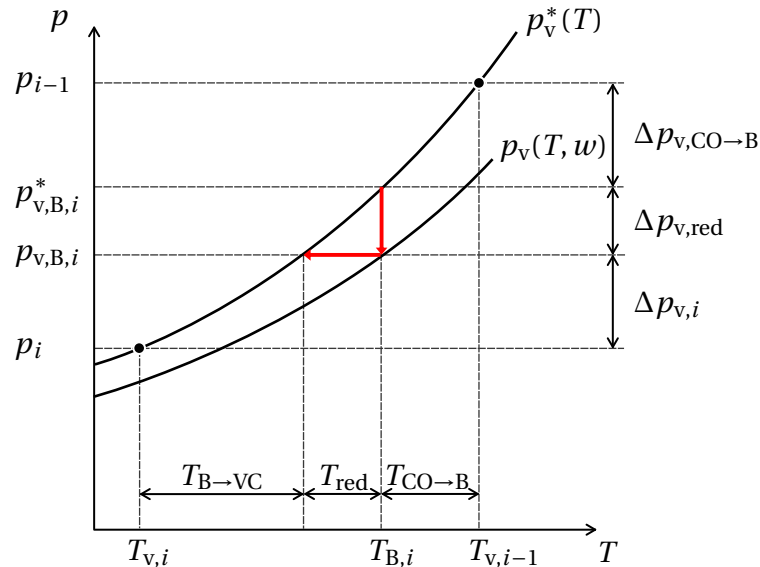


**Figure 2.4:** Qualitative sketch of pressure and temperature differences over one effect ($i$) due to concentration dependent vapor pressure reduction, heat and mass exchange [19].

sure $p_{\mathrm{v},i}$ of

$$\mathrm{NDPD}_i = p_{\mathrm{v,B},i} - p_i = \Delta p_{\mathrm{v},i}. \tag{2.4}$$

The NDPD entails the temperature and concentration polarization from the feed bulk to the feed side membrane surface.

For a multi-stage process, the distillate production can be estimated by summing up the $\mathrm{NDPD}_i$ of the stages. Increasing the number of stages helps to make the plant more efficient by reusing the heat of vaporization. At the same time, the losses are multiplied by the number of stages. For this reason an optimal number of stages exists.

## 2.2 Heat and Mass Transport in Vacuum Membrane Distillation

### 2.2.1 Polarization Effects

The evaporation of water at the membrane leads to a temperature reduction and a simultaneous solute concentration increase at the liquid-vapor interface. Both effects reduce the saturation vapor pressure and thus the driving force for evaporation.

**Concentration Polarization**
Due to the selectivity of the membrane, a concentration boundary layer is formed by the equilibrium of convective and diffusive transport. Since the selectivity is 100% for proper operation of MD, this concentration polarization does not influence the purity of the product water, but leads to a reduced vapor pressure directly at the membrane and thus a reduced driving force across the membrane. The film model for the solute mass fraction $w_j$ can be derived by integration of the steady-state convection-diffusion equation for a solute component $j$ in a solution with components $i$ in membrane normal direction. According to Melin et al. [45] and Bitter [46] it follows:

$$\frac{\mathrm{d}}{\mathrm{d}y}(w_j \, j_{\text{tot}}) - \frac{\mathrm{d}}{\mathrm{d}y}\left(\rho_\delta \, D_{ij} \frac{\mathrm{d}w_j}{\mathrm{d}y}\right) = 0. \tag{2.5}$$

With $w_j = w_{j,\mathrm{M}}\big|_{y=0}$ at the membrane and $w_j = w_{j,\mathrm{B}}\big|_{y=\delta}$ in the bulk phase outside the boundary layer with the thickness $\delta$ and under the assumption of zero salt mass content on the permeate side $w_{j,\mathrm{P}} = 0$ the integration leads to

$$\ln\left(\frac{w_{j,\mathrm{B}}}{w_{j,\mathrm{M}}}\right) = -j_{\mathrm{P}} \int_{y=0}^{\delta} \frac{1}{\rho_\delta \, D_{ij}} \mathrm{d}y. \tag{2.6}$$

Finally, the permeate flux is depending on the mass transfer coefficient $\beta_{\mathrm{B}\to\mathrm{M}} = D_{ij}/\delta$ resembling the mass transfer resistance from the bulk to the membrane for constant properties $\rho_\delta$, $D_{ij}$ in the film layer:

$$j_{\mathrm{P}} = -\rho_\delta \, \beta_{\mathrm{B}\to\mathrm{M}} \, \ln\left(\frac{w_{j,\mathrm{M}}}{w_{j,\mathrm{B}}}\right). \tag{2.7}$$

In contrast to filtration technologies and RO, the flux over the membrane is usually relatively small [1] and thus membrane normal velocities are lower, leading to a smaller concentration polarization. Another important difference is that evaporation takes place at the membrane in MD leading to a temperature drop and thus a strong temperature polarization effect.

**Temperature Polarization**

Due to vaporization of water at the membrane surface, the feed solution temperature drops. Similar to the concentration polarization, the temperature polarization can be described in dependency of the permeating mass as

$$T_{\mathrm{B}} - T_{\mathrm{M}} = \frac{j_{\mathrm{P}}\, h_{\mathrm{P}}}{\alpha_{\mathrm{B-M}}}. \tag{2.8}$$

Heat and mass transport to the membrane surface can be compared via Nusselt and Sherwood numbers. Due to the difference in order of magnitude between the salt diffusion coefficient $D \sim 1 \cdot 10^{-9}\,\mathrm{m^2 s^{-1}}$ and the thermal diffusivity $a \sim 1.5 \cdot 10^{-6}\,\mathrm{m^2 s^{-1}}$ the Prandtl and Schmidt numbers differ with a factor of around $10^3$. This leads to a larger boundary layer thickness for the temperature than for the salt mass fraction. Therefore, the interaction of the boundary layers with the complex flow field in the spacer filled feed channel differs.

**Hydrodynamics in Spacer Filled Channels**

The heat and mass transport from the feed bulk to the membrane surface is significantly influenced by the feed spacer (cf. Fig. 2.5). Its task is to mechanically stabilize the feed channel. Therefore, it has to touch the membrane and the heat transfer foil in regular distances. This brings three main drawbacks: The spacer filaments partially block the channel and therefore cause an increase in pressure drop compared to the empty channel. Further, flow separation and stagnation zones with reduced convective transport appear where the filaments touch the membrane or foil. Finally, the flow separation and stagnation zones at the spacer filaments are critical in terms of fouling. These areas provide higher salt concentration and are prone to particulate deposition [22]. The increase in pressure drop is the reason why spacer filled channels are mainly operated under laminar flow conditions. The spacer geome-

---

[1]Distillate fluxes in MD lie in the range of 1 - 30 $\mathrm{l\,m^{-2}\,h^{-1}}$ [11, 15] in comparison to approximately 50 $\mathrm{l\,m^{-2}\,h^{-1}}$ in RO [26, 45]

(a) Microscopy image of spacer; $L_1 = L_2 = 2\,\mathrm{mm}$, $\beta = 90°$.
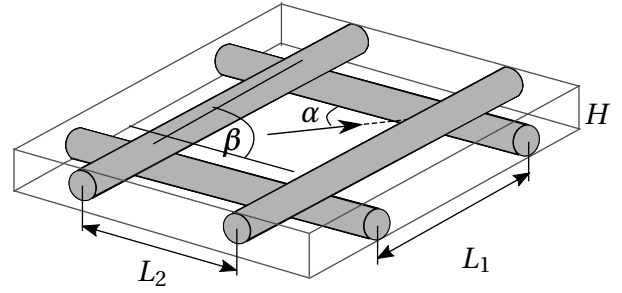
(b) Flow attack angle $\alpha$, mesh angle $\beta$, filament clearances $L_1$, $L_2$, channel height $H$.

**Figure 2.5:** Feed channel spacer mesh characterization.

tries lead to unsteady flow conditions for higher Reynolds numbers [47–49]. Ciofalo et al. [49] reported steady-state flow for $\mathrm{Re}^2 <$ 220-350 depending on the spacer orientation.

For correlating heat and mass transfer as well as pressure drop in process simulation, spacers were characterized according to Schock and Miquel [47] by their porosity $\varepsilon$, volume specific surface area $A_{\mathrm{V,SP}}$ and the channel height $H$. They found that mean Sherwood numbers correlate best with equations of the same type as known for turbulent flow through empty channels, although the predominant flow regime is laminar. They calculate the hydraulic diameter for different feed spacers from

$$d_{\mathrm{hydr}} = \frac{4\,\varepsilon}{2/H + (1-\varepsilon)\,A_{\mathrm{V,SP}}}. \tag{2.9}$$

The Reynolds number for the spacer filled channel is

$$\mathrm{Re}_{\mathrm{spacer}} = \frac{\bar{u}\,d_{\mathrm{hydr}}}{\nu}. \tag{2.10}$$

Accordingly, the friction coefficient is

$$\zeta = \frac{2\,\Delta p}{\rho\,\bar{u}^2}\,\frac{d_{\mathrm{hydr}}}{l}. \tag{2.11}$$

---

[2]Empty channel Reynolds number defined by $\mathrm{Re}_H = \bar{u}_{\mathrm{empty}}\,2H/\nu$ with the channel height $H$ and $\bar{u}_{\mathrm{empty}}$ being the volume flow rate divided by the empty channel cross section.

**Practical Correlations**

Finally, the Nusselt and Sherwood number are correlated with the spacer Reynolds number [47]:

$$\text{Sh} = a_1 \text{Re}^{b_1} \text{Sc}^{c_1}. \tag{2.12}$$

And applying heat and mass transfer analogy it is

$$\text{Nu} = a_2 \text{Re}^{b_2} \text{Pr}^{c_2}. \tag{2.13}$$

Accordingly, Schock and Miquel [47] investigated the friction coefficient for different commercial feed spacers. They found the following correlation independent from the spacer geometry and the channel height:

$$\zeta = 6.23 \, \text{Re}^{-0.3}. \tag{2.14}$$

### 2.2.2 Characterization of Heat and Mass Transport Across the Membrane

The mechanisms of mass transport across the membrane in Membrane Distillation can be separated in

- surface diffusion,
- Knudsen diffusion and molecular diffusion, and
- Poiseuille flow (viscous flow).

Applying electrical analogy, the three components are resistances connected in parallel. Knudsen and molecular diffusion can be transferred to a serial connection. [13]

The pore Knudsen number and the content of non-condensable gases can be used to characterize the dominating regime of mass transport. It is

$$\text{Kn} = \frac{\ell_i}{d_{\text{pore}}} \tag{2.15}$$

the Knudsen number of component $i$ inside the membrane pore. The mean free path length

$$\ell_i = \frac{k_{\text{B}} T}{\sqrt{2} \, \pi \, p_{\text{hydr,M}} \, \sigma_{\text{coll},i}^2} \tag{2.16}$$

is a function of the collision diameter[3] $\sigma_{\mathrm{coll}}$ of the molecules, temperature, and hydrostatic pressure inside the pores. [51]

For Kn $\ll$ 1 and with stagnant non-condensable gases in the membrane pores, molecular diffusion dominates the transport resistance for vapor molecules passing through the pores. For practical application the threshold beyond which other mechanisms can be neglected is generally set to Kn < 0.01 or $d_{\mathrm{pore}} > 100\,\ell_i$ [50].

For Kn $\ll$ 1 and without significant content of non-condensable gases in the pore, a hydrostatic pressure difference across the membrane leads to Poiseuille flow. In this case intermolecular collisions dominate the transport resistance. [50]

For Kn $\gg$ 1, which is the case for $d_{\mathrm{pore}} \ll \ell_i$, collisions between molecules and the walls dominate the diffusion. This case is called Knudsen regime and other mechanisms are generally neglected for Kn > 10 [50].

Surface diffusion can be generally neglected in MD, because of the low ratio of membrane matrix volume to pore volume and the material properties of MD membranes [13].

For VMD, the content of stagnant non-condensable gases in the pores is negligible. Therefore, Knudsen diffusion and Poiseuille flow dominate the transport through the membrane pores.

The Knudsen equation [51] for the molar flux of a gas $i$ in a capillary tube is

$$\dot{n}_i = -\frac{8}{3}\frac{r_{\mathrm{pore}}}{\sqrt{2\pi M_i RT}}\frac{\mathrm{d}p_i}{\mathrm{d}z}. \tag{2.17}$$

It is corrected with the ratio of void fraction to pore tortuosity $\varepsilon_{\mathrm{M}}/\chi_{\mathrm{M}}$, further referred to as membrane structure parameter, and integrated over the mean thickness of the modeled membrane layer $\delta_{\mathrm{M}}$. Finally, the effective mass flux can be written as

$$j_{i,\mathrm{M,Kn}} = \frac{8}{3}\frac{r_{\mathrm{pore}}}{\delta_{\mathrm{M}}}\frac{\varepsilon_{\mathrm{M}}}{\chi_{\mathrm{M}}}\sqrt{\frac{M_i}{2\pi RT}}\,\Delta p_{i,\mathrm{M}} = K_{\mathrm{M,Kn}}\,\Delta p_{i,\mathrm{M}}. \tag{2.18}$$

---

[3]Collision (kinetic) diameters according to Ismail et al. [50]: $\sigma_{\mathrm{coll}}(H_2O) = 2.65\cdot 10^{-10}\,\mathrm{m}$, $\sigma_{\mathrm{coll}}(N_2) = 3.64\cdot 10^{-10}\,\mathrm{m}$.

For the viscous flow regime, the mass flux averaged over the membrane area can be written as

$$j_{i,\text{M,Vis}} = \frac{r_{\text{pore}}^2}{\delta_\text{M}} \frac{\varepsilon_\text{M}}{\chi_\text{M}} \frac{p_{\text{hydr}} M_i}{8RT\mu} \Delta p_{i,\text{M}} = K_{\text{M,Vis}} \, \Delta p_{i,\text{M}}. \tag{2.19}$$

For the operation conditions typical in VMD and especially MEVMD, the Kn numbers prevailing are in a range of 1 to 20. Therefore, transitional flow (0.1 < Kn < 10, [50]) is expected in a wide operation range. The permeate flux can be written with the Knudsen resistance $K_{\text{M,Kn}}$ and the viscous flow resistance $K_{\text{M,Vis}}$ as

$$j_{\text{M,VMD}} = (K_{\text{M,Kn}} + K_{\text{M,Vis}}) \, \Delta p_\text{M} = K_\text{M} \, \Delta p_\text{M}. \tag{2.20}$$

Figure 2.6 shows the membrane permeability $K_\text{M} = K_{\text{M,Kn}} + K_{\text{M,Vis}}$ in dependency of the vapor channel pressure $p_{\text{VC}}$ and the temperature of the feed solution in the single phase water vapor region. The second y-axis shows the Knudsen permeability $K_{\text{M,Kn}}$ according to Eq. 2.18. Its iso-lines are parallel to the iso-temperature lines since it is solely temperature dependent. Thus, the impact of the viscous flow resistance can be directly calculated. It gains influence towards lower Knudsen numbers marked with iso-Knudsen number lines. The inlet and outlet properties of the bench scale experiments described in Sec. 3.2.2 are plotted as well as the boundary conditions used in scaling experiments described in Sec. 5.1. The operation range of the first stages of an MEVMD system can go up to 90°C resulting in a significant influence of viscous flow.

According to Basile et al. [13] heat transfer across membranes in MD is generally regarded as a superposition of

- conductive heat transfer across the membrane material,
- conductive heat transfer across the pore filling gases, and
- convection of vapor from the liquid-vapor interface at the feed side pore entrance to the permeate side.

Thermal conduction can be neglected due to small temperature differences between the membrane surface on the feed and permeate side apparent in VMD [52]. In contrast, the heat sink through evaporation of solvent on the feed side membrane surface significantly influences the process.
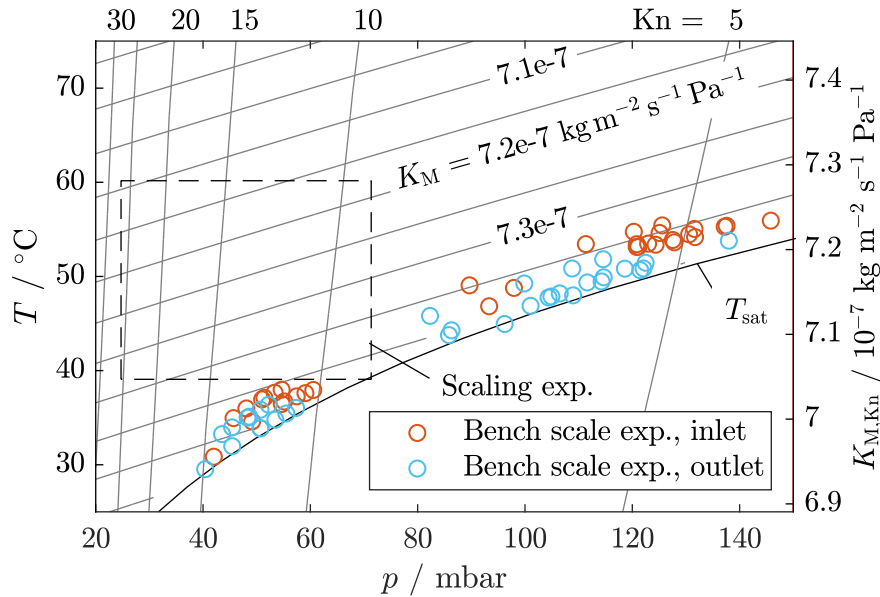
**Figure 2.6:** Membrane permeability for Knudsen diffusion $K_{M,Kn}$ and coupled Knudsen diffusion with viscous flow $K_M$ for the range of boundary conditions in bench scale and scaling experiments.

## 2.3 Thermodynamics of Salt Solutions

Heat and mass transfer in MD are further dominated by the thermophysical behavior of the feed solution. Therefore, necessary fundamentals and definitions are summarized in this section. They are used to describe state changes, liquid-vapor and solid-liquid equilibria, and irreversibilities appearing at elevated feed salt concentrations.

The general task of desalination is to separate the solvent (water) from a salt solution. This feed solution is characterized by

- the content of highly soluble salts (generally NaCl),
- the amount of other dissolved solids (especially sparingly soluble salts such as $CaCO_3$ or $CaSO_4$),
- dissolved gases (especially $CO_2$), and finally,
- suspended solids and biological substances.

From a thermodynamic point of view, this can be often simplified to a solution of solutes B in a solvent A. Concentration measures necessary for the further

description are

molar concentration $c_B = n_B/V$,

molality $b_B = n_B/m_A$,

mole fraction $x_B = n_B/n$,

and mass fraction $w_B = m_B/m$.

The derivations of this section are based on Atkins et al. [53], Clarke and Glew [54–56], and Wedler and Freund [57].

The focus is on describing the characteristics of salt solutions with high salt content up to saturation. The behavior of these solutions can significantly deviate from the behavior of what is known as an ideal solution. An ideal solution obeys Raoult's law for solvent and solute under the assumption that the vapor above the solution is an ideal gas

$$p_i = x_i \, p_i^*. \tag{2.21}$$

The vapor pressure $p_i$ of a component above an ideal solution is the vapor pressure of the pure substance $p_i^*$ scaled by the mole fraction of the solvent. In reality only mixtures of closely related liquids show this behavior. [53]

The behavior of the solute in solutions with small solute content $x_B \rightarrow 0$ is better described by Henry's law

$$p_B = x_B \, K_B. \tag{2.22}$$

The partial pressure of the solute is proportional to the solute mole fraction by an empirical factor $K_B$. A solution that obeys Henry's law for the solute and Raoult's law for the solvent is called ideal-dilute solution. At low concentrations and low pressures Henry's law can be used to approximate the influence of solved gases. Gases which interact with the water deviate strongly from Henry's law, even at low concentrations. [57]

If the solvent is a salt or more general an electrolyte, a substance that is (partially) dissociated into cations and anions, the behavior already deviates from that of an ideal solution at very low ion content. This is because the behavior of the dissociated ions significantly differs from the pure substance and the ions show electrostatic interaction [53, 58]. The following sections describe the behavior of real solutions and their deviation from ideal behavior.

### 2.3.1   Multi-Component Mixtures and Aqueous Electrolyte Solutions

It is useful to introduce the Gibbs free enthalpy or Gibbs energy

$$G = H - TS \tag{2.23}$$

when investigating solution processes and phase equilibria.

**Chemical Potential**

The partial molar Gibbs energy of a component $i$ defines the chemical potential of that component in a mixture

$$\mu_i = \left( \frac{\partial G}{\partial n_i} \right)_{p,T,n_{i \neq j}}. \tag{2.24}$$

It is the change in Gibbs energy through number change in a system at constant pressure, temperature, and number of all other components. For an open system the general change in Gibbs energy becomes

$$\mathrm{d}G = V\mathrm{d}p - S\mathrm{d}T + \sum_i \mu_i \mathrm{d}n_i, \tag{2.25}$$

where the last term is arising from changing composition of the system. The Gibbs-Duhem equation

$$\sum_i n_i \mathrm{d}\mu_i = 0 \tag{2.26}$$

links the partial molar quantities of the components during a state change.

For solutions, the chemical potentials of its components are defined in a similar manner as known for gases. The chemical potential of each component in an ideal solution is given with reference to the chemical potential of the pure component $\mu_i^*$ as

$$\mu_i = \mu_i^* + RT \ln x_i. \tag{2.27}$$

The Gibbs energy of mixing of two pure components A and B in an ideal solution is

$$\Delta_{\mathrm{mix}} G = nRT(x_{\mathrm{A}} \ln x_{\mathrm{A}} + x_{\mathrm{B}} \ln x_{\mathrm{B}}). \tag{2.28}$$

Electrolyte solutions show significant deviations from ideal behavior already at small solute concentrations. The deviation from an ideal solution behavior

can be expressed in excess functions for an extensive property $X$ as the excess property $X^{\mathrm{E}}$

$$X^{\mathrm{E}} = \Delta_{\mathrm{mix}}X - \Delta_{\mathrm{mix}}X^{\mathrm{ideal}}. \tag{2.29}$$

The activity is used to introduce this non-ideal behavior into the calculation the chemical potential. For the solvent A it is

$$\mu_{\mathrm{A}} = \mu_{\mathrm{A}}^{*} + RT\ln a_{\mathrm{A}}. \tag{2.30}$$

The solvent activity $a_{\mathrm{A}} = \gamma_{\mathrm{A}} x_{\mathrm{A}}$ approaches $x_{\mathrm{A}}$ for $x_{\mathrm{B}} \to 0$. $\gamma$ is called activity coefficient and describes the deviation from Raoult's law (cf. Eq. 2.21). Another measure for the solvents' deviation from non-ideal behavior in the solution is the osmotic coefficient $\phi$ which can be introduced for the calculation of the chemical potential of the liquid solvent [59]

$$\mu_{\mathrm{A}} = \mu_{\mathrm{A}}^{*} + \phi RT\ln x_{\mathrm{A}}. \tag{2.31}$$

With Eq. 2.27 and 2.30 it follows

$$\phi \equiv \frac{\ln a_{\mathrm{A}}}{\ln x_{\mathrm{A}}} = \frac{\Pi^{\mathrm{real}}}{\Pi^{\mathrm{ideal}}}. \tag{2.32}$$

It can be further interpreted as the relation between the osmotic pressure of a real solution $\Pi^{\mathrm{real}} = -RT/V_{\mathrm{A}}\ln a_{\mathrm{A}}$ to that of an ideal solution $\Pi^{\mathrm{ideal}}$ (refer to e.g. Atkins [53]). At infinite dilution $x_{\mathrm{B}} \to 0$ the osmotic coefficient $\phi$ approaches 1.

For the solute activity $a_{\mathrm{B}}$, Henry's law (cf. Eq. 2.22) is used as reference state. It follows

$$\mu_{\mathrm{B}} = \mu_{\mathrm{B}}^{*} + RT\ln\frac{K_{\mathrm{B}}}{p_{\mathrm{B}}^{*}} + RT\ln a_{\mathrm{B}} = \mu_{\mathrm{B}}^{\ominus} + RT\ln a_{\mathrm{B}}. \tag{2.33}$$

Thus, ideal solution behavior is approached for $\gamma_{\mathrm{B}} = a_{\mathrm{B}}/x_{\mathrm{B}} \to 1$ which is valid for $x_{\mathrm{B}} \to 0$. The superscript '$\ominus$' symbolizes the standard state.

For electrolytes, the pure state of the solute is not suitable as reference since it significantly differs from the behavior of the solute at infinite dilution. Therefore, it is customary to choose the ideal solution state at unit molality $b^{\ominus}$ [60]. Now, using the molality scale, it is $\gamma_{b} = a_{\mathrm{B}}/b$ the molal activity coefficient and finally

$$\mu_{i} = \mu_{i}^{\ominus,b} + RT\ln\left(b_{i}\,\gamma_{i,b}\right). \tag{2.34}$$

For aqueous salt solutions, the concept of an ideal solution is not applicable already at low molalities (generally $>1\,\mathrm{mmol\,kg^{-1}}$ [53]). A salt $A_aB_b$ dissolves in a solvent to $a$ cations and $b$ anions. Since it is not possible to experimentally distinguish between the contribution of the ions to the non-ideal behavior, a 'mean molal activity coefficient' is defined as

$$\gamma_\pm = \left(\gamma_+^a \gamma_-^b\right)^{1/s}, \text{ with } s = a + b. \tag{2.35}$$

The chemical potential of an ion $i$ is then

$$\mu_i = \mu_i^{\ominus,b} + RT\ln\frac{b_i}{b^\ominus} + RT\ln\gamma_\pm = \mu_i^{\mathrm{ideal}} + RT\ln\gamma_\pm. \tag{2.36}$$

For practical applications, it is useful to derive correlations for activity coefficients. The basic concepts are summarized in the following.

**Calculation of Activity Coefficients**

At low ion concentrations, long range electrostatic interactions dominate the behavior of the solution. This is approximated by the Debye-Hückel limiting law [54]

$$\log\gamma_\pm = -A_{\mathrm{DHLS}}|z_+ z_-| I^{1/2}. \tag{2.37}$$

with the Debye-Hückel limiting slope $A_{\mathrm{DHLS}}$ and the concentration of the electrolytes characterized by the ionic strength[4] $I$. Respecting Gibbs-Duhem relation, the osmotic coefficient can be calculated from

$$\phi = 1 - A_{\mathrm{DHLS}}\, b^{1/2}. \tag{2.38}$$

This law holds only for low ionic strength and is extended in virial expansions to so called Pitzer-type equations for activity coefficients. Here, thermodynamic properties for aqueous NaCl solutions are derived from an extended Pitzer-type equation for the osmotic coefficient given by Clarke and Glew [55]

$$\phi = 1 - A_{\mathrm{DHLS}}\, b^{1/2}\left(1 + 1.2\, b^{1/2}\right)^{-}1 + Q\, b\exp\left(-2b^{1/2}\right) + B\, b + C\, b^2 + D\, b^3 + E\, b^4. \tag{2.39}$$

The fitting parameters $Q$, $B$, $C$, $D$, and $E$ are functions of temperature. Excess functions for Gibbs energy, enthalpy, and heat capacity are derived from these equations as follows.

---

[4]Ionic strength $I = \frac{1}{2}\sum_i z_i^2(b_i/b^\ominus)$ with the charge number $z_i$.

**Derivation of Excess Functions**

Excess Gibbs energy $G^E$ of a mixture is, according to Eq. 2.29, the difference between the Gibbs energy of mixing with real solution behavior minus that of an ideal solution.

$$G^E = \Delta_{mix}G - \Delta_{mix}G^{ideal} = \Delta_{mix}G - nRT(x_A \ln x_A + x_B \ln x_B) \tag{2.40}$$

The enthalpy is related to Gibbs energy via the Gibbs-Helmholtz equation [55]

$$\left.\frac{\partial(G/T)}{\partial T}\right|_{p,\{x_i\}} = -\frac{H}{T^2}. \tag{2.41}$$

From this equation the relative enthalpy $H_{rel}$ and the relative heat capacity $C_{p,rel}$ can be calculated by derivation as [55]

$$\left.\frac{\partial}{\partial T}\left(\frac{\partial\left(G^E/T\right)}{\partial(1/T)}\right)\right|_{p,\{x_i\}} = \left.\frac{\partial H_{rel}}{\partial T}\right|_{p,\{x_i\}} = C_{p,rel}. \tag{2.42}$$

These excess properties are added to those of pure water [61] and pure salt to calculate the state of a real solution.

Empirical correlations collected by Conde-Petit [62] were used for aqueous solutions of $CaCl_2$. For practical application in simulation tools, parametrized equations for specific enthalpy, heat capacity, and solvent activity depending on solute mass fraction and temperature at ambient pressure were fitted from results generated with the Pitzer-type equation. The specific enthalpy $h(w, T)$ was calculated with respect to a reference enthalpy as shown in the next section.

### 2.3.2 Mixing State Changes

Mainly four types of mixing and separation processes are necessary to describe the phenomena observed in Membrane Distillation. These are the separation of water from a solution or the absorption of water into a solution, as well as the separation of solid salt from or its dissolution into a solution.

**Solvent Extraction**

A general separation task as shown in Fig. 2.7 is discussed. The Gibbs energy that has to be supplied to the process can be directly calculated from the chemical potential of the streams as

$$\Delta_{\text{sep}}G = -\Delta_{\text{mix}}G = G_1 + G_2 - G_0. \tag{2.43}$$

First, the desalination task, i.e. extraction of solvent (water) from the feed solution should be regarded. Mistry and Lienhard [64] defined a molar water recovery ratio as

$$\text{RR}_{\text{m}} = \frac{n_{\text{w},1}}{n_{\text{w},0}}. \tag{2.44}$$

With this, Eq. 2.43 can be written as

$$\frac{\Delta_{\text{sep}}G}{RT n_{\text{w},1}} = \ln\left(\frac{a_{\text{w},1}}{a_{\text{w},2}}\right) + b_{\text{s},1} M_{\text{w}} \ln\left(\frac{a_{\text{s},1}}{a_{\text{s},2}}\right) + \frac{1}{\text{RR}_{\text{m}}}\left(\ln\left(\frac{a_{\text{w},2}}{a_{\text{w},0}}\right) + b_{\text{s},0} M_{\text{w}} \ln\left(\frac{a_{\text{s},2}}{a_{\text{s},0}}\right)\right). \tag{2.45}$$

If the product stream '1' is the pure solvent (water) this can be simplified applying $b_{\text{s},1} = 0$ and therefore $a_{\text{w},1} = x_{\text{w},1}$. Further, Eq. 2.45 can be split into terms
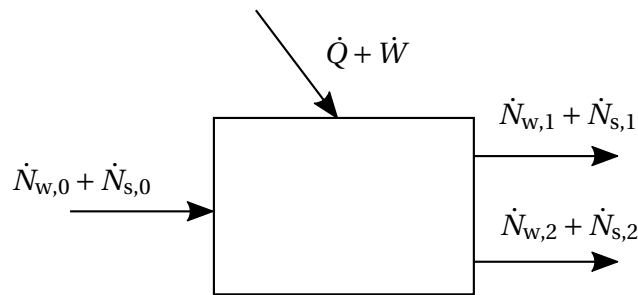


**Figure 2.7:** General separation process of a two component mixture (index w: solvent/water; index s: solute/salt), adapted from Cussler and Dutta [63] and Mistry and Lienhard [64].

describing the ideal solution behavior and those making up for the non-ideal behavior. It follows

$$
\frac{\Delta_{\text{sep}}G}{RT n_{\text{w},1}} = \overbrace{\ln\left(\frac{x_{\text{w},1}}{x_{\text{w},2}}\right) + \frac{1}{\text{RR}_{\text{m}}}\left(\ln\left(\frac{x_{\text{w},2}}{x_{\text{w},0}}\right) + \nu_s b_{\text{s},0} M_{\text{w}} \ln\left(\frac{x_{\text{s},2}}{x_{\text{s},0}}\right)\right)}^{\text{ideal solution}}
$$
$$
\underbrace{+ \ln\left(\frac{1}{\gamma_{\text{w},2}}\right) + \frac{1}{\text{RR}_{\text{m}}}\left(\ln\left(\frac{\gamma_{\text{w},2}}{\gamma_{\text{w},0}}\right) + \nu_s b_{\text{s},0} M_{\text{w}} \ln\left(\frac{\gamma_{\pm,\text{s},2}}{\gamma_{\pm,\text{s},0}}\right)\right)}_{\text{non}-\text{ideality}}. \tag{2.46}
$$

In Eq. 2.46, $\gamma_{\text{w},i}$ is the activity coefficient of the solvent, $\gamma_{\pm,\text{s},i}$ the mean molal activity coefficient of the solute and $\nu_s = \nu^+ + \nu^-$ its sum of stoichiometric coefficients. Equation 2.46 describes the least work of separation that would be necessary for a reversible desalination process. It is used as reference in Ch. 3. Further, the equation helps to determine when it is acceptable to approximate a feed solution as an ideal solution. This is shown in Fig. 2.8 for aqueous solutions of NaCl. Figure 2.8a shows the least heat of separation $\Delta_{\text{sep}}G$ per kg of feed solution in dependency of the feed salt mass fraction $w_1$ and the temperature at which the separation process takes place.

In Fig. 2.8b, the relative error

$$
\text{Rel. error} = \frac{\Delta_{\text{sep}}G^{\text{ideal}}}{\Delta_{\text{sep}}G^{\text{actual}}} - 1 \tag{2.47}
$$

is plotted in dependency of the feed concentration and recovery ratio. The relative error made when applying the ideal solution approximation to the energy balance for a separation task can be directly estimated from this figure. The values show a local maximum at $w_1 \approx 15\,\text{g}\,\text{kg}^{-1}$. The error becomes significant at high feed salt mass fraction and can be greater than 20% in the vicinity of NaCl saturation. The dotted line shows the solubility limit of NaCl. A detailed comparison of NaCl with seawater can be found in Mistry and Lienhard [64].
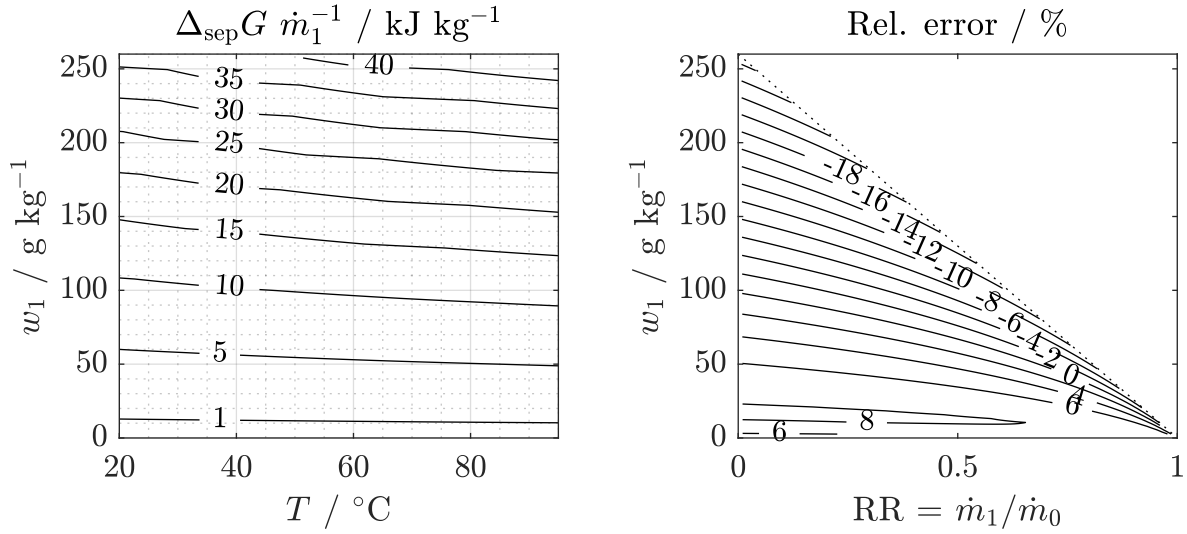
**(a)** Least heat of separation of water from aqueous NaCl solutions. **(b)** Relative error calculated according to Eq. 2.47.

**Figure 2.8:** Water extraction from aqueous NaCl solutions approximated with Pitzer-type correlation according to Clarke and Glew [55] and comparison with ideal solution approximation. Figure concept applied from Mistry and Lienhard [64].

## Specific Enthalpy of Salt Solutions

For engineering process simulation it is useful to derive a function for the specific enthalpy of the salt solution depending on temperature and salt mass fraction. It is

$$h(T, w) = \frac{\left(h_{A,ref} + \int_{T_{ref}}^{T} c_{p,A}(\tau) \, d\tau\right) m_{A,sys} + n_{B,sys} \, \Delta H^*_{m,B} + H_{rel,sys}}{m_{sys}} \quad (2.48)$$

with the system mass $m_{sys} = m_{A,sys} + n_{B,sys} \, M_B$, the mass specific enthalpy of pure water $h_{ref}$ at the reference temperature $T_{ref}$, and the standard molar enthalpy function of the solute $\Delta H^*_{m,B}$ with reference to $T_{ref}$. The reference values $T_{ref}$ and $h_{A,ref}$ are arbitrarily set to $0\,°C$ and $0\,kJ\,kg^{-1}\,K^{-1}$. $\Delta H^*_{m,B}$ is rescaled to the same reference point from data provided by Clarke and Glew [55]. The relative enthalpy $H_{rel,sys}$ is related to the apparent molal relative enthalpy $H^{\phi}_{rel}$ via

$$H_{rel,sys} = n_{B,sys} \, H^{\phi}_{rel}. \quad (2.49)$$

For calculating the temperature gradient at the membrane caused by vaporization of water, the negative value of the differential enthalpy of dilution is required in addition to the latent heat of evaporation of pure water. The differential heat of dilution is equal to the excess enthalpy. It is

$$\left(\frac{\partial H}{\partial n_A}\right)_{p,T,n_B} = H_A - H_A^* = \Delta_{dil}H = H_A^E. \qquad (2.50)$$

**Dissolution and Crystallization**

Finally, the dissolution process of solid salts in a solution and the formation of crystals from a solution is discussed. According to Wedler and Freund [57] the process of dissolution can be subdivided into three steps:

- Breaking of hydrogen bonds in water (endothermic process)
- Vaporization of salt ions into vacuum, requiring the lattice energy (endothermic process)
- Integration of the salt ions into the water, releasing the solvation energy (exothermic process)

The sum of these three steps determines whether the dissolution process is endothermic or exothermic. The integral and differential heats released or absorbed during a dissolution and dilution process are summarized in Fig. 2.9 for aqueous solutions of NaCl. The differential heat of dilution $\Delta_{dil}H$ and the last heat of solution $\Delta H_{last}(sol)$ are the two parameters required for energetically analyzing the processes which appear at the phase boundaries. The integral heat of solution $\Delta H(sol)$ (Fig. 2.9b) is the heat released or absorbed when preparing a solution from pure solvent and pure solute. The differential heat of dilution $\Delta_{dil}H$ is the slope of the integral heat of solution with respect to the mole number of water $n_{H_2O}$. It describes the heat released or absorbed when adding one mole of water to an infinite amount of solution. In this thesis it was used for calculating the heat required for extracting water from a solution. The intercept of a tangent to the iso-temperature line of $\Delta H(sol)$ with the ordinate, the differential heat of solution $\Delta_{sol}H$, can be used to calculate re-dissolution of crystals in an undersaturated solution during a cleaning process. The last point of each temperature iso-line in Fig. 2.9b is the last heat of solution $\Delta H_{last}(sol)$. It is the heat absorbed or released at the interface between

crystal and saturated solution, i.e. during crystallization process. Figure 2.9a shows this last heat of solution for a wider range of temperatures.
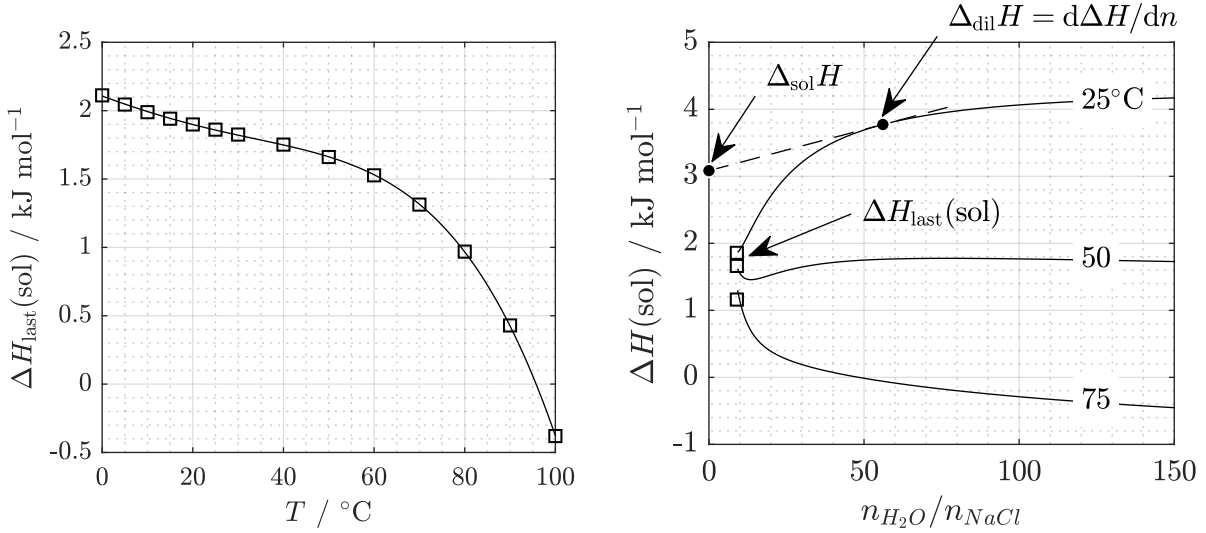


**(a)** Last heat of solution $\Delta H_{\text{last}}(\text{sol})$ at solubility limit of NaCl for different temperatures.

**(b)** Integral heat of solution $\Delta H(\text{sol})$ and derived properties; figure concept from Wedler and Freund [57] applied to NaCl solutions.

**Figure 2.9:** Heat of solution and dilution for aqueous solutions of NaCl; data calculated according to Clarke and Glew [55].

### 2.3.3 Phase Equilibria

In MD, three phases can be found at the same time. Volatile components evaporate from the liquid feed solutions generating an increased solute concentration which can lead to formation of a crystalline solid phase.

**Liquid-Vapor Interface**

At the feed side entrance of the membrane pore, water evaporates from the feed solution. The equilibrium condition can be written in terms of the chemical potentials of the solvent in the liquid and in the vapor phase as

$$\mu_A^* + RT \ln a_A = \mu_A^{\text{ig}} + RT \ln \frac{p_A}{p_A^*}, \tag{2.51}$$

with the reference state of the pure solvent $\mu_A^*$ in the liquid phase and that of the vapor regarded as ideal gas ($^{ig}$) [53]. When comparing the last terms on each side, the following expression evolves relating the vapor pressure of the pure solvent $p_A^*$ with that above the real solution $p_A$ via the solvent activity.

$$a_A = \frac{p_A}{p_A^*} \tag{2.52}$$

This is applied for calculation of equilibrium vapor pressures. The vapor pressure of pure water is calculated according to IAPWS 97 [61].

**Liquid-Solid Interface**

The interface between the crystalline solid phase (C) and the feed solution in equilibrium (sat, crystal growth equals dissolution) can be described according to Clarke and Glew [55] by

$$G_C = G_A^{\ominus} + 2RT \ln\left(b_{sat}\gamma_{\pm}\right). \tag{2.53}$$

The temperature dependency of the molality of this saturation state becomes

$$\ln b_{sat} = -\frac{1}{2R}\frac{\Delta G_{sat}^{\ominus}}{T} - \ln\gamma_{\pm}. \tag{2.54}$$

The degree of supersaturation $S$, the relative supersaturation $S_{rel}$, and the saturation index SI are measures for the salt content or activity relative to the saturation limit under equilibrium conditions. They are defined as follows:

$$S = \frac{w}{w_{sat}} \tag{2.55}$$

$$S_{rel} = S - 1 = \frac{\Delta w}{w_{sat}} \tag{2.56}$$

Alternatively to $S_{rel}$, the saturation index SI can be used, which is defined for a dissolution or precipitation reaction

$$A_a B_b \rightleftharpoons aA + bB \tag{2.57}$$

via its ion activity product $IAP = a_{A,actual}^a\, a_{B,actual}^b$ and solubility product $K_{sp} = a_{A,equil}^a\, a_{B,eqil}^b$ as

$$SI = \log_{10}\left(\frac{IAP}{K_{sp}}\right). \tag{2.58}$$

Figure 2.10 shows the solubility curves for NaCl and $CaCl_2$. The solubility limits are plotted over the solute mass fraction and temperature. The crystallization behavior of other (sparingly soluble) salts and their interaction with NaCl is discussed in the next section.

For NaCl (Fig. 2.10a), the solubility values were calculated according to Eq. 2.54 with data based on Clarke and Glew [55] (red line). The results are compared to values from Meyer [65] and a fit to data from Cohen-Adad and Lorimer [66]. From low to high salt mass fractions, the two phase regions are solution and ice, liquid solution and $NaCl \cdot 2\,H_2O$, and solution and NaCl. The solubility limit of NaCl ranging from $w_{NaCl} \approx 0.26$ to $0.27$ for $T = 0°C$ to $80°C$ is the solubility boundary relevant for the work at hand. It is weakly depending on temperature. Additionally, the figure shows the equilibrium vapor pressure above a solution. The values were calculated according to Eq. 2.52, and 2.39 with coefficients according to Clarke and Glew [55]. The iso-
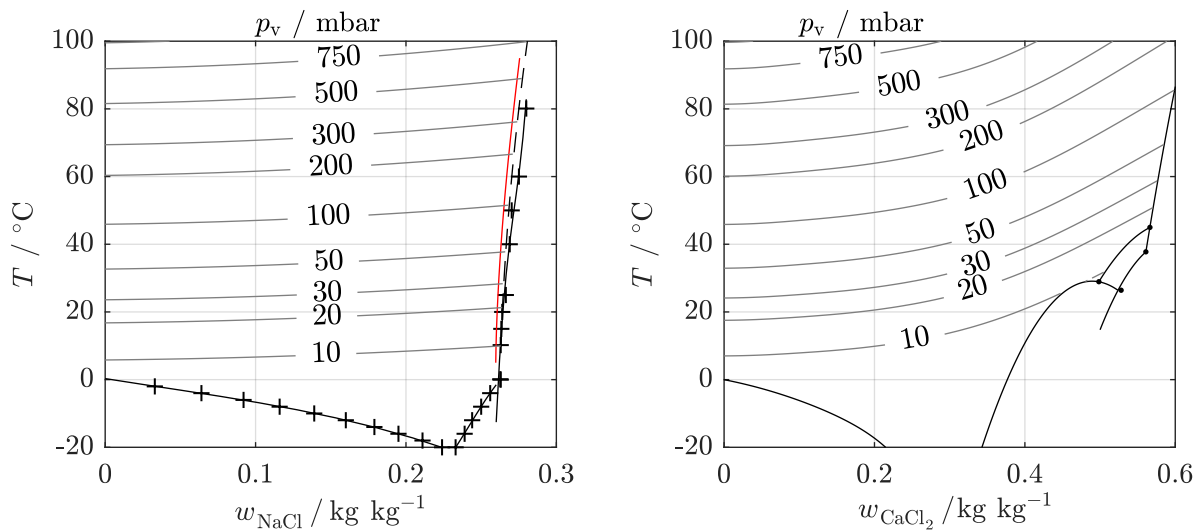


(a) NaCl(aq) according to [55]. Solubility limits: — Eq. 2.54, [55], + Meyer [65], - - IUPAC solubility data [66].

(b) $CaCl_2$(aq) calculated according to [62].

**Figure 2.10:** Temperature dependency of the solubility of aqueous solutions and saturation vapor pressure above these solutions.

bars show only a small increase towards higher salt mass fraction, compared to the strong temperature dependency.

Figure 2.10b shows the same plots for aqueous $CaCl_2$ based on data collected by Conde-Petit [62]. The solubility boundary is more complex since the following hydrates are formed in the temperature range displayed (from left to right): liquid solution plus ice, $CaCl_2 \cdot 6\,H_2O$, $CaCl_2 \cdot 4\,H_2O$ ($\alpha$, $\beta$), $CaCl_2 \cdot 2\,H_2O$. Besides the high solubility, $CaCl_2$ causes a stronger vapor pressure reduction towards its solubility limit, compared to NaCl. This is why solutions with $w_{CaCl_2}$ around 0.4 are used as liquid desiccants (cf. e.g. Rafique et al. [67]). The vapor pressures of aqueous solutions of NaCl and $CaCl_2$ differ about less than 5% in the range of $40°C < T < 100°C$ within the solubility range of NaCl. The better soluble $CaCl_2$ is therefore used in sensitivity analyses to provide continuous functions for the thermophysical properties and investigate a wide range of applications including conventional desalination and liquid desiccant regeneration.

## 2.4 Fundamentals of Crystallization Fouling in Membrane Distillation

This section summarizes the state of knowledge on crystallization fouling relevant for MD and carves out differences and common features with other membrane technologies. The fundamentals necessary to understand the derivation of a scaling model and the analysis of experimental results are provided. A vast field of research ranging from fundamental research on nucleation and growth to applied studies on fouling in heat and mass exchangers exists. For a review on existing nucleation and growth theories, fundamental literature should be referred to, such as Mullin [68] or Mersmann [69]. For the application to scaling, Amjad and Demadis [70] provide an exhaustive overview. In the following, only the application of the theory is reviewed from an engineering perspective.

### 2.4.1 Applied Crystallization Kinetics

The scaling process consists of nucleation and subsequent growth of crystals on the membrane or the deposition of crystalline material on the membrane surface.

**Nucleation**

The formation of a smallest metastable cluster of crystalline material is called nucleation. The exact mechanisms of this process are unknown [68]. Often, similar to droplets, a spherical shape is assumed for the nucleus, although this contradicts todays knowledge about crystal lattice shape. Nevertheless, this assumption provides a rough estimate of nuclei sizes for primary homogeneous nucleation. This means, the formation of a crystal embryo from a supersaturated solution without a secondary surface. According to Mullin [68],

$$\Delta G_{\text{crit}} = \frac{16\,\pi\,\sigma^3}{3(\Delta G_{\text{V}})^2} \qquad (2.59)$$

is the free energy of the critical nucleus. Its radius follows from

$$r_{\text{crit}} = \frac{-2\sigma}{\Delta G_{\text{V}}} \qquad (2.60)$$

and the mole number from

$$n_{\text{crit}} = V_{\text{crit}}/V_m. \qquad (2.61)$$

According to the model concept by Warsinger et al. [71] the mole number of a critical nucleus together with the volumetric distribution of salts in supersaturated solutions determines the nucleation rate. The necessary amount of ions has to be available long enough in a volume that is small enough to allow to form a nucleus. They suggest to calculate the spherical volume in which the amount of solute necessary to form the nucleus must be contained in.

$$r_{\text{crit,solution}} = 2r_{\text{crit}} \left( \frac{\rho_{\text{C}}}{M_{\text{w}}(x - x_{\text{sat}})} \right)^{1/3} \qquad (2.62)$$

$\Delta G_{\text{crit,hom}}$ is the largest possible energy barrier for nucleation. It can be significantly reduced if another surface is involved. This is then called primary

heterogeneous nucleation on foreign surfaces and secondary nucleation if already existing crystals are involved in the nucleation process. The result is a range of metastable boundaries for formation of nuclei in terms of required supersaturations

$$0 < S_{\text{rel,sec}} < S_{\text{rel,prim,het}} < S_{\text{rel,prim,hom}}. \tag{2.63}$$

The main challenge in scaling prediction is that the contamination of surfaces as well as convected particles can lead to significant narrowing of the metastable zone. The amount of non-dissolved solids can be, to a certain limit, controlled by filtration of the feed. This can lead to significant differences in tolerated supersaturation between filtrated and unfiltrated solutions [20]. Nevertheless, under laboratory conditions and especially in a real plant setup, it is always possible that particles, deposits, or crystals are convected to regions with favorable conditions for crystal growth. Already a short contact with air containing $> 10^6$ particles per $\text{cm}^3$ of a size <1 μm [68] will provide sufficient foreign particles to contradict the assumption of homogeneous nucleation in most cases, especially in industrial application.

If a third (second solid) phase is involved in the nucleation process, this can significantly reduce the energy barrier, depending on the contact angle $\theta$ between crystal and solid. The energy barrier for heterogeneous nucleation is

$$\Delta G_{\text{crit,het}} = \varphi \, \Delta G_{\text{crit}} \tag{2.64}$$

with $\varphi < 1$ for $0 < \theta < 180°$. Further reduction can be achieved by the presence of crystals of the same species. This secondary nucleation might be triggered by shearing and downstream growth of outgrowth or loosely bounded crystal units. [68]

Karanikola et al. [72] demonstrated how membrane surface hydrophobicity and porosity interact with gypsum scaling in DCMD. They showed that increasing hydrophobicity especially superhydrophobic (slippery) surfaces provide a better resistance to scaling. Further, they linked the Gibbs free energy of heterogeneous nucleation to the surface porosity and contact angle. The

membrane-crystal-solution system reaches the highest values of $\Delta G_{crit}$ for large contact angles and low porosity.

For statistical treatment of crystal nucleation it is useful to describe the nucleation process with nucleation rates. Classical nucleation theory derives nucleation rates based on an Arrhenius type equation [68]

$$\dot{N} = A_N \, \exp\left(\frac{-\Delta G_{crit}}{k_B T}\right) = A_N \, \exp\left(-\frac{16\pi\sigma^3 V_m^2}{3 k_B^3 T^3 (\ln S)^2}\right).$$ (2.65)

The dependency on the supersaturation $S$ can be derived from Eq. 2.59 and the Gibbs-Thomson relationship between particle size and solubility for calculating the volume excess free energy $\Delta G_V$ (cf. Mullin [68], p.108).

For practical application in industrial systems, empirical correlations are based on this fundamental relation. This can be done for example by fitting a rate constant $k_N$ and an 'apparent order of nucleation' $n$ to a correlation of the form

$$\dot{N} = k_N \, \Delta c_{max}^n.$$ (2.66)

The maximum allowable supersaturation $\Delta c_{max}$ is often called metastable zone width. [68]

Alternatively, as done by Kostoglou and Karabelas [73], Eq. 2.65 can be summarized to

$$\dot{N} = A_N \, \exp\left(-B_N / (\ln S)^2\right).$$ (2.67)

Parameter $B_N$ might be calculated with experimentally determined values for $S_{rel,het}$ or directly fitted to experiments together with the rate constant $A_N$.

According to Mullin [68], a time lag between the preparation of a supersaturated solution and the first detection of crystals can be observed in many crystallization experiments. This time span is generally referred to as induction time $t_{ind}$. It depends on the degree of supersaturation, the temperature, viscosity, and agitation of the solution as well as impurities contained. Experimental findings let assume that it can be subdivided into a relaxation time to reach steady-state distribution of molecules in the solution and a time for formation of the nucleus. Afterwards, the nuclei have to grow until they reach a detectable size. For aqueous electrolyte solutions, the relaxation time can

be very short. The exact mechanisms of nucleation are unknown. Finally, the discrepancy between nucleus size and detectable crystal size depends on the experimental method. In conclusion, induction times determined in experiments are not "a fundamental characteristic of a crystallizing system" [68, p. 208].

**Crystal Growth**

After a stable nucleus has been formed, the supersaturation of the surrounding solution drives the growth of the crystal until the system reaches equilibrium.

Researchers derived their crystal growth models based on surface energy, surface dislocation, and nucleation, or stepwise diffusion and reaction. During fundamental experiments, they found different growth rates on the different faces of crystals. Further, dissolution was observed to be often significantly faster than growth. Finally, different growth mechanisms were observed to superimpose. [68]

One widely used growth model is the kinetic growth theory by Burton, Cabrerea, and Frank, short BCF-model [74]. They derived a growth rate from theoretical investigation of a screw dislocation mechanism. It is

$$R_G = A_{BCF} \ S_{rel}^2 \ \tanh(B_{BCF}/S_{rel}) \tag{2.68}$$

the growth rate in dependency of the relative supersaturation and two complex, temperature dependent constants $A_{BCF}$ and $B_{BCF}$. For low degrees of supersaturation, it is $R \propto S_{rel}^2$. For higher values of $S_{rel}$, the function approaches a linear relation between the growth rate and the degree of supersaturation.

Although the model was initially derived for growth from vapor, Rodriguez-Clemente [75] applied the model to crystallization of NaCl from aqueous solutions. He observed a linear relation between the growth velocity of the crystal's faces and the supersaturation of the surrounding bulk solution.[5] Wide scattering of the measurement results were attributed to

---

[5]Rodriguez-Clemente [75] correlated the growth rates of a single NaCl crystal for a temperature range of 24-36 °C and $S_{rel} = 0-13 \cdot 10^{-3}$ and observed growth rates up to $R_G = 5 \cdot 10^{-5} \ cm \ s^{-1}$. Mullin [68] lists mean overall growth rates $\bar{v} = 0.5 \ R_G$ for NaCl from $2.5 \cdot 10^{-6} \ cm \ s^{-1}$ for $S_{rel} = 2 \cdot 10^{-3}$ and 50 °C up to $1.5 \cdot 10^{-5} \ cm \ s^{-1}$ for $S_{rel} = 3 \cdot 10^{-3}$ and 70 °C, increasing with temperature and supersaturation.

- the concentration of dislocations on the crystal surface,
- two-dimensional nucleation on steps, and
- impurities in the solution.

This demonstrates a major problem for applying fundamental growth theory to industrial systems. Therefore, empirical approaches dominate in this field (refer to e.g. Refs. [68, 70, 73, 76]).

According to Mullin [68], different sub-processes can be identified for electrolytes which crystallize from aqueous solutions including

- bulk diffusion steps,
- surface diffusion,
- dehydration and integration of the solute, and
- counterdiffusion of the solvent.

Each of these steps can limit the overall growth process. For practical application, based on diffusion-reaction theories, the growth rate can be written as

$$R_G = \frac{1}{A} \frac{dm}{dt} = K_G \, (c - c_{sat})^g. \tag{2.69}$$

This approach sums up all transport steps over the crystal surface $A$. From experimental results, the order of the process $g$ and the overall growth coefficient $K_G$ can be determined.

### 2.4.2 Scaling Potential of Real Brines

The scaling propensity of real brines, e.g. from brackish or seawater desalination, depends on numerous factors such as relative composition, temperature, solved gases, and non-dissolved solids. The major components of natural waters are discussed in the following and their interplay is analyzed.

The main components are chloride, sodium, sulfate, magnesium, calcium, and potassium. Major mineral scales that form in desalination applications are calcium carbonate ($CaCO_3$), calcium sulfate ($CaSO_4$), barium sulfate ($BaSO_4$), magnesium-based and silica scales [70]. In the following, the focus

is on $CaSO_4$ and $CaCO_3$ as sparingly soluble salts. They are the most critical scalants in a wide range of desalination and water treatment applications [26, 70, 77]. To reduce the complexity of the multi-component system, their temperature dependent solubility and their interaction with solved sodium chloride is investigated to extract relevant mineral compositions for the application at hand. One has to keep in mind that the operation range of VMD lies in a temperature window from 20 °C to 90 °C. Additionally, the feed solution is expected to be partially degassed over the length of a module depending on the applied vacuum pressure. For the calculations, the software tool PHREEQC[6] was used.

**Solubility of Calcium Sulfate**
The aqueous calcium sulfate system

$$Ca^{2+} + SO_4^{2-} + H_2O \rightleftharpoons CaSO_4 \cdot H_2O \rightleftharpoons CaSO_4 + H_2O \qquad (2.70)$$

forms the crystal phases gypsum (middle), anhydrite (right), and hemhydrate ($CaSO_4 \cdot 0.5\,H_2O$), whereas the latter is not stable under conditions relevant for this work. It can be relevant at temperatures above 100 °C where it remains metastable [80].

Solutions can be prepared by mixing stock solutions of calcium chloride and sodium sulphate

$$CaCl_2 \cdot 2\,H_2O + Na_2SO_4 \longrightarrow Ca^{2+} + 2\,Cl^- + 2\,Na^+ + SO_4^{2-} + 2\,H_2O. \qquad (2.71)$$

This allows to prepare supersaturated solutions. They always contain a NaCl molality of two times the $CaSO_4$ molality.

The solubility, its temperature dependency, and especially the transition temperature between gypsum and anhydrite depend on the water activity. This is influenced by the concentration of electrolytes in solution as derived in Sec. 2.3. The resulting solubility limits of the crystal phases gypsum and anhydrite are plotted in Fig. 2.11 over the solubility range of NaCl for different temperatures. The crystal phase with the lowest solubility at a given temperature and NaCl content is the stable phase.

---

[6]The Linux batch version of PHREEQC [78] 3.4.0-12927 was used. As databases pitzer.dat, phreeqc.dat, and din38404.10_2012.dat [79] were applied.
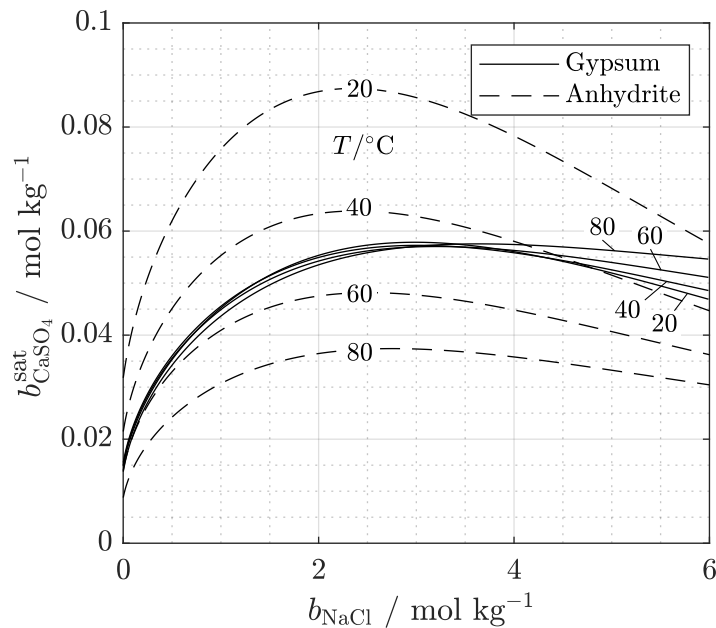
**Figure 2.11:** Dependency of the equilibrium solubility $b^{\text{sat}}_{\text{CaSO}_4}$ of gypsum and anhydrite on NaCl content and temperature (calculated with PREEQC [78], Database: Pitzer).

The transition points between gypsum and anhydrite are hard to determine in experiments due to the slow crystallization kinetics. This is why metastable phases can exist. For pure $CaSO_4$, the transition temperature range determined by experiments lies in the range of 25 °C to 52 °C. In practical application, especially metastable gypsum can be formed in regions where anhydrite would be the stable phase. The low nucleation rates of anhydrite and the presence of gypsum nuclei can lead to a significant shift of the transition towards higher temperatures. [80]

Two distinct concentration ranges of NaCl are analyzed in detail: Figure 2.12a shows the equilibrium solubilities of gypsum and anhydrite for the range of $0 \, \text{mol kg}^{-1} \leq b_{\text{NaCl}} \leq 0.1 \, \text{mol kg}^{-1}$. The mixture line marks the stoichiometric concentration of NaCl in the solution when it is prepared from $CaCl_2$ and $Na_2SO_4$ according to Eq. 2.71. This is the composition used for $CaSO_4$ scaling experiments in Ch. 5. Below 60°C gypsum is the stable solid phase and its solubility does not show a significant temperature dependency. The prac-

tical application of this case could be the treatment of brackish or seawater. Figure 2.12b shows the equilibrium solubilities for NaCl concentrations near the solubility limit of halite. The lines for the equilibrium solubility end when reaching the solubility limit of halite in the mixture. Anhydrite becomes the stable phase already at temperatures around 40 °C. The equilibrium solubility is strongly temperature dependent, whereas the concentration dependency has a lower impact on the solubility. This region is interesting for ZLD applications when reaching the solubility limit of NaCl.
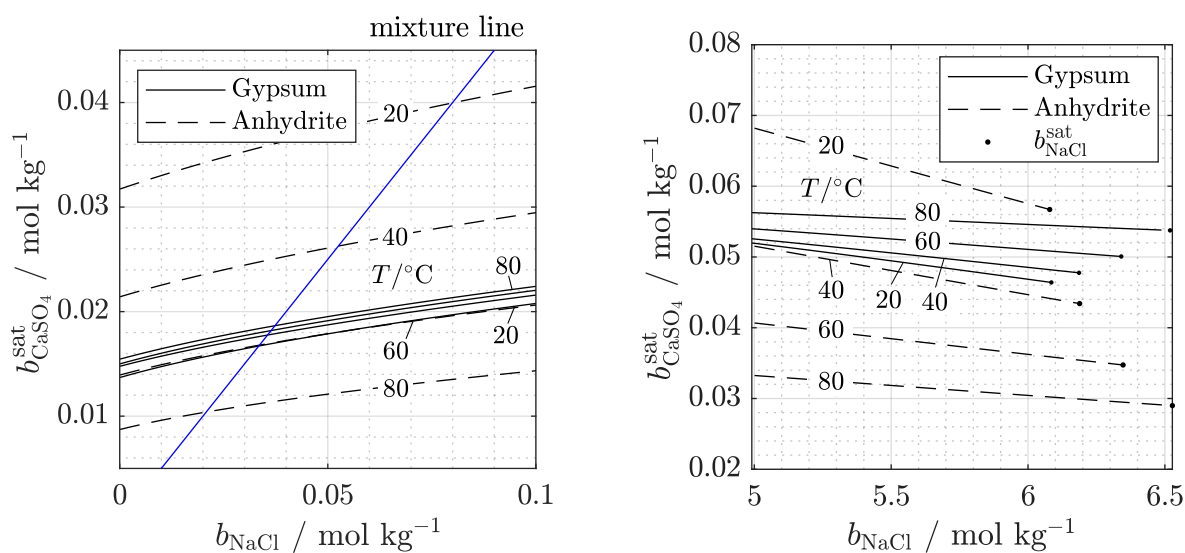


(a) Equilibrium solubility at low NaCl concentration; mixture line for solution preparation from $CaCl_2$ and $Na_2SO_4$.

(b) Equilibrium solubility at NaCl concentrations near saturation.

**Figure 2.12:** $CaSO_4$ equilibrium solubility $b_{CaSO_4}^{sat}$ at different operation windows (calculated with PREEQC [78], Database: Pitzer).

**Solubility of Calcium Carbonate**
Supersaturated solutions of calcium carbonate can be prepared by mixing stock solutions of $CaCl_{2(aq)}$ and $Na_2CO_{3(aq)}$ in water.

$$CaCl_2 \cdot 2\,H_2O + Na_2CO_3 \longrightarrow 2\,Na^+ + 2\,Cl^- + Ca^{2+} + CO_3^{2-} + 2\,H_2O \qquad (2.72)$$

The aqueous carbonate system on the right hand side is influenced by the pH of the mixture and therefore the amount of solved $CO_2$. The influence of pH is described when discussing the dissolution of gases and their influence on scaling below. Figure 2.13a shows the solubility of calcite (trigonal) and aragonite (orthorombic) in dependency of temperature and NaCl content of the solution. For this analysis, the solution is modeled with an equilibrium gas phase with a $CO_2$ partial pressure of $p_{CO_2} = 39\,Pa$. This is the $CO_2$ content of air under normal conditions. All other air components are considered as insoluble. Calcite is the stable phase for the application at hand. Nevertheless, amorphous calcium carbonate, vaterite, and aragonite can exist as metastable intermediate steps in a complex crystallization process [77].

**Dissolution of Gases and Their Influence on Scaling**
The solution of carbon dioxide ($CO_2$) significantly influences the scaling behavior of natural waters. The buffer system between carbon dioxide, carbonic acid, and hydrogencarbonate

$$CO_2 + H_2O \rightleftharpoons H_2CO_3 \rightleftharpoons HCO_3^- + H^+ \rightleftharpoons CO_3^{2-} + 2\,H^+ \qquad (2.73)$$
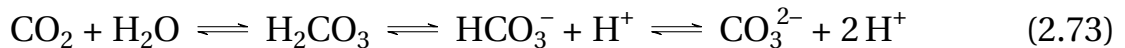
shifts in relative concentration from $H_2CO_3$ over $HCO_3^-$ to $CO_3^{2-}$ from low to high pH values [81]. Additionally, the $CO_2$ solubility is temperature, pressure, and concentration dependent. Open aquatic systems seek balance with the $CO_2$ pressure of air, whereas a degassing will take place in the vacuum system at hand. Therefore, a change in $CO_2$ concentration over the length of a module as well as over the boundary layer forming at the membrane can be expected.

Fig. 2.13b shows the temperature dependent phase stability of calcite and aragonite calculated for a reactor in equilibrium with a gas phase at atmospheric $CO_2$ pressure and without $CO_2$. The $CO_2$ significantly increases the solubility, especially at lower temperatures. It leads to the well known inverse solubility with rising temperature. It becomes obvious that it is not possible

to predict the solubility limit of carbonates without knowing the $CO_2$ content. Therefore, the knowledge of the dependency of the pH value on $CO_2$ content is valuable for evaluating experimental results. Decreasing the partial pressure of $CO_2$ significantly decreases the solubility of carbonates. As a countermeasure, strong acids can be added during pretreatment of the feed solutions. This way the formation of alkaline scales such as from $CaCO_3$ can be avoided [70, 82].
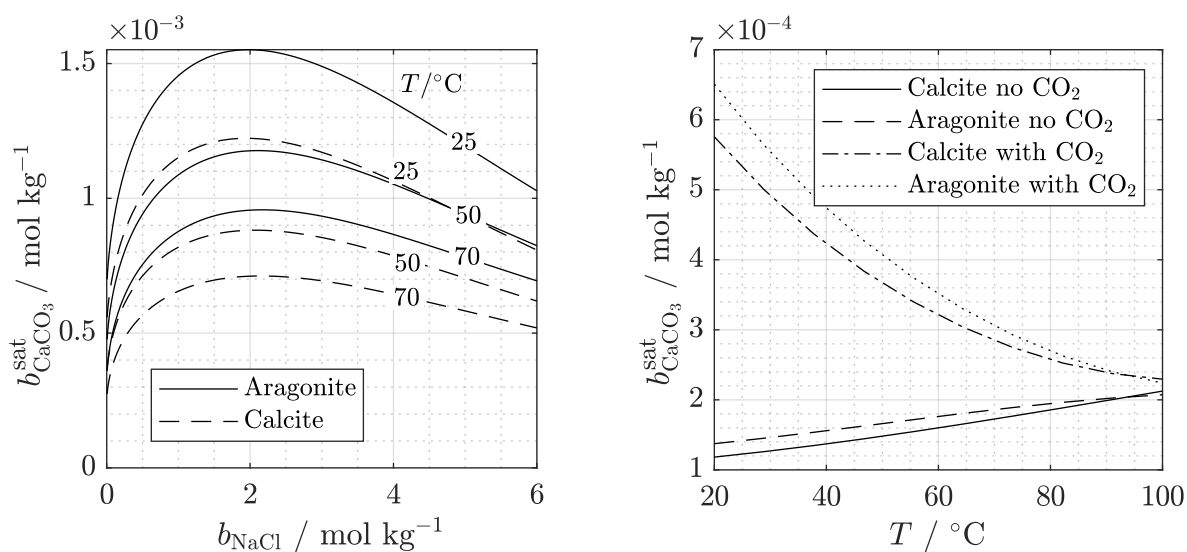


**(a)** Solubility depending on NaCl content in equilibrium with atmospheric $CO_2$ at $p_{CO_2} = 39\,Pa$.

**(b)** Calcite and aragonite solubility without adding $CO_2$ and with $p_{CO_2} = 39\,Pa$ in equilibrium.

**Figure 2.13:** Equilibrium solubility $b^{sat}_{CaCO_3}$ of aragonite and calcite calculated with PREEQC [78]; databases: (a) Pitzer, (b) DIN38404-10_2012.

# 3 Analysis of Multi-Effect Vacuum Membrane Distillation Systems

This chapter analyses the MEVMD process from a system perspective. In the first part, a theoretical analysis introduces to the concept of multi-staging and shows the influence of vapor pressure reduction on the plant performance from a theoretical perspective. In the second part, the experimental methods are described. The experiments were used to validate a system simulation model described in the third part of this chapter. This system simulation model is the core component of the tool chain for MEVMD system design developed in this thesis. Parts of this chapter were already published in Kiefer et al. [19, 83].

## 3.1 Theoretical Analysis

The key design feature of MEVMD plants is the number of installed stages. It determines how often the heat of vaporization of vapor produced in one stage is internally reused. The pressures in the vapor channels of the stages lie between the equilibrium vapor pressure of pure water at steam raiser temperature and that at condenser temperature.

For a feed solution with negligible vapor pressure reduction, the driving pressure difference across the membrane of stage $i$ can be calculated by

$$\Delta p_{v,i} = p_{v,B,i} - p_{VC,i} \tag{3.1}$$

which is the vapor pressure difference between that of pure water at the bulk feed temperature and that in the vapor channel (index VC) constituted by the condensation temperature level (cf. Sec. 2.1.3). The reduction of vapor pres-

sure due to the salt content leads to a reduction of the driving pressure difference according to equation 2.52.

$$\Delta p_{\text{loss},i} = p_{\text{v}}\left(T_{i,\text{B}}\right) - a\left(T_{i,\text{B}}, w_{i,\text{B}}\right)\, p_{\text{v}}\left(T_{i,\text{B}}\right) \tag{3.2}$$

The reduction of driving pressure difference due to reduced activity is inevitable and only depending on temperature, solute concentration, and solute composition for a given system configuration. If a multi-effect configuration is used, this loss mechanism reduces the performance of each effect and sums up as follows:

$$\Delta p_{\text{loss},\text{tot}} = \sum_{i=1}^{N} p_{\text{v}}\left(T_{i,\text{B}}\right)\left(1 - a\left(T_{i,\text{B}}, w_{i,\text{B}}\right)\right). \tag{3.3}$$

Only for low Recovery Ratios (RR)

$$\text{RR} = \frac{\dot{m}_{\text{D}}}{\dot{m}_{\text{F}}} \tag{3.4}$$

and small temperature differences it is possible to average the temperature and concentration over the length of one stage.

A first step towards investigating the influence of the solute dependent vapor pressure reduction on a multi-stage system was done with the following theoretical approximation. Each stage is simplified to have a constant temperature level and the system is assumed to operate a small recovery rate RR→0 so that the feed salt content is approximately constant throughout the whole system. The temperature of the feed in the first stage $T_{\text{high}}$ and the heat rejection temperature $T_{\text{low}}$ determine the Gross Driving Pressure Difference (GDPD, Eq. 2.3) of the system. Aqueous $CaCl_2$ is investigated as feed solution to cover a wide range of applications in terms of solute induced vapor pressure reduction (cf. Sec. 2.3.3). The GDPD is reduced according to Eq. 3.3. The remaining pressure is equally distributed to the number of stages $N$. This is done in an iterative procedure.

The resulting Net Driving Pressure Difference (NDPD) and Net Driving Temperature Difference (NDTD) for a one to six stage setup are shown in Fig. 3.1. The NDPD is calculated as

$$\text{NDPD} = \sum_{i=1}^{N}\left(p_{\text{v}}\left(T_{\text{sat}}(p_i, w_i = 0), w_i\right) - p_{i+1}\right). \tag{3.5}$$

It is the sum of the Net Driving Pressure Differences $NDPD_i$ of each stage $i$ from Eq. 2.4. The vapor pressure of the feed solution $p_v$ is estimated from the saturation temperature $T_{sat}(p_i, w_i = 0)$ of pure water at $p_i$ and the salt mass fraction $w_i$. If the feed solution is pure water, the pressure difference of each stage is $p_i - p_{i+1}$. It is reduced by the influence of the salt according to Eq. 3.2 when $w_i > 0$. Finally, the NDTD is calculated from the saturation temperatures.

Figure 3.1a shows the increasing influence of solute dependent vapor pressure reduction towards higher feed salt content $w_F$. Increasing the number of stages further reduces the NDPD. The influence of the upper temperature level is less pronounced for high salt mass fractions. A similar behavior can be observed for the NDTD in Fig. 3.1b. At around $w_F = 400\,\mathrm{g\,kg^{-1}}$ NDPD and NDTD become $< 0$ for six or more stages. With rising feed salt content this happens for systems with less stages.
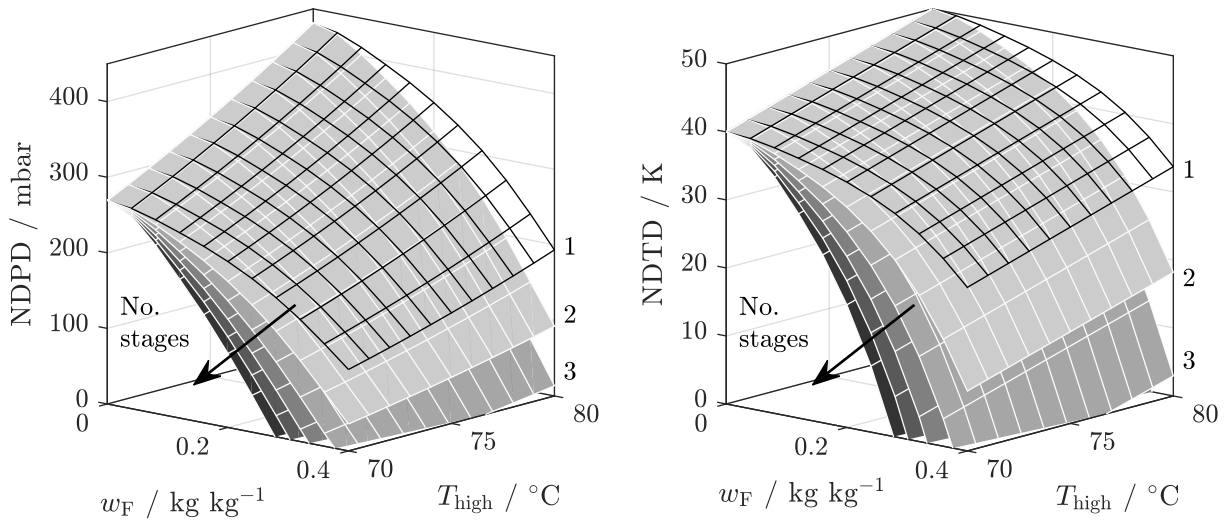


**(a)** Net Driving Pressure Difference (NDPD) [19].

**(b)** Net Driving Temperature Difference (NDTD) [19].

**Figure 3.1:** Estimated NDPD and NDTD for setups with a total number of $N = 1$ to 6 stages at different upper temperature levels $T_{high}$ ($T_{low} = 30°C$). The feed solute is $CaCl_2$; vapor pressures calculated according to Conde-Petit [62].

An operation in multi-effect mode is only possible if heat transfer is guaranteed by a continuously falling temperature over the stages and NDPD > 0. This is not possible anymore for a larger number of stages at higher feed concentrations or low upper temperature levels. For the real plant operation, one or more stages will automatically stop producing distillate under these extreme boundary conditions.

The theoretical assessment with the help of the NDPD gives a hint on the decrease of plant performance due to vapor pressure reduction with increasing salt mass fraction. The sum of NDPD is directly proportional to the distillate production. Nevertheless, it has to be kept in mind that temperature polarization at the foil as well as concentration and temperature polarization at the membrane have to be overcome additionally.

This first system analysis shows the theoretical dependency of a multi-stage system's performance on solute induced vapor pressure reduction. The following experiments and modeling work were conducted to gain a deeper insight into this phenomenon and finally to quantify its impact under realistic operating conditions.

## 3.2 Experimental Methods

Two experimental approaches were used to investigate the behavior of the MEVMD system. Experiments were conducted with an industrial system provided by Memsys tec AG. Here, the focus was on understanding the plant behavior and performance reduction for feed solutions with salt concentrations providing a significant vapor pressure reduction. From this industrial system, a bench scale test rig was derived and implemented. The motivation was to construct a channel assembly similar to the ones of the industrial system, where access to local properties was limited. This finally provided data for model calibration and verification.

### 3.2.1 Industrial Scale System

The industrial system was a Memsys 4-6.4 R&D plant. The hydraulic system and the membrane block with $6.4\,\mathrm{m}^2$ active membrane area distributed on four stages is depicted in Fig. 3.2. Heat supply was realized by a 7 kW electrical heater (E) over a heating circuit. This supplied the steam raiser (SR) with hot deionized water which partially evaporated over the $2.56\,\mathrm{m}^2$ membrane area and heated the feed solution in the first stage (E1). The distillate produced in the SR was recycled to the heating circuit via the heating steam distillate recovery (F). The stages (E1-E4) consisted of 11 frames each. They were equipped with $1.6\,\mathrm{m}^2$ membrane and foil for each stage. Due to the channel arrangement, the number of stages could be reduced from four to two. The steam leaving the last stage was led to the 17 condenser frames with a total foil area of $2.56\,\mathrm{m}^2$. The condenser (CO) was cooled via the condenser circuit and heat was rejected over a plate heat exchanger to a cooling water stream.

The system was equipped with temperature and pressure sensors at all in- and outgoing streams as well as in the vapor channels. The latter helped to analyze the proper functionality of the system. Additionally, a heat exchanger with temperature control was installed to preheat the feed solution (B). An additional automated valve in the cooling water stream helped to control the condenser inlet temperature. A list of the complete system specifications is

provided in appendix Tab. B.1 and the properties of the membrane are summarized in appendix Tab. B.2.

As model fluid an aqueous solution of calcium chloride ($CaCl_2$) was used. It shows a similar concentration dependency of the equilibrium vapor pressure as NaCl, but at a higher solubility. Therefore, the experiments can be easily transferred to applications with sodium chloride. At the same time, crystallization of the solvent is prevented which protects membranes and pumps. The increased solubility and therefore significantly decreased vapor pressure in a concentration range beyond the solubility of sodium chloride is a reason for the use of $CaCl_2$ solutions as liquid desiccants. This brings a second motivation for using $CaCl_2$ as solute.

The feed solution was supplied from a stirred feed tank (A) and its flow was adjusted with a manual valve (C). The feed was sucked into the stages by the reduced pressure prevailing in the plant, which is why no additional feed pump was necessary. The vacuum pump was connected to the brine (H) and distillate vessels (I) and via a pipe with reduced diameter to the condenser (CO, G) to ensure sufficient removal of non-condensable gases. The brine and distillate outlets were connected to vessels (H, I) operated at the lowest pressure of the system. A level control system initiated pumping against ambient pressure into a storage tank. Furthermore, these level control systems were calibrated and used for measuring the brine and distillate flow rates.

For all fluid streams Memsys' nomenclature was applied. The streams are marked with a two digit number, where the first digit names the stream and the second digit the position in the system (cf. Fig. 3.2). The streams are the heating circuit water (1), the feed solution (2), brine (3), distillate (4), condenser cooling water (6), and vapor (7).
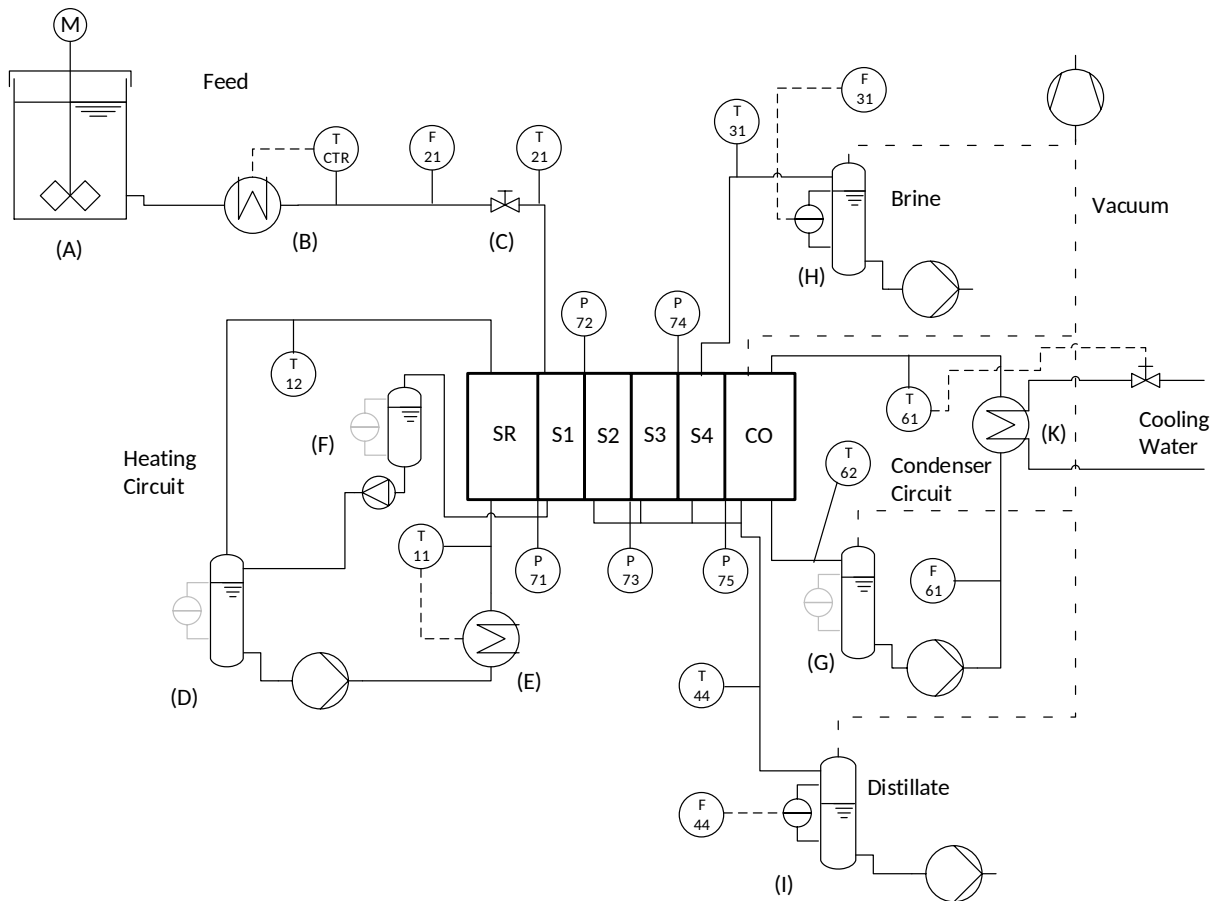
**Figure 3.2:** Piping and instrumentation diagram of the experimental setup (adapted from [44]) containing additional feed and cooling temperature control. SR: Steam Raiser, S1 - S4: Effects/Stages, CO: Condenser. (A) feed tank, (B) feed preheating with temperature control, (C) inlet throttle valve, (D) heating circuit compensation reservoir, (E) electrical heater with temperature control, (F) heating steam distillate recovery, (G) condenser circuit compensation reservoir, (H) brine tank with level control and flow calculation, (I) distillate tank with calibrated level control for flow rate calculation, (K) plate heat exchanger.

### 3.2.2  Bench-Scale Experimental Setup

A bench scale test rig was derived from the MEVMD system scale experimental setup. This was motivated by uncertainties arising from the specific design of the MEVMD system, lacking access for measurement equipment inbetween the stages as well as missing optical access to the membrane and permeate channel. The new test setup provided the following features:

- It resembled one membrane channel assembly of an MEVMD system with heating channel, feed channel, and vapor channel.
- All channels could be observed during operation, since polycarbonate was used as construction material for the cell and the heat transfer foil. Therefore, scaling in the feed channel as well as membrane wetting and crystal growth in the vapor channel could be monitored.
- The system contained a separately controllable feed and heating circuit, as well as an externally cooled condenser. This way, different positions in an MEVMD system could be experimentally simulated by adjusting the boundary conditions.
- It provided high flexibility for exchanging membranes and spacers.
- A uniform flow over the channel width was guaranteed by the cell construction. This was especially necessary for validating the 1D simulation model.

Figure 3.3 shows the cell concept: the feed channel with a length of 400 mm and a width of 300 mm (effective membrane and heat transfer area) was located between the heating and the vapor channel, both 2 mm in height. The membrane used in the bench scale experiments was the same as for the system scale experiments with the Memsys system (details listed in appendix Tab. B.2). The vapor channel was held open with a spacer.

For sake of consistency, the fluid streams are labeled as introduced for the industrial scale system in Sec. 3.2.1. The salt solution circulated through the feed channel from bottom (index 21) to top (index 22) to ensure complete venting. The flow direction of the heating water (index 11 and 12) was perpendicular to the flow direction of the feed solution (i.e. horizontal).

(A) Front plate
(B) Feed channel frame
(C) Vacuum channel frame
(D) Rear plate
(M) Membrane
(S) Heat transfer foil
[11] Heating fluid inlet
[12] Heating fluid outlet
[21] Feed inlet
[22] Feed outlet
[vac] Vacuum system
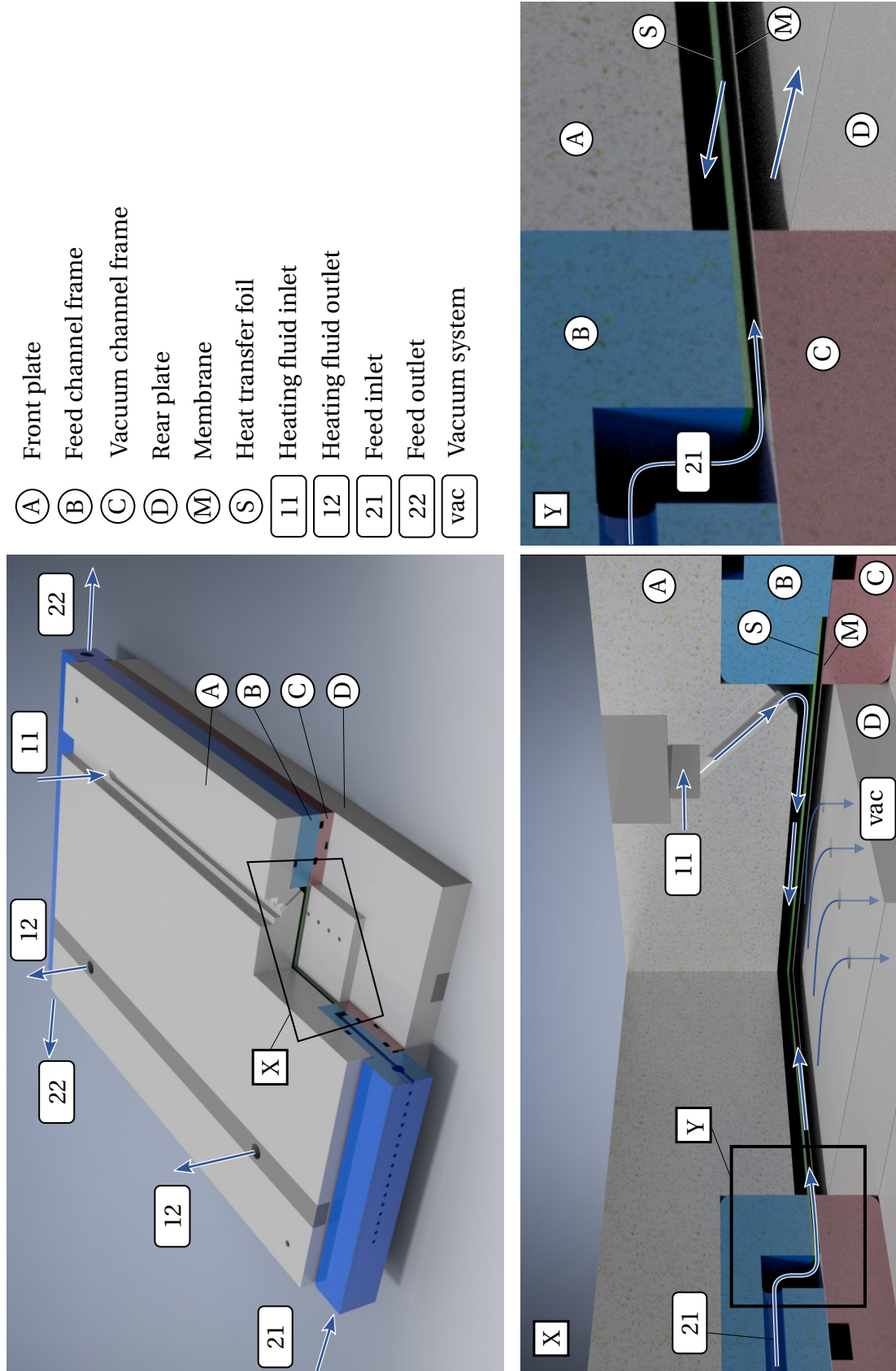
**Figure 3.3:** Bench scale triple-channel test cell with flow configuration.

The feed channel was stabilized by the feed spacer, whereas the sandwich structure of membrane, spacer, and heat exchanger foil was held in place by the pressure difference established between the three channels. This guaranteed a constant width of the feed channel over a wide range of operational conditions, which is an advantage over conventional test cell configurations using two channels with rigid walls. The experiments were conducted with a 34 mil AMI feed spacer. The vacuum channel spacer was manufactured from acrylic glass filaments providing a 2 mm channel height and a mesh clearance of $L_1 = L_2 = 4$ mm with a filament angle of $\beta = 90°$.

Figure 3.4 shows the piping and instrumentation diagram of the test rig. The core component was the membrane cell connected to the feed, the heating and the vapor circuit. The feed was electrically heated in a corrosion-resistant tank (V_F) and could be optionally filtrated in an Ultra Filtration module (UF). The solution was pumped with a gear pump which provided constant and pulsation free flow rates. The heating circuit was filled with distilled water and heated by a separate heater in the vessel V_H. Both circuits contained a flow sensor (F_11, F_21) as well as temperature and pressure sensors as listed in appendix Tab. B.3. The vapor channel was connected to an external condenser (C) that was cooled via a separate refrigerant circuit connected to a vapor compression chiller (CC) with temperature control. The distillate and remaining gases were discharged into the condensate vessel (V_C), where the distillate was stored under reduced pressure. The content of the vessel was pumped against ambient pressure regularly controlled by a level sensor (LC) or the operator. The vacuum pump was connected to the condensate vessel over an additional separator. An Oerlikon Leybold Trivac D8B laboratory vacuum pump was used to remove non-condensable gases. It provided a volume flow rate of $8\,\text{m}^3/\text{h}$ and was able to hold the system pressure below 5 mbar without feed flow. The distillate mass as well as the reduction of the feed mass were measured with scales (M_D1, M_F1). The vapor channel pressure (P_V1) was measured directly behind the membrane cell.
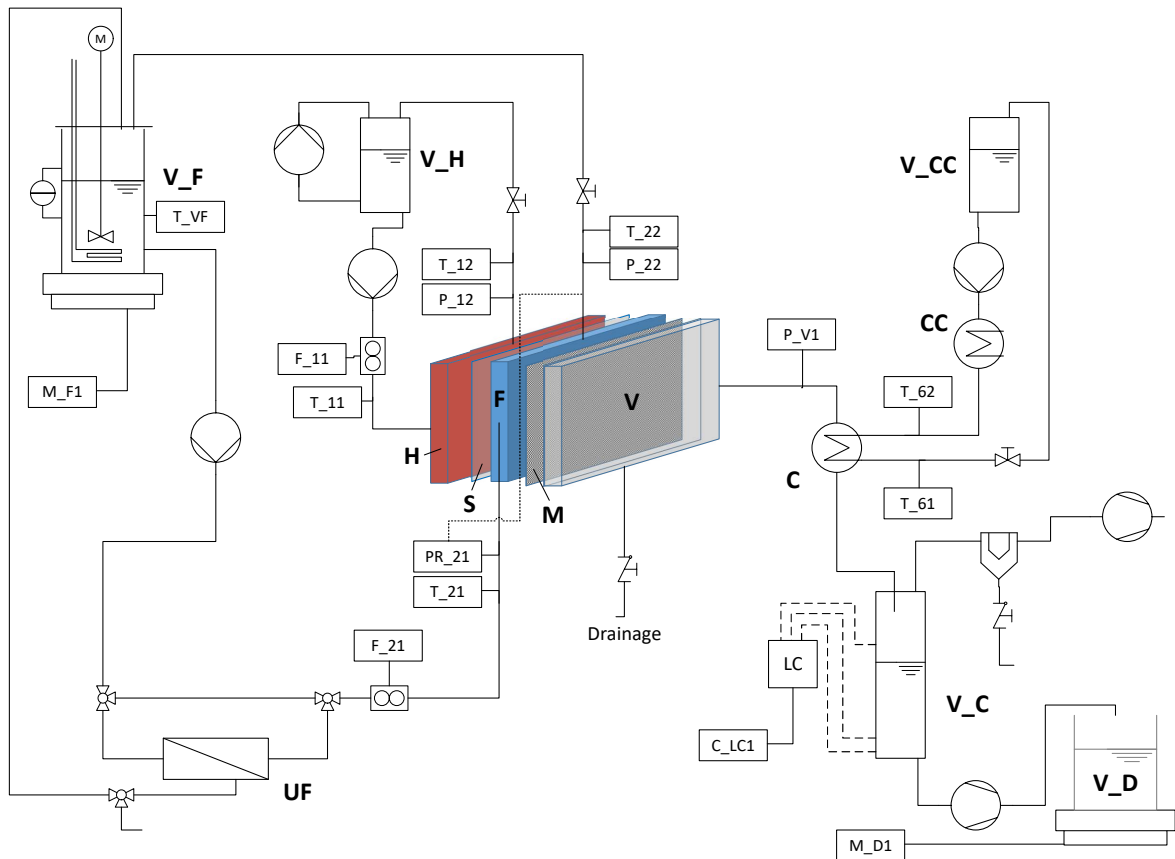
**Figure 3.4:** Piping and instrumentation diagram of the bench-scale test rig. (V_F) Feed tank, (V_H) Heating fluid storage vessel, (H) Heating channel, (S) Heat transfer foil, (F) Feed channel, (M) Membrane, (V) Vapor channel, (C) Condenser, (CC) Compression chiller, (V_CC) Cooling water storage vessel, (V_C) Condensate vessel, (V_D) Distillate tank, (UF) Ultra Filtration module [83].

**Measurement Procedure**

For steady-state measurements, a measurement period of approximately 45 minutes was used. During this steady-state period, the distillate was pumped three times from the storage vessel V_C and temperatures $T_{21}$, $T_{11}$, and $T_{61}$ were controlled. The duration of one pumping cycle was adjusted to the distillate flow rate to increase measurement accuracy. Error bars in distillate mass measurements (Fig. 3.5a, 3.5b) indicate the standard mean deviation between these three pumping cycles. Energy balance-based error estimates show the absolute error with a generic temperature measurement uncertainty of $\pm 0.1$ K. RO permeate was used for preparing the feed solutions. After the dissolution of the salt, the feed solutions were once filtered with the Ultra Filtration (UF) module (cf. Fig. 3.4) to remove particles and contaminants contained in the salt. Afterwards, the UF module was taken out of the feed circuit.

**Evaluation of Measurement Data**

To avoid systematic measurement errors and to characterize the operation range and plant behavior, a set of experiments was conducted (cf. appendix Tab. B.4, M09, M10). The coupling of membrane cell and external condenser was investigated in a sensitivity study of the cold side condenser outlet temperature $T_{62}$. The distillate mass flow rate was measured directly as described above and compared to the overall energy balance (cf. Fig. 3.5a, Eq. 3.6, 3.7).

$$\dot{Q}_v \approx (\dot{m}_{22}\, h_{22} - \dot{m}_{21}\, h_{21}) - \dot{m}_{11}\, (h_{12} - h_{11}) \qquad (3.6)$$

$$\dot{Q}_v \approx \dot{m}_v\, h_v''(T_{2,\mathrm{mean}}) \qquad (3.7)$$

The measured vapor channel pressure $p_{VC} = p_{\mathrm{meas}}$ was compared to the equilibrium vapor pressure of the feed inlet $p_{v,21}$ and outlet $p_{v,22}$, and the saturation vapor pressure of steam at the condenser outlet temperature $p_{v,62}$. The exponential increase in vapor pressure with a linear increase in condenser temperature leads to an increasing vapor channel pressure and thus reduction in distillate production.

The measured distillate amount was slightly lower than the amount calculated from the energy balance. This is intuitive, since a certain amount will always be extracted with the non-condensable gases via the vacuum pump. Additionally, thermal losses over the test cell surface reduce the produced distil-

late amount. The discrepancy between the two values increased significantly, when the temperature exceeded 25 °C; the condenser was not able to "dry" the non-condensable gases sufficiently. A large amount of vapor was extracted by the vacuum pump. Therefore, if not stated differently, the cold side condenser inlet temperature was controlled to $T_{61} = 10\,°\text{C}$.

Deeper insight into the coupling of the heating and feed channels was achieved by investigating the sensitivity of distillate production to the difference between the inlet temperatures of these two channels $T_{11} - T_{21}$ (cf. Fig. 3.5b). The discrepancy between the directly measured distillate amount and the distillate mass calculated with energy balances almost vanished in the measurement error.
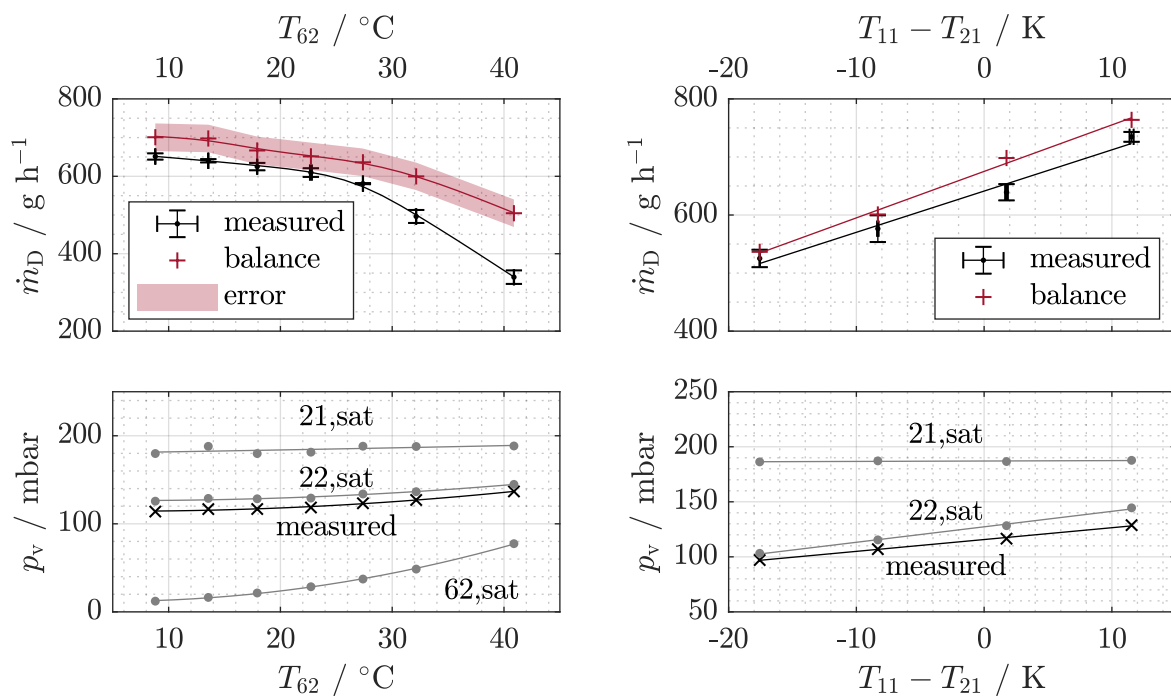


(a) Variation of the cold side outlet temperature of the external condenser $T_{62}$ [83].

(b) Variation of the heating channel inlet temperature $T_{11}$ at constant feed temperature $T_{21}$ [83].

**Figure 3.5:** Measurement uncertainty estimation via energy balances; saturation vapor pressures $p_{\text{v},21}$, $p_{\text{v},22}$, and $p_{\text{v},62}$ calculated based on temperature measurements; feed water is RO permeate (cf. appendix Tab. B.4, M09).

## 3.3   Modeling Approach

This section summarizes the quasi-2D simulation model for MEVMD systems and its sub-models. Furthermore, calibration and verification of the channel sub-model as well as comparison of the MEVMD model with experimental results is reported. The focus was on physical modeling of the heat and mass transfer in the system with a minimized set of empirical parameters. The resulting model is able to visualize the behavior of MEVMD systems over the whole operation range up to the solubility limit of salt solutions.

### 3.3.1   Channel Model

The channel model is the core component of the MEVMD system model. It describes the flow in the spacer filled feed channel, discretized in mean flow direction. The flow normal boundary conditions are those for the heat and mass transfer across the membrane, and the heat transfer across the foil (Fig. 3.6). Memsys' nomenclature as introduced in Sec. 3.2.1 is used to label the vapor (index $7i$ and $7i+1$) and feed (index $2i$).
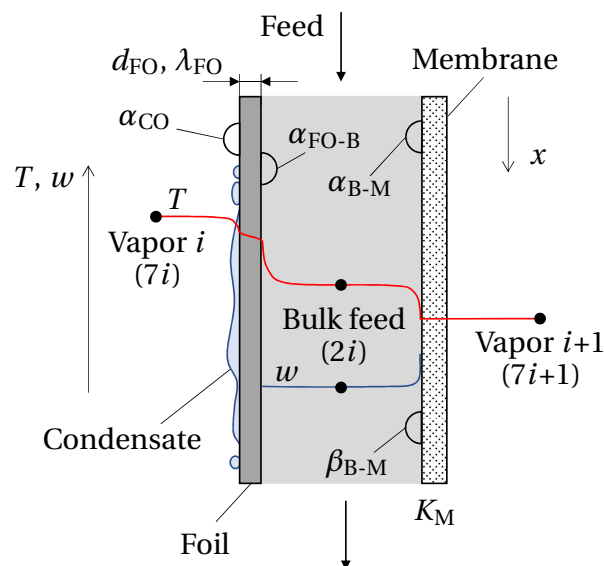


**Figure 3.6:** Channel cross-section with qualitative temperature $T$ and salt mass fraction $w$ profiles for a channel in stage $i$ [83].

Each channel assembly consists of three different channels: a condenser, a feed, and a vapor channel. Only the feed channel is discretized in flow direction. The adjacent vapor and heating channel are modeled as a single node each. The node model derived from Fig. 3.6 is shown in Fig. 3.7. Heat is transferred across a thin foil from the condenser channel to the feed solution. On the vapor side, only latent heat transfer is assumed to take place. Therefore, a constant temperature can be assumed over the whole vapor channel. Nevertheless, the energy balance of the condenser channel will take into account the superheat. Between the foil and the membrane, the feed channel is held open by a spacer which provides mixing of the laminar flow. To model the concentration and temperature polarization phenomena, the feed properties at the membrane ($X_{2i,\mathrm{M}}^{j}$) and at the foil ($X_{2i,\mathrm{FO}}^{j}$) are calculated. The vapor channel pressure on the other side of the membrane is again assumed to be constant for one stage ($p_{7i+1}$).
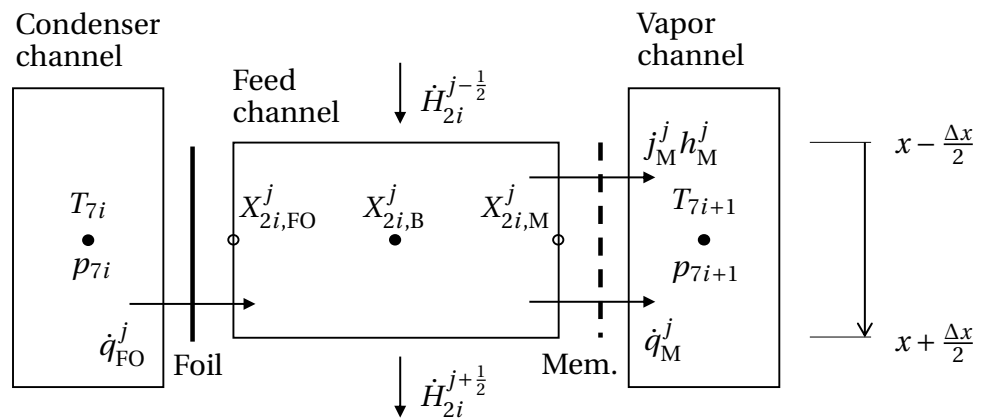


**Figure 3.7:** Enthalpy balance at volume element $j$ of the feed channel of stage $i$ and its coupling with the vapor and condenser channel. M, B, FO mark the state at the membrane, in the bulk, and at the foil.

The nonlinear system of ordinary differential equations consists of the mass conservation

$$\frac{\mathrm{d}\dot{m}_{2i}}{\mathrm{d}x} = -j_{\mathrm{M}}(x)\,\mathrm{d}A \tag{3.8}$$

and the energy conservation

$$\frac{\mathrm{d}h_{2i}}{\mathrm{d}x} = \frac{1}{\dot{m}_{2i}(x)}\left(\mathrm{d}A\left(\dot{q}_{\mathrm{F}}(x) - \dot{q}_{\mathrm{M}}(x)\right) - \frac{\mathrm{d}\dot{m}_{2i}}{\mathrm{d}x}\,h_{2i}(x)\right). \tag{3.9}$$

Heat and mass fluxes across membrane (M) as well as temperature and concentration polarization at channel position $(.)^j$ form the following nonlinear system of equations (cf. Sec. 2.2):

$$j_{\mathrm{M}}^j = K_{\mathrm{M}}^j\left(p_{\mathrm{v,M}}\left(T_{2i,\mathrm{M}}^j, w_{2i,\mathrm{M}}^j\right) - p_{7i+1}\right) \tag{3.10}$$

$$j_{\mathrm{M}}^j = \rho_{2i}^j\,\beta_{B-M}^j\,\ln\left(\frac{w_{2i,\mathrm{M}}^j}{w_{2i,\mathrm{B}}^j}\right) \tag{3.11}$$

$$\dot{q}_{\mathrm{M}}^j = \alpha_{B-M}^j\left(T_{2i,\mathrm{B}}^j - T_{2i,\mathrm{M}}^j\right) \tag{3.12}$$

$$\dot{q}_{\mathrm{M}}^j = j_M^j\,h_{7i+1}^j \tag{3.13}$$

The heat flux across the foil (FO) at channel position $(.)^j$ is

$$\dot{q}_{\mathrm{FO}}^j = \frac{T_{7i,\mathrm{sat}} - T_{2i,\mathrm{B}}^j}{1/\alpha_{\mathrm{B\text{-}FO}}^j + \delta_{\mathrm{FO}}/\lambda_{\mathrm{FO}} + 1/\alpha_{\mathrm{CO}}}, \tag{3.14}$$

including condensation on the foil surface, conduction across the foil, and convection from the foil surface to the bulk in $\alpha_{\mathrm{B\text{-}FO}}$.

The solver, as shown in Fig. 3.8, integrates the differential equations over the channel length using a variable step width Runge-Kutta approach. Heat and mass fluxes across the foil and membrane are calculated for the current channel position using local temperature and salt concentration. Finally, the heat and mass flux over foil and membrane are numerically integrated and their quantities are handed to the corresponding channel nodes ($X_{7i}$ and $X_{7i+1}$).
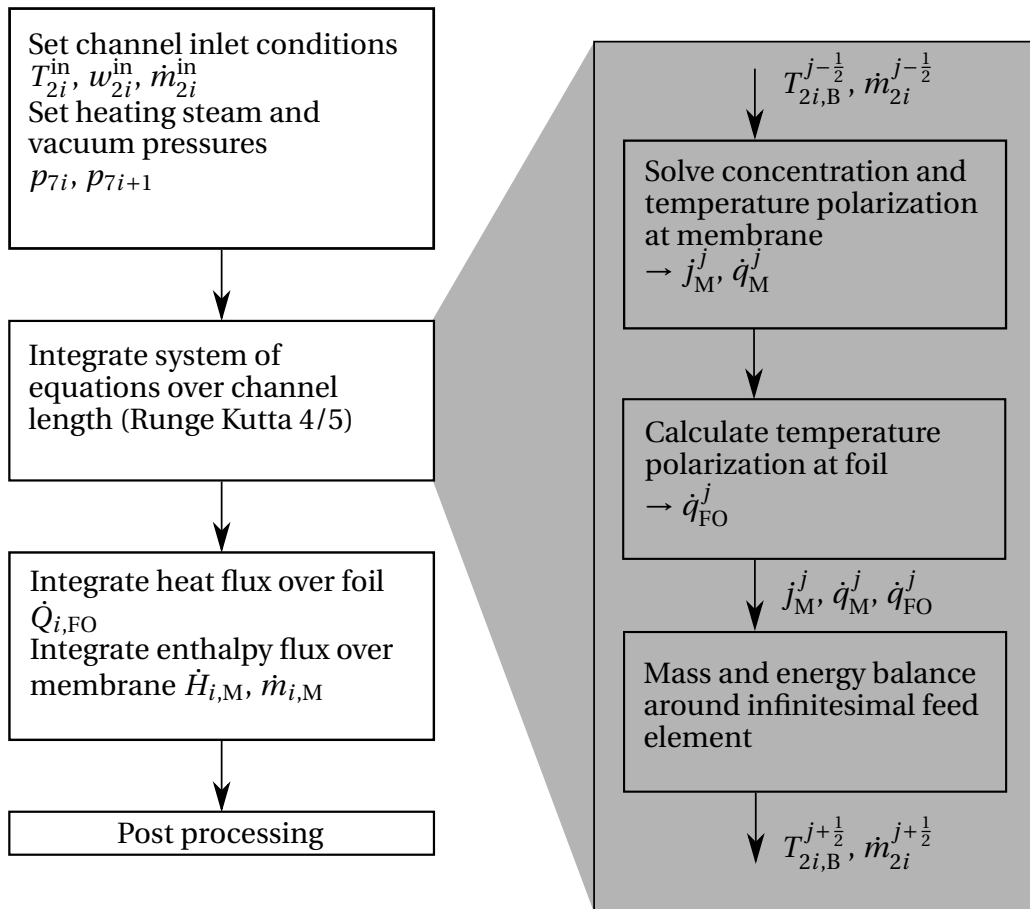
**Figure 3.8:** Solver concept for the quasi-2D channel model.

### 3.3.2 Model Calibration and Verification

The heat and mass transfer in the feed channel and across the membrane were calibrated with experimental results of the bench scale test rig described in Sec. 3.2.2. Three model parameters were adjusted in an iterative procedure. The first parameter, the membrane structure parameter $\varepsilon_M/\chi_M$ (cf. Eq. 2.18-2.20), summarizes the properties of the porous membrane. The second parameter, the Reynolds number pre-factor $a_{1,2}$ in Nu and Sh correlation (cf. Eq. 2.13, 2.12), accounts for the Reynolds dependency of heat and mass transfer coefficients from feed bulk to membrane and foil surface in the spacer filled channel. The exponents in these correlations were set constant to $b_{1,2} = 0.875$ and $c_{1,2} = 0.25$ according to Schock and Miquel [47]. The third parameter, the heat transfer coefficient on the heating fluid side of the foil $\alpha_{CO}$ (cf. Eq. 3.14), is an empirical model parameter used to decouple the investigation of the feed channel and membrane behavior from the sensible heating used in the bench-scale test rig. It will be replaced by the heat transfer coefficient of condensation heat transfer when including the channel model into the MEVMD system model. Together, the three model parameters form the parameter vector $\mathbf{X}$ which was adjusted to minimize the root-mean square error between the simulated and the experimental results. The boundary conditions for this optimization were $\mathbf{B}_i = [T_{11}, T_{21}, \dot{m}_{11}, \dot{m}_{21}, w_{21}, p_{VC}]$ of experiment $i = 1...N_{cs}$ for the $N_{cs}$ calibration sets. From the resulting output vectors $\mathbf{Y}_{0,i}^{exp} = [T_{12}, T_{22}, \dot{m}_D]$ from the experiments and $\mathbf{Y}_{0,i}^{sim} = [T_{12}, T_{22}, \dot{m}_D, \dot{Q}_F]$ from the simulation, the optimization target vectors $\mathbf{Y}_i^{exp,sim} = [\dot{m}_D^{exp,sim}, \Delta\dot{H}_2^{exp,sim}]$ were calculated. The optimization problem can be written as

$$\min_{\mathbf{X}\in[\mathbf{X}_{lb},\mathbf{X}_{ub}]} \left\| \sum_{i=1}^{N_{cs}} \frac{\mathbf{Y}_i^{sim} - \mathbf{Y}_i^{exp}}{\mathbf{Y}_i^{exp}} \right\|. \tag{3.15}$$

The parameters were calibrated with a set of experiments conducted with pure water (calibration set). This was done due to the fact that all calibration parameters are independent from the feed salt content. The resulting model parameters and the related equations are listed in Tab. 3.1. A separate set of experiments (verification set) was used for validating the model. The validation experiments were conducted with feed solutions containing NaCl up to its solubility limit.

**Table 3.1:** Experimentally identified model parameters for triple channel VMD setup according to the given equations.

| Parameter | Equation | Value |
|---|---|---|
| $\varepsilon_M/\chi_M$ / - | Eq. 2.18-2.20 | 0.4155 |
| $a_{1,2}$ / - | Eq. 2.13, 2.12 | 0.1071 |
| $\alpha_{CO}$ / W m$^{-2}$ K$^{-1}$ | Eq. 3.14 | 468 |

Figure 3.9 shows the accuracy of the model for a calibration and a verification set in terms of the distillate production and the heat input over the foil. Both, mass and heat transfer are in good agreement with the experiments. The comparison of the model with the measurement shows a coefficient of determination $R^2$ of 0.977 for the distillate production and 0.915 for the foil heat transfer. The root mean square deviations (RMSD) are 39.1 g/h and 18.6 W respectively. Deviations were mainly caused by heat losses over the heating channel and the feed inlet and outlet section. The feed temperature change from inlet to outlet shows an RMSD of 1.69 K.



**(a)** Distillate flow rate [83].

**(b)** Heat transfer over foil [83].
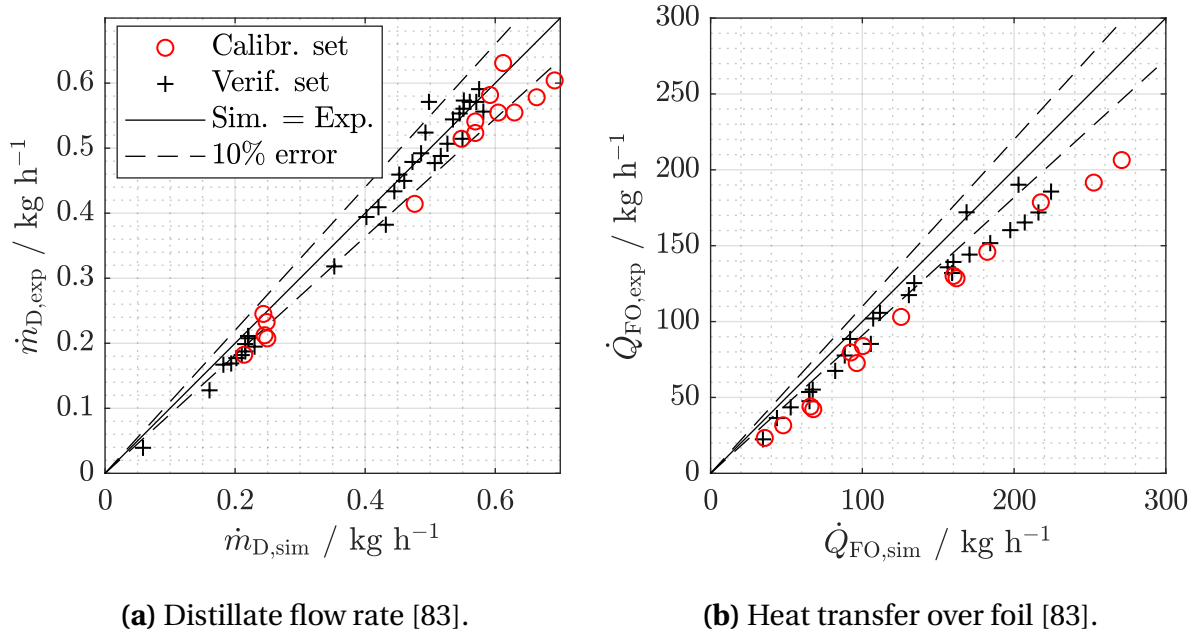
**Figure 3.9:** Comparison of experimental results and simulation results for calibration data set (M01, M02) and verification set (M03-M06, M08, M09, cf. appendix Tab. B.4).

A more practical picture of the system behavior and the model accuracy can be gained from the following comparison of experiments and simulation. Figure 3.10 shows the sensitivity of distillate production on a variation of feed temperature, salt mass fraction, and feed flow rate. It compares simulation results with the experiments in terms of the distillate production $\dot{m}_\mathrm{D}$. The distillate flow rate was calculated from the time averaged distillate amount collected in the condensate vessel or, if stated explicitly (meas. EB), via an energy balance over the test cell.

Figure 3.10a shows the dependency of distillate production on the feed temperature $T_{21}$ for pure water. The heating channel inlet temperature $T_{11}$ was set equal to the feed temperature. A temperature increase results in an exponential increase of distillate output. Further, the feed outlet temperature $T_{22}$ increases. For both values, the simulation results are in good agreement with the experiments. To explain the coupling of distillate increase and brine temperature, the vapor pressures are plotted below. The pressure $p_{\mathrm{v,meas}}$ measured at the outlet of the vapor channel is compared to the saturation vapor pressure of the feed inlet $p_{\mathrm{v,21}}$ and the feed outlet $p_{\mathrm{v,22}}$. The measured vapor channel pressure is below the equilibrium vapor pressure of the feed along the whole test cell. This means that evaporation takes place over the whole membrane area with highest fluxes near the feed inlet where the highest vapor pressure difference prevails. The measured vapor channel pressure increases with rising temperature and therefore increasing distillate production. The increase in distillate production is partially attenuated by this increase in vapor channel pressure. Additionally, the figure shows the equilibrium vapor pressure $p_{\mathrm{v,62}}$ of pure water at the cold side condenser outlet temperature. The value is almost constant, which means the condenser power is sufficient and not process limiting as shown in Fig. 3.5a.

Figure 3.10b shows the decrease in distillate production $\Delta\dot{m}_\mathrm{D}$ compared to the case with pure water due to an increase in feed salt content $w_{21}$. The measured distillate amount is compared with the distillate amount estimated via an energy balance over the system (meas. EB) and the simulated values. The latter include a simulation conducted with the vacuum channel pressure as measured in the experiments (sim. meas.) and with the same boundary condi-

tions, but a constant vacuum channel pressure (sim. ref.). The first case (sim. meas.) shows that the simulation results are in good agreement with the experiments. This shows in particular that the model calibration by experiments
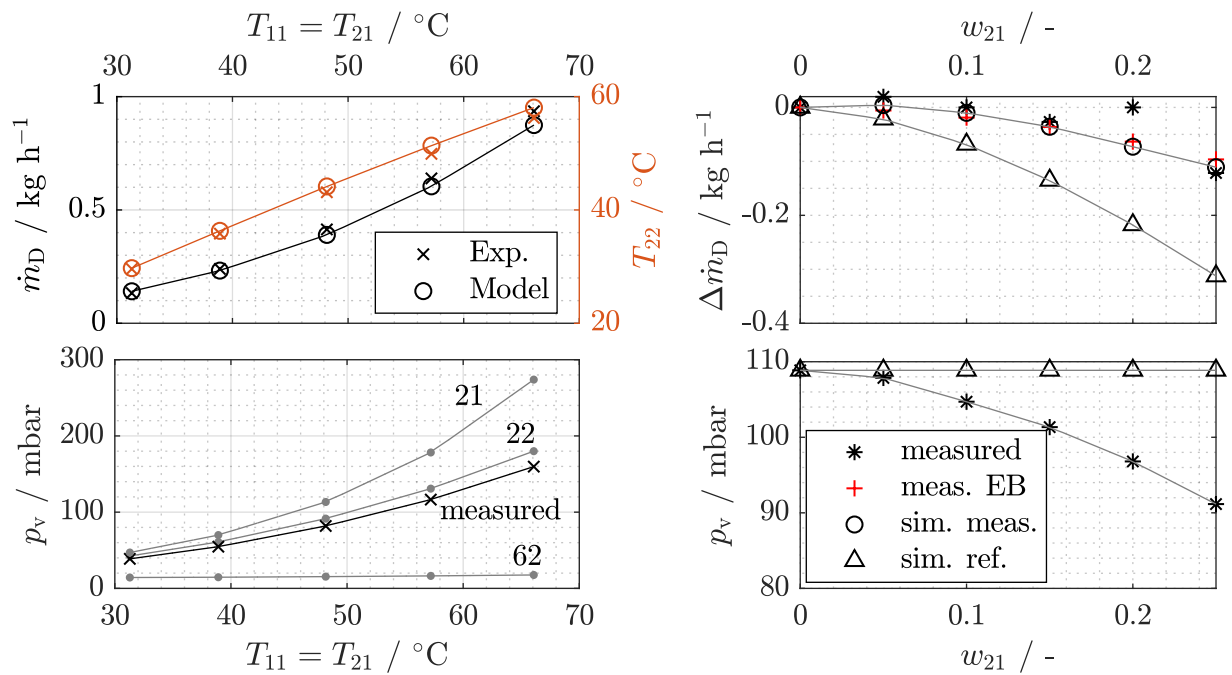


**(a)** Dependency on feed temperature $T_{21}$; $w_{21} = 0$; experiments M09.

**(b)** Dependency on feed salt mass fraction $w_{21}$; solute is NaCl; experiments M03.
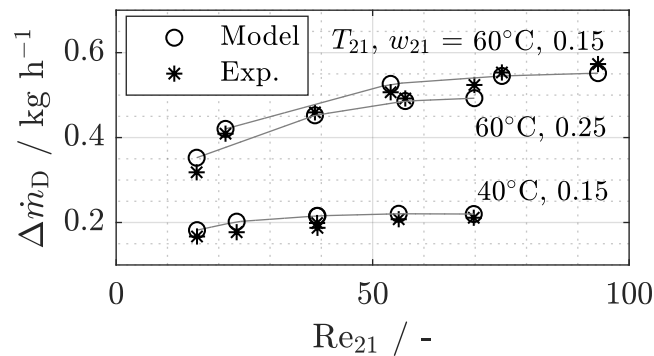
**(c)** Dependency on feed Reynolds number $Re_{21}$; solute is NaCl; experiments M04, M05.

**Figure 3.10:** Comparison of experimental and simulation results for different boundary conditions [83]. Experimental boundary conditions are listed in appendix Tab. B.4.

conducted with pure water was reasonable. Further, Fig. 3.10b shows that the measured decline in distillate production with increasing salt concentration is relatively weak. To demonstrate the influence of the coupling of flux decline with vapor channel pressure decrease, Fig. 3.10b additionally shows the simulated flux decline for a constant pressure level ($p_v = 109$ mbar, sim. ref.). This would be the behavior if the vapor channel pressure could be kept constant during the experiments.

Both sensitivity analyses show that it is not possible to get a clear statement about the influence of one parameter on the performance. In experiments with the bench-scale test cell, the vapor channel pressure is self-adjusting and therefore cannot be fixed when varying a parameter which influences the distillate flux.

Finally, Fig. 3.10c shows the distillate production in dependency of the feed Reynolds number. The distillate output increases with increasing Reynolds number. The model predicts the behavior well. Here, the approximation made by calibrating the Nusselt and Sherwood correlation by setting the Reynolds number pre-factor in Eq. 2.13 on basis of experiments with pure water also proves to be sufficient.

### 3.3.3 Multi-Effect System Model

The multi-effect system introduced in Sec. 2.1.3 and 3.2.1 consists of several stages (S1, ..., SN) each equipped with foil-membrane channel assemblies connected in parallel. The feed flow is distributed on the channels of one stage. The stages are connected via their feed in- and outlet (indices $2i$ and $2i+1$, respectively). Furthermore, the vapor channel of one stage is connected to the condenser channel of the next stage. Additionally, the system contains the steam raiser (SR) which is only equipped with membrane frames, and the condenser (CO) which only contains foil frames.

This configuration of the system was translated to a computational model by implementing the numerical channel model from Sec. 3.3.1. Parallel channels in a stage are simply implemented via multiplication factors for the in- and outgoing streams. The serial connection in terms of feed flow direction is implemented by passing the feed outlet properties to the input of the downstream channel (cf. Fig. 3.11). The computational channel model of a channel in stage $i$ requires the vapor channel pressure $p_{7i+1}$ as input. These vapor pressures were used as variables $\mathbf{x} = \left( p_{71}\, p_{72} \dots p_{7N+1} \right)^{\mathsf{T}}$ to the optimization problem

$$\min_{\mathbf{x}} \| F(\mathbf{x}) \|. \tag{3.16}$$

The optimization algorithm adjusts the vapor pressures until the vapor mass flow rate of each stage $\dot{m}_{7i}^{(\mathrm{v})}$ equals the condensate mass flow rate of the next stage $\dot{m}_{4i}^{(\mathrm{l})}$. The resulting system of equations $F(\mathbf{x}) = 0$ can be written as

$$\dot{m}_{7i}^{(\mathrm{v})}(p_{7i-1}, p_{7i}) - \dot{m}_{4i}^{(\mathrm{l})}(p_{7i}, p_{7i+1}) = 0, \text{ with } i = 1, \dots, N+1. \tag{3.17}$$

With $N$ being the number of stages it consists of $N+1$ equations and variables. For each equation the quasi-2D channel model from Sec. 3.3.1 is solved.

Optionally, the distillate can be led from stage to stage as done in the Memsys system. Liquid distillate $\dot{m}_{4i-1}^{(\mathrm{l})}$ that enters a stage partially flashes due to the reduced pressure. This vapor ($\dot{m}_{4i-1,\mathrm{flash}}^{(\mathrm{v})}$) is reused in the condenser channel to heat the feed solution, which has a positive effect on the process efficiency. Figure 3.11 depicts the model concept including the distillate flashing from stage S2 to the condenser (CO) for a two-stage system. For systems with
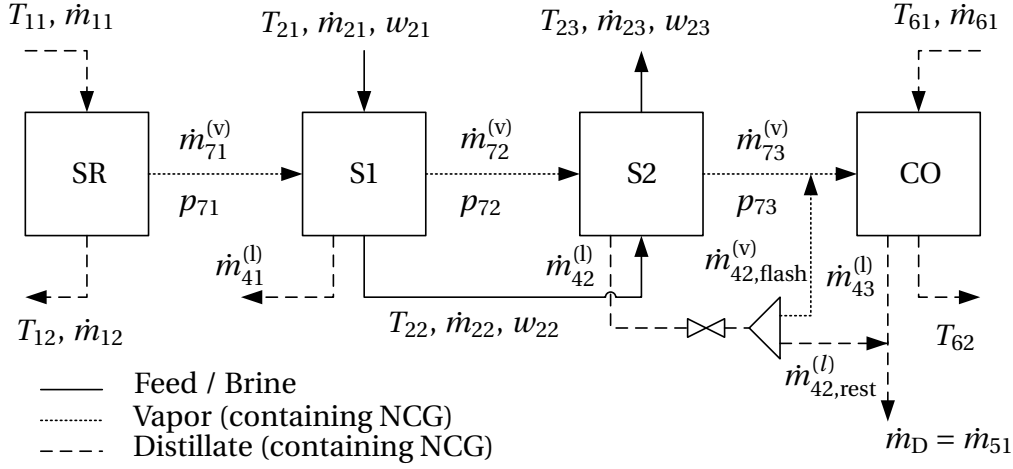
**Figure 3.11:** System model concept for a plant with two stages (S1, S2) and distillate flashing.

more than two stages, condensate flashing takes place at the inlet to the condenser channel of the third and all following stages. The amount of distillate that flashes depends on the distillate temperature and the pressure difference between the stages. The process was approximated with an isenthalpic throttle. The mass fraction $x_i$ of distillate condensed in stage $i$ ($\forall i > 1$) can be calculated via a balance over the throttle from

$$h'(p_{7i}) - h'(p_{7i+1}) = x_i \left( h''(p_{7i+1} - h'(p_{7i+1})) \right), \qquad (3.18)$$

where $h'(p)$ is the enthalpy of saturated liquid and $h''(p)$ the enthalpy of saturated vapor at pressure $p$. Simulation results show that the influence of the distillate flash on the product output is below 1% of the total distillate mass for relevant operation conditions.

Figure 3.12 shows the comparison of experimental results gained with the Memsys MEVMD system in a configuration with two stages and the simulation model. Here, larger discrepancies can be observed. With the parameter set identified from the bench scale test rig, the simulation model was able to qualitatively predict the behavior of the industrial system. The distillate output was greatly underpredicted over the whole range of experiments. Reasons are the channel geometry, different spacers in feed, steam raiser, and condenser channels and the diagonal flow through the feed channels which causes different macroscopic flow patterns for different volume flow rates.

Additionally, heat losses over the plant surface, leakages, and accumulation of non-condensible gases as well as inaccuracy of the flow rate measurements did not allow a quantitative comparison. Nevertheless, the plant behavior and especially the pressure staging was well predicted and the model could be applied to investigate the behavior of a multi-stage setup.
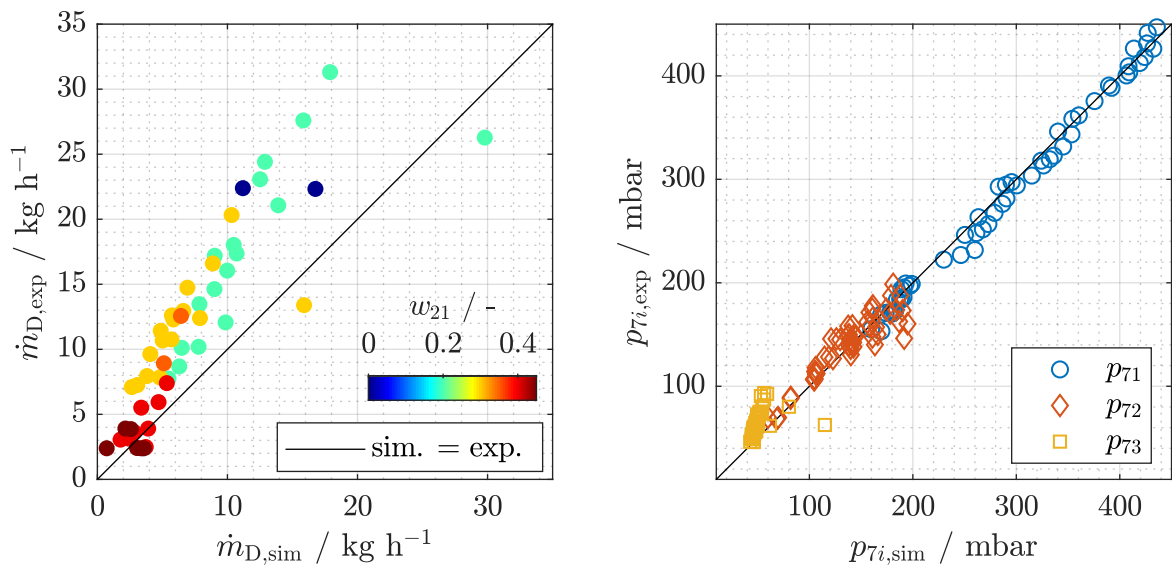


**(a)** Comparison of simulated distillate mass flow rate with measured values.

**(b)** Comparison of simulated pressures with measured values.

**Figure 3.12:** Comparison of experimental results with simulation results for a two-stage plant configuration [83].

## 3.4 System Analysis

This section applies the system simulation tool to investigate the distribution of temperature, pressure, and salt concentration in multi-stage systems. The underlying aim is to better understand the system behavior, especially the sensitivity to multi-staging and salt concentration increase.

### 3.4.1 Derivation of Performance Measures

Common performance measures of thermal desalination systems are the water recovery from the feed solution in terms of the plant's Recovery Ratio

$$RR = \dot{m}_{Product} / \dot{m}_F \tag{3.19}$$

and the Gained Output Ratio[1]

$$GOR = \frac{\dot{m}_{Product} \, \Delta h_{v,ref}}{\dot{Q}_{in}}. \tag{3.20}$$

The latter compares the thermal energy requirement with the heat of vaporization that would be required at a reference temperature level. It is used to compare different systems based on their ability to internally reuse the specific heat of vaporization.

Here, three different definitions are used. GOR includes only the steam raiser power $\dot{Q}_1 = \dot{m}_{71} \, h_{71}$. $GOR_{preh}$ uses the complete heat input $\dot{Q}_{in} = \dot{Q}_1 + \dot{Q}_2$ where $\dot{Q}_2$ is the heat required to bring the feed solution from ambient temperature $T_\infty$ to the feed inlet temperature $T_F$. In the following, $T_\infty$ is set to 25°C. The third variant of GOR is used for analyzing systems with heat recovery from discharge streams or brine recycling. For $GOR_{sys}$, the input heat is

$$\dot{Q}_{in} = \dot{Q}_1 + \dot{m}_F \left( h(w_F, T_F) - h(w_F, T_{F,re}) \right). \tag{3.21}$$

The feed temperature $T_{F,re}$ after heat recycling is used instead of the ambient temperature $T_\infty$.

---

[1]In literature two different definitions exist for this dimensionless number. The terms GOR and Performance Ratio (PR) are used in different publications for both definitions. The older definition is based on the ratio of distillate mass and heating steam mass. This measure was extended by the assumption that the heating steam releases 1 000 Btu/lb while condensing. In metric units this lead to $\Delta h_{v,ref} = 2\,326$ kJ/kg. [84]

Compared to the least heat of separation introduced in Sec. 2.3.2 the reference heat of vaporization is huge. According to Fig. 2.8a, approximately $40\,\mathrm{kJ\,kg^{-1}}$ are required to extract water from a saturated NaCl solution. This would correspond to a GOR of 58.

### 3.4.2 Reference System Analysis

With the help of the simulation tool it is now possible to analyze the plant behavior and identify optimization potentials. In the following, a four stage system with geometrical boundary conditions similar to the Memsys R&D plant is analyzed. The feed solution contains $w_\mathrm{F} = 80\,\mathrm{g\,kg^{-1}}$ NaCl and enters the first stage with $\dot{m}_\mathrm{F} = 100\,\mathrm{kg\,h^{-1}}$ at $T_\mathrm{F} = 50°C$. The steam raiser operates at 70°C and the condenser at 25°C. The geometry and all other boundary conditions are listed in appendix Tab. C.1 and C.2. The salt concentration of the feed solution was chosen to be in the range typical for brine from a seawater RO plant. Therefore, the following analysis can be regarded as typical for brine concentration.

Figure 3.13 shows the evolution of temperatures and salt mass fractions as well as the resulting vapor pressures and flux along the flow path of the feed solution through the system. On the left, the properties in the four stages are displayed. The temperature plot shows the bulk temperatures and the values on the membrane surface. At the inlet to each stage, a steep gradient in temperature can be observed. Further downstream, the feed stays at an almost constant temperature level, in the following referred to as the equilibrium temperature level of a stage.

The inlet section of the first stage differs from that of all following stages. A rising temperature from the feed inlet to the equilibrium temperature level of the stage can be observed. In the following, this will be referred to as internal feed preheating. In all other stages, a decrease in temperature is observed in the inlet sections.

For the second and following stages, the temperature polarization in the inlet section of the stage is especially high. The underlying reason is the large vapor pressure difference across the membrane. The temperature drops from

the inlet downstream in flow direction. The solute concentration increases. Therefore, the bulk vapor pressure at the channel inlet is the highest and reduces in flow direction. Consequently, the driving potential for mass transfer across the membrane is the highest at the channel inlet. The resulting high flux leads to strong temperature and concentration polarization. For the case on display the highest salt concentrations can be found at the membrane near the stage inlet. While the temperature values are almost constant throughout the rest of the channel, the concentration continuously increases due to water recovery.

The equilibrium temperature level of a stage evolves through balancing the heat input via the condenser foil and the evaporation across the membrane. According to Sec. 2.1.3, the heat input via the condenser foil is determined by the temperature difference between saturation temperature of steam from the previous stage or steam raiser and the feed temperature. The vapor pressure difference between feed solution and vapor channel determines the evaporation rate across the membrane. Finally, the stages need to fulfill the global mass and energy balances from Sec. 3.3.3. The pressure plot in Fig. 3.13 shows the equilibrium vapor pressure of the feed solution at bulk properties. Its slope is similar to that of the bulk temperature. The dashed horizontal lines show the pressures in the vapor channels. At each position $x$, the difference between the upper pressure level and the bulk value is proportional to the heat transfer from condensate to feed. The gray area, which is the difference between the bulk value and the pressure level of the downstream vapor channel (Gross Driving Pressure Difference), depicts the driving force for mass transfer across the membrane. An almost constant feed temperature and therefore vapor pressure level is established after the inlet section to the stage. The resulting flux $j_M$ shows sharp maxima at the inlet section of each stage.

The system's performance results from the coupling of the stages with a steam raiser and a condenser. The coupling is done via steam channels. Steam raiser and condenser are operated at a high flow rate to reduce temperature changes over the channel length. The steam raiser power is determined by the first stage, including internal preheating and distillate production.
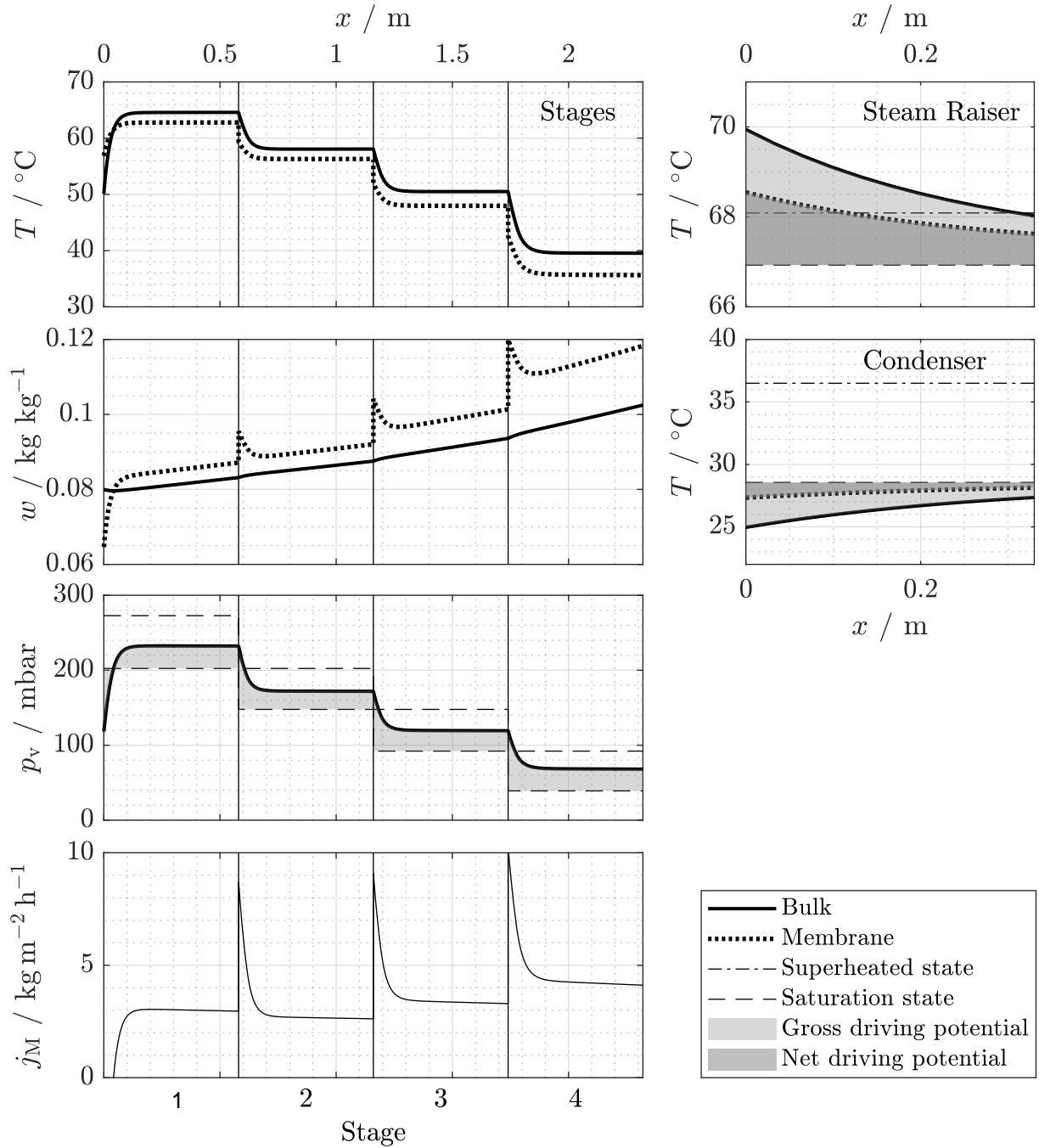
**Figure 3.13:** Reference system with four stages and $w_{\text{F,NaCl}} = 80\,\text{g kg}^{-1}$; plant setup specified in appendix Tab. C.1 and boundary conditions listed in Tab. C.2.

Figure 3.13 shows the temperature plots of steam raiser and condenser on the right side. As for the stages, the bulk and membrane temperature are plotted. Additionally, the figure shows the saturation temperature of steam at the vapor channel pressure. The temperature difference between the bulk temperature and this saturation temperature at a position $x$ is proportional to the Gross Driving Pressure Difference (light gray). It is reduced to the net driving potential due to temperature polarization (dark gray). Since the temperature of liquid water at the membrane is higher than the saturation temperature level, the steam produced at a position $x$ can be in superheated state. Therefore, the adiabatic mixing temperature of the steam leaving the steam raiser is slightly higher than the saturation temperature. The same applies for the steam entering the condenser.

It can be summarized, that the system performance is strongly influenced by the coupled heat and mass transfer and the resulting interplay of the stages. The inlet section of the first stage plays an important role in system performance. The inlet sections all following stages show extrema in flux and consequently in concentration and temperature polarization.

### 3.4.3 Sensitivity of the System Behavior to Multi-Staging

The number of stages is a key feature of any multi-effect desalination system. Unfortunately, the underlying aim of reusing the heat of vaporization from a previous stage is defeated by the colligative vapor pressure lowering appearing at high feed salt content (cf. Sec. 3.1). Nevertheless, a slower decline of the concentration dependency of distillate production, compared to theoretical considerations, was observed in experiments using the industrial MEVMD system (cf. Kiefer et al. [19]). The underlying effects are demonstrated in the following with the help of the simulation tool.

Three plant configurations show the influence of an increase in feed salt concentration on the plant behavior. The first case is a four stage setup with parameters equal to those of the reference system (cf. Tab. C.2). Now the feed solution is an aqueous solution of $CaCl_2$ with $w_F = 0.2$. Figure 3.14 shows the vapor pressure plots and Fig. 3.15 summarizes the global plant performance of the three cases. Compared to the reference system from the previous section with $w_F = 0.08$, Case 1 already shows a significant flux decline and GOR reduction.

In Case 2, the feed salt content is further increased to $w_F = 0.3$ which results in a further decrease in distillate amount. The net vapor production in the first stage of Case 3 is zero. Therefore, in the first stage only the feed temperature increases. Also the second stage's distillate production tends towards zero, since no heating steam from the first stage is available. Only stages 3 and 4 function properly.

Consequently, in Case 3 one stage is removed. The first stage is still occupied with internal preheating. The performance of stages 2 and 3 is similar to that of stages 3 and 4 in Case 2. The total distillate production of Case 3 is slightly higher than that of Case 2. The GOR is only 2.2% lower.

From these three cases, two major parameters influencing the system performance for increasing salt concentration could be identified. These are internal preheating and the number of stages. A low feed temperature depresses the performance of the first stage. This negative effect extends into to the fol-
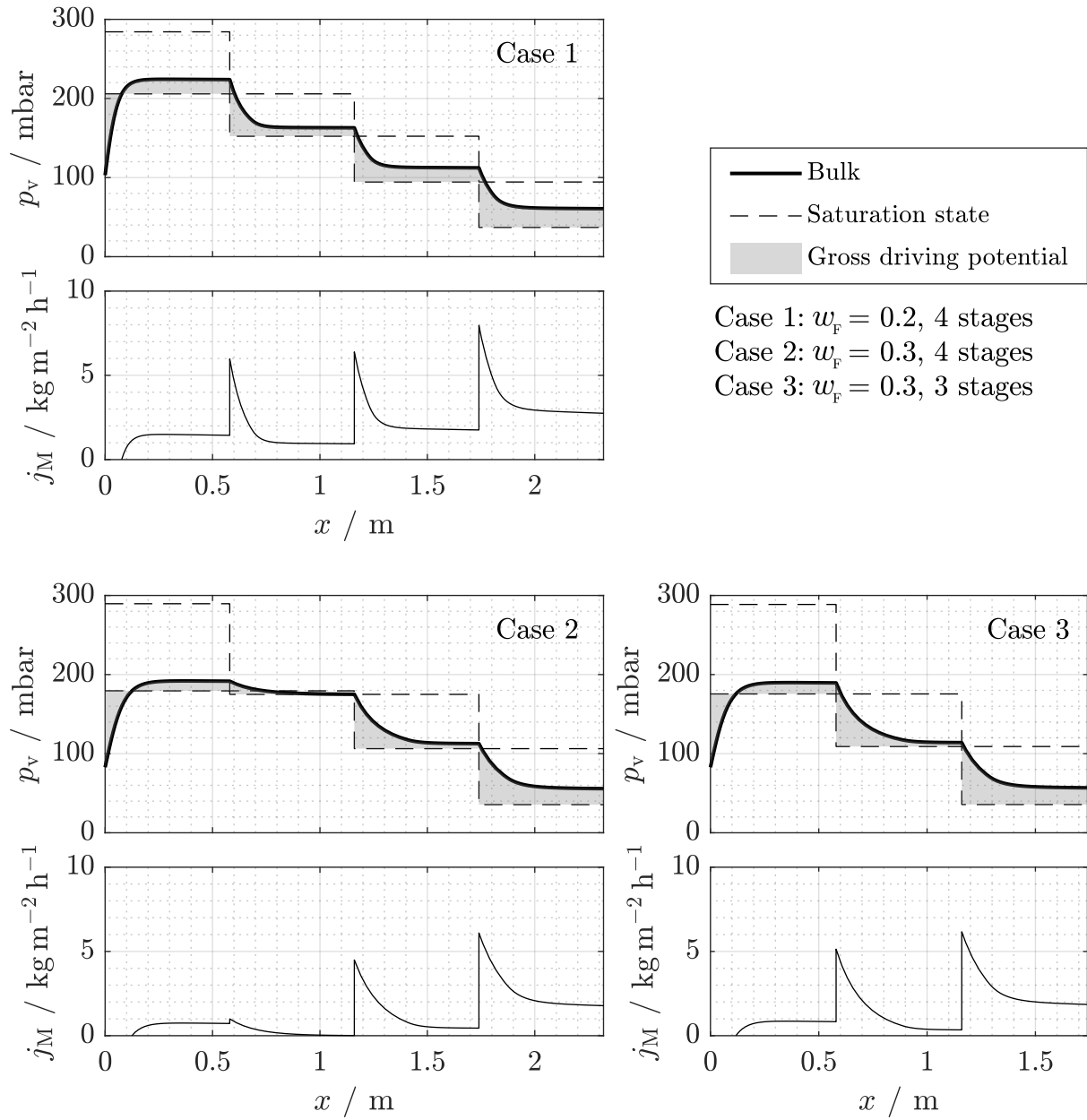
**Figure 3.14:** Self-regulating reduction of active thermodynamic effects; feed solute is $CaCl_2$; boundary conditions listed in Tab. C.2.

lowing stages. Secondly, a higher number of stages does not necessarily result in better efficiency of the plant when working with higher salt concentrations. The concentration dependent vapor pressure reduction leads to irreversibilities in each stage. It can be observed that the actually working number of stages is reduced with increasing feed salt content. Thus, a reduced number of stages contributes to the loss in driving pressure via concentration dependent vapor pressure reduction and the remaining pressure difference distributes to the working stages. Consequently, the performance reduction is not as high as predicted in Sec. 3.1. Finally, it can be concluded that specific plant optimization is necessary for different application areas concerning the feed salt content and the associated vapor pressure reduction.
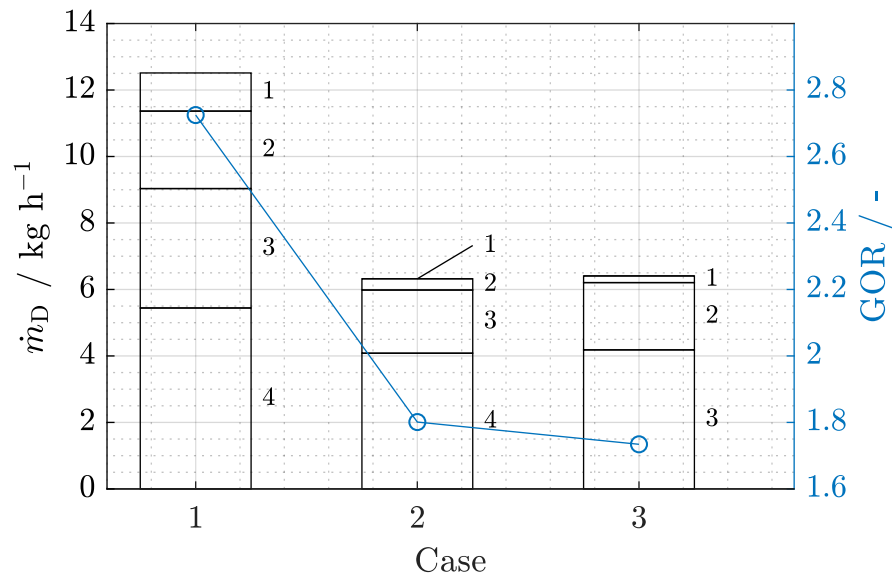


**Figure 3.15:** Summary of stage-wise distillate production and GOR of the three cases presented in Fig. 3.14. Case 1: $w_F = 0.2$, 4 stages; Case 2: $w_F = 0.3$, 4 stages; Case 3: $w_F = 0.3$, 3 stages.

# 4 Microscopic Analysis of Coupled Heat and Mass Transfer in Spacer Filled Channels

The macroscopic analysis of the system in the last chapter revealed a major influence of the temperature and concentration distribution along the feed channel on the system performance. The system simulation model estimates properties at the membrane surface with Nusselt and Sherwood correlations averaging over local fluctuations in the spacer mesh. For predicting scaling, these local fluctuations are of interest since maxima in supersaturation will determine the highest scaling propensity. Thus, this chapter introduces CFD simulations of flow, heat and mass transfer in MD using OpenFOAM. The methods are used to calculate the local heat and mass transfer in spacer filled channels and membrane test cells. Finally, a correlation is derived for predicting local concentration maxima in spacer filled channels with respect to application in MEVMD system analysis.

## 4.1 Governing Equations, Boundary Conditions, and Solution Procedure

**Governing Equations**
To describe the transport phenomena in the feed channel, two transport equations are needed in addition to the Navier-Stokes equations.

The steady-state energy conservation equation based on the sensible enthalpy neglecting compression work is

$$\nabla \cdot (\rho \mathbf{u} h) + \nabla \cdot \left( \rho \, a_{\text{eff}} \nabla h \right) = 0. \tag{4.1}$$

The enthalpy is calculated according to Eq. 2.48. For small changes in salt mass fraction over the computational domain, the dependency of temperature changes on salt mass fraction changes can be neglected in good approximation. The energetic aspects of the phase transition occurring at the membrane surface are treated within a boundary condition as described below. Kinetic and potential energy originally implemented in the OpenFOAM heat transfer solver are not relevant for the cases at hand. The thermal diffusivity for laminar flows is included as

$$a_{\text{eff}} = \nu/\text{Pr}. \tag{4.2}$$

Additionally, the scalar $w$ for the salt mass fraction is transported via an incompressible convection-diffusion equation

$$\nabla(\rho \mathbf{u} w) - \nabla \cdot \left( D_{\text{eff}} \nabla \left( \rho \ w \right) \right) = 0. \tag{4.3}$$

**Boundary Conditions**

The functionality of the membrane is described in a set of boundary conditions based on the approach by Präbst et al. [85] for RO. For the MD membrane, a momentum, mass fraction, and heat transfer boundary is needed in addition to the wall pressure ($\nabla p = 0$) boundary condition.

The flux boundary condition combines no-slip in membrane tangential direction with a wall normal flux

$$\frac{\dot{j}}{\rho_{\text{w}}} = \mathbf{u}_{\text{M}} \cdot \mathbf{n}_{\text{M}}, \tag{4.4}$$

which includes the membrane model (cf. Eq. 2.20) as

$$\mathbf{u}_{\text{M}} \cdot \mathbf{n}_{\text{M}} = \frac{K_{\text{M}}}{\rho_{\text{w}}} \left( p_{\text{v},i} - p_{\text{v,permeate}} \right). \tag{4.5}$$

The membrane heat transfer is written in terms of the temperature gradient at the wall as

$$\nabla T = \frac{\Delta h_{\text{v}} + \Delta h_{\text{unmix}}}{\lambda_{\text{eff}}} \rho \ (\mathbf{u}_{\text{M}} \cdot \mathbf{n}_{\text{M}}), \tag{4.6}$$

omitting sensible heat transfer across the membrane as stated in Sec. 2.2.2. Finally, for the scalar transport equation of $w$ the boundary condition of a membrane with 100% salt rejection is

$$\nabla w = (\mathbf{u}_{\text{M}} \cdot \mathbf{n}_{\text{M}}) \frac{1}{D_{\text{eff}}} w_{\text{M}}. \tag{4.7}$$

**Solution Procedure**

The open source tool OpenFOAM[1] was used to solve the steady-state problem. The solver is based on OpenFOAM's heat transfer solver `buoyantSimpleFoam` which was extended by the scalar transport equation for the salt mass fraction $w$ (`wEqn`) and a thermophysical model containing enthalpy formulation, transport properties, and a concentration and temperature dependent equation of state. The discretization schemes used are listed in App. D.2.

**Thermophysical and Transport Model**

The thermophysical model implemented is based on OpenFOAM's `rhoThermo` class as used by the solver and provides a model combination of

| | |
|---|---|
| `rhoThermo` | standard library density based solvers |
| `heRhoThermo` | standard library enthalpy or total energy based |
| `pureMixture` | standard library pure component |
| `sensibleEnthalpy` | standard library |
| `hSaltWaterThermo` | enthalpy formulation for electrolyte solutions |
| `rhoSaltWater` | equation of state with $\rho = f(T, w)$ |
| `specie` | standard library including `saltWaterTransport`. |

All libraries listed above had to be extended to incorporate the temperature and the salt mass fraction field. The actual model equations are polynomial fits to the thermophysical models derived in Sec. 2.3 and listed in App. A. The turbulence model was set to laminar and had to be recompiled using the new transport libraries.

## 4.2   Geometry Model

Different geometry models were generated to approximate the real geometry of feed channels.

**Spacer Filled Channels**

For simulating the flow in spacer filled channels, a unit cell approach was chosen. This means that the periodicity of the geometric pattern of obstacles in

---

the flow is used to reduce the simulation domain. Periodically reappearing spacer filaments are identified as can be seen in Fig. 4.1 and the computational domain is reduced to one or two of these smallest periodically reappearing unit cells. This approach was reported in literature amongst others by Koutsou et al. [86]. For sensitivity analyses and worst case estimation concerning the salt concentration at the membrane, a "zigzag" arrangement of spacer filaments (cf. Fig. 4.1a) was chosen as representative 2D configuration for woven and non woven spacers with different flow attack angle [85]. This geometry includes spacer filaments at the membrane surface and the opposite wall and is therefore expected to qualitatively represent the relevant mechanisms from a worst case perspective. The mixing in realistic 3D geometries with respect to the state of the feed solution at the membrane surface is expected to be better than in this 2D approximation due to the following reasons:

- Vortical flow structures in the spacer mesh as demonstrated in Fig. 4.1a for a flow attack angle of 45° and cylindrical spacer filaments enhance the mixing in the channel.
- Attachment areas of the spacer filaments with the membrane are reduced by
    - tapering of spacer filaments between their nodes (cf. Fig. 2.5a) which leads to contact with the membrane only at the filament's nodes or
    - the corrugated membrane structure in VMD caused by the pressure difference across the membrane and the coarse backing spacer mesh,
  both leading to smaller flow separation zones at the membrane.
- The arrangement of spacer filaments at the membrane surface parallel to the flow direction as demonstrated in Fig. 4.1b for single sided membrane channels significantly reduces the size of flow separation zones at the membrane.

Further, the 2D worst case scenario significantly reduces computational effort, especially by reducing the number of possible geometry variations. For real geometries the following variations and geometrical uncertainties exist:

- The influence of the real spacer geometry on the flow field compared to model spacer geometries [87].

- Flow attack angles and variations throughout a membrane channel.
- The interference with the membrane macro structure in VMD for corrugated membrane surfaces.
- Uncertainties in channel height and spacer-membrane attachment.
- Blockage of spacer through particles or local deviations in geometry.



**(a)** Flow field for spacer configuration with $\alpha = 45°$.



**(b)** Flow field for spacer configurations with $\alpha = 0°$ or $90°$.
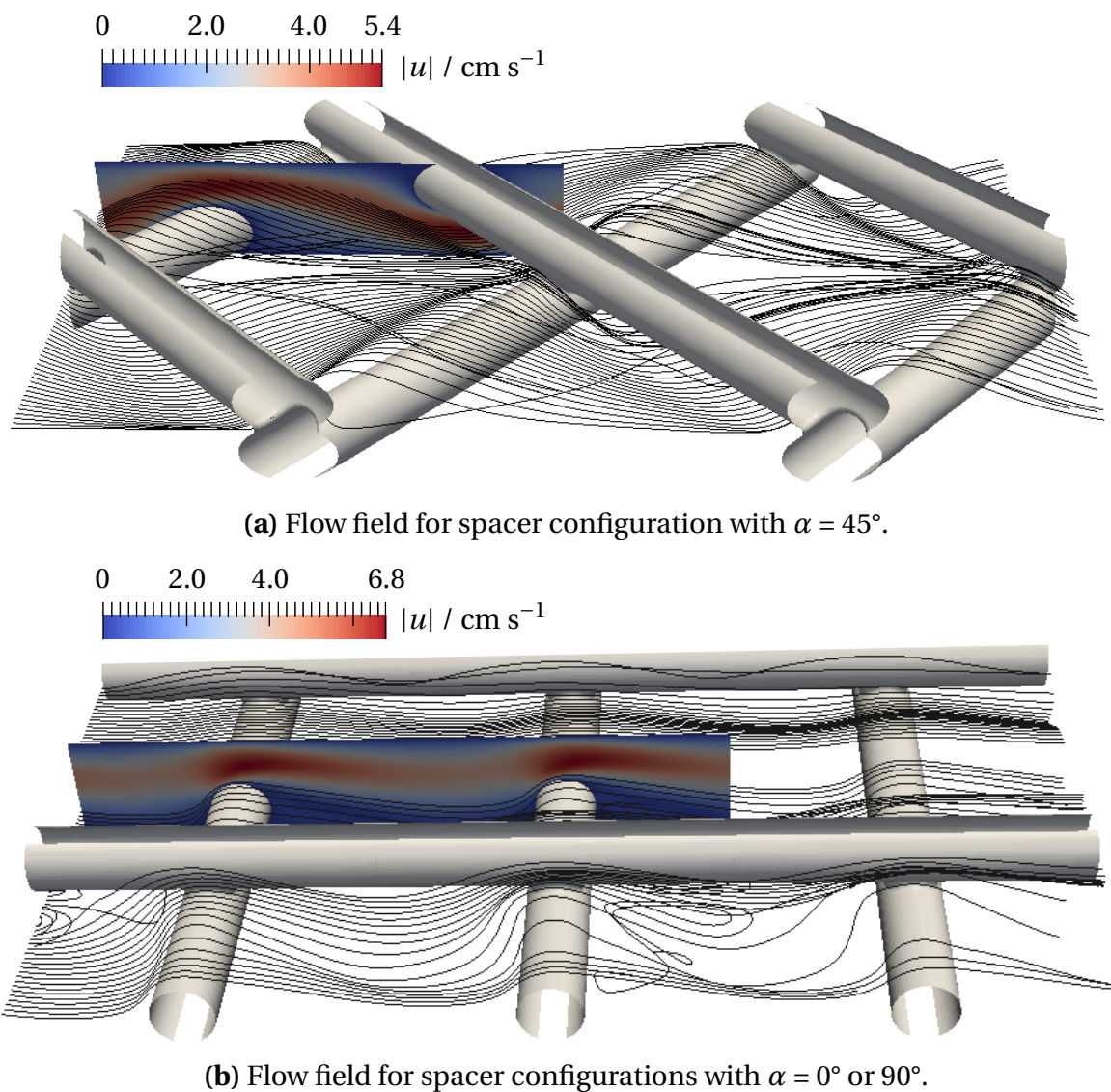
**Figure 4.1:** Flow in spacer filled channels for empty channel Reynolds number $\mathrm{Re}_H = 40$.

**Test Cell Geometries**

Additionally to the unit cell approach, the geometry of the optical scaling test cell was approximated with a 2D geometry. Figure 4.2 shows the fluid volume in the test cell. This geometry has either a flat membrane boundary at the bottom of the cell or a corrugated membrane. The latter approximates the geometry for permeate spacer filaments at the membrane which are perpendicular to the flow direction. In most scaling experiments a feed channel without spacers was investigated. The aim was to create homogeneous conditions on the membrane surface on a relatively large membrane area and to ensure undisturbed optical access. For experiments with feed spacer, channel geometries similar to those shown in Fig. 4.1 were realized. The strong corrugation of the membrane was due to the relatively large pressure differences applied across the membrane. Section 5.1 applies these geometry models.

The computational meshes were generated using the OpenFOAM tools `blockMesh` and `snappyHexMesh`. For each geometry a grid convergence study documented in App. D.1 was conducted to ensure that the simulation results are independent from the mesh.
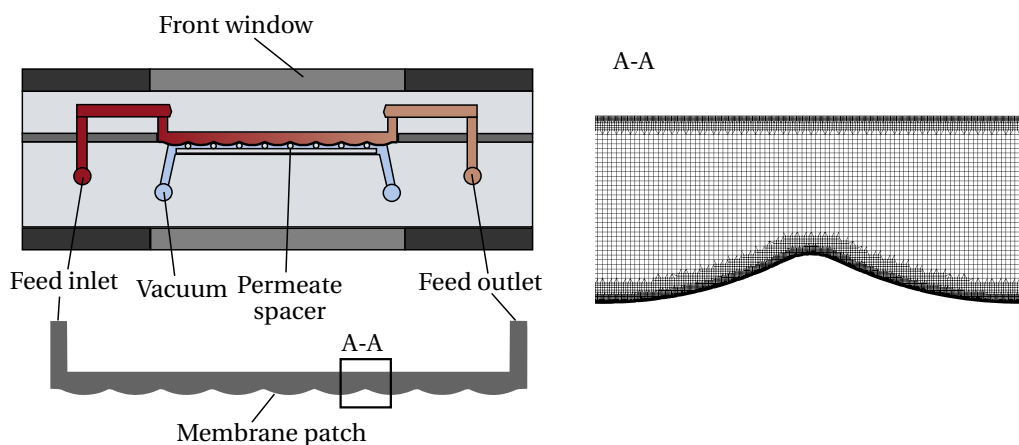


**Figure 4.2:** Computational domain and mesh in test cell.

## 4.3 Model Verification and Model Simplifications

With help of the test cell shown in Fig. 4.2, which was intended to be used for scaling experiments, a set of reference data for model verification was generated. The experiments were conducted with pure water at different temperature levels, feed flow rates, and vacuum pressures. Heat fluxes were calculated from the temperature drop measured between feed inlet and outlet of the cell. They were compared with results from CFD simulations to verify the membrane permeability as well as the general ability of the solver to quantitatively predict the system's behavior.

**Calibration of the Membrane Permeability Constant**

Figure 4.3 shows how the membrane permeability constant $K_M$ was derived from CFD results and experiments at a given feed temperature, flow rate, and vacuum pressure. The intercept of the mean flux determined from experiments and the flux calculated from CFD simulations with different membrane permeabilities lies at $K_M = 1.03 \cdot 10^{-6}$ kg Pa$^{-1}$ m$^{-2}$ (experimental uncertainty $0.78 \cdot 10^{-6} < K_M$ / (kg Pa$^{-1}$ m$^{-2}$) $< 1.46 \cdot 10^{-6}$). This goes in hand with the membrane permeabilities in the range of $6.9 \cdot 10^{-7}$ and $7.3 \cdot 10^{-7}$ kg Pa$^{-1}$ m$^{-2}$ determined with the bench scale test rig as described in Sec. 3.3.2.

Although the experimental results show a substantial scatter, the ratio between the transport resistance from bulk to membrane and across the membrane is in a range still providing good accuracy. The CFD curve shows a saturation for large membrane permeabilities, when heat transport in the boundary layer becomes rate limiting. This regime is not yet reached for the membrane in use and the boundary conditions applied to the verification experiments.

**Model Verification**

The membrane permeability constant evaluated before is now used for further CFD simulations presented in Fig. 4.4. The figure shows the measured distillate heat flux $\dot{q}_v$ compared to CFD simulations. The simulation results for different vacuum pressures, feed temperatures, and Reynolds numbers go in hand with the experimental results. Deviations can be attributed to the uncertainties of the measurement approach. Especially the fact that reference
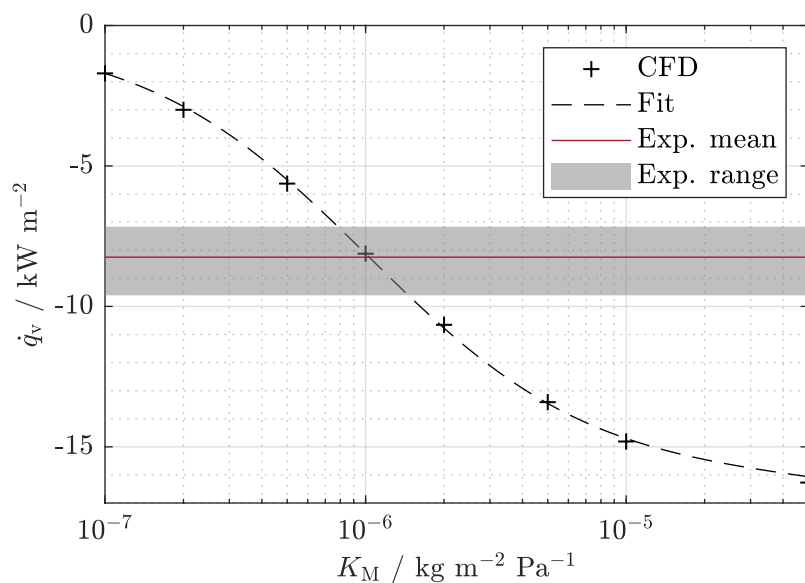
**Figure 4.3:** Calibration of the membrane permeability with CFD simulations and measurement results. Boundary conditions: $T_{in} = 50°C$, Re = 136, $p_{vac} = 30\,mbar$.

experiments were needed to account for thermal losses across the test cell and piping, leads to relatively large scattering of the experimental results. The comparison of experiment and simulation with different vacuum pressures shows that the CFD membrane boundary condition allows negative fluxes, i.e. absorption of vapor from the vacuum channel. This does not necessarily take place in the experiments and should be handled with care or turned off where necessary. Especially when the feed solution shows a low solute induced vapor pressure reduction (i.e. low salt concentration), the membrane temperature will be approximately equal to the saturation temperature and the vapor can condense on the vapor channel side of the membrane instead of diffusing back to the feed solution.

**Passive Scalar Transport and Periodic Boundary Conditions**
For sensitivity analyses it was helpful to decouple flow simulation from heat and mass transport. This was especially necessary for simulation of unit cells with mapped boundary condition for the temperature and salt mass fraction field. In these simulations, the temperature and concentration profiles were
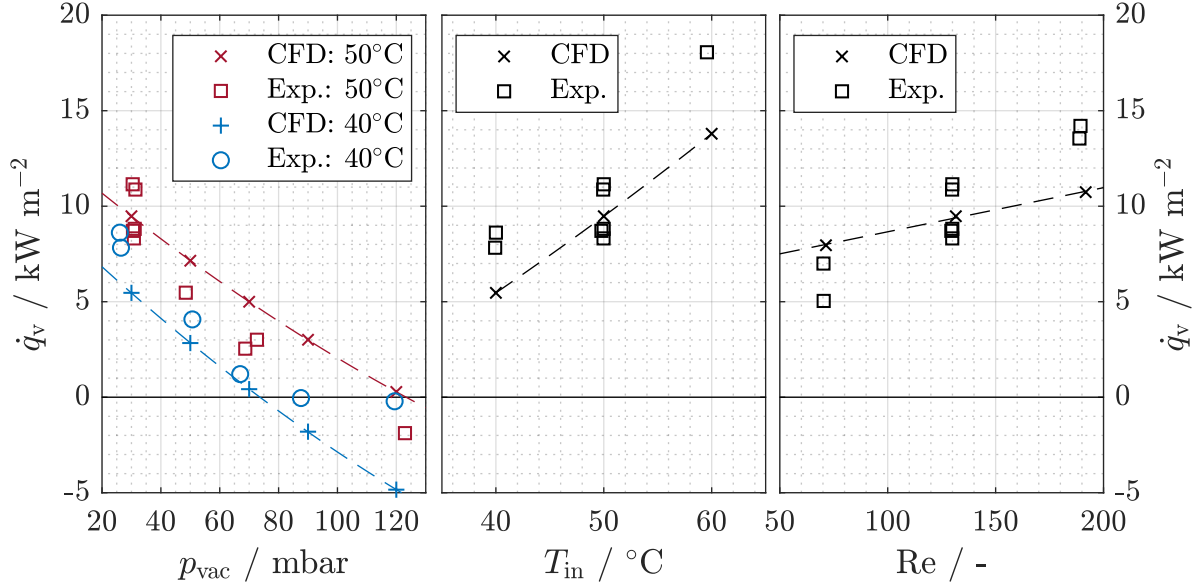
**Figure 4.4:** Verification of CFD results with flux measurements. Left: Variation of vacuum pressure $p_{vac}$ at Re $\approx$ 130. Middle: Variation of feed temperature $T_{in}$ at Re $\approx$ 130, $p_{vac} \approx$ 30 mbar. Right: Variation of feed Reynolds number at $T_{in} \approx$ 50°C, $p_{vac} \approx$ 30 mbar. Membrane permeability as derived from Fig. 4.3.

mapped from the unit cell outlet onto the inlet boundary. The profiles for $\Phi = w,\ T$ were normalized and the average value $\Phi_{set}$ was set according to

$$\underline{\Phi}(x_{in}, y) = \frac{\underline{\Phi}(x_{out}, y)}{\sum\left(\underline{\Phi}(x_{out}, y)\,\underline{A}\right)/\sum \underline{A}}\ \Phi_{set}. \tag{4.8}$$

This results in slow convergence and therefore it is suitable to reduce the number of equations. The fully developed periodic flow field was calculated in a first simulation step for the desired Reynolds number. Afterwards, the scalar transport equations were calculated using boundary condition mapping for the feed inlet. The values were sampled at the outlet, rescaled according to Eq. 4.8 and written on the inlet boundary. To close the problem, zero gradient was applied to the outlet boundary conditions of the fields $T$ and $w$. The error caused by this assumption is negligible for cases dominated by convective transport normal to the outlet boundary with Peclet numbers around 5 000 for the temperature field and 260 000 for the solute transport with respect to a unit cell length of 8 mm. Decoupling of flow field and scalar transport re-

sulted in a maximum deviation of below 5% for the scalar fields and the flux compared to the fully coupled simulation.

## 4.4   Analysis of Local Concentration Polarization

For practical application in plant design and control, it is desirable to define a safety margin that takes into account the local increase in concentration at the membrane surface. A worst case estimate for the concentration polarization in flow separation zones at spacer filaments is derived in the following. Figure 4.5 shows the Reynolds number dependency of the concentration field calculated for the 2D case with periodic boundary conditions as described above. It shows the actual salt mass fraction and the relative salt mass fraction normalized with the bulk value

$$w_{\text{rel}} = \frac{w_{\text{M}}(\mathbf{x}) - w_{\text{B}}}{w_{\text{B}}}. \tag{4.9}$$

Further, the figure depicts the probability density function of the salt mass fraction on the membrane surface $w_{\text{M}}$. The plots show the fraction of the membrane area $A_{\text{M}}$ that experiences a certain salt concentration. Increasing the Reynolds number lowers the mean concentration on the membrane. At the same time, the width of the histogram is reduced. This is desirable since the highest salt mass fraction on the membrane is relevant for scaling.

If solutes with significantly temperature-dependent solubility are investigated, the local temperature distribution must also be taken into account. Hence, the local Saturation Index (SI) has to be calculated. For solutes with inverse solubility, it is a general advantage of MD that the temperature of the solution declines towards the membrane surface. This positively influences the SI for example for $CaCO_3$.

In the following, the two maxima in salt mass fraction at the lower spacer filament are investigated. They are located in the stagnation point (SP) at the membrane upstream from the filament and in the recirculation zone (RZ) downstream from the filament.
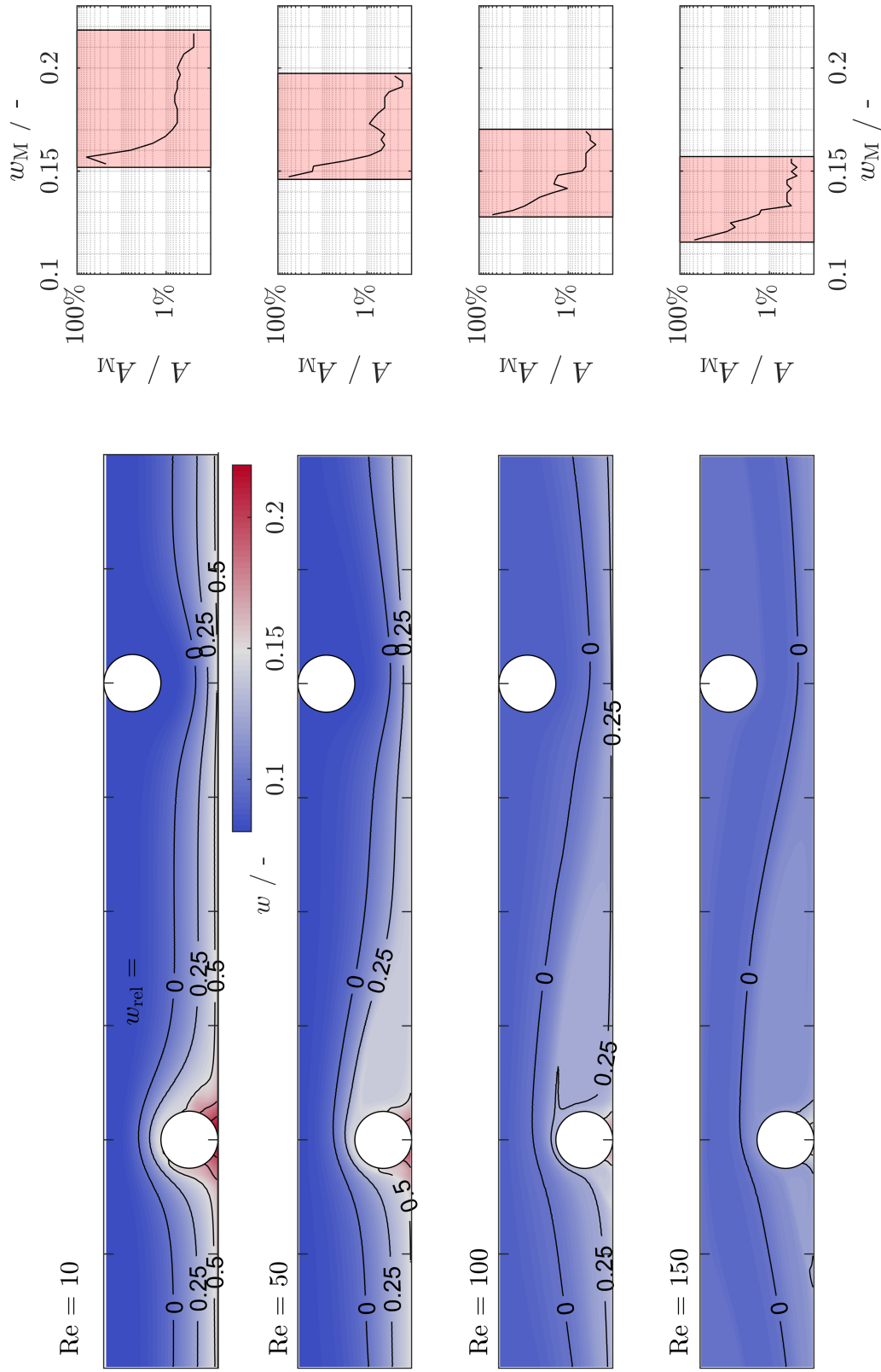
**Figure 4.5:** Reynolds number dependency of salt mass fraction field and distribution on membrane surface.

From a sensitivity study on Reynolds number and vacuum pressure, the values for the relative salt mass fraction in points SP and RZ were determined, as well as average properties and fluxes on the membrane. Fig. 4.6a shows the results. Instead of the local mass fraction relative to the mass fraction apparent in the bulk solution the local mass fraction in points SP and RZ is normalized with the mean salt mass fraction on the membrane surface

$$w_{\mathrm{M,rel}} = \frac{w_{\mathrm{M}}(\mathbf{x}) - \bar{w}_{\mathrm{M}}}{\bar{w}_{\mathrm{M}}}. \tag{4.10}$$

This way, the dependency on the Reynolds number can be almost eliminated. This applies especially to the largest of the two local maxima in points SP and RZ. This global maximum is the relevant design parameter. In contrast to the low Re dependency, the values strongly depend on the distillate flux (cf. Fig. 4.6b). For practical application, a worst case is estimated with a linear fit of $\max(w_{\mathrm{M,rel}})$ at a reasonable minimum Re number. Figure 4.6 shows this fit



(a) Re dependency of $w_{\mathrm{M,rel}}$ for different vacuum pressure levels.

(b) Flux dependency of $w_{\mathrm{M,rel}}$ with $w_{\mathrm{M,max}}^{\mathrm{estim}}$ marked at $\mathrm{Re}_H = 10$.
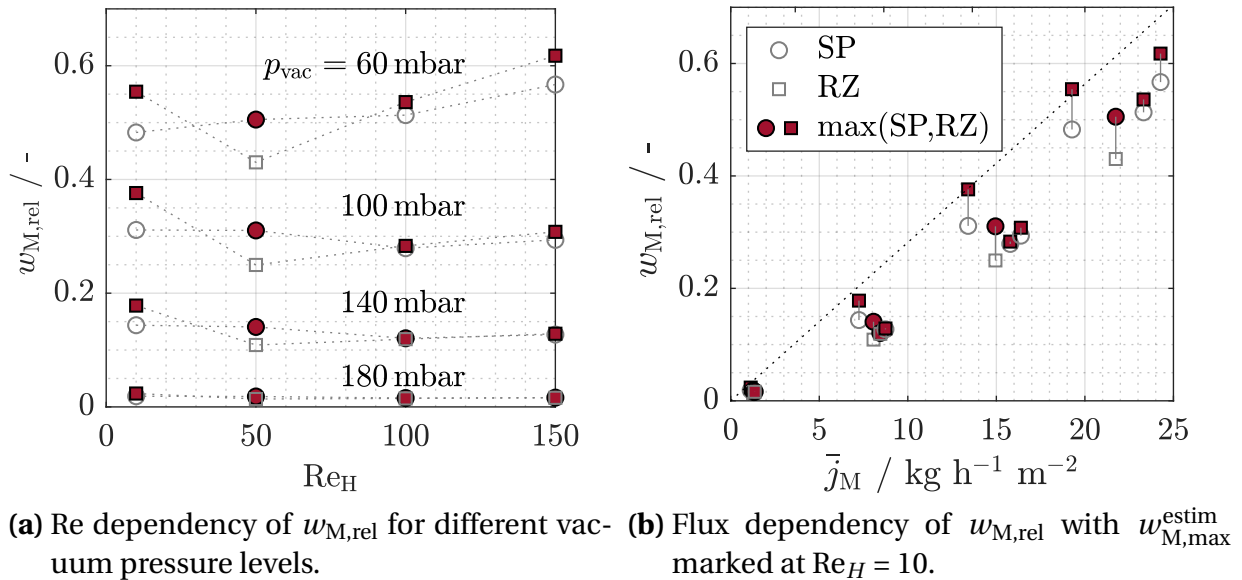
**Figure 4.6:** Worst case estimate for maximum salt mass fraction at the membrane in positions SP (stagnation point upstream of spacer filament) and RZ (recirculation zone downstream of spacer filament); maximum of position SP and RZ marked in red.

for $\text{Re}_H = 10$. Consequently, the maximum salt concentration at the membrane can be estimated with

$$w_{M,max}^{estim.} = 0.0282 \, \frac{h\,m^2}{kg} \, \bar{j}_M \, \bar{w}_M + \bar{w}_M. \qquad (4.11)$$

This result is intended for use during system design. For 3D geometries in spacer filled channels the maximum salt mass fraction is expected to be lower than this worst case estimate, according to the considerations on spacer filled channels from Sec. 4.2. The result given in Eq. 4.11 is to be regarded as a safety margin. Results from 3D simulations with the real spacer geometry will result in a smaller value for $w_{M,max}^{estim.}$ and therefore lead to higher design water recovery for a system. $w_{M,max}^{estim.}$ can be calculated from locally averaged flux $\bar{j}_M$ and salt mass fraction $\bar{w}_M$ determined with the system simulation tool from Ch. 3. This completes the data necessary to estimate the local scaling propensity.

# 5   Scaling and Membrane Wetting

With the simulation model derived in Ch. 3, regions in an MEVMD plant that are prone to scaling were identified. The CFD study from the previous chapter helped to identify the local distribution of flux, salt saturation, and boundary layer height at the membrane surface. With this background, the scaling kinetics will be investigated in the current chapter. The focus is on the highly soluble NaCl and the sparingly soluble $CaSO_4$ and $CaCO_3$. The investigation of scale formation from NaCl in membrane systems is relatively new [88], whereas scaling of $CaSO_4$ and $CaCO_3$ was described for all types of membrane desalination systems [70]. The reason for this is the high solubility of NaCl. It is not possible to reach its solubility limit in conventional membrane desalination systems but in MD.

The following sections describe an experimental approach to observe the kinetics of scaling in VMD systems. Further, the influence of scaling on process parameters and its interplay with membrane wetting are discussed. Finally, the findings are summarized with respect to MEVMD system design. Parts of this chapter were already published in Kiefer et al. [89, 90].

## 5.1   Methods

The experimental methods comprise light microscopy for observing the feed side of the membrane and tracer-based Laser Induced Fluorescence (LIF) for membrane wetting detection. Both methods were applied to a VMD membrane channel to observe the scaling and wetting process in-situ. For further ex-situ analysis of membranes and scales, Scanning Electron Microscopy (SEM) and Energy-Dispersive X-ray Spectroscopy (EDS) were used. Combining these methods helps overcome the challenges of monitoring scaling and

wetting in VMD. It is now possible to solve shortcomings of wetting detection via permeate conductivity measurement often applied to other MD types [91] and to investigate scale growth in-situ. In contrast to light microscopy applied to scaling in RO [92, 93], the optical and morphological properties of the membrane in VMD demanded more advanced image processing. This was especially necessary for automated image analysis. Hilal et al. [94] recently published a detailed review of state-of-the-art methods for membrane investigation. A literature review on experimental methods for scaling and wetting investigation in VMD is documented in Kiefer et al. [89].

### 5.1.1 Experimental Setup for Crystal Growth Tracking and Membrane Wetting Detection

The experimental setup consisted of a VMD test cell as shown in Fig. 5.1 which is integrated into a feed and vacuum circuit (Fig. 5.2). It was manufactured from polycarbonate to allow optical access to the membrane. Feed and permeate channel had a height of 2 mm and could be equipped with a spacer filling the channel height. The permeate spacer was used in all experiments, with a filament orientation at the membrane either parallel or perpendicular to the mean flow. The feed spacer was inserted optionally. Fig. 5.3 summarizes all spacer configurations and the resulting feed channel geometries. Those are the two configurations with empty feed channel EA and EB with feed flow parallel and flow perpendicular permeate spacer filaments at the membrane respectively. The flow parallel filaments (EA) lead to a flat channel in flow direction, whereas the flow perpendicular filaments (EB) result in a corrugated membrane, i.e. obstructions of the channel in flow direction. Due to the absolute pressure difference between feed and vacuum channel, the membrane showed severe corrugation which influenced the flow field. Based on the two configurations with empty feed channels, four additional variations are achieved when inserting a feed spacer with 0° or 90° flow attack angle. Configurations AA and BB lead to line contact of the feed spacer filaments with the membrane, whereas configurations AB and BA show only point contact of the spacer and the membrane in the feed channel. The spacers were fabricated from polycarbonate filaments with a diameter of 1 mm arranged

Feed outlet

Optical access
membrane
backing

Vaccum

LIF laser
light sheet

Front side
illumination

Optical access
feed side membrane

Feed inlet
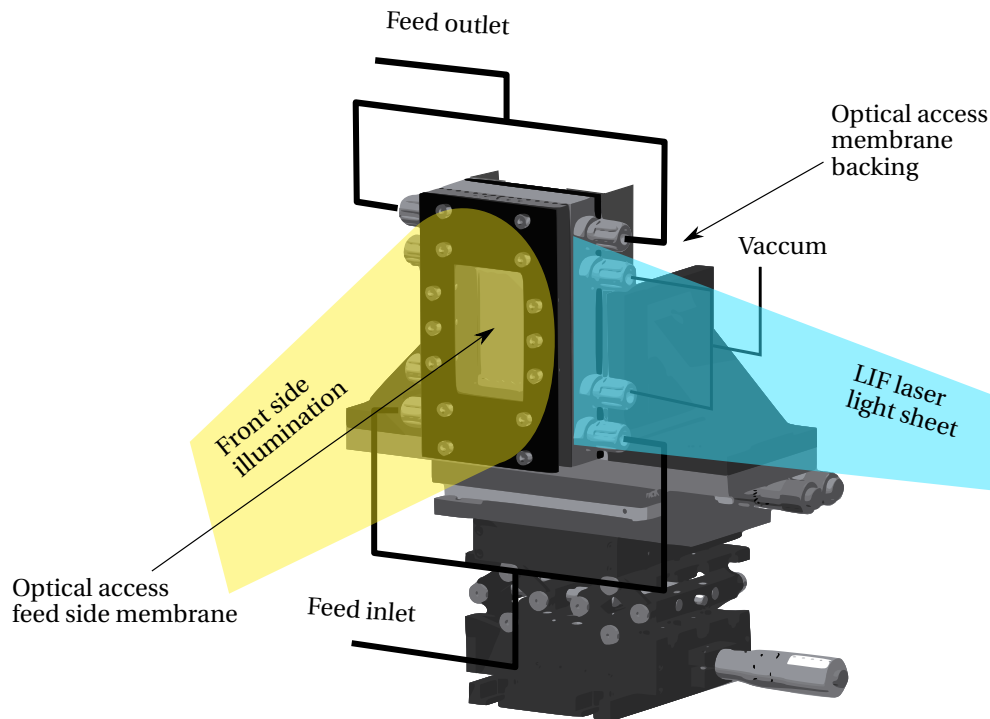
**Figure 5.1:** Test cell with 3D-translation stages [89].

as a mesh with an angle of 90° and with a filament clearance of 6 mm. The membrane in use was a GE Aspire QL822 PTFE laminate [36] with the properties listed in appendix Tab. B.2. The active membrane area in contact with the feed solution had a length of 56 mm in flow direction and a width of 30 mm.

The test cell provided optical access to the feed side of the membrane to investigate scaling (cf. Fig. 5.1). Furthermore, the permeate side of the membrane could be observed through a second window. The latter allowed to track membrane leakage. The cell was mounted on an assembly of high precision stages to adjust the membrane orientation relative to the microscope. The whole optical setup was mounted on an optical table to reduce vibration induced shift of the images acquired with the microscope.

As shown in Fig. 5.2, a gear pump circulated the feed solution through the feed channel. The salt solutions were mixed in a beaker, continuously stirred and preheated on a hot plate with a magnetic stirrer. For a finer control of the feed temperature (deviation from the set temperature $< \pm 0.15\,\text{K}$), an additional heating cartridge was installed in the feed cycle. The heat flux over the

membrane was calculated from measured feed inlet and outlet temperatures as

$$\dot{q}_v \approx \frac{\dot{m}_F}{A_M} \left( h\left(T_{F,in}, w_F\right) - h\left(T_{F,out}, w_F\right) \right).$$  (5.1)

The feed flow rate for a given pumping speed was determined with the help of scales. A differential pressure sensor, installed between the feed inlet and the vacuum channel, measured the maximum hydrostatic pressure difference applied across the membrane.

On the vacuum side of the membrane, an absolute pressure sensor measured the pressure in the vapor channel. The vapor channel pressure was adjusted with a mechanical pressure control valve and established by a laboratory vac-
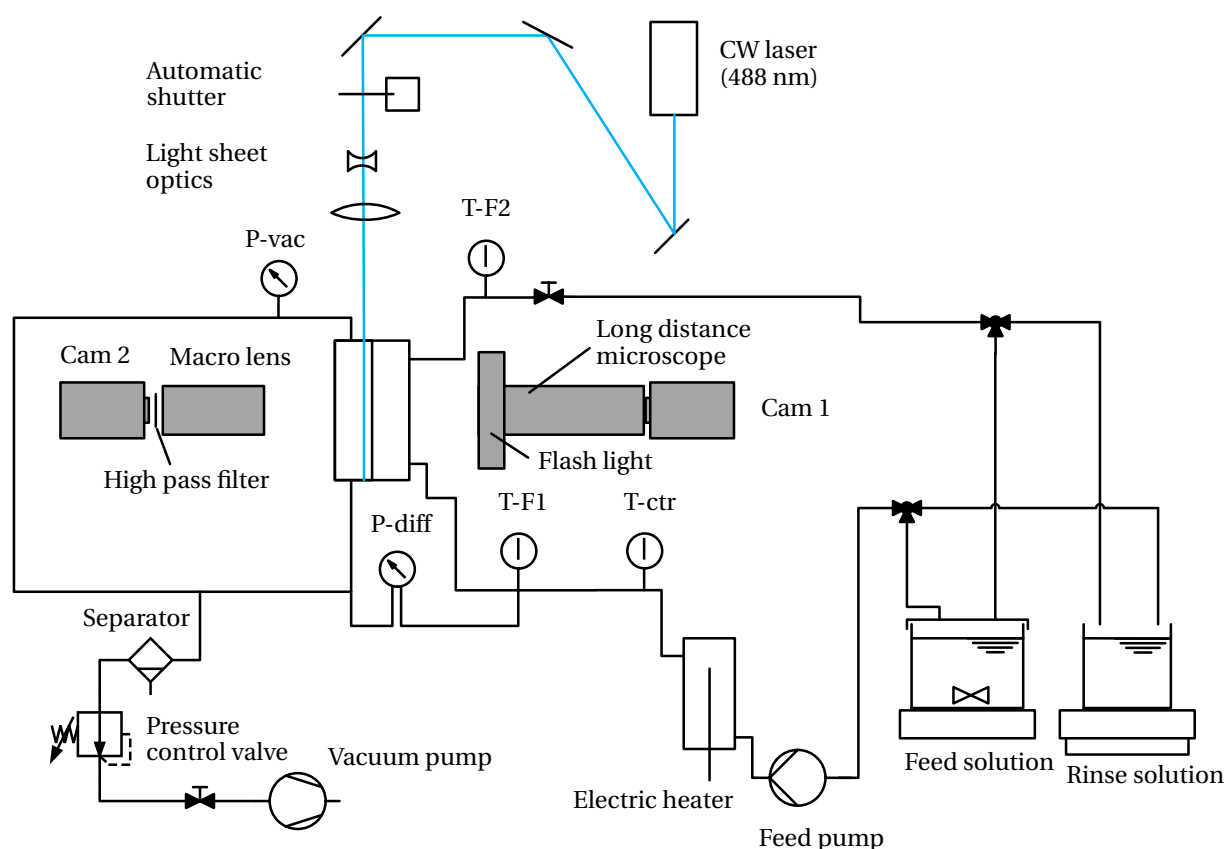


**Figure 5.2:** Piping and instrumentation diagram of the test rig with optical setup for feed side crystal growth tracking and LIF based membrane wetting detection; components listed in appendix Tab. B.5 [89].

(a) Empty feed channel

(b) Spacer filled channel

(c) Config.: EA

(f) Config.: EB

(d) Config: AA

(g) Config.: AB

(e) Config.: BA

(h) Config.: BB
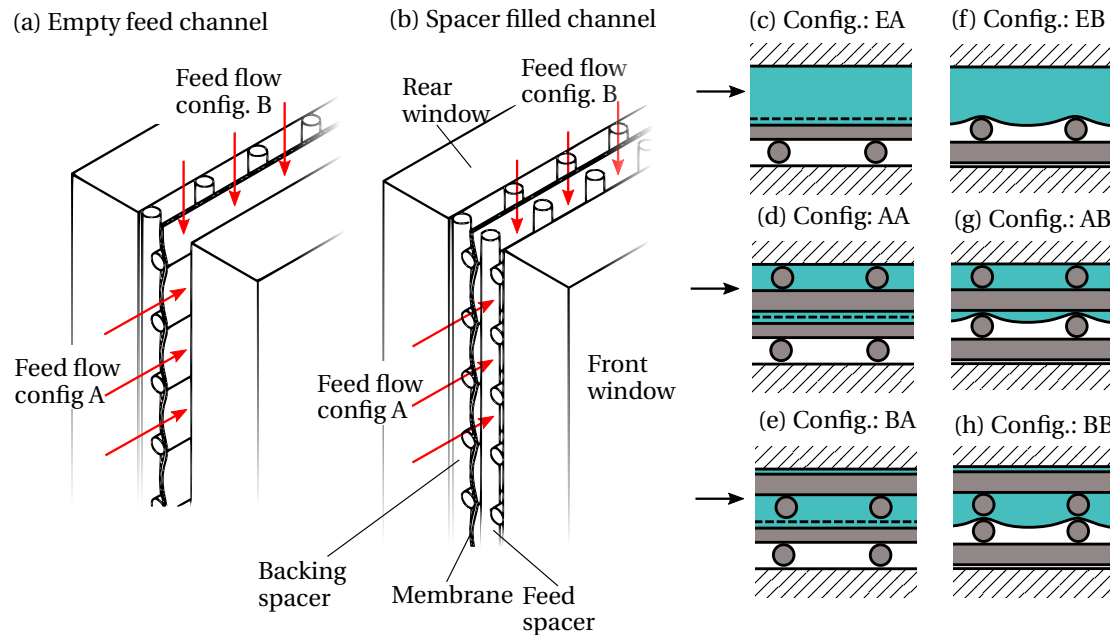
**Figure 5.3:** Spacer configurations for feed and backing spacer in VMD scaling test cell [90].

uum pump. To reduce the load of the vacuum pump and prevent droplets from entering the control valve or pump, a separator was installed upstream of the valve. All components and their specifications are listed in appendix Tab. B.5.

**Tracking of Scale Growth**

Scale growth in the feed channel was observed using incident light microscopy. Reasons for this choice are the corrugated membrane and necessary sealings around the membrane. These did not allow to illuminate the membrane from the side as done by Uchymiak et al. [92] or Benecke et al. [93]. Background illumination was not possible, since it would have lead to artifacts from the vacuum channel.

A long distance microscope[1] supplied with a ring flash was used. The images were taken with a mirrorless digital camera[2]. For scale growth of NaCl, a frame rate of 1/s was chosen. For scaling from sparingly soluble salts, a much lower frame rate was adjusted. The camera and ring flash were triggered by

---

[1]Long distance microscope Infinity K2/Sc CF-3

[2]Feed side scaling observation camera: Fujifilm XT10

electronic relays. Alternatively to the microscope setup, the feed side camera could be equipped with a macro lens setup to observe the complete membrane sheet.

**Membrane Wetting Detection**

Simultaneously, the membrane backside was observed to detect leakages. Therefore, the tracer uranine[3] was added to the feed solution. A continuous wave (CW) laser[4] providing a wave length of 488 nm was used to excite the tracer. The wavelength lies well in the excitation maximum of uranine ranging from 475 to 490 nm [95]. The laser beam was expanded to a thin sheet entering the permeate channel parallel to the membrane surface (cf. Fig. 5.2). This way, only feed solution which leaked through the membrane was illuminated. A second camera[5] supplied with a long-pass filter[6] and a zoom lens with macro spacer rings[7] monitored the membrane backside. The lens was adjusted to observe approximately 3/4 of the membrane area measured from the feed entrance. The optical filter with a transmission wavelength band of 539-1200 nm filtered out the excitation light. Thus, the camera recorded only the light emitted by the tracer with a wavelength of $\approx 560$ nm. A tracer concentration of 1 mg/kg solution was used. With this and the high laser power, even for small leakage amounts a high intensity could be achieved. Therefore, a large membrane area could be observed. Comparing experiments with and without tracer showed that the tracer does not influence the wetting behavior nor the crystallization of other salts. Crystallization of the tracer itself did not take place due to its high solubility and the low concentration applied in the experiments.

**Triggering and Image Recording**

The feed side image acquisition time step was used for synchronization of the images and the sensor data (i.e. the temperature, pressure, and feed volume flow rate data). The illumination of the feed side membrane area using the ring flash and the permeate side using the excitation laser were triggered in alter-

---

[3]Fluorescein sodium salt; Basacid yellow 226, BASF, [95]
[4]Coherent Genesis CX488-4000; adjusted to approx. 0.6 W for a light sheet of approx. 1 x 50 mm
[5]LIF wetting detection camera: PCO SensiCam CCD camera
[6]Optical filter: Razor Edge LP 532 RU
[7]LIF camera lens: Tamron SP zoom lens, 24-135 mm, 1:3.5-5.6

nating order. An electronic shutter interrupted the laser beam. To synchronize the images, the time-stamp of each image was stored and synchronized with the sensor data.

Due to large differences in time scales of crystal growth and membrane wetting, an event triggered image recording was implemented for the membrane wetting observation. Since the frame rate of this camera was equal to the frame rate of the scaling camera, images were temporarily stored in a buffer loop. Permanent storage of the images on the hard disk was initiated by a trigger. The trigger was set manually by the operator or through real-time evaluation of the image intensity. After setting the trigger, the images of the buffer loop were stored together with all following images. This procedure helped to save disk space and at the same time to reliably record the onset of the leakage breakthrough.

### 5.1.2   Image Processing and Statistical Evaluation

Three synchronized data sets were recorded for each experiment. These were the data of temperature and pressure sensors, the feed side images with information about crystal growth, and the permeate side images with information about membrane leakage. In the following, the image processing and statistical evaluation of the feed side scaling images is described.

**Image Processing**

A digital image processing procedure was implemented to overcome the following challenges associated with the feed side crystal images:

- The images show only low contrast between the translucent crystal material and the membrane surface.
- The membrane surface shows a clearly visible structure which stems from laminating the membrane's PTFE layer onto the PP backing structure.
- Images of different timesteps are slightly displaced in relation to each other due to vibrations.

Therefore, the following procedure was applied. Since the resulting images are similar to dark field microscopy images, it is called Digitally Simulated Dark Field Microscopy.

1. Preprocessing: Meta-data is extracted from the images and synchronized with the global timestamp. The images are converted to grayscale images.
2. Digitally Simulated Dark Field:
   (a) A reference image of the clean membrane is selected as the background.
   (b) A feature-based image registration[8] between each image and the reference image detects the displacement between the images.
   (c) Each image is transformed based on the result of the image registration.
   (d) The reference image (background) is subtracted from the transformed images to remove the background. The borders of the resulting image are cropped to remove artifacts which stem from spatially shifting the images.
   (e) A denoising algorithm removes small speckles resulting from the image subtraction.
3. Postprocessing: The resulting images provide a high contrast between background and deposits on the membrane. Therefore, the images can be binarized using a threshold. Setting this threshold is robust due to steep gradients in intensity between fore- and background. For visualization purposes, the images can be enhanced via histogram equalization.

The process is visualized in Fig. 5.4 for a selected image with NaCl growth on the membrane. From left to right the figure shows the gray-scale raw image, the simulated dark field (SDF) image, the threshold based binary image, and the resulting crystal borders printed in red in the SDF image (II).

**Statistical Evaluation**

The feature detection from the binary images was done with Matlab's image segmentation algorithm `bwconncomp`. It detects connected foreground and

---

[8]Matlab's Computer Vision Toolbox [96] was used to automatically detect features such as blobs (binary large objects) and corners. With the help of the Image Processing Toolbox [97], the features of the actual and the reference image were compared and repeating features were used to estimate the transformation necessary to match a maximum number of features.

(I) Raw image    (II) SDF image    (III) Binary image    (IV) Identified crystals

Digital dark field simulation    Binarization    Image segmentation
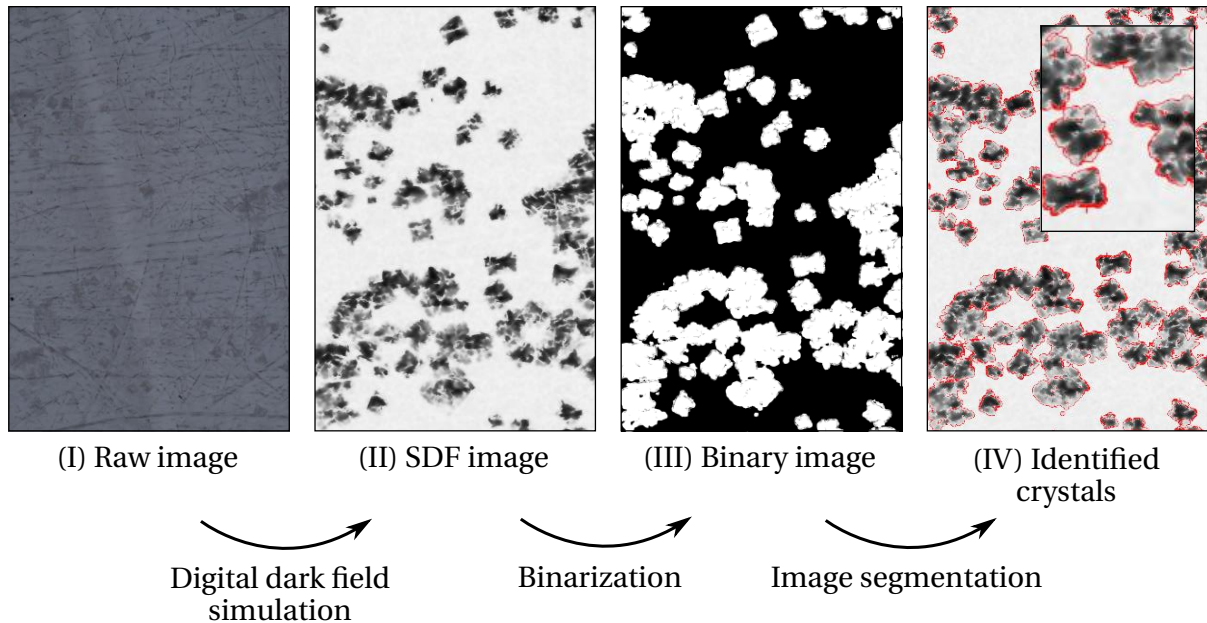
**Figure 5.4:** Image processing procedure including the Simulated Dark Field (SDF) image.

background areas. A connectivity of 8 was used, meaning that pixels connected via their edges or corners are adjoined to the same segment. All segments of all timesteps were stored in a matrix. By comparison of the complex geometries (pixel maps) of segments of a timestep with those of the previous timestep, ancestors of a crystal could be detected. This way, the growth and coalescence in terms of areal joining could be tracked throughout the growth process. Furthermore, artifacts could be sorted out. These were especially particles in the bulk flow that have only a short residence time in the field of view. Finally, statistical properties like covered membrane area, crystal number, and birth and death rates were extracted for each timestep.

### 5.1.3   Scanning Electron Microscopy

Scanning Electron Microscopy (SEM) helped to achieve a deeper understanding of the interaction between scales and membrane. Membranes were prepared by careful rinsing with deionized water and subsequent drying. Images were acquired for the untreated probes using a Jeol JSM-7500F field emission

SEM at 0.5 to 1.0 kV. The probes were further analyzed with energy-dispersive X-ray spectroscopy (EDS) using the electron beam in the SEM. The image quality was significantly enhanced by using a cold trap.

### 5.1.4 Discussion of the Applied Methodology

By using light microscopy for crystal growth tracking, the image magnification could be flexibly adjusted and a high time resolution was achieved. Challenges arising from the necessary incident light illumination of the probe were tackled using image processing. The complete methodological approach comprising image acquisition, image processing, and statistical analysis is assessed in the following.

The optical characteristics of light microscopy demanded for trade-offs between resolution and field of view (FOV) as well as between vibration resistance by reduced shutter time and depth of focus (DOF) or thermal influence of the illumination light. The first compromise included statistical considerations such as smallest detectable crystal size and number of crystals in the FOV. The second compromise was mainly determined by the used LED flash light and the necessary DOF for reaching a sharp image over the whole range of the bended membrane surface. Further, the image processing, especially the background removal, influenced the final image resolution. Characteristic sizes for halite scaling from sea salt experiments were estimated from different experiments and are collected in Tab. 5.1.

**Table 5.1:** Characterization of the microscopy approach including the simulated dark field procedure and automated evaluation as applied for scaling experiments with sea salt.

| Attribute | Value or estimate |
|---|---|
| Field of view (FOV) | 12.5×8.3 mm |
| Depth of field (DOF) | ≈ 100 µm |
| Resolution | 2.56 µm/px |
| Smallest detected crystal radius | ≈ 8 µm |
| Crystal contour detection accuracy | ≈ 10 µm |
| Minimum time resolution (shutter time) | 1/180 s |

Due to the incident light configuration, the approach was also applicable when a feed spacer was used. The polycarbonate feed spacers even allowed to detect scaling in the area behind the filaments. Only the quantitative evaluation of crystal size in these regions was impaired, since the different refraction indices of polycarbonate and feed solution distorted the image.

For halite crystals, the microscopy and image processing approach provided reliable results over a wide range of magnifications. No quantitative growth tracking was possible for $CaCO_3$ scaling. The magnification of the microscope would have to be increased to detect agglomerations of crystals (cf. Sec. 5.2.3). Then, the turbidity of the solution would significantly influence the image quality.

For gypsum scaling, a reliable growth tracking was possible for distinct crystal rosettes. The needle-like structure complicated the process of finding a threshold to distinguish between background noise and crystal. The algorithm provided good results even in the outer areas with fewer needles and therefore very low contrast.

### 5.1.5 Determination of Local Properties on the Membrane Surface

The knowledge of the local degree of supersaturation at the membrane surface is required to derive crystal nucleation and growth rates. This was achieved using CFD simulations of the feed channel. As described in Sec. 4.2, a 2D cross section of the feed channel was simulated applying the boundary conditions measured during the experiments.

Additionally to the CFD-based determination, the unknown properties at the membrane surface were estimated analytically. A position $\mathbf{x}$ in the field of view (FOV) of the microscope is regarded. Whereas the hydraulic entrance length is reached upstream from the FOV for the flow velocities investigated, the temperature and concentration field are not fully evolved. Thus, following derivation founds on the assumption that

- the Sh and Nu number at a fixed position in the channel stay nearly constant with the same hydrodynamic conditions and only small variations in concentration and temperature,

- the small recovery rate over the short membrane channel allows to assume constant bulk properties over the cell length.

As shown in Sec. 3.3.1 for a discrete location in channel direction, the following set of equations for the local flux $j_M$ across the membrane can be derived:

$$j_M = \rho\, \beta\, \ln\left(w_M / w_B\right) \tag{5.2}$$

$$j_M = \frac{\alpha}{h_v(T_M)}\, (T_B - T_M) \tag{5.3}$$

$$j_M = K_M\, \left(p_{v,M}(T_M, w_M) - p_v\right) \tag{5.4}$$

With this system of equations, the unknown salt concentration at the membrane $w_M$ can be estimated from bulk properties (index B) by applying some simplifications. For a relevant small temperature and concentration range (40°C < $T$ < 50°C, 0.26 < $w$ < 0.28), the vapor pressure can be written as a second order polynomial function of the temperature, neglecting its concentration dependency. This results in

$$p_v(T, w) \approx p_v(T) = C_1\, T^2 + C_2\, T + C_3 \tag{5.5}$$

with the coefficients $C_1 = 8.055\,\mathrm{Pa\,K^{-2}}$, $C_2 = -4760\,\mathrm{Pa\,K^{-1}}$, $C_3 = 7.062 \cdot 10^5\,\mathrm{Pa}$ at $R^2 = 0.9952$ compared to values calculated according to Clarke and Glew [55]. Furthermore, the temperature dependency of the specific enthalpy of the vapor $h_v$ is neglected. The heat and mass transfer coefficients are constant for the same mean flow velocity, assuming constant physical properties of the fluid for the small concentration and temperature range. The coefficients can be related using heat and mass transfer analogy [98]

$$\mathrm{Nu/Sh} = \left(\mathrm{Pr/Sc}\right)^{1/3} \tag{5.6}$$

and again calculating the thermophysical properties at constant $T$ and $w$. Finally, the system of equations 5.2, 5.3, and 5.4 can be solved with respect to $w_M$. It solely depends on the bulk properties $T_B$ and $w_B$, the membrane permeability $K_M$ which has been determined in Sec. 3.3.2 and 4.3 for the membrane at hand, and the vacuum channel pressure $p_v$.

### 5.1.6 Experimental Procedure

Different feed solutions were used to investigate the scaling behavior of different salts and the interaction of the resulting scales with the membrane.

**NaCl and sea salt experiments:** Feed solutions were prepared from sea salt (natural sea salt "Sea salt 1", composition listed in appendix Tab. B.6) or pure NaCl (99.5% purity) solved in RO permeate ($\kappa < 40\,\mu\text{S cm}^{-1}$). The solutions were heated and constantly stirred. After inserting a new membrane, the system was initially run for 30 min with the solution at a vacuum pressure of 200 mbar. Afterwards, several experiments were conducted with the same membrane. Each experiment consisted of steady-state operation without mass transfer across the membrane for 5 min at approximately 150 mbar permeate channel pressure. Afterwards, the cameras were started and a jump in vacuum pressure was initiated by adjusting the control valve. The low pressure level was held constant until almost the whole membrane was covered with crystals. Finally, the pressure was increased again and the system was rinsed with RO permeate until all crystals were dissolved. To prepare for the next experiment, the system was run at increased vacuum pressure until steady-state was reached again.

**CaSO$_4$ experiments:** Experiments with the sparingly soluble CaSO$_4$ were first run with RO permeate as feed for approximately 30 min. Each experiment was conducted with a new membrane. The vacuum pressure was adjusted to the desired level, allowing mass transfer. After this initial phase, stock solutions of CaCl$_2$ and NaSO$_4$ were injected into the feed tank until the desired concentration was reached. Hence, the solutions contained 2 mol Na and Cl ions per mole Ca (cf. Eq. 2.71). The operation was then continued until massive coverage of the membrane was observed.

**CaCO$_3$ experiments:** The experimental procedure for CaCO$_3$ solutions equaled that of CaSO$_4$. The feed concentration was reached by injecting solutions of CaCl$_2$ and NaCO$_3$. The solutions contained 2 mol Na and Cl ions per mol Ca (cf. Eq. 2.72).

All feed solutions were prepared as described above. In the feed vessel, the salt solutions were in contact with ambient air. No degassing, filtration, or further pretreatment were applied.

## 5.2 Kinetics of Scale Formation

This section summarizes the experimental results regarding the scale formation for NaCl and sea water, as well as for sparingly soluble $CaSO_4$ and $CaCO_3$. These help describing the influence of process conditions and spacers on the scaling kinetics.

### 5.2.1 Scale Formation from Sodium Chloride

Experiments using sea salt were conducted to investigate the response to vacuum pressure jumps. In a first step the whole membrane sheet was observed without the microscope. Based on the findings of this first step, the microscopic investigations were conducted.

**Macroscopic Investigations**
The macroscopic investigation included the inlet region and helped monitoring uneven flow distribution and its influence on scaling in the empty feed channel. Fig. 5.5 shows a representative result of the full cell analysis. The left side displays the distribution of scaled membrane area for five distinct times. The right diagram shows how the membrane coverage evolved over channel length and time. The curves show the area fraction covered by crystals, integrated over the channel width. Due to the decrease in resolution compared to microscopy, only larger crystals or accumulations could be monitored.

The flux was determined from the temperatures measured at the feed inlet and outlet via an energy balance. It showed a slow response to the pressure jump in comparison to the fast crystal growth process, similar to the result of the microscopic analysis shown in Fig. 5.7. Reasons are thermal inertia of temperature sensors as well as a flow velocity corresponding time lag and fluid mixing. This resulted in a superposition of measured flux increase after the pressure jump and observed crystal growth. Therefore, a direct correlation between flux decline and membrane coverage by crystals could not be drawn for these fast processes.

For the following microscopy experiments, a field of view (FOV) in the upper half of the test cell was chosen. Its center was located in a position of
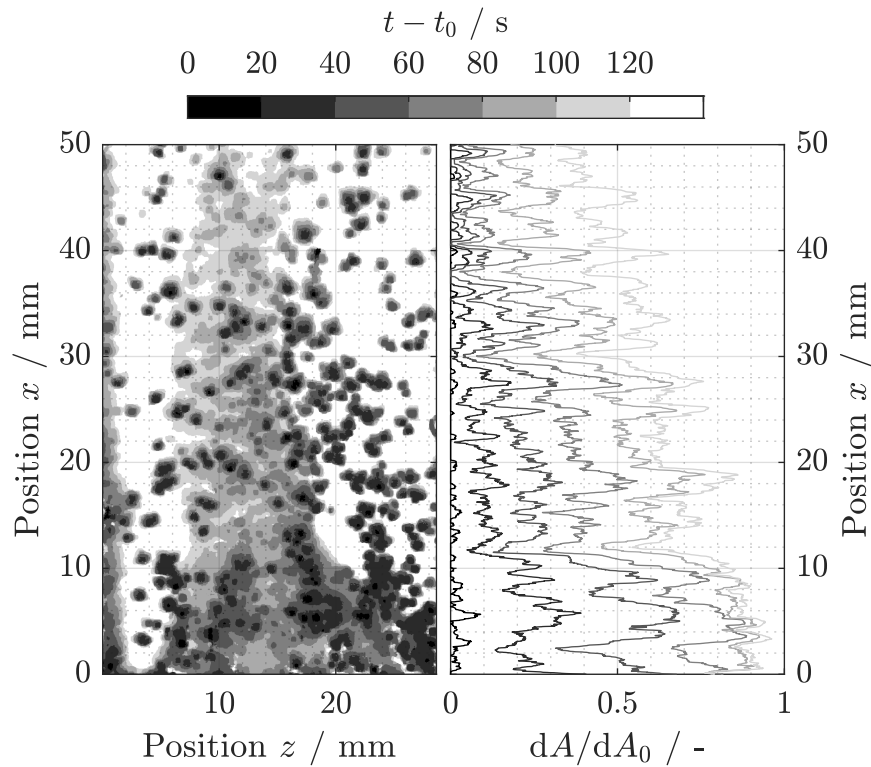
**Figure 5.5:** Full cell analysis (cf. CEx 21-02, appendix Tab. B.7); left: membrane coverage; right: covered membrane fraction at position $x$ [89].

$x = 40$ mm from the channel entrance and $z = 18$ mm to cover two full backing spacer meshes. The FOV had a size of $12.5 \times 8.3$ mm.

**Qualitative Analysis of Sodium Chloride Crystal Growth**

Figure 5.6 shows microscopy images acquired in the feed channel and model sketches for different crystal shapes. High supersaturation, achieved through high vapor flux across the membrane, leads to a large number of active nucleation sites. Distinct cubic crystals appeared in an early phase of the experiment (cf. Fig. 5.6a). Their shape showed a 90° halite lattice which hints at integration limited growth [75]. These crystals continued to grow and nucleation continued at less energetically favorable locations. After the initial phase and for high supersaturation at the membrane, growth continued as a pyramidal dendrite structure (cf. Fig. 5.6b). This indicates a steep concentration profile at the membrane and is limited to a near membrane region with supersaturated

100 µm

(a) Early stage, high supersat., CEx-11, 55°C, 30 mbar, 0.02 m s$^{-1}$.

532 µm

(b) Growth at high supersat., CEx-11, 55°C, 35 mbar, 0.02 m s$^{-1}$.

953 µm

(c) Growth at reduced boundary layer thickness (feed spacer), CEx-14, 50°C, 35 mbar.
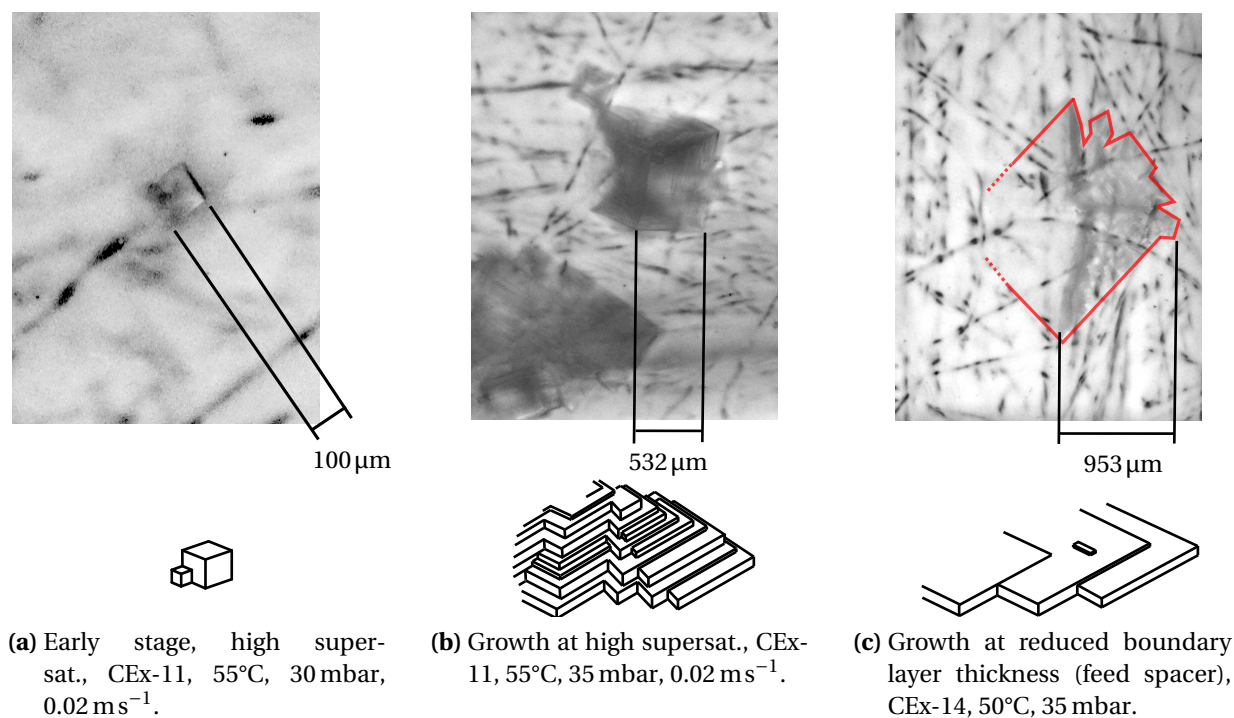
**Figure 5.6:** Images of different crystal shapes (light microscopy, in-situ) for sea salt and model sketches. Boundary conditions according to appendix Tab. B.7 [89].

solution. The growth process was influenced by vapor flux and convection.

Crystals grew in a thin plate-like structure for later times and thinner concentration boundary layers (higher feed Re numbers) (cf. Fig. 5.6c). These plates do not show many steps, are highly transparent and therefore hard to detect.

**Quantitative Analysis of Sodium Chloride Crystal Growth**

The growth process of NaCl from a sea salt solution, initiated by a vacuum pressure jump, is described in the following for the microscopy setup. Fig. 5.7 shows the measured vacuum pressure $p_v$ (a) and vapor heat flux across the membrane $\dot{q}_v$ (b) calculated from measured temperatures at feed in- and outlet. Further, it shows the results from the crystal growth images (membrane coverage $A_C/A_M$ (c), number of detected crystals $N_C$ (c), areal growth rate $G_A$ (d), and crystal nucleation rate $\dot{N}_C$ (d)). The experiment was conducted without feed spacer and with a feed solute mass fraction of
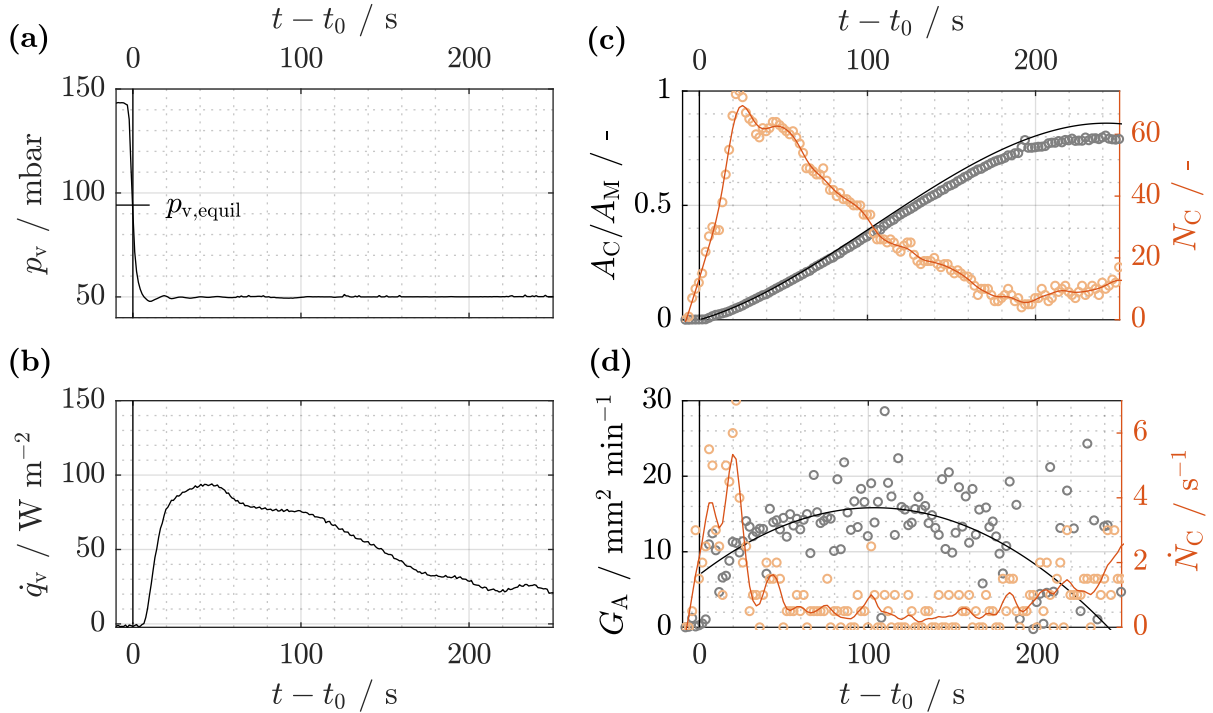
**Figure 5.7:** Growth process for the empty channel experiment CEx-04-05 (c.f. appendix Tab. B.7). Vacuum pressure step ($p_v$) and step responses in: vapor heat flux $\dot{q}_v$, membrane area fraction covered by crystal $A_C/A_M$ and number of crystals $N_C$, areal growth rate $G_A$ and nucleation rate $\dot{N}_C$. Spacer configuration: EA; Re = 100; $T_{F1}$ = 55 °C; $w_F$ = 0.26; solute: Sea salt 1. [89]

0.26 kg sea salt per kg solution. The equilibrium vapor pressure for reaching a saturation index of $S = 1$ was estimated from the feed solution properties. It is marked in the plots of Fig. 5.7 in terms of $p_{v,equil}$ first reached at $t_0$.

The scaling process starts almost instantly after the vacuum pressure falls below the equilibrium vapor pressure. Before reaching $t_0$, the images already show artifacts ($N_C > 0$). This can always be observed because the reference image shows particles from the feed solution. These particles will move away and become artifacts in the following images.

The delay from reaching $p_{v,equil}$ and first detected crystals for crystallization of NaCl is dominated by the timescale of the flow and the number of nucleation sites. The latter significantly influences the statistical relevance of the exper-

iments. A trade-off between high resolution, which results in an early detection, and a large field of view, which results in a larger number of observed nucleation sites, had to be found.

The whole process is a superposition of supersaturation build-up in the first approximately 20 s with nucleation and growth. Coalescence in terms of areal joining of crystals dominates after approximately 40 s. The continuous surface coverage quickly leads to a decrease in vapor flux, which is proportional to the vapor heat flux

$$\dot{q}_v \approx \frac{\dot{m}_v}{A_M \; h(T_{sat}(p_v))} \; .$$ (5.7)

After approximately 200 s the growth process stagnates, since the surface is almost completely covered. The areal growth rate $G_A$ (Fig. 5.7 (d)) was derived from a polynomial fit through the areal coverage $A_C/A_M$ (Fig. 5.7 (c)) and plotted over the growth rate calculated for each image (gray dots).

**Sensitivity to Process Parameters**
In the following, different scaling experiments with sea salt solution are compared by monitoring the crystal growth until the time $t_{P10}$. This point was reached when 10% of the membrane in the FOV were covered by crystals. The mean areal growth rate for this phase was

$$\bar{G}_{P10} = \frac{A_C(t_{P10})}{t_{P10} - t_0}.$$ (5.8)

Together with the number of crystals detected in the FOV at $t_{P10}$, it is a reliable measure summarizing the main characteristics of the growth process. Crystal nucleation and growth are the pervasive mechanisms in this period.

Figure 5.8a shows the system's response to a variation of the feed temperature $T_F$. Spacer configuration EA (cf. Fig. 5.3) was chosen, since it best approximates a 2D channel flow. The different experiments are labeled with "E.$i$" for the $i$th experiment. An increase in feed temperature at constant vacuum pressure leads to an increase in mean growth rate $\bar{G}_{P10}$. This is intuitive, since a higher feed temperature level results in a greater equilibrium vapor pressure and therefore greater driving potential across the membrane. The greater vapor pressure difference across the membrane leads to an increase in flux and

therefore stronger concentration polarization. Additionally, the dependency on $p_v$ is displayed. Decreasing $p_v$ (cf. Fig. 5.8a, 3rd) in most cases leads to an increase in the number of crystals (Fig. 5.8a, 2nd) due to increased initial supersaturation. In comparison, the growth rate increases only slightly (Fig. 5.8a, 1st).

Varying the feed velocity (Fig. 5.8b) showed a more complex behavior. Due to the large latent heat of evaporation, the temperature decline towards the membrane and over the channel length were limiting for mass transfer. An increase in feed flow rate resulted in a better convective transport to the bulk and a greater heat capacity rate ($\dot{m}_F \cdot c_p$). Therefore, the distillate flux over the whole membrane area was increased which again influenced the concentration polarization.
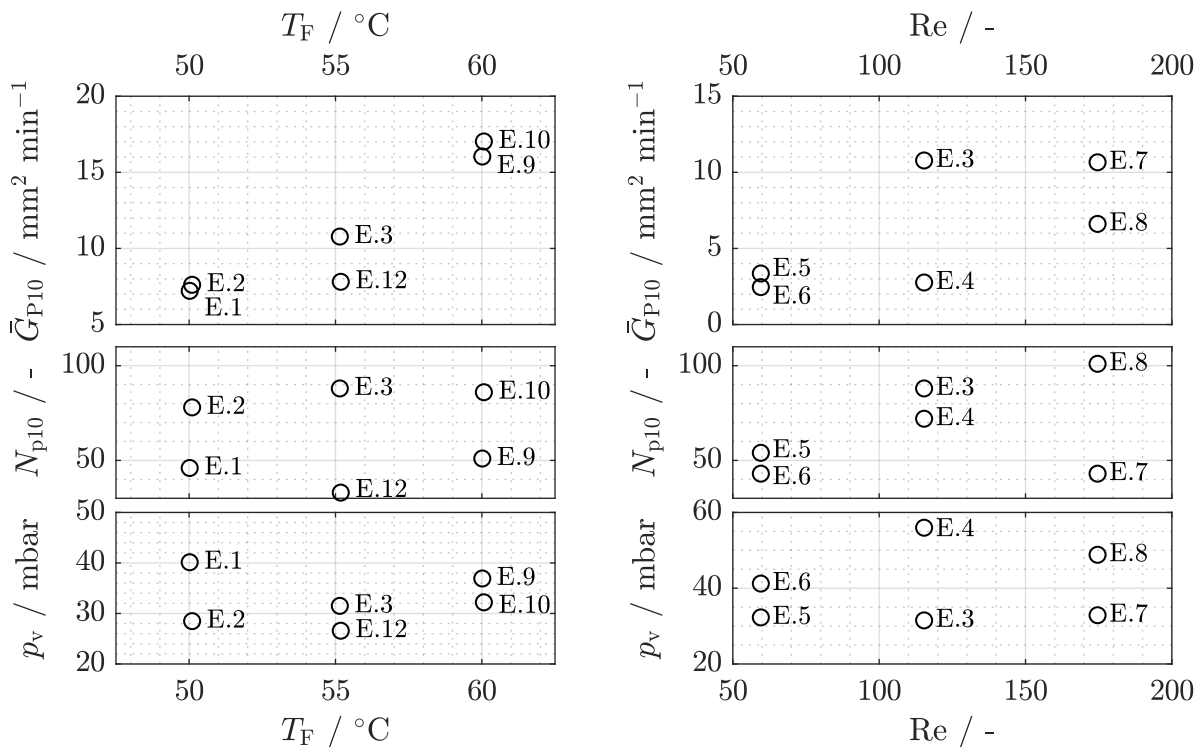


**(a)** Variation of feed temperature [90].

**(b)** Variation of feed velocity [90].

**Figure 5.8:** Sensitivity of mean initial growth rate $\bar{G}_{P10}$ and crystal number $N_{P10}$ on feed temperature $T_F$ and Re number. Solute: Sea salt 1.

A third set of experiments was conducted to investigate the sensitivity of crystal growth on the vacuum pressure level. The experiments were conducted at constant flow conditions and a single temperature level. This helped estimating temperature and concentration at the membrane surface and calculating the degree of supersaturation as derived in Sec. 5.1.5.

Fig. 5.9a (upper part) shows the mean growth rate until reaching a 10% coverage of the FOV depending on the adjusted vacuum pressure. It exponentially increases with decreasing vacuum pressure. Different symbols identify different sets of experiments each using a new membrane. Therefore, the number of crystal spots can differ significantly.

The system of equations 5.2, 5.3, and 5.4 is solved with respect to the salt mass fraction at the membrane surface $w_M$. Besides the unknown state variables at the membrane surface and the flux, the system of equations contains the unknown Sh number. Motivated by the growth model from Eq. 2.69 the crystal growth rates can be correlated with

$$G_A \approx G_V \frac{1}{\delta_C} = \frac{\mathrm{d}m_C}{\mathrm{d}t} \frac{1}{\delta_C \, \rho_C} = k_{G,n} \, S_{rel}^n, \tag{5.9}$$

using the two parameters $k_{G,n}$ and $n$. The resulting three unknowns are calculated from the measurement results using least square minimization to fit the Sh number, the growth coefficient $k_{G,n}$, and the order of the growth process $n$.

Fig. 5.9a (upper part) shows the resulting fit with Sh = 11.7, $k_{G,n}$ = 167.2 mm$^2$ min$^{-1}$, and $n$ = 3. The growth coefficients $k_{G,n}$ and $n$ include the nucleation of new crystal sites and the change in surface area over the time $t_{P10}$.

In Fig. 5.9b, the fit from Fig. 5.9a is plotted over a larger range of vacuum pressures to extrapolate to equilibrium solubility at the membrane. It further shows the estimated salt mass fraction at the membrane and the calculated supersaturation. When the relative supersaturation at the membrane exceeds $S_{rel,M} = 0$, the nucleation and growth process can start. The salt mass fraction at the channel entry of $w_F = 0.26$ lies below saturation. Therefore, a part of the vacuum pressure (approx. 9 mbar) is needed to reach the necessary concentration polarization. The plot further shows an almost linear dependency of

the relative supersaturation at the membrane on the vacuum pressure.

If the state on the membrane surface is determined with help of CFD simulations, a lower flux and therefore lower supersaturation is predicted. Consequently, the model parameters change to $k_{G,n} = 64.3\,\text{mm}^2\,\text{min}^{-1}$ ($15.5\,\text{mm}^2\,\text{min}^{-1}$) for a growth order of $n = 3$ (2). The discrepancy between the two sets of parameters shows the uncertainty of local property determination. Concerning the statistical scattering of the growth rates, the discrepancy lies within these fluctuations.
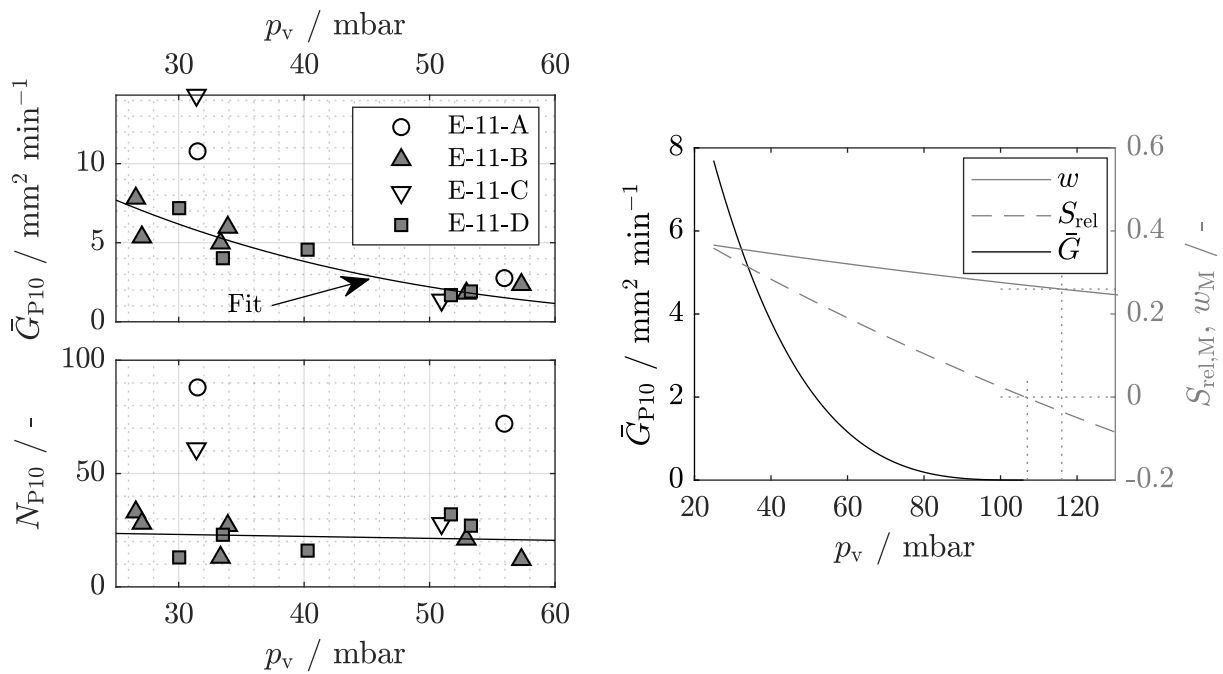


**(a)** Variation of vacuum pressure (4 membrane samples) [90].

**(b)** Extrapolation of the curve fit, estimated salt mass fraction and relative supersaturation [90].

**Figure 5.9:** Influence of vacuum pressure on growth process. Experiments E-11-B and E-11-D (cf. appendix Tab. B.7) are included in the fit. Spacer configuration EA; $T_F = 55\,°\text{C}$; $w_F = 0.26$; solute: Sea salt 1.

### 5.2.2 Influence of Spacers on Scale Formation

The feed spacer has a significant influence on the flow pattern in the feed channel. Flow separation zones at spacer filaments at the membrane surface are expected to be prone to scaling (cf. Sec. 4). For VMD, the backing spacer orientation additionally influences the channel geometry. The membrane bends over the backing spacer filaments depending on the absolute pressure difference applied across the membrane. Therefore, two sets of experiments were conducted for backing spacer filaments parallel and perpendicular to the feed flow direction with an empty feed channel (cf. Fig. 5.3, config. EA and EB). Additionally, two cases with feed spacer were investigated. Configuration BA combines flow parallel backing spacer filaments and flow perpendicular feed spacer filaments at the membrane. Configuration AB uses flow parallel feed spacer and perpendicular backing spacer filaments. Both configurations provide only point contact of the feed spacer with the membrane, in contrast to configurations AA and BB, which would provide line contact and therefore were expected to show a much higher fouling propensity.

Fig. 5.10 shows the resulting mean initial growth rates $\bar{G}_{P10}$ for the different configurations. The empty channel configurations show a larger mean growth rate for the flow parallel backing spacer filaments (EA). If the backing spacer filaments at the membrane were arranged perpendicular to the flow (EB), significantly lower mean areal growth rates were observed. This is mainly attributed to improved mixing due to the corrugated membrane. CFD results for the four cases support this conclusion. The flat membrane leads to a 20% higher degree of supersaturation on the membrane surface in the field of view than the corrugated membrane. Higher feed temperature and therefore higher distillate flux resulted in larger growth rates for both backing spacer configurations. The influence of the feed spacer strongly depended on the applied feed flow rate. Adding a feed spacer to channel configuration EB results in configuration AB. For the same mean flow velocity of $\bar{u}_F$ a greater growth rate was measured. In contrast to this, adding a feed spacer to the empty channel configuration EA did not significantly change the measured growth rate.

For optimal design of the feed channel, the corrugation of the membrane must be taken into account. This can have an advantageous effect on the mixing. In practical applications, a feed spacer is required in most cases. This feed spacer must be designed in such a way that stagnation and flow separation zones are as small as possible.
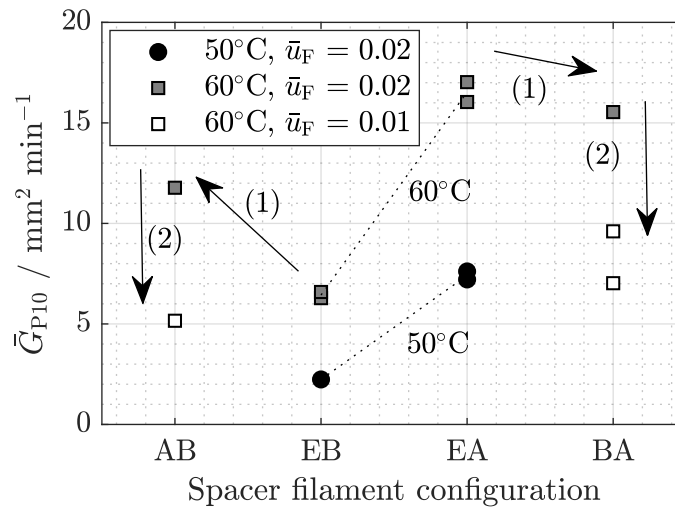


**Figure 5.10:** NaCl scaling (sea salt) for different spacer configurations according to Fig. 5.3. (1) Add a feed spacer to the given backing spacer configuration, (2) decrease the feed velocity. Feed temperatures $T_{F-1} = 50$ or $60\,°C$, mean velocities $\bar{u}_F = 0.01$ or $0.02\,\mathrm{m\,s^{-1}}$ (empty channel cross section), $p_{vac} = 30\pm2\,\mathrm{mbar}$, solute: Sea salt 1. [90]

### 5.2.3 Scale Formation from Sparingly Soluble Salts

The methods introduced above were also applied to investigate scaling from sparingly soluble salts, such as $CaSO_4$ and $CaCO_3$. They are the most relevant scalants in a wide range of natural waters and industrial applications [70].

**Qualitative Analysis**

The scale growth from supersaturated $CaSO_4$ solution ($b_{Ca}$ = 29 mmol kg$^{-1}$, CEx-S01, appendix Tab. B.7) showed rosette-like crystals growing at distinct places on the membrane. This hints at heterogeneous or secondary nucleation on the membrane surface and subsequent growth [72]. The operation conditions as well as the crystal shape showed that gypsum ($CaSO_4 \cdot 2\,H_2O$) was formed. After approximately 3h of operation, the massively scaled membrane was analyzed ex-situ with a light microscope and SEM. Still, distinct large crystal rosettes were visible. In between, there were smaller rosettes and deposited needles. The whole image showed a needle shaped, porous layer with highest density around the nuclei of crystal rosettes. This goes in hand with observations of gypsum scaling on RO membranes [72, 99]. SEM images show a complete dense coverage of the membrane with multiple layers of gypsum needles (cf. Fig. 5.11a).

The in-situ detection was able to identify larger rosettes but had shortcomings with identifying deposited needles and smaller agglomerations. The image registration procedure stopped working after a certain coverage of the membrane was reached. Then, the algorithm was not able to identify enough points to correlate the images. Turning off the vibration suppression does not lead to better results, since significant noise can appear. Nevertheless, for the initial phase up to more than 50% coverage, the procedure works well.

In contrast to sodium chloride and calcium sulphate, the calcium carbonate scaling experiments ($b_{Ca}$ = 0.8 mmol kg$^{-1}$, pH 10.1 declined to pH 9.2 over 3h experiment, CEx-C02, appendix Tab. B.7) showed only a marginal flux decline of approximately 10% within 2.2 h of operation. The in-situ microscopy did not reveal a coverage for the chosen magnification. Only a slight change in membrane surface color could be observed. Nevertheless, SEM analysis of the fouled membrane probes showed significant coverage of the membrane.

Fig. 5.11b shows the state of the membrane after approx. 3 h of operation. Multiple layers of small crystals of various shapes are deposited on almost the complete membrane area. Regions without crystals were mainly identified to have lower membrane porosity. These are regions where the PTFE layer touches the backing structure. An EDS analysis (cf. App. B.4) revealed that the various crystal shapes are all from $CaCO_3$.

The membrane of an experiment with calcium carbonate and sulfate, stopped after 30 min operation with scalants, is presented in Fig. 5.11c. Only $CaCO_3$ crystals could be detected (cf. EDS in App. B.4). Their size and morphology resemble that of crystals observed in the experiments conducted with pure $CaCO_3$. Similarly, the crystals are located on top of the membrane surface and do not interact with the membrane or reach into membrane pores.

Several conclusions can be drawn from the findings derived from the SEM images of $CaCO_3$ scales:

- The morphology of $CaCO_3$ crystals hints at their formation in an upstream position or in the bulk and later deposition on the membrane. This goes in hand with the inverse solubility of $CaCO_3$. Saturation indices are expected to be higher in the heater and in the bulk than on the membrane surface, where the temperature is lower. Furthermore, an increased turbidity of the feed solution could be observed after injection of the stock solutions.
- The different crystal shapes suggest their formation under different conditions in the process.
- The crystals build a relatively thin and porous layer on the membrane surface. This supports the low flux decline observed in the measurements.
- The missing interaction with the membrane coincides with the fact that no membrane wetting was observed (refer to Sec. 5.3.2).
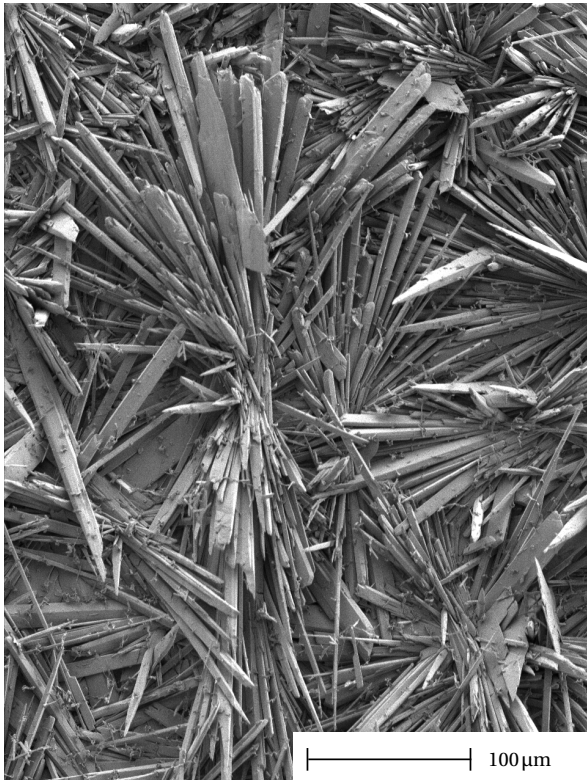
(a) Gypsum scale from CaCl$_2$+NaSO$_4$ solution after approx. 3h (CEx-S01, appendix Tab. B.7).
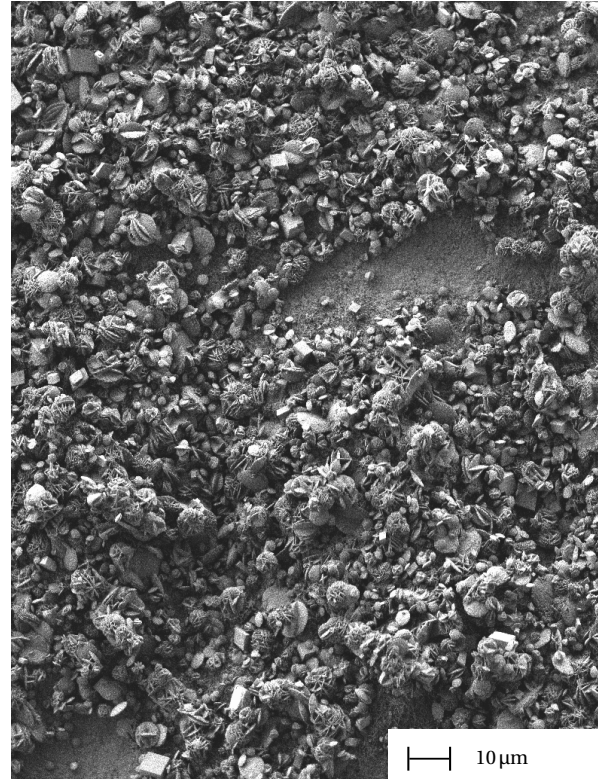
(b) Massive CaCO$_3$ deposition from CaCl$_2$+NaCO$_3$ solution (CEx-C02, appendix Tab. B.7).
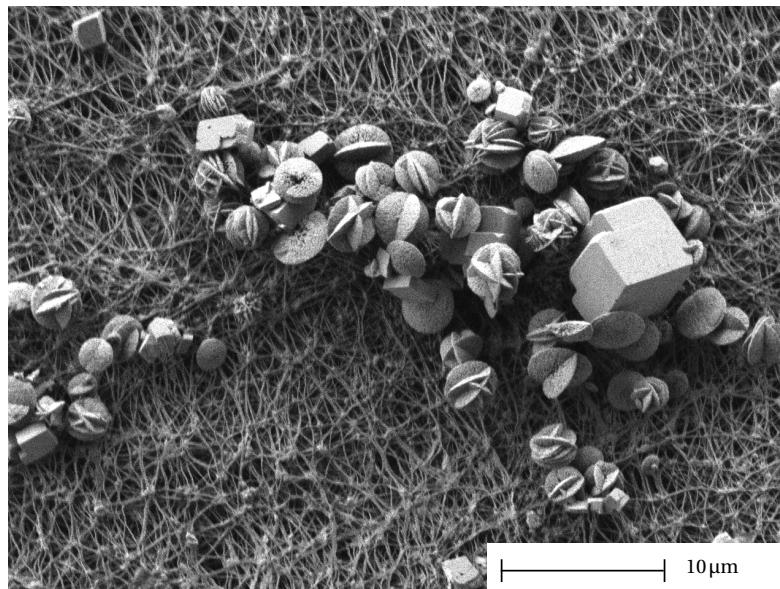
(c) Early stage CaCO$_3$ deposition from CaCl$_2$+NaSO$_4$+NaCO$_3$ solution (CEx-CS01, appendix Tab. B.7).

**Figure 5.11:** SEM images of crystals (scale) on the membrane [89]. Corresponding EDS in App. B.4.

**Quantitative Analysis of Gypsum Scaling Kinetics**

In the following, the scale formation process from a supersaturated $CaSO_4$ solution with $b_{CaSO_4} = 29\,mmol\,kg^{-1}$ is analyzed. Figure 5.12a shows the temporal evolution of vacuum pressure, distillate heat flux, and areal coverage of the membrane. For the first 80 min at a vacuum pressure of 40±1 mbar, a moderate flux decline was observed, while an exponential growth of crystal covered membrane area $A_C$ was identified from microscopy images. After this period, due to increasing membrane coverage and therefore strongly decreasing distillate flux, the pressure controller was not able to hold the pressure level anymore. Then, the vacuum pressure continuously decreased with decreasing vapor flux. Finally, at about 100 min, when the calculated heat flux over the membrane reached zero, the vacuum pump was operating against the membrane sealed by the scaling layer. In the following, the initial phase with constant vacuum pressure will be discussed.

Gilron and Hasson [99] distinguish two fundamental mechanisms leading to flux decline by scaling. Each mechanism has a characteristic crystal growth and flux decline behavior.

The first mechanism is generally characterized by lateral growth of distinct crystal sites on the membrane. These growth sites are of incompressible crystalline material and block the membrane. Around the growth sites, the flux across the membrane is similar to that in a clean module. The resulting flux decline $FD$ is characterized by the membrane area covered with crystal $A_C$

$$FD = 1 - \frac{\dot{m}_M}{\dot{m}_{M,0}} = \frac{A_C}{A_0}. \tag{5.10}$$

Assuming a constant height $\delta_C$ and constant density $\rho_C$ of the crystal layer, which has been proven to be acceptable by Gilron and Hasson [99] for gypsum scales, it follows

$$FD = \frac{1}{\rho_C\,\delta_C} \frac{m_C}{A_0}. \tag{5.11}$$

This means a linear dependency of the flux on the surface coverage or material accumulation.

The second mechanism, the deposition of crystalline material, can be described by the classical cake layer theory [99]. A porous cake layer builds up on the membrane. Its growth direction is membrane normal. For pressure driven separation processes, this cake layer is a resistance adding to the membrane resistance. For the process at hand, the cake layer is expected to act like a porous medium on the membrane that is wetted and therefore has an internal concentration and temperature polarization. The porosity as a fluid-dynamic resistance to the membrane flux is expected to be of minor influence, compared to filtration techniques.

For real applications, coupling of these two major mechanisms is expected. On the one hand, crystalline deposits will grow and cover the membrane. On the other hand, crystals that grow on the membrane do not necessarily show a tight, impermeable structure.
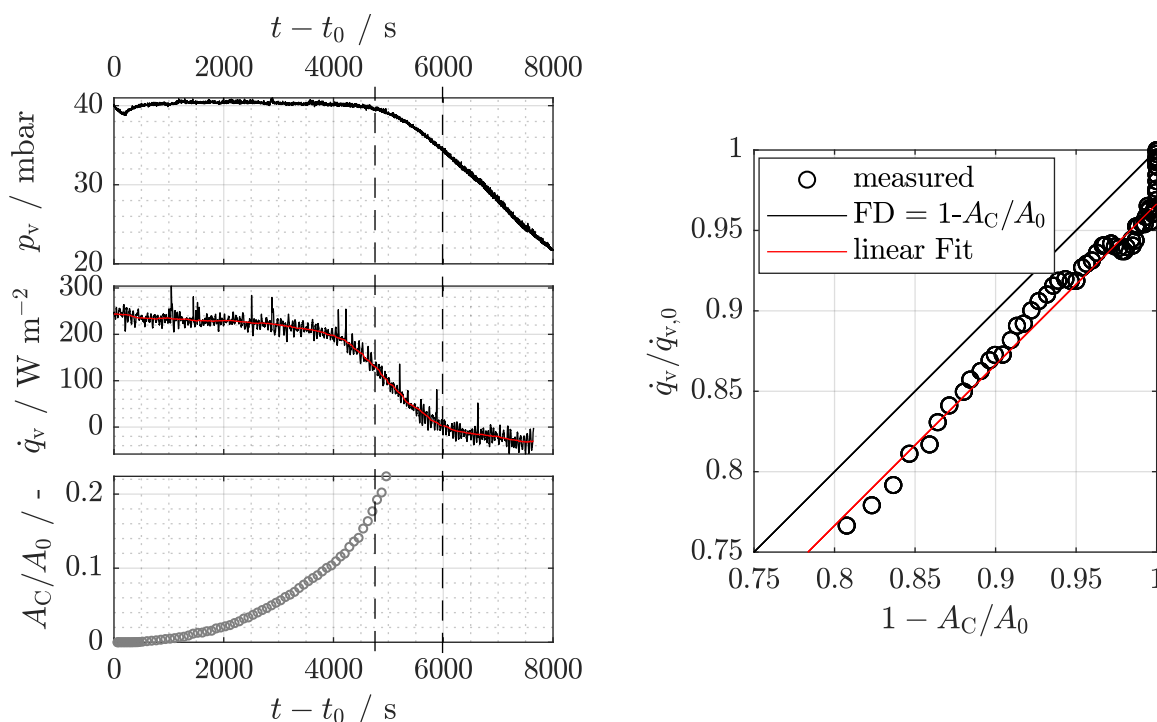


**(a)** Measured vacuum pressure, distillate flux, and membrane coverage.

**(b)** Relative flux decline compared to model from Eq. 5.10.

**Figure 5.12:** Scale growth from supersaturated $CaSO_4$ solution [89]. Experiment CEx-S01, appendix Tab. B.7.

For the gypsum scaling experiment at hand, the initial phase up to 20% surface coverage shows a linear dependency of flux decline on the uncovered area fraction (cf. Fig. 5.12b). The measurements show a deviation from the linear flux decline model for impermeable scales according to Eq. 5.10. This approximately parallel shift can have different reasons. The FOV investigated with the microscope covered only a small part of the membrane in the second half of the flow cell. This area is less prone to scaling than the inlet, which results in an underestimation of the membrane coverage of the whole cell. Furthermore, the detection algorithm suffers from contrast between crystal phase and membrane. Therefore, it is most likely that the covered area is underestimated. As discussed before, the gypsum crystals have a porous, needle-shaped structure. However, the linear flux dependency and the complete sealing of the membrane as shown in Fig. 5.12b indicate that the formed crystal layer is dense. The growth rates measured in the crystallization experiment with $CaSO_4$ were about one order of magnitude lower than those measured for scaling of NaCl.

## 5.3 Scaling Induced Membrane Wetting

### 5.3.1 Phenomenology of Membrane Wetting

Membrane wetting in VMD leads to filtration of the feed through the membrane driven by the absolute pressure difference between the feed and vacuum channel. This results in a flow rate of feed leaking through the membrane which is proportional to the wetted area. It dissipates vacuum and consequently reduces the driving force for the distillation process. The equivalent volume has to be removed by the vacuum pump. Besides the need for a technical solution to separate this leakage flow from the steam, additional mechanical work from the vacuum pump is needed.

The filtration of feed solution through the membrane can lead to deposition of particles and the formation of scales at the pore entrance and inside the pores. This was observed after a certain period in an ex-situ analysis of exper-

iments with Sea salt 1 (cf. appendix Tab. B.6). Fig. 5.13b shows a membrane after rinsing the feed channel with clean water. Regions with high concentration polarization are prone to membrane wetting due to the high degree of supersaturation and thus crystal growth. This can be either due to flow separation or stagnation zones caused by walls and spacer filaments or due to high distillate flux as found in the inlet zone. Furthermore, the membrane can easily be damaged at the channel edges by compression with the sealing and bending what can also lead to leakages.

Fig. 5.13a shows a LIF image of the wetted membrane. The image is desaturated and inverted. Label A marks large leakages and label B recent small droplets developed behind wetted pores. As the penetrated area increases and the permeated feed cannot be sufficiently removed with the vapor, the permeate channel shows larger feed accumulations. Fig. 5.13b shows an ex-situ image of a membrane after massive permeation through wetted areas. These regions are visible through deposits after rinsing the channel. The image contrast was significantly increased for better visualization.
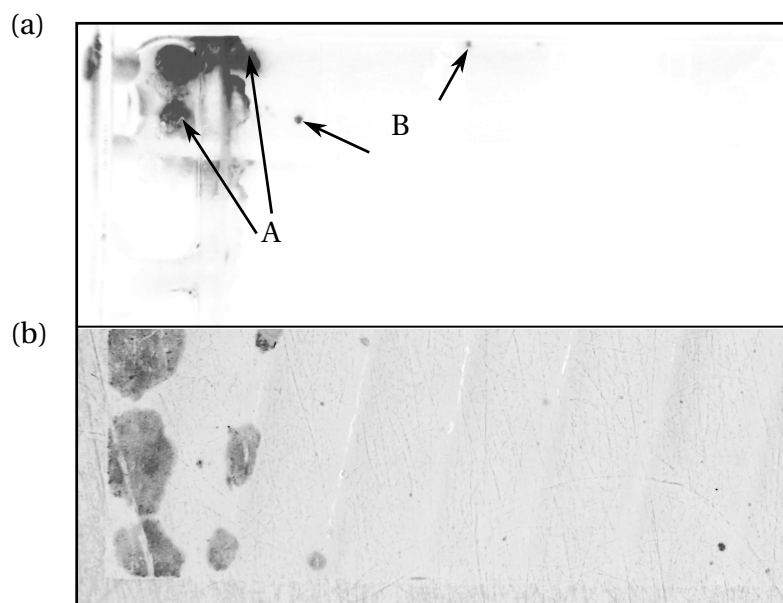


**Figure 5.13:** Membrane wetting: (a) In-situ image with tracer LIF (image inverted and desaturated) (b) Ex-situ feed side image. Feed flow direction from left to right, empty feed channel. Feed solution: sea salt. [89]

### 5.3.2 Interplay of Scaling and Membrane Wetting

Membrane wetting was monitored during most of the scaling experiments. Using pure NaCl in the feed did not lead to membrane wetting. Also, for scaling experiments with $CaSO_4$ and $CaCO_3$, no wetting was detected during the experimental runs. For $CaCO_3$, this goes in hand with the observations from SEM. Fig. 5.11 shows deposited calcite and vaterite crystals rather than growth of crystals at the pore entrance or into the pores.

Wetting was mainly observed for experiments with sea salt (Sea salt 1, appendix Tab. B.6). Approximately 4-10 cycles of scaling and scale removal (total 2-5 h operating time) with sea salt were necessary until membrane wetting was detected. Afterwards, the wetted membrane area expanded relatively fast within another 2-5 cycles. When larger regions were intruded with feed it was not possible to operate the system anymore.

The regions where membrane wetting was observed were analyzed using EDS. The test cell was rinsed with deionized water to avoid crystallization of NaCl after dismantling the cell. SEM and EDS of wetted areas after rinsing the system revealed calcium and sodium content (Fig. 5.14, ROI 2) in comparison to regions where no wetting was observed (ROI 1).

This result can be interpreted as follows. The scales detected via SEM and EDS in the wetted regions originate either from deposition of crystals at the pore entrance during operation of the system after a leakage was established or from crystals that initiated the wetting. Arguments in favor for the second case are that $CaCO_3$ and other calcium salts were undersaturated in the feed bulk, which means that only through concentration polarization they can reach a supersaturated state. Water recovery over the cell length is not sufficient for that. The highest flux and therefore the highest concentration at the membrane occurs at the entrance of the test cell. In this region, membrane wetting was detected first in most cases. A further supporting argument is that in experiments with pure NaCl no wetting could be observed. For experiments with $CaCO_3$ supersaturated in the bulk solution, crystallization in upstream components and deposition of crystals on the membrane was observed (cf. Sec. 5.2.3), which did not directly lead to membrane wetting. It is likely that

in these cases supersaturation was preferentially reduced by growth of exist-ing crystals already deposited on the membrane. In contrast to that, the sea salt solution lead to supersaturation of sparingly soluble salts only in regions with strong concentration polarization. In these regions membrane wetting was observed. This is an indication of $CaCO_3$'s involvement in the wetting pro-cess, provided the conditions for nucleation at pore entry were met.

Membrane wetting started in most experiments near the feed inlet to the test cell, where the highest flux and therefore highest concentration polarization appears. From there, it continuously spread further downstream. Since the re-covery rates over the short membrane sheet were negligibly small, the increase in bulk concentration towards the outlet of the test cell did not counterbalance the flux decrease caused by the temperature drop along the flow path. Other regions prone to wetting were near feed spacer filaments, if such a spacer was used. Reasons for membrane wetting not originating from scaling were de-struction of the membrane at the channel edges.
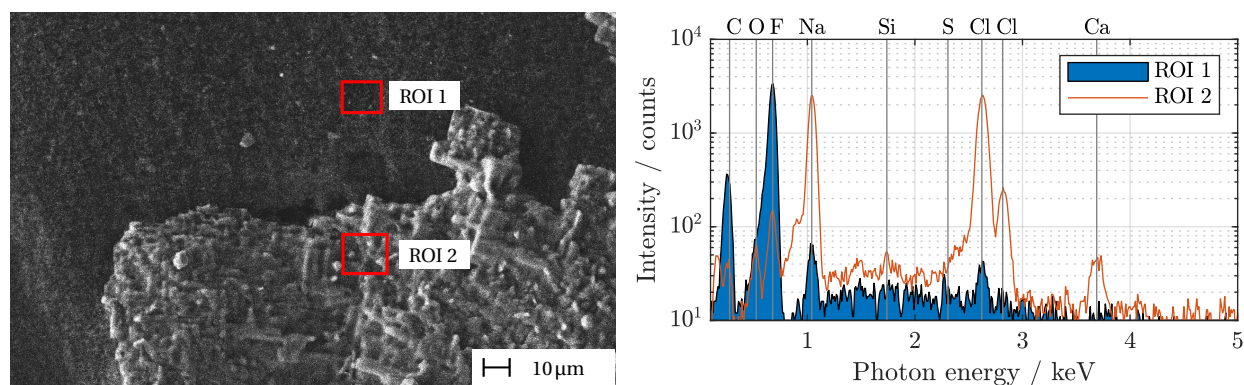


**(a)** SEM with EDS scanning regions (ROI) marked.

**(b)** EDS spectra for ROI 1 and ROI 2.

| mol/mol | C | O | F | Na | Cl | Ca |
|---|---|---|---|---|---|---|
| ROI 1 | 0.308 | 0 | 0.681 | 0.009 | 0.001 | 0 |
| ROI 2 | 0.255 | 5.3 | 0.094 | 0.339 | 0.254 | 0.004 |

**(c)** Quantitative results of relevant peaks in EDS spectra.

**Figure 5.14:** EDS spectra for ROI 1 and ROI 2 as marked in Fig. 5.14a and mole fraction of the main elements [89]. Scaling experiment CEx-03, appendix Tab. B.7.

## 5.4   Coupling of System Simulation and Scaling Prediction

The previous experimental studies have shown how scaling influences the VMD process through membrane coverage and wetting. Therefore, scaling prediction is necessary during plant design, especially for multi-component solutions. In this section, a scaling prediction tool is introduced, that adds to the tool chain for prediction of scaling in MEVMD systems. This tool is further applied to simulate complete ZLD systems in order to identify and design pretreatment methods. This is necessary to optimize the integration of MEVMD in ZLD systems.

The tool is based on the software PHREEQC [78] for chemical calculations in aqueous solutions. In the work at hand, it is used for speciation calculations in equilibrium state. The following assumptions and simplifications were made:

- Equilibrium thermodynamics of electrolyte solutions
- (Quasi-) steady-state behavior of the VMD system
- Pitzer model for multi-component solutions

A Matlab interface for PHREEQC was implemented to simulate water recovery, chemical treatment, and predict scaling propensity. Further, it allows post-processing of output from the MEVMD system simulation tool from Sec. 3.3.3. Figure 5.15a shows the general functionality of this model. It can be described as the combination of three process components. An ideal separator extracts water from an ingoing stream. The brine flows to a batch reactor that is perfectly stirred, heated to temperature $T$, and allows the brine to equilibriate with air having a given $CO_2$ partial pressure $p_{CO_2}$. Further, chemicals can be added in this reactor. The residence time of the solution is long enough to reach equilibrium. Downstream, a separator removes all solids. These are in the following referred to as precipitates.

This system was represented in Matlab and PHREEQC as shown in Fig. 5.15b. The interface allows to input the composition of the ingoing salt solution $\underline{b}_{in}$, the reactor temperature, the water recovery rate, and the partial pressure of $CO_2$. Further, chemicals can be added (molality vector $\underline{b}_{Chem}$). The results are the composition of the outgoing salt solution $\underline{b}_{out}$ and the molalities of all pre-

(a) Separator model

(b) Matlab - PHREEQC interface

(c) Coupling with MEVMD simulation
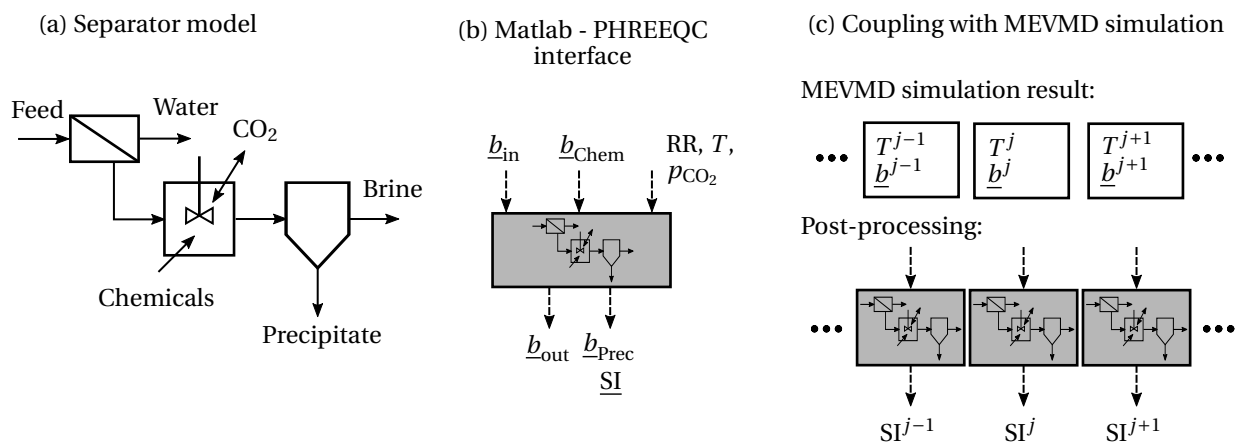
**Figure 5.15:** Model for water recovery dependent precipitation or SI determination using PHREEQC batch reactors with optional chemical dosing.

cipitates $\underline{b}_{\text{Prec}} = \left(b_{\text{Calcite}}, b_{\text{Aragonite}}, \ldots\right)^{\text{T}}$ or the respective SI values of the salts. All salts that can form from a given feed solution are created as equilibrium phases in PHREEQC. The salts relevant in the following analyses and their chemical formulas are listed in appendix Tab. C.3. The solution in the reactor is not allowed to build solid phases, if an output in terms of SI values is selected. This is useful for determining the scaling propensity of a salt solution.

The model was applied for two purposes: first, to simulate desalination systems including pretreatment steps in a simplified manner to estimate change in solution composition and, secondly, to post-process simulation results from the MEVMD system model with respect to scaling propensity. The first approach is applied in the following to investigate a complete ZLD system. The second approach will be used later for further optimizing an MEVMD system. Figure 5.15c depicts how the post-processing works. For each computational cell of the MEVMD system simulation result, a separate reactor is simulated. It uses the temperature and solution composition of the computational cell as input. The result is a vector of saturation indices $\underline{SI}^{j}$ for every computational cell $j$ of the MEVMD system simulation result.

The batch reactor model was applied to simulate a ZLD or near-ZLD system

including an MEVMD plant for treatment of seawater. Figure 5.16 presents a sketch of the system, the resulting solution composition at all intermediate states, precipitates forming in the subsystems, and salt saturation at the inlet and outlet of all subsystems. The ZLD system includes the following eight treatment steps:

1. The first step is the classical pretreatment of the feed to the RO stage. This can contain filtration, chemical treatment, aeration, or other measures to avoid fouling in the downstream stages. It must especially consider bio- and particulate fouling, critical in the first RO stage. [26]
2. The RO stage should be designed with respect to maximum recovery and therefore can contain several subsystems with or without energy recovery. Depending on the hardness of the feed solution, chemical pretreatment or intermediate treatment can be incorporated. The aim in a ZLD system should be to reach the pressure limit for RO without scaling. This subsystem provides the highest energy efficiency and lowest capital cost.
3. The temperature is increased in a first step to enhance the efficiency of downstream chemical softening [100]. The applicable temperature level depends on the solution composition and is limited by the scaling propensity of species with inverse solubility.
4. Hardness can be efficiently removed by chemical softening [101]. The additives have to be selected regarding the solution composition.
5. Settling and filtration removes precipitates. Afterwards, pH is adjusted to reach an SI<0 for carbonate hardness.
6. The feed solution is heated to the desired inlet temperature of the MEVMD subsystem. Here, or in the fist stage of the MEVMD system, the feed solution experiences the highest temperature. This is critical for salts with inverse solubility.
7. In the MEVMD subsystem that can consist of several multi-stage systems, further water recovery up to halite (NaCl) saturation is achieved.
8. The final step is an evaporation pond. Alternatively, a crystallizer can be applied.

The focus of the system design must be on the three steps (1, 4, and 5 in Fig. 5.16) that change the solution composition. For the given feed composition of standard seawater according to Millero et al. [102] and with a water

recovery of approx. 50%, the brine rejected from the RO reaches an osmotic pressure of almost 60 bar and saturation of gypsum. Concentration polarization in the RO modules must be considered.

Chemical softening (stages 3-5) reduces the hardness of the feed. For the given composition, it is efficient to remove Ca ions by adding 40 mmol/kg soda ash ($Na_2CO_3$). After filtration, pH must be adjusted to a level that avoids calcite scaling in downstream components. The comparison of the SI with (dark green) and without intermediate chemical softening (light green/red) shows that the plant can be operated without reaching the solubility limit of sparingly soluble salts almost up to the solubility limit of halite.

This provides the boundary conditions for design of the MEVMD system. A safety margin for local concentration polarization in the MEVMD system is left. This has to be checked in a detailed simulation which is documented in Sec. 6.2.
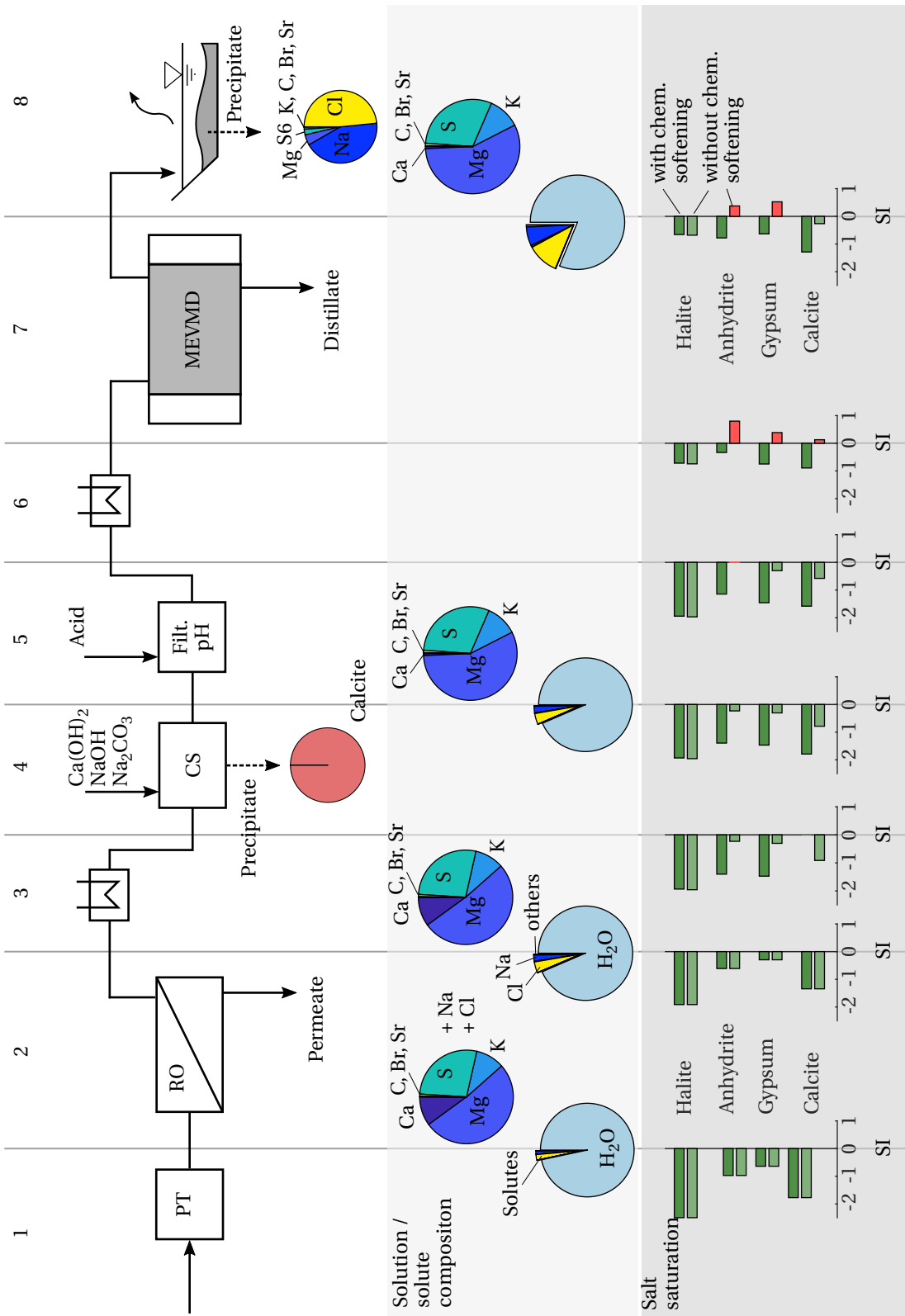
**Figure 5.16:** ZLD system with RO stage (1,2), intermediate chemical softening (CS), filtration, pH adjustment (3,4,5), MEVMD stage (6,7), and evaporation pond (8).

## 5.5 Application of the Findings to Scaling and Membrane Wetting in ZLD Systems

The findings of the chapter are summarized with respect to the application of MEVMD in ZLD systems and their respective plant and pretreatment design. The experimental results contradict the use of VMD to feed a crystallizer operating at the solubility limit of NaCl. There are mainly three reasons for this:

- Sodium chloride has a thin metastable zone. Therefore, no substantial supersaturation can be generated in a VMD module without risking scale formation.
- The solubility depends only to a small extent on temperature (cf. Sec. 2.3.3). Consequently, it would be necessary to significantly reduce the temperature in a crystallizer, but this would adversely impact the energy efficiency of the ZLD system [28].
- The highly soluble NaCl causes large deposit volumes already at moderate degrees of supersaturation which lead to rapid coverage of the membrane (cf. Sec. 5.2.1). The scales that were formed efficiently sealed the membrane and inhibited mass transfer. Although the scales can be easily removed by rinsing with water, this would again result in a brine stream of increased salinity.

Scaling has to be prevented, especially since it can cause membrane wetting. The interplay of scaling and membrane wetting can be summarized as follows (cf. Sec. 5.3.2):

- For the investigated artificial sea water (Sea salt 1, appendix Tab. B.6) membrane wetting is expected to be caused especially by $CaCO_3$. Scale formation from $CaCO_3$ can be hidden by other scalants, which lead to larger deposit volumes.
- The location of supersaturation and crystal nucleation influences the propensity towards membrane wetting. Deposited crystals do not directly lead to membrane wetting.
- Supersaturation on the membrane is critical for scale formation and membrane wetting. Local spots on the membrane show a significantly

higher salt concentration than the bulk solution at the module outlet (cf. Sec. 4.4).

- Feed and permeate spacers influence the scaling behavior (cf. Sec. 5.2.2, 4.4). Their design must be taken into account during the process layout.

The scaling experiments further revealed that it is not possible to reliably monitor scaling with the help of global plant performance parameters such as flux or outlet temperatures due to the following reasons:

- Crystallization kinetics and precipitate specifications influence the response of the membrane system to scaling. $CaCO_3$ deposits showed a porous structure and did not lead to a measurable flux decline (cf. Sec. 5.2.3).
- Depending on the solubility limit of a species and the resulting precipitate mass, the effect of scaling on process performance can be slower than on membrane wetting (cf. Fig. 5.7, Fig. 5.12, Sec. 5.2.1).
- Due to the strong influence of temperature on vapor pressure and therefore on distillate flux of VMD, a partial coverage of the membrane surface does not necessarily result in a measurable flux decline, which further complicates the interpretation of temperature data during plant operation (cf. Sec. 5.2.1, 5.2.3).

Consequently, pretreatment has to be adjusted to the respective feed solution to avoid deposits of any specie inside the module. Local concentration at the membrane surface has to be taken into account. This finally determines to what extent water recovery is possible from a brine stream.

# 6 Application-Specific Process Optimization

The previous chapters described the MEVMD systems in a top-down manner. Based on the system investigation, problems were derived at a channel flow level and a microscopic level on the membrane. The findings of these three detail levels and the tools implemented are now collected and used for application-specific process optimization.

Two case studies demonstrate how the findings can be applied to MEVMD systems with different separation tasks. The first case investigates the treatment of RO brine in a ZLD application. The second case regards how MEVMD can be applied for regenerating solutions with extreme vapor pressure reduction, e.g. for LDAC. This is preceded by a section on general optimization measures.

Optimization aims for MEVMD systems in high salinity application can differ significantly from those for conventional membrane desalination techniques such as RO or ED. This is in the first place due to the following reasons:

- Heat is available to the system at a defined temperature level. This maximum temperature depends on the heat source (e.g. solar thermal or waste heat) and is limited by the membrane and construction material of the MEVMD system.
- The temperature span between upper and lower temperature level governs the performance of an MEVMD plant. Therefore, the temperature level of heat rejection should be as low as possible. It is generally given by the ambient temperature level or the temperature of the feed (sea-) water source.
- In contrast to RO which is characterized by high permeate flux, low specific energy requirement, and therefore low investment and operation cost, MEVMD suffers from low fluxes and a lower degree of development

and availability. Heat supply to MEVMD is often considered as cheap, if an integration of waste heat is possible. Then the focus is no longer solely on minimizing energy requirements.

- The applications at hand, namely regeneration of liquid desiccants and ZLD of RO brine, hold new challenges concerning feed properties such as vapor pressure reduction and scaling potential.

## 6.1 General Measures

In the following subsections, different measures for process optimization are tested with the help of sensitivity analyses. The basic system configuration is the reference system introduced in Sec. 3.4.2 (c.f. appendix Tab. C.1, C.2). Variations in terms of boundary conditions, number of stages, or additional equipment are described in the following sections. Aqueous solutions of $CaCl_2$ were used as feed to investigate a wide range of solute dependent vapor pressure reduction. The performance measures GOR, $GOR_{preh}$, and RR, as introduced in Sec. 3.4.1, are used in the following to describe system performance.

### 6.1.1 Feed Preheating

External feed preheating was identified as one of the major optimization potentials for system performance. This can be especially beneficial if sensible heat from the brine can be recovered. Figure 6.1 shows three configurations for feed preheating. These are a once-through system without heat recovery from brine, a once-through system with brine heat recovery (BHR), and a system with brine recycling.

Figure 6.2a shows the distillate production and GOR for a system with four stages and a feed salt mass fraction of $w_F = 0$ and 0.2. Further, the shaded areas display the heating power $\dot{Q}_1$ supplied by the steam raiser and the heat introduced into the system by external feed preheating $\dot{Q}_2$. An increase in total distillate production can be observed for the pure water and the salty feed. The $GOR_{preh}$, counting $\dot{Q}_1 + \dot{Q}_2$ as system input, rise with increasing feed tem-

**(a)** Once-through system with external feed preheating.

**(b)** Once-through system with brine heat recovery (BHR).

**(c)** Brine recycling.
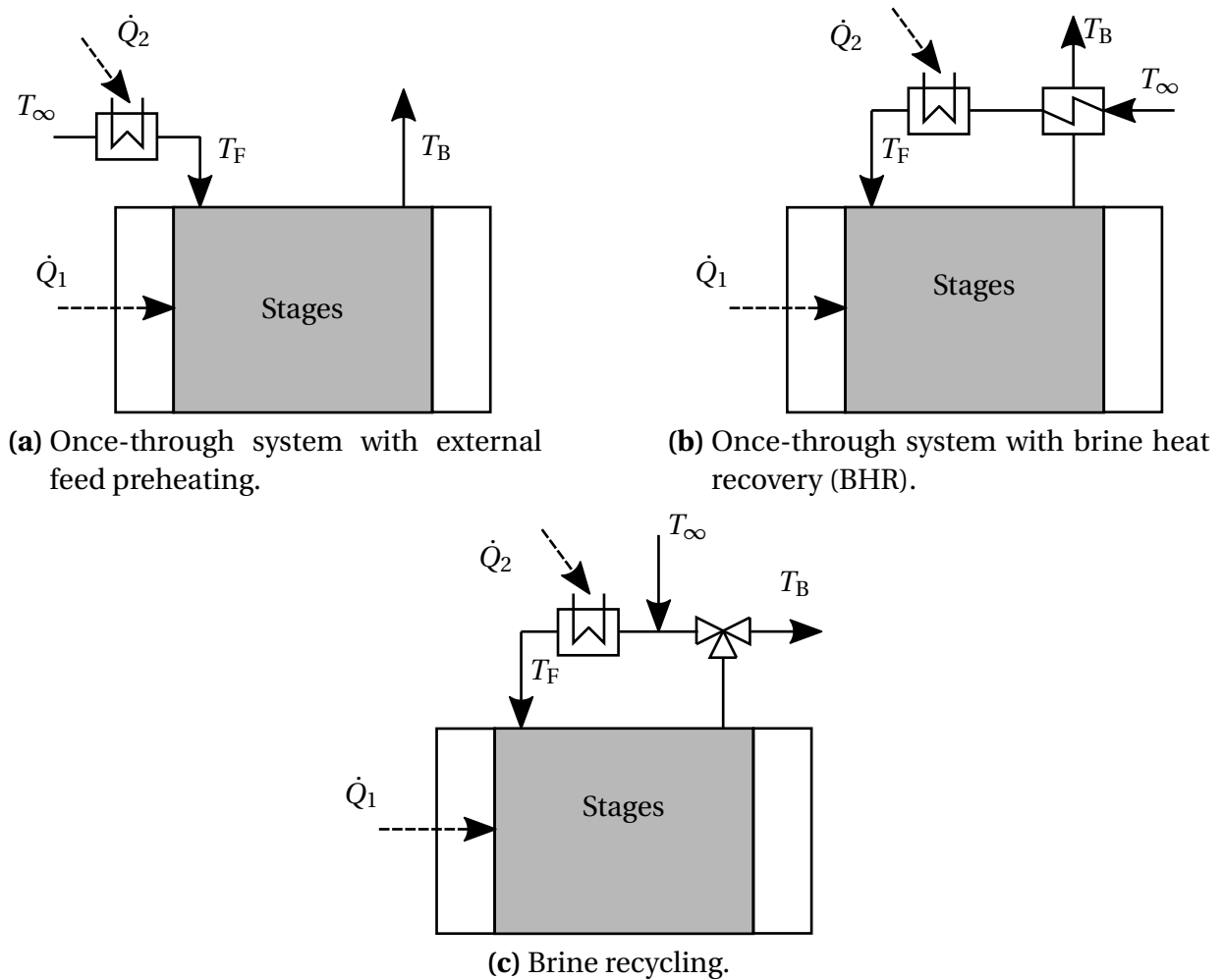
**Figure 6.1:** System configurations for feed preheating and external heat recovery from brine.

perature. For the pure water, a saturation in GOR increase can be observed when the feed temperature reaches the first stage's equilibrium temperature ($\approx 65°C$). Above that temperature, the potential of the steam raiser is not used anymore. Finally, the upper temperature level is increased which is a reason for a continuously increasing GOR.

For the case of a feed salt mass fraction of $w_F = 0.4$, a stronger influence of the feed temperature is observed (cf. Fig. 6.2b). Increasing the feed temperature above 50°C starts to reactivate the first stage in the case of the 2-stage setup. Above 62°C the 2-stage system is energetically favorable over the 4-
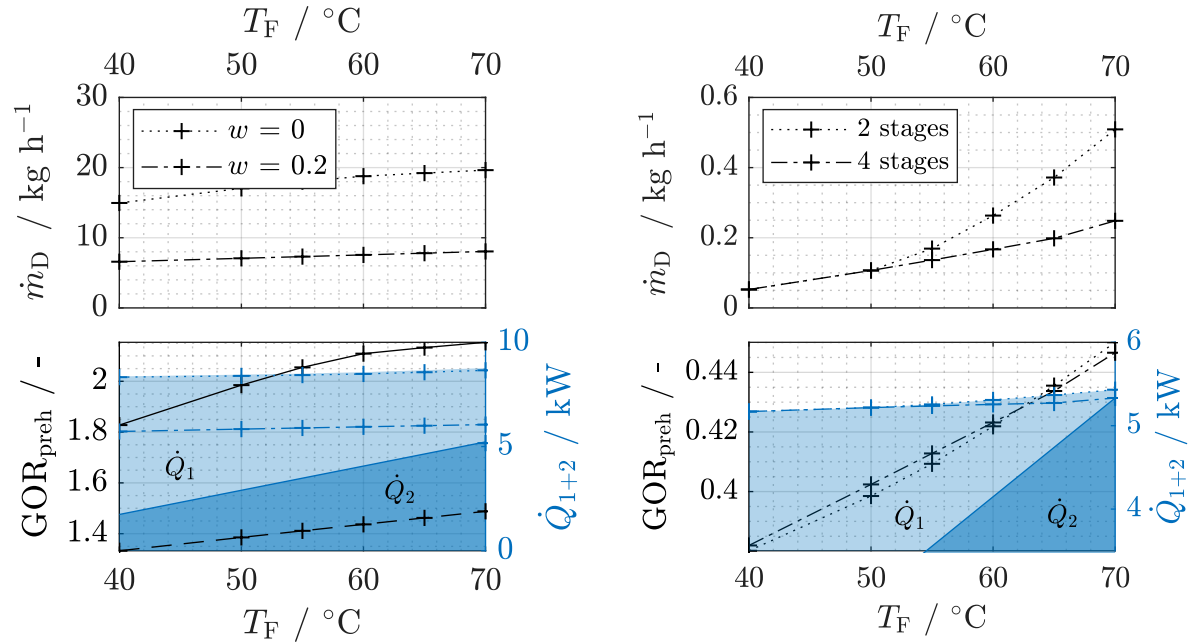
**(a)** Low feed salt content ($w_F = 0$, 0.2), 4-stage system.

**(b)** High feed salt content ($w_F = 0.4$), 4- and 2-stage system.

**Figure 6.2:** Influence of the feed temperature $T_F$ on the system performance and the source of heat input. Reference system (c.f. Sec. 3.4.2, appendix Tab. C.1, C.2) operated with $CaCl_2$ at $40 < T_F < 70°C$ and 2 or 4 stages.

stage system. Still, the substantial vapor pressure reduction significantly impacts the performance. Extremely low recovery rates require efficient heat recovery from brine streams if not circulated in batch operation.

For the practical implementation of feed preheating, the following considerations can be summarized:

- Depending on the application area and RR of the plant, waste heat streams from the process, such as condenser output or sensible heat from the brine, can be recuperated.

- Other waste heat sources with a temperature level lower than the steam generator temperature can be integrated.

- Economic considerations should especially include the construction material that needs to be corrosion resistant. The heat exchanger can be operated at ambient pressure, which is a plus. Internal preheating relies on the membrane based steam raiser and results in an inefficient use of the membrane area in the first stage. Therefore, external preheating is expected to be economically advantageous although an additional component is needed.

### 6.1.2   Recovery Rate Adjustment

Together with the GOR, the Recovery Rate (RR) is a key performance parameter of desalination plants. In general, for a given plant configuration (i.e. membrane area and stage arrangement), SEC and RR behave proportional. This also applies to MEVMD systems operated with feed solutions with low and medium salt concentration.

Fig. 6.3a shows an increase in distillate production with increasing feed flow rate. Reasons are the larger heat capacity rate $\dot{m}_F c_p$, better mixing in the feed channel, and a lower concentration factor over the plant. Both GOR and RR decline with increasing feed flow rate. Consequently, the feed flow rate can be used to adjust the recovery rate. During plant design, the desired RR should be considered for reaching the system capacity.

For high feed salt concentrations (cf. Fig. 6.3b) an exponential decrease for both RR and GOR is observed when increasing the feed flow rate. The distillate amount produced by the plant shows a maximum value, caused by the interplay of heat capacity rate and internal preheating. For the given system configuration it is at around $\dot{m}_F = 50 \, \text{kg h}^{-1}$. In this salt concentration range, the distillate amounts lie around 1% of those achievable for very low salt concentrations. More distillate is produced with the two-stage system at feed flow rates below $100 \, \text{kg h}^{-1}$ compared to the four-stage setup. This stems from the first stage, where lower feed flow rates lead to a stronger increase in feed temperature. If the system has two stages, the temperature differences across the stages are larger. Therefore, the potential for internal feed preheating is greater. The resulting influence on $\text{GOR}_{\text{preh}}$ is negligible and even the gain in RR is only visible towards very low feed flow rates.

In summary, the determination of an optimal RR must be based on economic considerations. Especially for high salt concentrations and low recovery rates, an efficient heat recovery from the brine stream or brine recycling is essential.
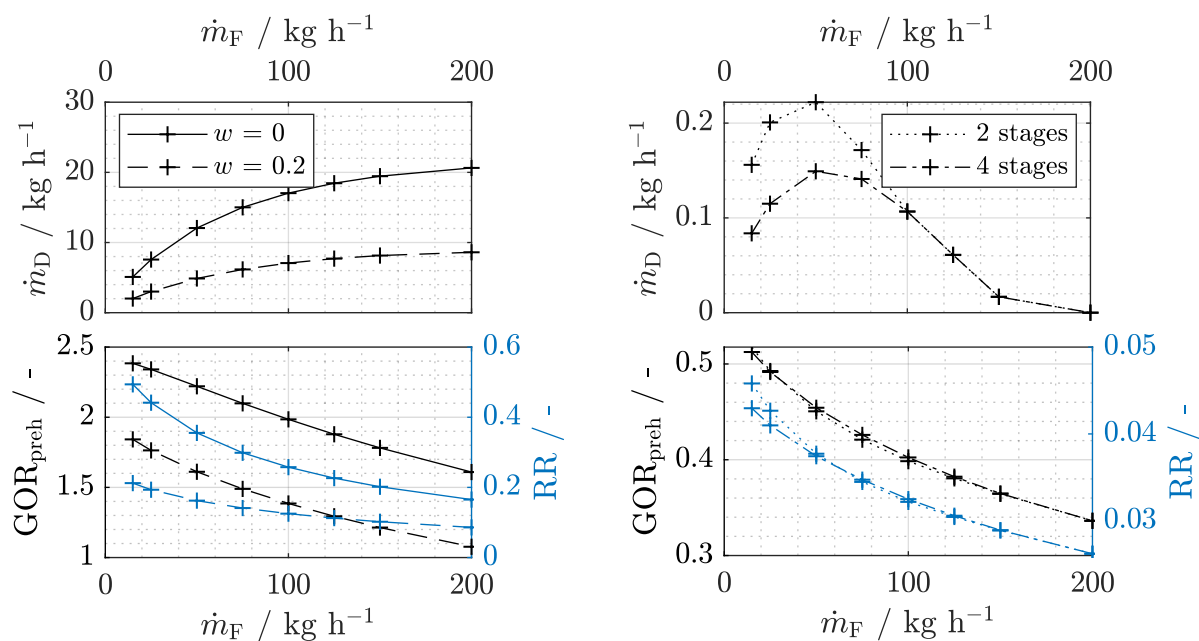


**(a)** Low feed salt content ($w_F = 0, 0.2$) and four stage system.

**(b)** Feed salt content $w = 0.4$ for two and four stage system.

**Figure 6.3:** Influence of the feed flow rate $\dot{m}_F$ on the system performance and the recovery rate RR. Reference system (c.f. Sec. 3.4.2, appendix Tab. C.1, C.2) operated with $CaCl_2$ at $\dot{m}_F \leq 200\,\mathrm{kg\,h^{-1}}$ and 2 or 4 stages.

### 6.1.3 Optimum Number of Stages

The sensitivity analyses shown in this chapter and in Sec. 3.4.3 hint at the existence of an optimum number of stages for a given feed salt concentration. In contrast to most heat and mass transfer applications, where only an economic optimum exists, for the MEVMD system a thermodynamic optimum can be found. In the following, the four performance parameters distillate flux $j_M$, total distillate amount $\dot{m}_D$, GOR, and $GOR_{preh}$ are regarded. Figure 6.4 shows the four parameters for different numbers of stages and $CaCl_2$ salt mass fractions of $0 \leq w_F \leq 0.45$.

The average membrane area specific distillate flux $j_M$ decreases with increasing feed salt content, mainly due to the decrease of equilibrium vapor pressure of the feed solution. The decline reaches a saturation for higher salt concentrations. The highest flux can always be observed for the system with the smallest number of stages. For a system with a small number of stages, the driving vapor pressure difference applied across the membrane is always higher than for a system with more stages. Thus, the distillate flux is a measure for how efficiently the plant uses the membrane area in terms of product output. This has to be considered in an economic optimization.

Regarding the total distillate production of the system $\dot{m}_D$, an optimum number of stages for each feed salt concentration can be found. Figure 6.4a (bottom) shows the relative difference between a plant with $N$ stages and a plant with $N-1$ stages. This means the positive or negative effect when adding one stage to a system. For small salt mass fractions $w_F \approx 0$ the distillate production $\dot{m}_D$ can be increased by adding stages. This increase

$$\Delta \dot{m}_{D,N} = \dot{m}_{D,N} - \dot{m}_{D,N-1} \tag{6.1}$$

through adding a stage $N$ is getting smaller with higher number of stages. For increasing salt mass fraction, the solute dependent vapor pressure reduction that reduces the driving pressure difference in every stage (cf. Sec. 2.1.3) quickly reduces the benefit of adding an extra stage and results in a negative effect ($\Delta \dot{m}_D < 0$) towards higher salt mass fractions. Finally, further increasing $w_F$ causes more and more stages to stop working (cf. Sec. 3.4.3) and therefore the difference between a system with $N$ and $N-1$ stages vanishes $\Delta \dot{m}_D \rightarrow 0$.
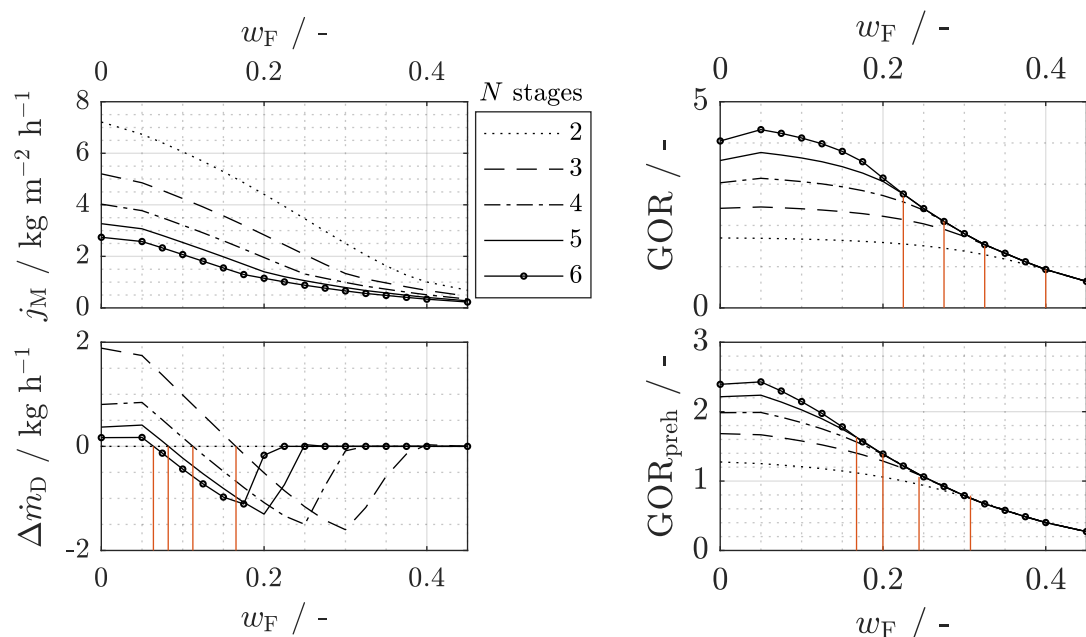
**(a)** Average flux $j_M$ and relative distillate increase by adding one stage $\Delta \dot{m}_D = \dot{m}_{D,N} - \dot{m}_{D,N-1}$ $(N = 3, 4, 5, 6)$.

**(b)** Gained Output Ratio (GOR) and GOR$_{\mathrm{preh}}$ including the preheating power from 25°C to $T_{21}$.

**Figure 6.4:** Influence of the feed salt content $w_F$ and the number of stages $N$ on the system performance. Reference system (c.f. Sec. 3.4.2, appendix Tab. C.1, C.2) operated with $CaCl_2$ and 2 - 6 stages.

With increasing salt mass fraction, step by step the optimum number of stages is reduced. The transition points where the optimum is reduced by one stage are marked with vertical lines.

The same applies to GOR and GOR$_{\mathrm{preh}}$, but at different concentration levels. Further, the GOR does not show an optimum for the number of stages, but a point beyond which adding a stage does not increase GOR. Then, the system with the smaller number of stages will be economically advantageous.

Figure 6.5 summarizes the performance criteria. The optimum number of stages increases towards lower feed concentration for all three criteria. The feed inlet temperature does not affect the optimum number of stages, although it increases GOR and distillate production. An increase in steam raiser inlet temperature $T_{11}$ leads to a shift of all three criteria towards higher feed salt concentration.
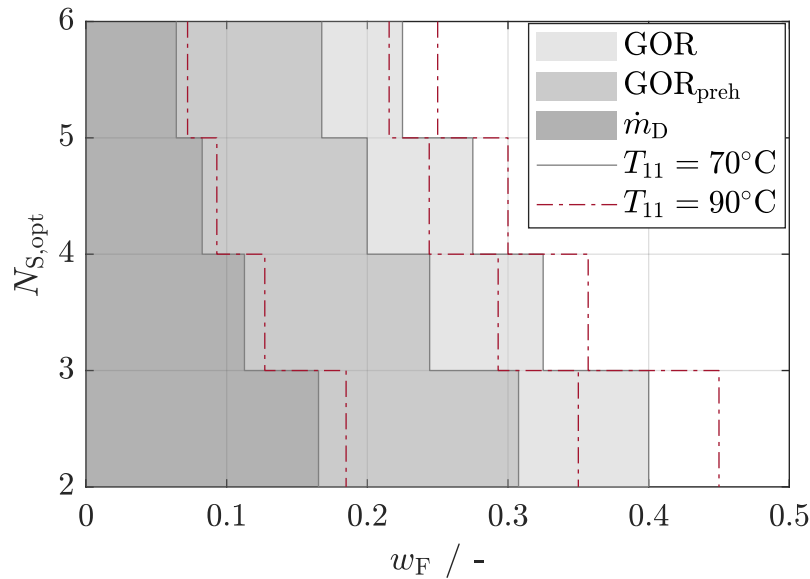
**Figure 6.5:** Feed concentration dependency of the optimum number of stages.

## 6.2 High-Recovery Desalination and Zero Liquid Discharge

This section demonstrates how the tool chain derived in this thesis can be applied to ZLD systems operating with RO brine from brackish or sea water desalination. Such a ZLD system was analyzed in Sec. 5.4 from a system perspective. Now, the brine treatment system including intermediate treatment (Fig. 5.16, stages 3 to 5) and the MEVMD stage (Fig. 5.16, stages 6, 7) are investigated. This brine treatment system must reach a high RR while avoiding scale formation. The aim of this case study is to apply the tools derived in this thesis to predict the scaling propensity in the MEVMD system. Using the results, suitable pretreatment measures and feed specific system adjustment are identified and tested in simulations.

The system configuration is based on the findings from previous sections, especially when designing the RR (cf. Sec. 6.1.2) and the number of stages (cf. Sec. 6.1.3) of the subsystems. The stage size of the reference plant from Sec. 3.4.2 is varied, which determines the system capacity. The MEVMD system (stages 6 and 7 in Fig. 5.16) contains two subsystems connected as shown in Fig. 6.6. The first subsystem is fed with RO brine with a total amount of dis-
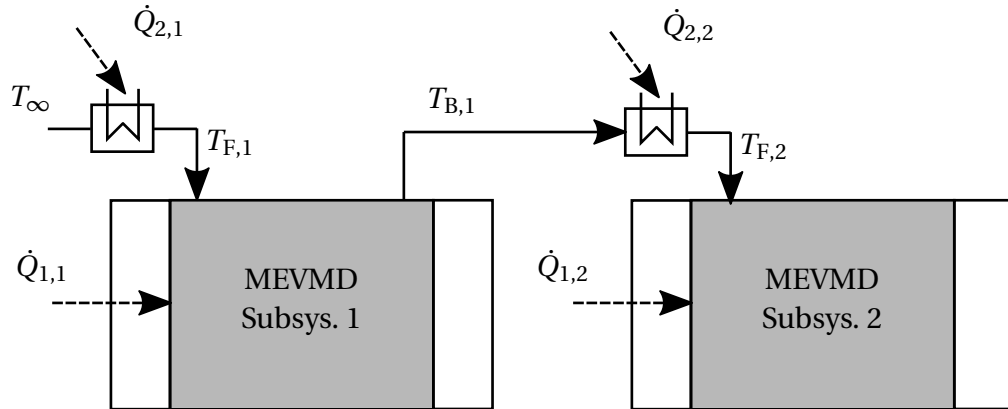
**Figure 6.6:** MEVMD with two subsystems for integration in ZLD plant.

solved solids (TDS) of $80\,\mathrm{g\,kg^{-1}}$. Within six stages a water recovery of approximately 50% is reached. Downstream, a second subsystem with three stages further increases the salt concentration.

Simulations were conducted using the system simulation tool and property functions for NaCl. Since NaCl is the dominating solvent, sparingly soluble salts were only regarded in a post-processing step. The PHREEQC-based post-processor described in Sec. 5.4 was used. Precipitation was turned off for calculating the SI values along the channels and the equilibrium partial pressure of $CO_2$ was held constant at $p_{CO_2} = 39\,\mathrm{Pa}$. At each position $x$ in the channel a reactor was calculated using the local temperature, salt mass fraction $w$, and solute composition $\xi_i$ defined as

$$\xi_i = \frac{n_i}{n}, \quad n = \sum_{i=1}^{N_{\mathrm{solutes}}} n_i. \tag{6.2}$$

Two model salt compositions as listed in Tab. 6.2 were investigated. These were the standard sea water composition according to Millero [102] and the sea salt used during the scaling experiments, here referred to as "Sea salt 1".

Figure 6.7 shows the evolution of temperature and concentration along the channel in the feed bulk as well as at the membrane and foil. Furthermore, the findings from Ch. 4 were applied. The CFD-based worst case estimate for concentration polarization as described by Eq. 4.11 was calculated as a further post-processing step and fed to the speciation simulation. Consequently, the relevant maximum salt mass fraction on the membrane and the estimated
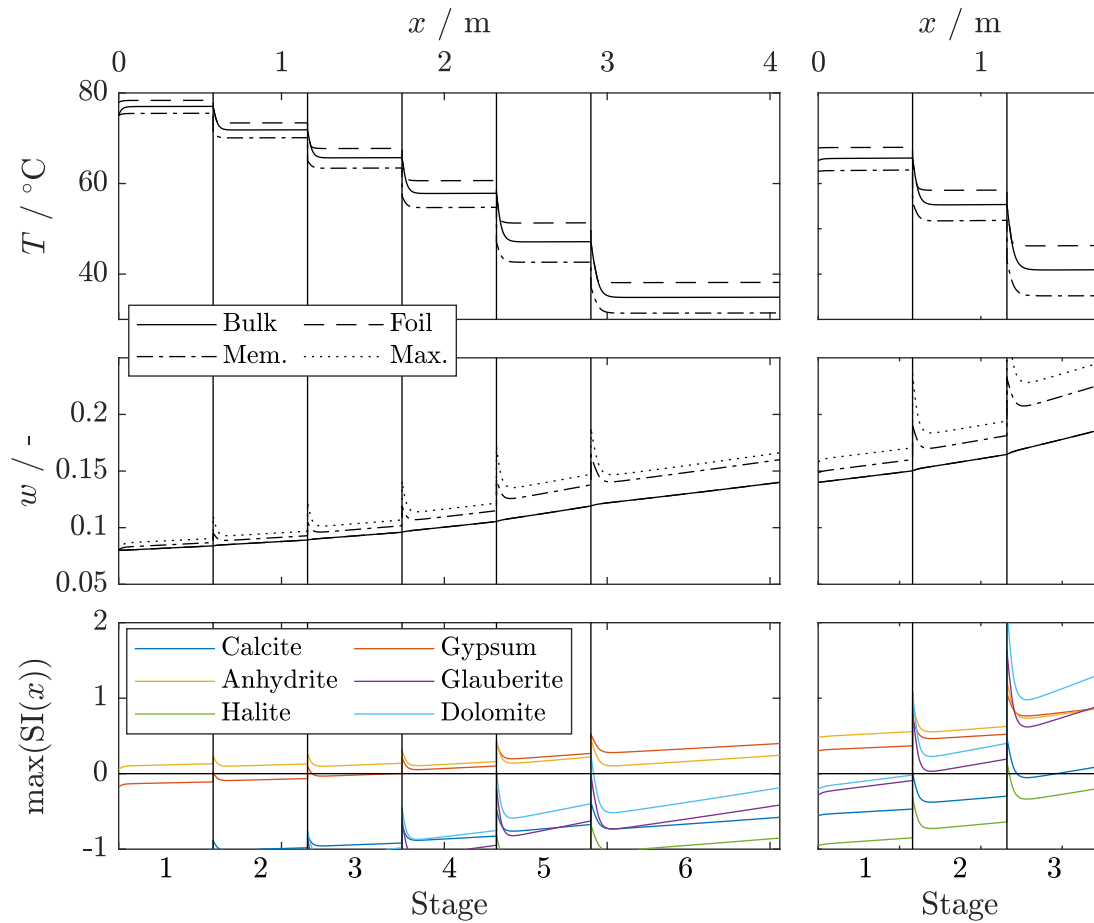
**Figure 6.7:** ZLD system with precipitation: the feed solution composition is standard seawater according to Millero [102] at $80\,\mathrm{g\,kg^{-1}}$ (cf. Tab. 6.1, case C1).

scaling propensity increased further. Figure 6.7 shows the saturation indices for relevant solid phases and the Millero standard seawater composition at this estimate of the maximum salt mass fraction. Values $SI > 0$ have to be expected to lead to deposits. In the case shown, the concentration polarization always causes the highest SI at a position $x$ to be located on the membrane. The temperature dependency of the solubility influences the result. Due to the high sulfur content of the seawater, gypsum and anhydrite show $SI > 0$ over the complete system. As shown in the experiments documented in Sec. 5.2.3, this can be expected to significantly impact the process and require membrane cleaning already after several hours of operation.

To analyze the influence of pretreatment, Tab. 6.1 compares the simulation

results for the two feed waters, different pretreatment methods, and two approaches to estimate the concentration polarization (CP model). Both feed solutions have a total solute content of $80 \, \mathrm{g \, kg^{-1}}$. The solute composition of Millero's standard sea water (cases C1-C5) is compared to that of "Sea salt 1" (C6-C8) which has the same composition as the salt used for scaling experiments described in Ch. 5. The table compares cases without pretreatment (C1, C2, C6, C7) with different pretreatment measures (C3-C5, C8). The table's last two columns list precipitates (i.e. SI > 0) and the respective locations in the plant (i.e. stages).

The result from Fig. 6.7 with Millero's sea water is listed in Tab. 6.1 as case C1 and C2, whereas scaling is predicted for both CP models. For "Sea salt 1" (case C6), the speciation calculation predicts only calcite ($CaCO_3$) and dolomite ($CaMg(CO_3)_2$) scaling in the second subsystem for pH = 8.0 due to the lower sulfur content of the solutes. If the maximum salt mass fraction at the membrane is used for estimating the scaling propensity (case C7), halite (NaCl) is supersaturated in a small region at the inlet of the last stage for both feed water compositions.

For both feed solutions, membrane scaling is predicted although the TDS of the brine rejected by the second subsystem stays below $200 \, \mathrm{g \, kg^{-1}}$ and halite does not reach saturation at the outlet of the second subsystem. Further, the composition of the brine rejected from the last stage does not necessarily show SI > 0 of any component. Nevertheless, local SI can be substantially higher, caused by concentration polarization and increased temperatures at the inlet of a stage. Consequently, the further optimization steps have to increase the RR in order to maximize the water recovery and decrease the SI of sparingly soluble salts. The final optimization aim is to reach a brine with a TDS near the saturation limit of NaCl.

**Measures to Avoid Scale Formation**

Possible ways to avoid scaling and realize a high recovery are to remove critical components, reduce their scaling propensity, or reduce concentration polarization. Table 6.1 summarizes approaches for the two salt compositions. Whereas the system geometry does not significantly reduce the concentration polarization, pretreatment shows to be most efficient. This is especially the

case since the critical components are hardness, which can be selectively removed. For example Ion Exchange (IX) or lime softening could be used. IX is used to exchange hardness ($Ca^{2+}$, $Mg^{2+}$) with $Na^+$, which results in a constant TDS but higher solubility [101]. Lime softening describes the addition of lime-water $Ca(OH)_2$ to remove hardness via precipitation. Soda ash ($Na_2CO_3$) can be added to improve hardness reduction [100]. This softening method results in a reduction of TDS. Other methods would be limestone filtration or addition of caustic soda (NaOH)[26, 100].

Figure 6.8 (case C4 in Tab. 6.1) shows the SI values for the Millero sea water composition after introducing lime softening as pretreatment. The simulated pretreatment consisted of three steps. In the first step, 20 mmol $Na_2CO_3$ per kg water were added to the feed at 60°C to reduce the hardness. In the second step, all resulting precipitates were removed from the solution which can be realized by settling and filtration. In the last step, pH = 6.5 was adjusted which can be done through acid dosing. Two post-processing runs for the MEVMD system simulation were compared. In the first run, the concentration polarization was estimated with mean Sherwood numbers as presented in Sec. 2.2 and introduced into the simulation tool in Sec. 3.3.2. With this approach, no scaling was predicted as SI < 0 for all sparingly soluble salts over the whole module (Tab. 6.1 C3). In a second run, the CFD-based worst case estimate for concentration polarization derived in Sec. 5.1.5 was used to estimate the local maximum supersaturation (Tab. 6.1 C4, Fig. 6.8). For this case, SI > 0 for several minerals can be observed in the last stage. This can be avoided by increasing
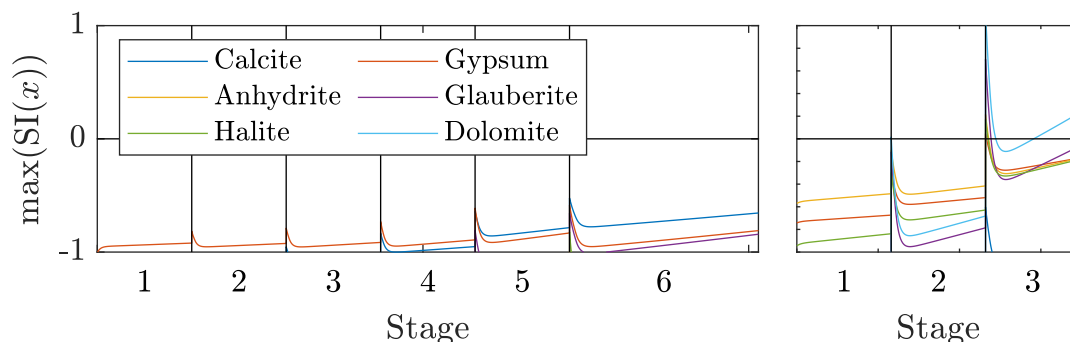


**Figure 6.8:** SI after applying lime softening to feed solution (cf. Tab. 6.1, case C4).

the amount of soda ash (Tab. 6.1, C5).

For feed with the composition of "Sea salt 1", it is possible to avoid scaling by adjusting pH (cf. Sec. 2.4.2). This is due to the strong dependency of the solubility of $CaCO_3$ on pH. For the example case it is expected to be sufficient to reduce pH below 7.5 (Tab. 6.1, C6-C8). Referring to the experimental results from Sec. 5.2.3 on $CaCO_3$ scaling, the convective transport of $CaCO_3$ crystals leads to a decrease in flux, but not directly to membrane wetting. Consequently, crystallization and subsequent filtration or deposition of $CaCO_3$ before entering the MEVMD system would be an opportunity. If crystals are convected into the system, these can be removed for example by air backwashing [103] or dissolution in acidic cleaning solutions.

After applying pretreatment to both feed solutions, the scaling risk of sparingly soluble salts was eliminated. Only halite shows small supersaturation at the entrance to the last stage in Subsystem 2. This can be solved by adjusting the process parameters or changing the plant geometry to reduce the flux in the last stage.

It can be concluded that a salt mass balance over the components of a ZLD system and an analysis of the composition of the brines is no reliable method to predict the scaling potential. Both the change in feed properties along the channels of an MEVMD plant as well as their local distribution in the spacer mesh influence the scaling propensity. With help of the system simulation tool, CFD results, and the scaling post-processor the scaling potential can be estimated and measures to avoid scaling can be derived.

**Table 6.1:** ZLD configurations and pretreatment options.

| Case | CP model | Feed water | Pretreatment | Precipitates | Stages with precipitation |
|---|---|---|---|---|---|
| C1 | mean | Millero | none, pH = 7 | Gypsum, Anyhdrite, Glauberite | Subsys. 1: Stages 1-6; Subsys. 2: Stages 1-3 |
| C2 | max. | Millero | none, pH = 7 | Gypsum, Anyhdrite, Glauberite | Subsys. 1: Stages 1-6; Subsys. 2: Stages 1-3 |
| C3 | mean | Millero | lime softening | - | - |
| C4 | max. | Millero | lime softening, pH = 6.5, $Na_2CO_3$: 0.02 mmol kg$^{-1}$ | Gypsum, Anyhdrite, Glauberite, Dolomite | Subsys. 2: Stage 3 |
| C5 | max. | Millero | lime softening, pH = 6.5, $Na_2CO_3$: 0.025 mmol kg$^{-1}$ | Halite (SI = 0.172) | Subsys. 2: Stage 3 |
| C6 | mean | Sea salt 1 | pH = 8 | Calcite, Dolomite | Subsys. 2: Stages 2,3 |
| C7 | max. | Sea salt 1 | pH = 8 | Calcite, Dolomite, Halite | Subsys. 1: Stage 6; Subsys. 2: Stages 2,3 |
| C8 | max. | Sea salt 1 | pH = 7.5 | Halite | Subsys. 2: Stage 3 |

**Table 6.2:** Feed salt composition of the investigated model solutions (based on Millero et al. [102] and appendix Tab. B.6).

| | | | | | Salt composition $\xi_i = n_i / n_{\text{solute}}$ | | | | | |
|---|---|---|---|---|---|---|---|---|---|---|
| **Name** | **Ca** | **Fe** | **K** | **Mg** | **Na** | **Sr** | **S** | **Cl** | **F** | **Br** |
| Millero | 9.20e-03 | 0 | 9.14e-03 | 4.73e-02 | 0.420 | 8.12e-05 | 2.53e-02 | 0.489 | 6.11e-05 | 7.54e-04 |
| Sea salt 1 | 2.12e-4 | 5.99e-06 | 1.3e-04 | 4.79e-05 | 0.54 | 5.74e-06 | 6.26e-04 | 0.46 | 0 | 0 |

## 6.3   Treatment of Low-Vapor Pressure Fluids

Whereas the equilibrium vapor pressure above sodium chloride solutions is limited to 23.8 mbar at 25°C [65] by the solubility of the salt, it can be desirable to generate solutions providing a lower vapor pressure. Liquid desiccant air conditioning (LDAC) is a technology that relies on the principle of solute dependent vapor pressure reduction. A liquid with a low vapor pressure is used to dehumidify air. Generally, aqueous solution of $CaCl_2$ or LiCl are applied since these salts are highly soluble and show a low vapor pressure compared to water at ambient temperatures [62]. During dehumidification of air, the liquid desiccant absorbs water which must be extracted in a regeneration process to guarantee a continuous operation. The conventional regeneration in a liquid-air mass exchanger is highly energy intensive why alternative methods are searched for [19]. Since $CaCl_2$ is cheap and readily available, it is often used in aqueous solutions as liquid desiccant, as done in the following investigations with a typical solute mass fraction of around 400 g kg$^{-1}$.

In the following, an MEVMD plant is optimized for regenerating a desiccant solution. The case study is based on the findings from Sec. 6.1. Twelve membrane channels are used to construct different geometrical configurations (cf. Fig. 6.9), each one with the same membrane area. The number of stages and the length of the stages are varied. The results are three systems with a channel length of $L_{fr}$ and one to three stages (cases 1-3) and three systems with the double channel length per stage $2 \cdot L_{fr}$ (cases 4-6). The intention when comparing systems with long and short channels was to investigate how the membrane surface can be used most efficiently. The resulting standardized systems can be scaled up by increasing the number of parallel membrane channels to reach the capacity required.

The feed solution contains 0.35 kg $CaCl_2$ per kg solution. A design RR of 12.5% is set to reach a brine salt mass fraction of $w_B = w_F / (1 - RR) = 0.4$. Latter lies in the operation range typical for LDAC applications. A series of feed flow rates was simulated. The value for the feed flow necessary to reach the design RR was then determined by interpolation. The feed and steam raiser temperature level were $T_{F,1} = 85°C$ and $T_{SR,1} = 90°C$ respectively. Ambient temperature and
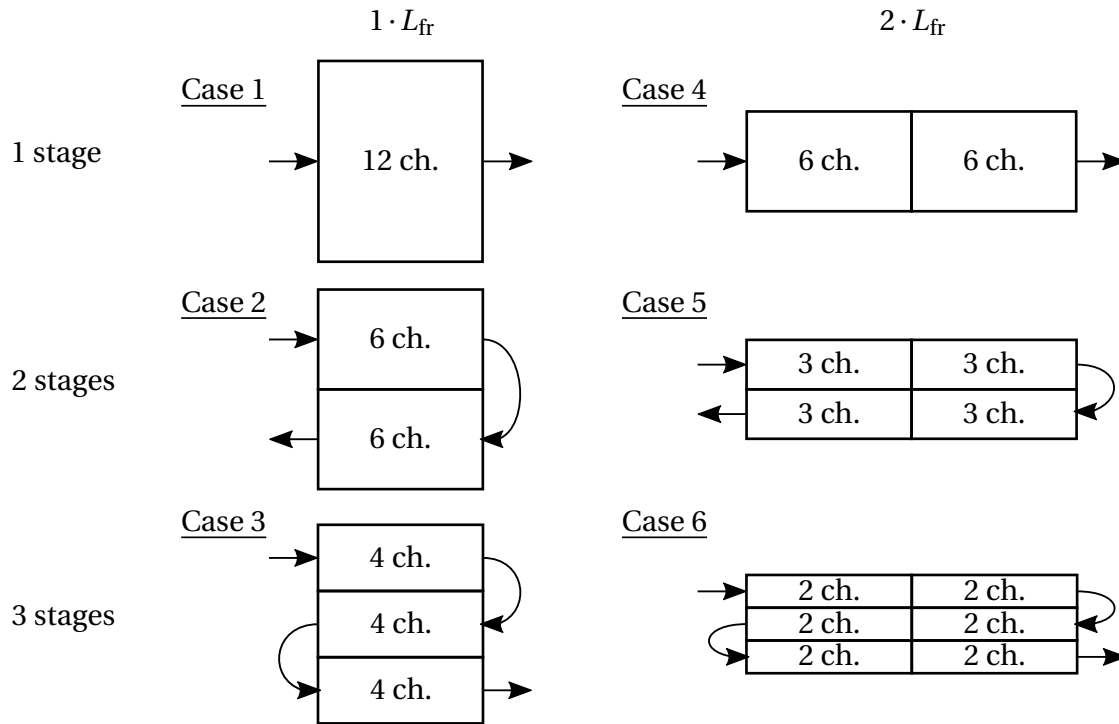
**Figure 6.9:** Plant configurations as variations of 12 feed channels with a channel length $L_{\mathrm{fr}}$ of each frame.

condenser inlet were set to 25°C. For all other parameters, the values from the reference case were applied (cf. appendix Tab. C.1 and C.2). If brine heat recovery (BHR) is considered, a pinch point temperature difference of 5 K was assumed for the counter flow heat exchanger (cf. Fig. 6.1b).

Figure 6.10 summarizes the simulation results. The upper sub-figure shows the feed mass flow rate per frame $\dot{m}_{\mathrm{F,fr}}$ for the six plant configurations from Fig. 6.9 plotted over the resulting RR. The gray region marks the possible range of feed flow rates. The upper limit is determined by a ballooning effect of the feed channel assembly. This appears when the absolute pressure in the feed channel is higher than that prevailing in the upstream vapor channel. Then, the condenser foil will not be pressed onto the feed spacer anymore and the channel assembly becomes unstable. Economic considerations together with the maximum achievable RR determine the lower limit.

The lower sub-figure shows the corresponding GOR including preheating and brine heat recovery. As already derived in Sec. 6.1, GOR increases with increas-
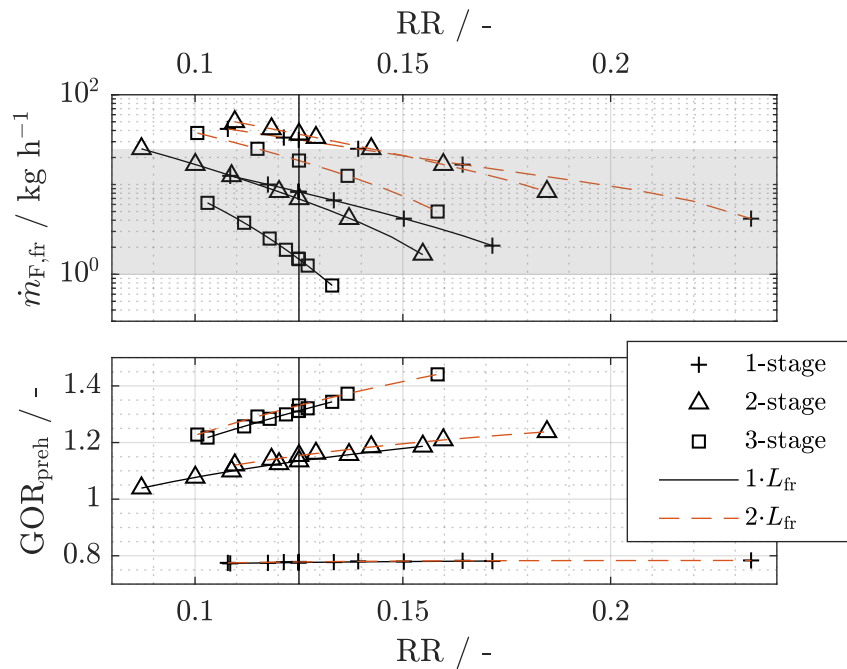
**Figure 6.10:** Comparison of 1-, 2-, 3-stage system in terms of feed flow rate per frame $\dot{m}_{F,fr}$ and GOR including preheating and brine heat recovery. Design water recovery RR = 0.125 shown by vertical lines.

ing water recovery. Further, the configuration with double channel length $(2 \cdot L_{fr})$ are slightly superior to configurations with short channels $(2 \cdot L_{fr})$. A vertical line marks the design RR of 12.5% in both sub-figures. The results for this point are summarized in Fig. 6.11.

The stage length only shows a small influence on GOR but a significant influence on the plant capacity. For the cases presented in Fig. 6.11, it is always advantageous to built stages with longer channels than more channels in parallel. The main reason is the need for higher flow rates in the $2 \cdot L_{fr}$-setup to reach the design RR. Higher feed flow rates result in a higher heat capacity rate and better mixing in the channel. The potential for optimization by extending the channel is limited by the pressure loss that increases with the length of the channel. Operation at higher RR is therefore recommended. Only for the single-stage setup the longer channel can show a lower GOR than the short-
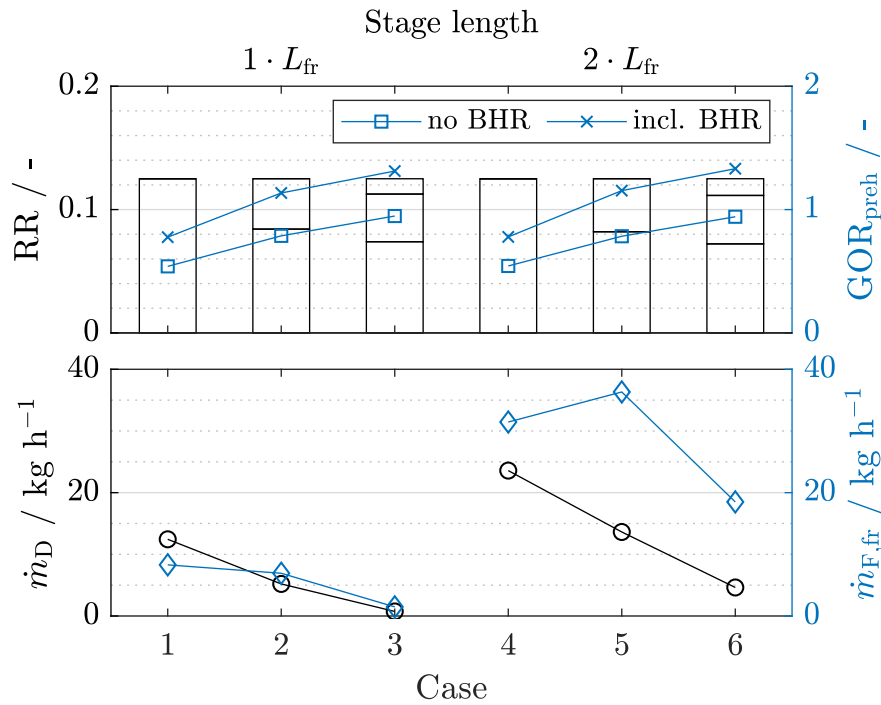
**Figure 6.11:** Comparison of the six system configurations from Fig. 6.9 at design water recovery RR = 0.125.

channel setup at high recovery rates.

The influence of the number of stages on the system performance was discussed in Sec. 6.1.3. As detailed there, an increase in number of stages leads to an increase in GOR and a decrease in distillate capacity. The single stage system can only provide a $GOR_{preh} < 1$, even with BHR. For all other systems displayed, BHR is necessary to reach a $GOR_{preh} > 1$. The three-stage setup reaches a $GOR_{preh}$ of approximately 1.3 with BHR. The first stage contributes only little to the total distillate production. Further increasing the stage number will not have any benefit. The setup with standard frame length suffers from extremely low flow rates and distillate fluxes.

BHR shows its highest potential at low RR. This is due to the resulting high brine temperature and therefore large potential for sensible energy recovery. For the cases displayed in Fig. 6.11, an increase in $GOR_{preh} > 40\%$ can be achieved using BHR. Besides applying BHR, brine recycling was introduced

in Fig. 6.1c. This is an option if a high RR is required but cannot be achieved with the desired setup. Depending on the recycling rate, BHR may be still advantageous.

In summary, the following conclusions can be drawn with regard to the operation window and the integration of MEMVD systems into liquid desiccant air conditioning. The operation window is mainly influenced by economic considerations and the feed flow rate per frame. The latter determines the heat capacity rate, the mixing in the channel and the pressure drop over the channel length. The vapor pressures in the the stages determine the highest tolerable pressure loss. Above a plant specific limit, the feed channel widens and the spacer will not be attached to either membrane or foil. Finally, the plant configuration has to be selected considering the operation window, the required plant capacity, and an economically reasonable balance between GOR and membrane area.

# 7  Summary and Conclusion

The purpose of this work was to investigate the treatment of saline solutions with elevated salt content using Vacuum Membrane Distillation. This was motivated by the challenge of designing multi-effect configurations of Vacuum Membrane distillation, which arises from the complexity of coupled heat and mass transfer phenomena. These appear at multiple scales, between multiple phases, and involving multi-component salt solutions.

To solve this challenge, three objectives were pursued. The first objective was to determine the application limits and optimization potential with regard to the vapor pressure reduction of feed solutions in multi-stage systems. The second objective was to understand how scaling and scaling-induced membrane wetting influences the system performance and the reliability of the process. The third objective was to investigate the applicability of Vacuum Membrane Distillation for high-recovery desalination, especially its integration into Membrane Distillation-crystallizer assemblies.

In order to meet these objectives, it was necessary to understand in detail how the colligative properties of the feed solution influence the behavior of the desalination system. In addition, the process-relevant kinetics of scale formation and the interaction of crystals and membranes had to be investigated.

The challenges were addressed by developing a tool chain for the analysis and design of Multi-Effect Vacuum Membrane Distillation systems. The tool chain includes the following simulation tools and experimental methods:

- A system simulation tool to predict performance and allow optimization of Multi-Effect Vacuum Membrane Distillation systems: The mechanistic model includes the physical coupling of stages in multi-effect assemblies. In addition, the stages were resolved along the flow direction, which helped overcome uncertainties in state-of-the-art models. Finally,

the distillate flux along the channels can be predicted and thus temperature and concentration can be resolved. The simulation tool was experimentally calibrated and verified.

- A computational fluid dynamics approach for detailed analysis of heat and mass transport phenomena in membrane channels: With the knowledge of temperature and salt mass fraction distribution in the spacer mesh the maximum supersaturation in membrane channels could be estimated. This was used to predict the local propensity to scale formation. In addition, the method was used to evaluate experimental results. Finally, a CFD-based worst case-estimate for concentration polarization in flow separation and stagnation zones was derived and applied to predict scaling during Multi-Effect Vacuum Membrane Distillation system design.

- A post-processing tool for scaling prediction in Multi-Effect Vacuum Membrane Distillation systems operated with multi-component salt solutions: Using this equilibrium chemistry-based approach, the link between the Multi-Effect Vacuum Membrane Distillation system simulation and the scaling prediction was established. The tool is intended for system layout and operational design in cases with multi-solute feed solutions.

- An experimental approach for the investigation of scaling and scaling induced membrane wetting under process conditions: The combination of light microscopy with advanced image processing and laser-induced fluorescence allowed to investigate scaling and membrane wetting in-situ. From the experimental results, the kinetics of scale formation and the influence of scaling on system performance were derived. Furthermore, salts and operation conditions critical for membrane wetting were identified.

In the next step, application specific system analyses were made on the basis of these models and the findings of the investigations. From this, design rules and application limits for Multi-Effect Vacuum Membrane Distillation systems used for treatment of low-vapor-pressure feed waters or in Zero Liq-

uid Discharge were derived. The following conclusions can be summarized:

- Multi-effect systems must be optimized with respect to the solute-specific vapor pressure reduction. With increasing salt content in the feed solution the gain in efficiency by adding additional stages to a plant decreases. For $CaCl_2$ solutions in the system under consideration, this was noticeable above a feed salt mass fraction of approximately 20%. Below this threshold, e.g. for seawater desalination or brine treatment, stage numbers up to 6 and above enhance the energy efficiency. For Liquid Desiccant Air Conditioning applications near 40% $CaCl_2$, more than two stages are no longer advisable. In the case of a strong solute-specific vapor pressure reduction, optimization potentials lie not only in the correct number of stages but also in the preconditioning of the feed in order to use the system efficiently. Furthermore, efficient heat recovery from discharge streams is essential.

- Scaling in Multi-Effect Vacuum Membrane Distillation systems shows special characteristics compared to other membrane systems. The main reasons for this are the large operating temperature range and the possibility of treating solutions with high osmotic pressure and thus different solute compositions. Highly soluble salts such as NaCl gain influence, as does the inverse solubility of carbonates. In contrast to other desalination processes, the deposition of NaCl can have a considerable influence on the process. Exceeding saturation leads to large deposit volumes and rapid performance reduction. With regard to sparingly soluble salts it was observed that $CaCO_3$, as a component of sea water, leads to wetting of the membrane. However, this depends on the location of supersaturation and resulting crystal nucleation and growth relative to the liquid-vapor interface at the membrane surface.

- Due to the susceptibility of the membrane to scaling induced wetting, especially in flow separation and stagnation zones at the feed spacer, the possibility of crystallization must be prevented. Critical regions in Multi-Effect Vacuum Membrane Distillation systems can be identified on the basis of equilibrium thermodynamics of multi-component salt solutions with the tool chain developed in this work.

In short, the design of Multi-Effect Vacuum Membrane Distillation systems must take into account vapor pressure reduction, coupled heat and mass transfer, and solute composition throughout the whole desalination system. The methods and tools described in this thesis support the process of designing and optimizing Multi-Effect Vacuum Membrane Distillation plants.

# Bibliography

[1] World Water Assessment Programme. Water: A shared responsibility; the United Nations world water development Report 2, executive summary, 2006. URL `https://unesdoc.unesco.org/ark:/48223/pf0000144409`. accessed: 2019-08-09.

[2] IEA. Water Energy Nexus - Excerpt from the World Energy Outlook 2016. Technical report, International Energy Agency, 2016. URL `https://webstore.iea.org/weo-2016-special-report-water-energy-nexus`. accessed: 2019-05-03.

[3] S. Lattemann. *Development of an environmental impact assessment and decision support system for seawater desalination plants.* Ph.D. Thesis, Delft University of Technology, Delft, 2010.

[4] E. Jones, M. Qadir, M. van Vliet, V. Smakhtin, and S. Kang. The state of desalination and brine production: A global outlook. *Science of The Total Environment*, 657:1343–1356, 2019. doi: 10.1016/j.scitotenv.2018.12.076.

[5] P. K. Cornejo, M. V. E. Santana, D. R. Hokanson, J. R. Mihelcic, and Q. Zhang. Carbon footprint of water reuse and desalination: A review of greenhouse gas emissions and estimation tools. *Journal of Water Reuse and Desalination*, 4(4):238–252, 2014. doi: 10.2166/wrd.2014.058.

[6] T. Tong and M. Elimelech. The global rise of zero liquid discharge for wastewater management: Drivers, technologies, and future directions. *Environmental Science & Technology*, 50(13):6846–6855, 2016. doi: 10.1021/acs.est.6b01000.

[7] J. Gilron. Brine treatment and high recovery desalination. In *Emerging Membrane Technology for Sustainable Water Treatment*, pages 297–324. Elsevier, 2016. ISBN 978-0-444-63312-5. doi: 10.1016/B978-0-444-63312-5.00012-7.

[8] DESWARE. Encyclopedia of desalination and water resources (DESWARE) - Energy requirements of desalination processes. `http://www.desware.net/Energy-Requirements-Desalination-Processes.aspx`, visited 2019-05-30.

[9] A. Cipollina, G. Micale, and L. Rizzuti, editors. *Seawater desalination: Conventional and renewable energy processes*. Green Energy and Technology. Springer, Heidelberg ; New York, 2009. ISBN 978-3-642-01149-8 978-3-642-01150-4.

[10] J. Koschikowski. *Entwicklung von energieautark arbeitenden Wasserentsalzungsanlagen auf Basis der Membrandestillation*. Fraunhofer Verl., Stuttgart, 2011. ISBN 3-8396-0260-2.

[11] K. Zhao, W. Heinzl, M. Wenzel, S. Büttner, F. Bollen, G. Lange, S. Heinzl, and N. Sarda. Experimental study of the memsys Vacuum-Multi-Effect-Membrane-Distillation (V-MEMD) module. *Desalination*, 323:150–160, 2013. doi: 10.1016/j.desal.2012.12.003.

[12] M. E. Findley. Vaporization through porous membranes. *I&EC Process Design and Development*, 6(2):226–230, 1967.

[13] A. Basile, A. Figoli, and M. Khayet, editors. *Pervaporation, Vapour Permeation and Membrane Distillation: Principles and applications*. Number number 77 in Woodhead Publishing Series in Energy. Elsevier, Woodhead Publishing, Cambridge, UK, 2015. ISBN 978-1-78242-246-4.

[14] D. Winter. *Membrane Distillation: A thermodynamic, technological and economic analysis*. Schriftenreihe der Reiner Lemoine-Stiftung. Shaker, Aachen, 2015. ISBN 978-3-8440-3706-7.

[15] J.-P. Mericq, S. Laborie, and C. Cabassud. Vacuum Membrane Distillation for an integrated seawater desalination process. *Desalination and Water Treatment*, 9:287–296, 2009.

[16] J.-P. Mericq, S. Laborie, and C. Cabassud. Vacuum Membrane Distillation of seawater Reverse Osmosis brines. *Water Research*, 44(18):5260–5273, 2010. doi: 10.1016/j.watres.2010.06.052.

[17] E. K. Summers and J. H. Lienhard V. Cycle performance of Multi-Stage Vacuum Membrane Distillation (MS-VMD) systems. In *The International Desalination Association World Congress on Desalination and Water Reuse 2013, Tianjin, China*, Tianjin, China, 2013.

[18] M. Wenzel, S. Büttner, W. Heinzl, and S. Heinzl. Distillation of high concentrated salt solution by Vacuum Multi Effect Membrane Distillation (VMEMD) of memsys. *Water Practice and Technology*, 10(3):478–485, 2015. doi: 10.2166/wpt.2015.055.

[19] F. Kiefer, F. Schummer, A. Präbst, M. Spinnler, and T. Sattelmayer. Theoretical and experimental study of Multi-Effect Vacuum Membrane Distillation systems for liquid desiccant air conditioning and zero liquid discharge. *Desalination and water treatment*, 69:190–201, 2017. doi: 10.5004/dwt.2017.20299.

[20] D. M. Warsinger, J. Swaminathan, E. Guillen-Burrieza, H. A. Arafat, and J. H. Lienhard V. Scaling and fouling in Membrane Distillation for desalination applications: A review. *Desalination*, 356:294–313, 2015. doi: 10.1016/j.desal.2014.06.031.

[21] D. M. Warsinger, J. Swaminathan, H. W. Chung, S. Jeong, and J. H. Lienhard V. The effect of filtration and particulate fouling in membrane distillation. In *The International Desalination Association World Congress on Desalination and Water Reuse 2015*, San Diego, CA, 2015.

[22] A. I. Radu. *Modeling fouling in spiral wound membrane systems*. Dissertation, TU Delft, Delft, 2014.

[23] M. Gryta. Concentration of NaCl solution by Membrane Distillation integrated with crystallization. *Separation Science and Technology*, 37(15): 3535–3558, 2002. doi: 10.1081/SS-120014442.

[24] M. Gryta. Fouling in Direct Contact Membrane Distillation process. *Journal of Membrane Science*, 325(1):383–394, 2008. doi: 10.1016/j. memsci.2008.08.001.

[25] Y. Chen, Z. Wang, G. K. Jennings, and S. Lin. Probing pore wetting in Membrane Distillation using impedance: Early detection and mechanism of surfactant-induced wetting. *Environmental Science & Technology Letters*, 4(11):505–510, 2017. doi: 10.1021/acs.estlett.7b00372.

[26] Dow Water & Process Solutions. FILMTEC Reverse Osmosis membranes technical manual, form no. 609-00071-0309, 2013.

[27] B. Bornak. Desalination by Ion Exchange. In J. Kucera, editor, *Desalination*, pages 503–520. John Wiley & Sons, Inc., Hoboken, NJ, USA, 2014. ISBN 978-1-118-90485-5 978-1-118-20852-6. doi: 10.1002/ 9781118904855.ch11.

[28] C. E. Pantoja, Y. N. Nariyoshi, and M. M. Seckler. Membrane Distillation Crystallization applied to brine desalination: Additional design criteria. *Industrial & Engineering Chemistry Research*, 55(4):1004–1012, 2016. doi: 10.1021/acs.iecr.5b03807.

[29] E. Drioli, A. Ali, and F. Macedonio. Membrane Distillation: Recent developments and perspectives. *Desalination*, 356:56–84, 2015. doi: 10.1016/j.desal.2014.10.028.

[30] C. A. Quist-Jensen, A. Ali, S. Mondal, F. Macedonio, and E. Drioli. A study of Membrane Distillation and crystallization for lithium recovery from high-concentrated aqueous solutions. *Journal of Membrane Science*, 505:167–173, 2016. doi: 10.1016/j.memsci.2016.01.033.

[31] G. Guan, R. Wang, F. Wicaksana, X. Yang, and A. G. Fane. Analysis of Membrane Distillation Crystallization system for high salinity brine

treatment with zero discharge using aspen flowsheet simulation. *Industrial & Engineering Chemistry Research*, 51(41):13405–13413, 2012. doi: 10.1021/ie3002183.

[32] F. Edwie and T.-S. Chung. Development of Simultaneous Membrane Distillation-Crystallization (SMDC) technology for treatment of saturated brine. *Chemical Engineering Science*, 98:160–172, 2013. doi: 10.1016/j.ces.2013.05.008.

[33] R. Creusen, J. van Medevoort, M. Roelands, A. van Renesse van Duivenbode, J. H. Hanemaaijer, and R. van Leerdam. Integrated Membrane Distillation-Crystallization: Process design and cost estimations for seawater treatment and fluxes of single salt solutions. *Desalination*, 323: 8–16, 2013. doi: 10.1016/j.desal.2013.02.013.

[34] C. M. Tun, A. G. Fane, J. T. Matheickal, and R. Sheikholeslami. Membrane Distillation Crystallization of concentrated salts - Flux and crystal formation. *Journal of Membrane Science*, 257(1-2):144–155, 2005. doi: 10.1016/j.memsci.2004.09.051.

[35] X. Ji, E. Curcio, S. Al Obaidani, G. Di Profio, E. Fontananova, and E. Drioli. Membrane Distillation-Crystallization of seawater Reverse Osmosis brines. *Separation and Purification Technology*, 71(1):76–82, 2010. doi: 10.1016/j.seppur.2009.11.004.

[36] General Electric Company. Aspire (TM) Microfiltration Membranes - data sheet, Product QL833, 2007.

[37] R. B. Saffarini, B. Mansoor, R. Thomas, and H. A. Arafat. Effect of temperature-dependent microstructure evolution on pore wetting in PTFE membranes under Membrane Distillation conditions. *Journal of Membrane Science*, 429:282–294, 2013. doi: 10.1016/j.memsci.2012.11.049.

[38] M.R. Qtaishat and T. Matsuura. Modelling of pore wetting in Membrane Distillation compared with Pervaporation. In *Pervaporation, Vapour Permeation and Membrane Distillation*, pages 385–413. Elsevier, 2015. ISBN 978-1-78242-246-4. doi: 10.1016/B978-1-78242-246-4.00013-1.

[39] K. Nikolaus. *Trink- und Reinstwassergewinnung mittels Membrandestillation*, volume 10 of *Fortschritt-Berichte*. Techn. Univ. Kaiserslautern, 2013. ISBN 978-3-943995-49-7.

[40] K. W. Lawson and D. R. Lloyd. Membrane Distillation. *Journal of Membrane Science*, 124(1):1–25, 1997. doi: 10.1016/S0376-7388(96)00236-0.

[41] M. S. El-Bourawi, Z. Ding, R. Ma, and M. Khayet. A Framework for better understanding Membrane Distillation separation process. *Journal of Membrane Science*, 285(1-2):4–29, 2006. doi: 10.1016/j.memsci.2006.08.002.

[42] M. Gryta. Osmotic MD and other Membrane Distillation variants. *Journal of Membrane Science*, 246(2):145–156, 2005. doi: 10.1016/j.memsci.2004.07.029.

[43] H. W. Chung, J. Swaminathan, D. M. Warsinger, and J. H. Lienhard V. Multistage Vacuum Membrane Distillation (MSVMD) systems for high salinity applications. *Journal of Membrane Science*, 497:128–141, 2016. doi: 10.1016/j.memsci.2015.09.009.

[44] memsys clearwater Pte. Ltd. memDist 4-6.4 - Technical description of process, modules and applications, 2014.

[45] T. Melin and R. Rautenbach. *Membranverfahren: Grundlagen der Modul- und Anlagenauslegung*. Verfahrenstechnik. Springer, Berlin [u.a.], 2. edition, 2004. ISBN 3-540-00071-2.

[46] J. G. A. Bitter. *Transport mechanisms in membrane separation processes*. The Plenum Chemical Engineering Series. Plenum Press, New York, 1991. ISBN 978-0-306-43849-3.

[47] G. Schock and A. Miquel. Mass transfer and pressure loss in spiral wound modules. *Desalination*, 64:339–352, 1987. doi: 10.1016/0011-9164(87)90107-X.

[48] S. M. Mojab, A. Pollard, J. G. Pharoah, S. B. Beale, and E. S. Hanff. Unsteady laminar to turbulent flow in a spacer-filled channel. *Flow,*

*Turbulence and Combustion*, 92(1-2):563–577, 2014. doi: 10.1007/s10494-013-9514-4.

[49] M. Ciofalo, F. Ponzio, A. Tamburini, A. Cipollina, and G. Micale. Unsteadiness and transition to turbulence in woven spacer filled channels for Membrane Distillation. *Journal of Physics: Conference Series*, 796, 2017. doi: 10.1088/1742-6596/796/1/012003.

[50] Ahmad Fauzi Ismail, Kailash C. Khulbe, and Takeshi Matsuura. *Gas separation membranes: Polymeric and inorganic*. Springer International Publishing, Cham Heidelberg New York Dordrecht London, 2015. ISBN 978-3-319-01095-3 978-3-319-01094-6.

[51] R. B. Bird, W. E. Stewart, and E. N. Lightfoot. *Transport phenomena*. Wiley, New York, rev. 2. ed edition, 2007. ISBN 978-0-470-11539-8.

[52] M. Khayet. Membranes and theoretical modeling of Membrane Distillation: A review. *Advances in Colloid and Interface Science*, 164(1-2):56–88, 2011. doi: 10.1016/j.cis.2010.09.005.

[53] P. W. Atkins. *Atkins' physical chemistry*. Oxford University Press, Oxford; New York, 10th edition edition, 2014. ISBN 978-0-19-969740-3.

[54] E. C. W. Clarke and D. N. Glew. Evaluation of Debye–Hückel limiting slopes for water between 0 and 150°C. *Journal of the Chemical Society, Faraday Transactions 1: Physical Chemistry in Condensed Phases*, 76(0): 1911, 1980. doi: 10.1039/f19807601911.

[55] E. C. W. Clarke and D. N. Glew. Evaluation of the thermodynamic functions for aqueous sodium chloride from equilibrium and calorimetric measurements below 154°C. *Journal of Physical and Chemical Reference Data*, 14(2):489, 1985. doi: 10.1063/1.555730.

[56] E. C. W. Clarke and D. N. Glew. Erratum: Evaluation of the thermodynamic functions for aqueous sodium chloride from equilibrium and calorimetric measurements below 154°C [J. Phys. Chem. Ref. Data 14, 489 (1985)]. *Journal of Physical and Chemical Reference Data*, 18(1):545, 1989. doi: 10.1063/1.555824.

[57] G. Wedler and H.-J. Freund. *Lehr- und Arbeitsbuch Physikalische Chemie.* Wiley-VCH Verlag GmbH & Co. KGaA, Weinheim, 7 edition, 2018. ISBN 978-3-527-34611-0.

[58] M. Luckas and J. Krissmann. *Thermodynamik der Elektrolytlösungen.* Springer Berlin Heidelberg, Berlin, Heidelberg, 2001. ISBN 978-3-642-62619-7 978-3-642-56785-8.

[59] M. Nič, J. Jirát, B. Košata, A. Jenkins, and A. McNaught, editors. *IUPAC compendium of chemical terminology: Gold book.* IUPAC, Research Triagle Park, NC, 2.1.0 edition, 2009. ISBN 978-0-9678550-9-7. doi: 10.1351/goldbook.

[60] J. Gmehling, editor. *Chemical thermodynamics for process simulation.* Wiley-VCH, Weinheim, 2012. ISBN 978-3-527-31277-1.

[61] IAPWS. Revised release on the IAPWS industrial formulation 1997 for the thermodynamic properties of water and steam, 2007.

[62] Manuel R. Conde-Petit. *Aqueous solutions of lithium and calcium chlorides: Property formulations for use in air conditioning equipment design.* Zürich, Switzerland, 2009.

[63] E. L. Cussler and B. K. Dutta. On separation efficiency. *AIChE Journal*, 58(12):3825–3831, 2012. doi: 10.1002/aic.13779.

[64] Karan H. Mistry and John H. Lienhard. Effect of nonideal solution behavior on desalination of a sodium chloride (NaCl) solution and comparison to seawater. *Journal of Energy Resources Technology*, 135(4): 042003, 2013. doi: 10.1115/1.4024544.

[65] R. J. Meyer. *Natrium Ergänzungsband, Lieferung 7. Halogenide Systeme. Lösungen.* Springer, Berlin, Heidelberg, 1972. ISBN 978-3-662-11947-1.

[66] R. Cohen-Adad and J.W. Lorimer. Alkali metal and ammonium halides in water and heavy water. *IUPAC Solubility Data Series*, 47, 1991.

[67] M. M. Rafique, P. Gandhidasan, and H. M.S. Bahaidarah. Liquid desiccant materials and dehumidifiers - A review. *Renewable and Sustainable Energy Reviews*, 56:179–195, 2016. doi: 10.1016/j.rser.2015.11.061.

[68] J. W. Mullin. *Crystallization.* Butterworth-Heinemann, Oxford, Boston, 4th ed edition, 2001. ISBN 978-0-7506-4833-2.

[69] Alfons Mersmann, editor. *Crystallization technology handbook.* Marcel Dekker, New York, 2nd ed., rev. and expanded edition, 2001. ISBN 978-0-8247-0528-2.

[70] Zahid Amjad and Konstantinos D. Demadis, editors. *Mineral scales and deposits: Scientific and technological approaches.* Elsevier, Amsterdam, 2015. ISBN 978-0-444-63228-9.

[71] D. M. Warsinger, E. W. Tow, J. Swaminathan, and J. H. Lienhard V. Theoretical framework for predicting inorganic fouling in Membrane Distillation and experimental validation with calcium sulfate. *Journal of Membrane Science*, 528:381–390, 2017. doi: 10.1016/j.memsci.2017.01.031.

[72] V. Karanikola, C. Boo, J. Rolf, and M. Elimelech. Engineered slippery surface to mitigate gypsum scaling in Membrane Distillation for treatment of hypersaline industrial wastewaters. *Environmental Science & Technology*, 2018. doi: 10.1021/acs.est.8b04836.

[73] M. Kostoglou and A. J. Karabelas. Modeling scale formation in flat-sheet membrane modules during water desalination. *AIChE Journal*, 59(8): 2917–2927, 2013. doi: 10.1002/aic.14045.

[74] W. K. Burton, N. Cabrera, and F. C. Frank. The growth of crystals and the equilibrium structure of their surfaces. *Philosophical Transactions of the Royal Society A: Mathematical, Physical and Engineering Sciences*, 243(866):299–358, 1951. doi: 10.1098/rsta.1951.0006.

[75] R. Rodriguez-Clemente. Crystal growth kinetics of sodium chloride from solution. In J. W. Mullin, editor, *Industrial Crystallization*, pages 187–199. Springer US, Boston, MA, 1976. doi: 10.1007/978-1-4615-7258-9_17.

[76] T.M. Pääkkönen, M. Riihimäki, C.J. Simonson, E. Muurinen, and R.L. Keiski. Modeling CaCO3 crystallization fouling on a heat exchanger surface – Definition of fouling layer properties and model parameters. *In-*

*ternational Journal of Heat and Mass Transfer*, 83:84–98, April 2015. doi: 10.1016/j.ijheatmasstransfer.2014.11.073.

[77] A. Antony, J. H. Low, S. Gray, A. E. Childress, P. Le-Clech, and G. Leslie. Scale formation and control in high pressure membrane water treatment systems: A review. *Journal of Membrane Science*, 383(1-2):1–16, 2011. doi: 10.1016/j.memsci.2011.08.054.

[78] D.L. Parkhurst and C.A.J. Appelo. Description of input and examples for PHREEQC Version 3 - A computer program for speciation, batch-reaction, one-dimensional transport, and inverse geochemical calculations, 2013.

[79] P. J. de Moel, A. W. C. van der Helm, M. van Rijn, J. C. van Dijk, and W. G. J. van der Meer. Assessment of calculation methods for calcium carbonate saturation in drinking water for DIN 38404-10 compliance. *Drinking Water Engineering and Science*, 6(2):115–124, 2013. doi: 10.5194/dwes-6-115-2013.

[80] D. Freyer and W. Voigt. Crystallization and phase stability of CaSO4 and CaSO4 - based salts. *Monatshefte fuer Chemie / Chemical Monthly*, 134 (5):693–719, 2003. doi: 10.1007/s00706-003-0590-3.

[81] C. E. Mortimer and U. Müller. *Chemie: das Basiswissen der Chemie*. Thieme, Stuttgart, 7 edition, 2001. ISBN 978-3-13-484307-1 978-3-13-102766-5.

[82] R. A. Johnson and M. H. Nguyen. *Understanding Membrane Distillation and Osmotic Distillation*. Wiley, Hoboken, NJ, 2017. ISBN 978-0-470-12216-7.

[83] F. Kiefer, M. Spinnler, and T. Sattelmayer. Multi-Effect Vacuum Membrane Distillation systems: Model derivation and calibration. *Desalination*, 438:97 – 111, 2018. doi: 10.1016/j.desal.2018.03.024.

[84] J. Tonner. Barriers to Thermal Desalination in the United States. Technical Report 144, U.S. Department of the Interior, Bureau of Reclamation, 2008.

[85] A. Präbst, F. Kiefer, A. Kroiss, M. Spinnler, and T. Sattelmayer. Influence of dynamic operation of reverse osmosis systems on fluid dynamics and mass transfer by investigation of 2-D spacer filled channels. *Desalination and water treatment*, 73:30–45, 2017. doi: 10.5004/dwt.2017.2053.

[86] C.P. Koutsou, S.G. Yiantsios, and A.J. Karabelas. A numerical and experimental study of mass transfer in spacer-filled channels: Effects of spacer geometrical characteristics and Schmidt number. *Journal of Membrane Science*, 326(1):234–251, 2009. doi: 10.1016/j.memsci.2008.10.007.

[87] N. Horstmeyer, T. Lippert, D. Schön, F. Schlederer, C. Picioreanu, K. Achterhold, F. Pfeiffer, and J. E. Drewes. CT scanning of membrane feed spacers – Impact of spacer model accuracy on hydrodynamic and solute transport modeling in membrane feed channels. *Journal of Membrane Science*, 564:133–145, 2018. doi: 10.1016/j.memsci.2018.07.006.

[88] H. Julian, Y. Ye, H. Li, and V. Chen. Scaling mitigation in submerged vacuum membrane distillation and crystallization (VMDC) with periodic air-backwash. *Journal of Membrane Science*, 547:19–33, 2018. doi: 10.1016/j.memsci.2017.10.035.

[89] F. Kiefer, A. Präbst, K. S. Rodewald, and T. Sattelmayer. Membrane scaling in Vacuum Membrane Distillation - Part 1: In-situ observation of crystal growth and membrane wetting. *Journal of Membrane Science*, 590, 2019. doi: 10.1016/j.memsci.2019.117294.

[90] F. Kiefer, A. Präbst, and T. Sattelmayer. Membrane scaling in Vacuum Membrane Distillation - Part 2: Crystallization kinetics and process performance. *Journal of Membrane Science*, 590, 2019. doi: 10.1016/j.memsci.2019.117293.

[91] E. Guillen-Burrieza, M.O. Mavukkandy, M.R. Bilad, and H.A. Arafat. Understanding wetting phenomena in Membrane Distillation and how operational parameters can affect it. *Journal of Membrane Science*, 515: 163–174, 2016. doi: 10.1016/j.memsci.2016.05.051.

[92] M. Uchymiak, E. Lyster, J. Glater, and Y. Cohen. Kinetics of gypsum crys-

tal growth on a Reverse Osmosis membrane. *Journal of Membrane Science*, 314(1-2):163–172, 2008. doi: 10.1016/j.memsci.2008.01.041.

[93] J. Benecke, M. Haas, F. Baur, and M. Ernst. Investigating the development and reproducibility of heterogeneous gypsum scaling on Reverse Osmosis membranes using real-time membrane surface imaging. *Desalination*, 428:161–171, 2018. doi: 10.1016/j.desal.2017.11.025.

[94] N. Hilal, A. F. Ismail, T. Matsuura, and D. Oatley-Radcliffe, editors. *Membrane characterization*. Elsevier, Amsterdam, Netherlands, 2017. ISBN 978-0-444-63776-5.

[95] Eva-Maria Loew. *Analyse von Verbrennungsvorgängen im selbstzündungsdominierten Regime mittels Mischungsstatistik*. Dissertation, Technische Universität München, Munich, 2016.

[96] Inc. The MathWorks. Computer Vision Toolbox User's Guide, Revised for Version 8.2 (Release R2018b), 2018. URL https://de.mathworks.com/help/pdf_doc/vision/index.html.

[97] Inc. The MathWorks. Image Processing Toolbox User's Guide, Revised for Version 10.3 (Release 2018b), 2018. URL https://cde.mathworks.com/help/pdf_doc/images/index.html.

[98] H. D. Baehr and K. Stephan. *Wärme- und Stoffübertragung*. Springer-Verlag Berlin Heidelberg, Berlin, Heidelberg, 2010. ISBN 978-3-642-10194-6.

[99] J. Gilron and D. Hasson. Calcium sulphate fouling of reverse osmosis membranes: Flux decline mechanism. *Chemical Engineering Science*, 42(10):2351–2360, 1987. doi: 10.1016/0009-2509(87)80109-4.

[100] Suez Water Technologies & Solutions. *Handbook of Industrial Water Treatment*. 2019. URL https://www.suezwatertechnologies.com/handbook/handbook-industrial-water-treatment. accessed: 2019-08-12.

[101] P. J. de Moel, J. Q. J. C. Verberk, and J. C. van Dijk. *Drinking water: Principles and practices*. World Scientific, New Jersey, Hong Kong, 2006. ISBN 978-981-256-836-6.

[102] F. J. Millero, R. Feistel, D. G. Wright, and T. J. McDougall. The composition of standard seawater and the definition of the reference-composition salinity scale. *Deep Sea Research Part I: Oceanographic Research Papers*, 55(1):50–72, 2008. doi: 10.1016/j.dsr.2007.10.001.

[103] D. M. Warsinger, A. Servi, S. Van Belleghem, J. Gonzalez, J. Swaminathan, J. Kharraz, H. W. Chung, H. A. Arafat, K. K. Gleason, and J. H. Lienhard V. Combining air recharging and membrane superhydrophobicity for fouling prevention in Membrane Distillation. *Journal of Membrane Science*, 505:241–252, 2016. doi: 10.1016/j.memsci.2016.01.018.

[104] J. Kestin, H. E. Khalifa, and R. J. Correia. Tables of the dynamic and kinematic viscosity of aqueous NaCl solutions in the temperature range 20–150 °C and the pressure range 0.1–35 MPa. *Journal of Physical and Chemical Reference Data*, 10(1):71–88, 1981. doi: 10.1063/1.555641.

[105] A. I. Simion, C.-G. Grigoraș, and A.-M. Roșu. Mathematical modelling of density and viscosity of NaCl aqueous solutions. *Journal of Agroalimentary Processes and Technologies*, page 12, 2015.

[106] A. A. Aleksandrov, E. V. Dzhuraeva, and V. F. Utenkov. Thermal conductivity of sodium chloride aqueous solutions. *Thermal Engineering*, 60 (3):190–194, 2013. doi: 10.1134/S0040601513030026.

[107] V. M. M. Lobo. Mutual diffusion coefficients in aqueous electrolyte solutions. *Pure & Appl. Chem.*, 65(12):2613–2640, 1993.

[108] L. N. Plummer, D. L. Parkhurst, G. W. Fleming, and S. A. Dunkle. A computer program incorporating Pitzer's equations for calculation of geochemical reactions in brines. Water-Resources Investigations Report 88-4153, U.S. Geological Survey, 1988.

[109] P. J. Roache. Perspective: A method for uniform reporting of grid refinement studies. *Journal of Fluids Engineering*, 116(3):405, 1994. doi: 10.1115/1.2910291.

# BIBLIOGRAPHY

# A   Appendix: Thermophysical Properties of Salt Solutions

The following table summarizes the literature on thermophysical models and correlations for salt solutions as implemented in the system simulation and CFD models.

**Table A.1:** Models and correlations for thermophysical properties of aqueous salt solutions.

| Property | | Salt | Reference |
| --- | --- | --- | --- |
| Specific heat capacity | $c_p$ | NaCl | Clarke and Glew [55] |
| | | $CaCl_2$ | Conde-Petit [62] |
| Heat of dilution | $\Delta_{\text{dil}} H$ | NaCl | Clarke and Glew [55] |
| | | $CaCl_2$ | Conde-Petit [62] |
| Kinematic viscosity | $\nu$ | NaCl | Kestin et al. [104] |
| | | $CaCl_2$ | Conde-Petit [62] |
| Density | $\rho$ | NaCl | Simion et al. [105] |
| | | $CaCl_2$ | Conde-Petit [62] |
| Thermal conductivity | $\lambda$ | NaCl | Aleksandrov et al. [106] |
| | | $CaCl_2$ | Conde-Petit [62] |
| Mutual diffusion coefficient | $D$ | NaCl | Lobo [107] |
| | | $CaCl_2$ | Conde-Petit [62] |
| Properties of pure water and steam | | | IAPWS [61] |
| Models used in PHREEQC [78] | | | Plummer et al. [108] |
| | | | de Moel et al. [79] |

# B Appendix: Experimental Setups and Experiments

## B.1 Industrial Scale System

**Table B.1:** Specifications of the memsys 4-6.4 R&D unit [44].

| Specification | Unit | Value |
|---|---|---|
| Supplier | | memsys tec AG, Grafing, Germany |
| Type | | 4-6.4 R&D |
| Year of production | | 2014 |
| Stages | | 4 |
| Steam raiser membrane area | $m^2$ | 2.56 |
| Frames in steam raiser | | 17 |
| Stage membrane area | $m^2$ | 4 x 1.6 |
| Frames per stage | | 11 |
| Condenser foil area | $m^2$ | 2.56 |
| Frames in condenser | | 11 |
| Steam raiser nominal flow rate | $L\,h^{-1}$ | 1800 |
| Condenser nominal flow rate | $L\,h^{-1}$ | 1800 |
| Feed flow rate range | $L\,h^{-1}$ | 50 - 150 |
| Electrical heater power | kW | 17 |

**Table B.2:** Membrane specifications [36].

| Property | Unit | Value |
|---|---|---|
| Vendor | | GE Energy |
| Product type | | ASPIRE QL822 |
| Active layer material | | PTFE |
| Backing material | | PP |
| Reference pore diameter | µm | 0.2 |
| Thickness | mm | 0.12-0.22 |
| Water entry pressure | bar | > 3.5 |

## B.2   Bench Scale System

**Table B.3:** Measurement equipment of bench scale test rig.

| Short | Description | Range (calib.) | Error |
|---|---|---|---|
| T_XX | PT1000 4-wire RTD | 20-100 °C | 0.1 K |
| F_H1 | Magnetic flow meter Krohne Optiflux 5100C, DN6 | 0-200 l/h | 0.4%+1 mm/s |
| F_H2 | Magnetic flow meter Krohne Optiflux 5100C, DN4 | 0-200 l/h | 0.4%+1 mm/s |
| P_V1 | Pressure sensor Wika S20 | 0-1 bar, abs | 0.25% BFSL |
| M_D1 | Scales Kern KMB-TM | 0-6 kg | 0.2 g |
| M_D2 | Scales Sartorius Combics 1 | 0-30 kg | 1 g |

**Table B.4:** Overview of measurement data sets with triple channel bench scale test rig; each measurement campaign contains the given number of steady state measurement points (sets).

| Campaign (Sets) | Range | Description |
|---|---|---|
| M01 (10) | $w = 0$; $T_{H1} = T_{21} = 40,60\,°C$ | used for model calibration |
| M02 (4) | $w = 0$; $T_{H1} = 40,60\,°C$; $T_{21} = 55...70\,°C$ | used for model calibration |
| M03 (6) | $w = 0...0.25$ NaCl; $T_{11,21} = 60\,°C$ | NaCl feed concentration row |
| M04 (10) | $w = 0.15$ NaCl; $T_{11,21} = 40,60\,°C$ | Feed flow rate variation at 15% NaCl |
| M05 (4) | $w = 0.25$ NaCl; $T_{11,21} = 40,60\,°C$ | Feed flow rate variation at $w = 25$ NaCl; membrane wetting and crystal growth in vapor channel |
| M06 (6) | $w = 0...25\%$ CaCl$_2$; $T_{11,21} = 60\,°C$ | CaCl$_2$ feed concentration row |
| M07 (21) | $w = 0$; $T_{11,21} = 30...60\,°C$ | Heat exchanger experiments (no vacuum); feed flow rate variation |
| M08 (8) | $w = 0$; $T_{21} = 40,60\,°C$ | Feed flow rate variation; heating channel empty |
| M09 (8) | $w = 0$; $T_{11,21} = 30...70\,°C$ | Variation of $T_{11}$ and $T_{11} - T_{21}$ |
| M10 (10) | $w = 0$; $T_{62} = 5...40\,°C$ | Variation of $T_{62}$ |

## B.3 Microscopy Setup

**Table B.5:** Test rig components of the microscopy setup for scaling and membrane wetting detection (cf. Fig. 5.2).

| Name | Description | Value/Range | Error |
|---|---|---|---|
| **Sensors and measurement equipment** | | | |
| Temperature (T-F1,T-F2,T-ctr) | 4-wire RTD: PT1000 | 20-90 °C (calib.) | ±0.1 K |
| Vacuum pressure (P-vac) | Wika S20 | 0-1 bar abs | 0.25% BFSL |
| Differential pressure (P-diff) | Keller PD-23 | 0-2 bar | ±0.5% BFSL |
| Scales | Kern | 1-6200 g | 0.1 g |
| **Pumps, valves, heaters** | | | |
| Feed pump | Ismatec Reglo-Z | $2.1\text{-}210\,\mathrm{ml\,min^{-1}}$ | - |
| Vacuum pump | Oerlikon Leybold Trivac D8B, lowest pressure $\leq 10^{-4}$ mbar | $8\,\mathrm{m^3\,h^{-1}}$ | - |
| Pressure control valve | Vacuum precision pressure control valve R250, RP14VU | -1 - 0.14 bar | < 2 mbar |
| Heating plate | Magnetic hotplate stirrer VMS-C10 ADVANCED | 1500 W | - |
| Electric heater | 230 V ohmic heating cartridge with relay | max. 400 W | - |
| **Optical equipment** | | | |
| Microscope (Cam 1) | Infinity K2/Sc CF-3, WD 92-125 mm | MAG 3.05-2.06 + 4x | - |
| Flash light | Travor RF600 Macro LED Ring Flash | - | - |
| Camera (Cam 1) | Fujifilm XT10 mirrorless CMOS camera | 16.3 Mpx | - |
| Lens (Cam 2) | Tamron SP zoom lens | 24-135 mm, 1:3.5-5.6 | - |
| Filter adapter (Cam 2) | Nikon to C-mount filter adapter | - | - |
| Camera (Cam 2) | PCO SensiCam CCD camera | 1280 x 1024 px | - |
| Longpass filter (Cam 2) | Razor Edge LP 532 RU | transmission 539-1200 nm | - |
| CW laser | Coherent Genesis CX 488-4000 STM | 0.02-4 W, 488 nm | - |

**Table B.6:** Composition of feed solution with Sea salt 1 determined with AAS and ion chromatography. [*] Value below the limit of determination, due to high $Cl^-$ concentration.

| Parameter | Method | Value / $mg\,l^{-1}$ |
|---|---|---|
| Ca | AAS, DIN EN ISO 7980, DEV E3a | 78.8 |
| Fe | AAS, DIN 38406, DEV E32 | 3.1 |
| K | AAS, DIN 38406, DEV E13 | 37.1 |
| Mg | AAS, DIN EN ISO 7980, DEV E3a | 10.8 |
| Na | AAS, DIN 38406, DEV E14 | 115,000 |
| Sr | AAS | 4.66 |
| $Br^-$ | DIN EN ISO 10304-1, DEV D20 | < 600 [*] |
| $Cl^-$ | DIN EN ISO 10304-1, DEV D20 | 151,000 |
| $F^-$ | DIN EN ISO 10304-1, DEV D20 | < 600 [*] |
| $SO_4^{2-}$ | DIN EN ISO 10304-1, DEV D20 | 186 |

**Table B.7:** Boundary conditions for the scaling and membrane wetting experiments.

| Label | Spacer config. | Solute | Feed salt content $w_F, b_F$ | Feed temperature $T_F$ / °C | Mean feed velocity $\bar{u}_F$ / $m\,s^{-1}$ |
|---|---|---|---|---|---|
| CEx-03 | EB | sea salt | 0.26 | 50 | 0.02 |
| CEx-04-05 | EA | sea salt | 0.26 | 50 | 0.02 |
| CEx-11 (3 sets) | EA | sea salt | 0.26 | 50, 55, 60 | 0.01, 0.02, 0.03 |
| CEx-14 | EB | sea salt | 0.26 | 50, 60 | 0.02 |
| CEx-15 | BA | sea salt | 0.26 | 50, 60 | 0.01, 0.02 |
| CEx-16 | AB | sea salt | 0.26 | 50, 60 | 0.01, 0.02 |
| CEx-21 -full membrane | EA | sea salt | 0.26 | 55 | 0.02 |
| CEx-S01 | EA | $CaSO_4$ | $b_{Ca}$ = 29 mmol/kg | 55 | 0.02 |
| CEx-C02 | EA | $CaCO_3$ | $b_{Ca}$ = 0.8 mmol/kg | 55 | 0.02 |
| CEx-CS01 | EA | $CaCO_3$+$CaSO_4$ | $b_{Ca}$ = 29.8 mmol/kg | 55 | 0.02 |

## B.4 Results of the Energy-Dispersive X-Ray Spectroscopy (EDS) Analysis
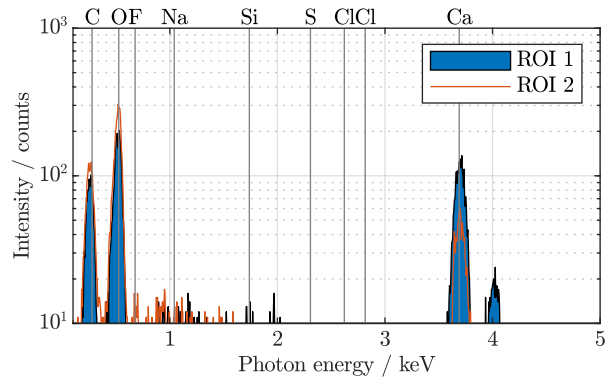


**Figure B.1:** EDS analysis for the $CaCO_3$ experiment (CEx-C02, cf. Tab. B.7). ROI 1 and 2 are analyses for different crystal shapes. [89]
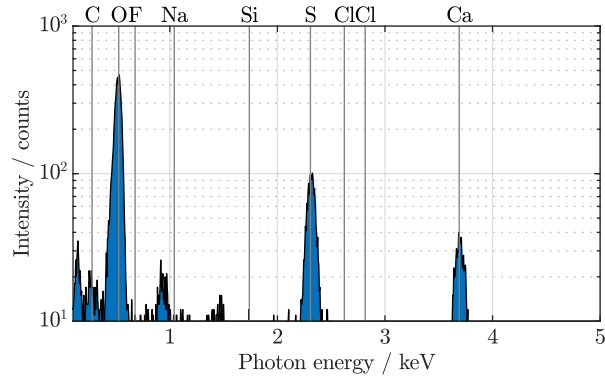


**Figure B.2:** EDS analysis for the $CaSO_4$ experiment (CEx-S01, cf. Tab. B.7). [89]
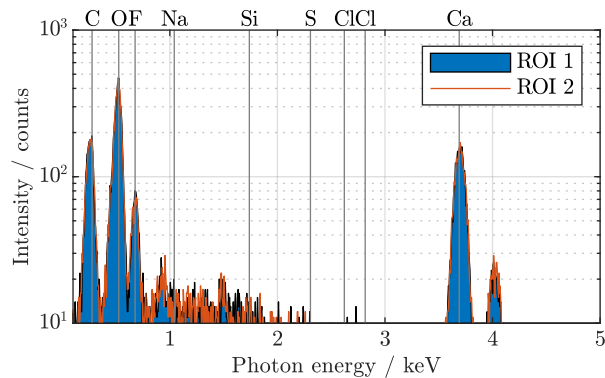


**Figure B.3:** EDS analysis for the $CaSO_4$+$CaCO_3$ experiment (CEx-CS01, cf. Tab. B.7). [89]

# C   Appendix: MEVMD System Simulation

**Table C.1:** Geometrical setup of the reference system.

| Component | Variable | Value / Range |
|---|---|---|
| Steam raiser (SR) | Frame type | double membrane, high flow |
| | Membrane area | $2.56\,\text{m}^2$ |
| | Spacer type | high flow |
| | Parallel channels | 17 |
| Stage (E) | Frame type | membrane-foil, low flow |
| | Membrane area | $1.6\,\text{m}^2$ |
| | Foil area | $1.6\,\text{m}^2$ |
| | Spacer type | feed spacer |
| | Parallel channels | 11 |
| Condenser (CO) | Frame type | double membrane, high flow |
| | Foil area | $2.56\,\text{m}^2$ |
| | Spacer type | high flow |
| | Parallel channels | 17 |

**Table C.2:** Boundary conditions for the reference system.

| Component | Variable | Unit | Value / Range |
|---|---|---|---|
| Steam raiser (SR) | $T_{11}$ | °C | 70 |
| | $\dot{m}_{11}$ | $\text{kg}\,\text{h}^{-1}$ | 1800 |
| Feed (F) | $T_{21}$ | °C | 50 |
| | $\dot{m}_{21}$ | $\text{kg}\,\text{h}^{-1}$ | 100 |
| | $w_{21}$ | $\text{g}\,\text{kg}^{-1}$ | 80 |
| Condenser (CO) | $T_{61}$ | °C | 30 |
| | $\dot{m}_{61}$ | $\text{kg}\,\text{h}^{-1}$ | 1800 |

**Table C.3:** Relevant phases displayed in speciation calculation results.

| Name | Chemical formula |
|------|------------------|
| Anhydrite | $CaSO_4$ |
| Aragonite | $CaCO_3$ |
| Calcite | $CaCO_3$ |
| Dolomite | $CaMg(CO_3)_2$ |
| Glauberite | $Na_2Ca(SO_4)_2$ |
| Gypsum | $CaSO_4 \cdot 2\,H_2O$ |
| Halite | $NaCl$ |

# D   Appendix: Computational Fluid Dynamics

## D.1   Grid Convergence Study

A grid convergence study according to Roache [109] was conducted to ensure independence of the numerical solution from the grid and estimate the discretization error. The finest mesh was applied for the simulations.
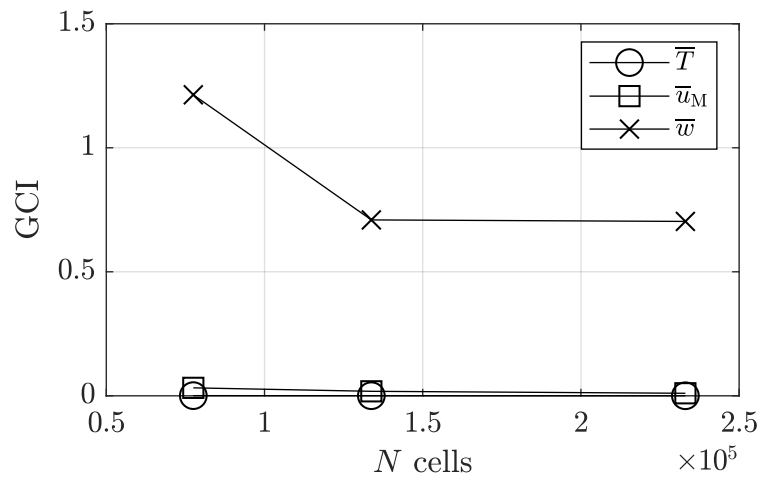


**Figure D.1:** Grid convergence index (GCI) for salt mass fraction, temperature, and flux at membrane boundary.

## D.2   Discretization Schemes

For the steady-state solution spatial gradients and divergence terms were approximated using a central difference scheme limited with a factor of 0.2 ("limitedLinear 0.2") which is between first and second order. In the case of

the scalar field for salt mass fraction, "vanLeer" scheme was applied. Laplacian as well as surface normal terms were approximated using the second order scheme "corrected".

# Previous Publications

Parts of this thesis were previously published by the author in journal papers [19,83,85,89,90] and a project report (F. Kiefer, M. Spinnler, T. Sattelmayer, Experimentelle und theoretische Untersuchungen zu einem hocheffizienten, solarbetriebenen Klimatisierungsverfahren auf Basis flüssiger Sorbenzien: Solar Powered Air Conditioning Efficiency (SPACE) – Schlussbericht Förderkennzeichen BMBF 01DH13019, doi 10.2314/GBV:101095900X). These publications were registered according to the valid doctoral regulations. However, not all of them are cited explicitly everywhere. Whether these personal previously printed publications were referenced depends on maintaining comprehensibility and providing all necessary context.